THESE DE DOCTORAT DE

L'INSTITUT NATIONAL DES SCIENCES
APPLIQUEES RENNES

COMUE UNIVERSITE BRETAGNE LOIRE

ECOLE DOCTORALE N° 601
*Mathématiques et Sciences et Technologies
de l'Information et de la Communication*
Spécialité : *Télécommunications*

Par

Mohamed SHEHATA

Hybrid Analog and Digital Techniques Applied to Massive MIMO Systems for 5G Transmission at Millimeter Waves

Rapporteurs avant soutenance :

Marie-Laure Boucheret   Professeur, ENSEEIHT, Toulouse
Sébastien Roy   Professeure, Université de Sherbrooke

Composition du Jury :

Président :	Méroune Debbah	Professeur, CentraleSupelec, Paris
Examinateurs :	Marie-Laure Boucheret	Professeur, ENSEEIHT, Toulouse
	Sébastien Roy	Professeure, Université de Sherbrooke
	Méroune Debbah	Professeur, CentraleSupelec, Paris
	André Doll	Ingénieur expert, Radio Frequency Systems
Dir. de thèse :	Maryline Hélard	Professeure, INSA de Rennes
Co-dir. de thèse :	Matthieu Crussière	Maître de conférences, HDR ,INSA de Rennes
	Patrice Pajusco	Maître de conférences, IMT Atlantique, Brest

Invité(s)

Claude Desset   Senior wireless communications researcher, imec, Belgium

Intitulé de la thèse :

Hybrid Analog and Digital Techniques Applied to Massive MIMO Systems for 5G

Transmission at Millimeter Waves.

Mohamed SHEHATA

En partenariat avec :

Preface

This work represents my PhD thesis done at INSA de Rennes, in the Communications System department (SYSCOM). This work was carried out during the period from October 2016 to September 2019 in Rennes in INSA de Rennes at the Institut d'Électronique et de Télécommunications de Rennes (IETR).

Rennes, 07-09-2019

signature
Mohamed Shehata

RÉSUMÉ EN FRANÇAIS

Introduction

La technologie massive MIMO est considérée comme un acteur clé dans les transmissions Multi Utilisateurs (MU) [1], du fait qu'avec un grand nombre d'antennes, des faisceaux quasi orthogonaux peuvent être formés pour plusieurs Utilisateurs (UEs). Désormais, il est possible de desservir plusieurs utilisateurs sur les mêmes ressources de temps et de fréquence et de les différencier dans l'espace, ce qui améliore considérablement l'efficacité spectrale (SE) et la couverture du réseau.

Afin d'envisager la mise en œuvre concrète du MU massive MIMO, deux facteurs principaux doivent être pris en compte. Le premier facteur est le nombre d'antennes, car les études théoriques considèrent un très grand nombre d'antennes, c'est pratiquement impossible aux fréquences micro-ondes conventionnelles (< 6 GHz) [2]). De plus, même si la base station (BS) peut déployer un très grand réseau MIMO aux hyperfréquences, il n'est pas possible de déployer un grand nombre d'antennes côté UE à ces fréquences. Le deuxième facteur limitant pour MU massive MIMO est la complexité du matériel et la consommation d'énergie [3]. Compte tenu du fait que, pour prendre en charge les scénarios MU avec un précodage numérique massive MIMO, il convient de prendre en compte le précodage.

Dans ce cas, une chaîne de radiofréquence (RF) dédiée est nécessaire par antenne d'émission, ce qui représente une complexité matérielle extrêmement élevée et une consommation énergétique importante, car les amplificateurs de puissance ne sont pas parfaits dans des scénarios réalistes.

Contrairement aux systèmes à micro-ondes classiques (< 6 GHz), les systèmes mmWave exploitent la bande de 28 GHz à 300 GHz. Poussés par des ressources spectrales aussi vastes, les systèmes mmWave associés à un massive MIMO sont considérés comme l'un des principaux catalyseurs de la 5G.

Dans les systèmes MU mmWave massive MIMO, le problème de perte de propagation sur les fréquences mmWave est résolu en utilisant le gain de transmission offert par le grand nombre d'antennes de transmission.

En outre, le problème de la taille des massive MIMO est résolu aux fréquences millimétriques, car, grâce à la faible longueur d'onde, le réseau d'antennes peut être déployé avec une taille acceptable.

De plus, les problèmes de matériel et de consommation d'énergie des systèmes MIMO mmWave massifs de MU peuvent être résolus à l'aide de la technique de formation de faisceau récemment proposée, La formation de faisceau hybride (HBF) [4, 5]. Contrairement au précodage numérique conventionnel utilisé pour les systèmes massive MIMO nécessitant une chaîne RF dédiée par antenne, le HBF n'a besoin que d'un reduit nombre de chaînes RF par rapport au nombre d'antennes d'émission. Malgré la réduction importante de la complexité matérielle et de la consommation d'énergie, le HBF peut toujours obtenir une SE proche par rapport aux solutions de précodage entièrement numériques aux fréquences mmWave [5, 6]. Cela est dû au fait que, en bandes millimétriques, le canal est clair (avec une composante dominante line of sight (LoS)). Désormais, quelques chaînes RF suffisent pour contrôler complètement les chemins dominants du canal [7, 8].

Tout au long de la thèse, nous considérons formation de faisceau hybride (HBF) dans les systèmes MU MIMO masssif mmWave. Nous fournissons des etudes analytiques pour certains précodeurs analogiques et numériques linéaires dans des canaux mmWave à dominante LoS avec un réseau d'antennes d'émission massif.

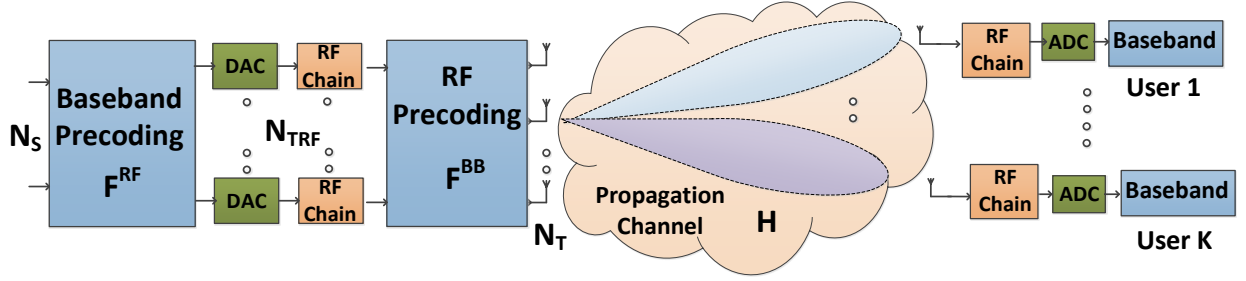## Contexte des Systèmes Hybrides Onde Millimétrique Massive MIMO

Figure 1: L'Architecture Hybride du Beamforming

Poussé par les inconvénients de la formation de faisceau analogique et numérique pour les systèmes MU mmWave massive MIMO, l'émergence de HBF est devenue une nécessité pour que ces systèmes fonctionnent efficacement [8]. L'idée principale de HBF est de trouver un équilibre entre le SE élevé offert par la mise en forme de faisceau numérique et la faible complexité matérielle et la consommation d'énergie offertes par la mise en forme de faisceau analogique. Comme le montre la Figure 1, l'architecture HBF est flexible, le traitement du signal est partagé entre les domaines analogique et numérique. Dans le domaine analogique, un réseau de déphaseurs [5] ou un réseau de formation de faisceaux analogique fixe [9] peut être utilisé pour préformer des faisceaux physiques dans les directions des équipements d'utilisateur. Ensuite, les dimensions du canal sont compressées.

Modèle de Système

Au cas où, faisceaux hybrides sont appliqués dans un MU MISO système, comme indiqué à la Figure 1, lorsque chaque utilisateur est équipé d'une seule antenne de réception $N_R = 1$ et ne peut recevoir qu'un seul flux, le vecteur de signal reçu $\mathbf{r} = [r_1, r_2, ..., r_K]$ peut être exprimé comme suit:

$$\mathbf{r} = \sqrt{P_T}\mathbf{H}\mathbf{F}^{RF}\mathbf{F}^{BB}\mathbf{s} + \mathbf{n} \tag{1}$$

où P_T est la puissance d'émission, $\mathbf{H} \in \mathbb{C}^{K \times N_T}$ est la matrice de canaux multi-utilisateurs, où K est le nombre total d'utilisateurs et N_T est le nombre d'antennes d'émission. $\mathbf{s} \in \mathbb{C}^{K \times 1}$ est le vecteur du signal de transmission avant le pré-codage et $\mathbf{n} \in \mathbb{C}^{K \times 1}$ représente le vecteur de bruit blanc gaussien additif (AWGN). Dans ce cas, le précodeur hybride consiste en une partie

analogique $\mathbf{F}^{RF}$ de dimensions $N_T \times N_{TRF}$, où N_{TRF} est le nombre de chaînes Radio Frequency (RF) transmises, et une partie numérique $\mathbf{F}^{BB}$ de dimensions $N_{TRF} \times K$.

Modèle de Canal

Le vecteur de canal à bande étroite pour chaque utilisateur k avec une seule antenne de réception $\mathbf{h}_k$ est représenté comme suit::

$$\mathbf{h}_k = \sqrt{\frac{N_T}{N_p{}^k}} \sum_{p=1}^{N_p{}^k} \alpha_{k,p} \mathbf{a}_t(\phi^t{}_{k,p})^H \tag{2}$$

où $\alpha_{k,p}$ est l'amplitude complexe du chemin de propagation p qui est l'un des chemins reçus par l'utilisateur k, N_{pk}, avec l'effet de perte de chemin, tel que $\alpha_{k,p} \sim \mathcal{CN}(0,1)$. Tandis que $\phi^t{}_{k,p}$, présente le angle de départ (AoD) pour le chemin p d'utilisateur k, tel que $\phi^t{}_{k,p} \in [0, 2\pi]$. Enfin, $\mathbf{a}_t(\phi^t{}_{k,p})$ est le vecteur de direction de la matrice de transmission qui dépend de la géométrie du réseau d'antennes.

Analyse Analytique pour la Formation de Faisceau Hybride dans des Canaux d'Ondes Millimétriques Massive MIMO

Dans le chapitre 3, nous fournissons une etude analytique pour formation de faisceau hybride. Nous commençons par considérer un canal à seul trajet (LoS) et définissons la condition pour laquelle formation de faisceau hybride (HBF) et la formation de faisceau entièrement numérique permettent d'obtenir une SE similaire.

Nous prouvons mathématiquement que HBF et la mise en forme de faisceau entièrement numérique peuvent atteindre exactement le même SE avec une consommation d'énergie minimale lorsque le canal est supposé pur LoS, et que un precodage de type Zero Forcing (ZF) est utilisé par la partie numérique du HBF. De plus, nous montrons que cette équivalence est remplie avec les exigences matérielles minimales possibles pour HBF (le nombre de chaînes RF émises est égal au nombre de flux spatiaux desservis). Enfin, nous validons nos propositions par des résultats de simulation comme le montre la Figure 2.

Ensuite, nous fournissons de manière analytique une expression pour le SE de la direction de faisceau LoS analogique et le HBF correspondant dans un canal LoS pur et le vérifons avec les résultats de la simulation, comme indiqué à la Figure 3.

Systèmes à Multi-Utilisateurs Ondes Millimétriques Massive MIMO à Faible Complexité

Dans le chapitre 4, nous fournissons des techniques de traitement du signal de faible complexité afin de permettre la mise en œuvre de systèmes MU mmWave massive MIMO.

Nous commençons par examiner un système de formation de faisceaux et d'allocation de puissance pour les canaux mmWave à dominante LoS. Ce cadre angulaire repose sur l'orientation du faisceau (DBS) pour la formation du faisceau et l'allocation de puissance basée sur les
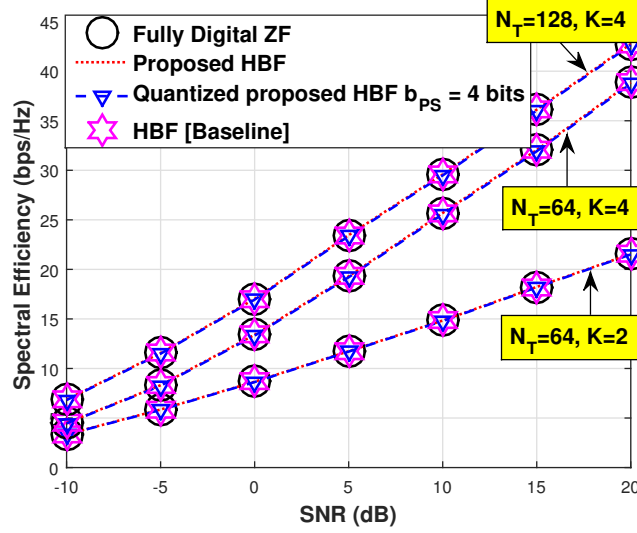
1) Comparaison SE des architectures de formation de faisceau proposées pour différents N_T et K.
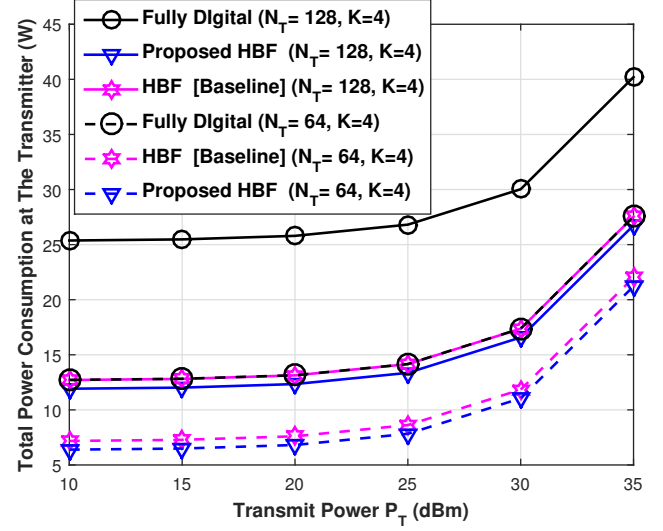
2) Comparaison de la consommation d'énergie de l'émetteur pour les architectures de formation de faisceau proposées pour différents N_T et K.

Figure 2: Comparaisons SE et consommation d'énergie pour les architectures de formation de faisceau proposées pour différents N_T et K.

fuites (LBPA) pour l'allocation de puissance. Bien que DBS soit une technique de précodage numérique, sa complexité est faible.

La Figure 4 montre que DBS-LBPA présente les avantages suivants: Il convient mieux aux systèmes MU MIMO à dominance LoS avec une connaissance partielle du canal que les solutions complexes traditionnelles (telles que ZF).Il garantit un seuil d'équité relatif entre les équipements utilisateur, en minimisant les fuites.

Plus tard, nous proposons un nouvel algorithme de sélection des UEs basé sur le rapport signal sur fuite et rapport de bruit (SLNR) pour maximiser le SE du système avec des exigences de complexité faible. Ensuite, nous mettons en évidence par des simulations les gains potentiels obtenus par l'approche de sélection des UE consciente du brouillage par rapport aux techniques de l'état de la technique illustrées à la Figure 5.

Formation de Faisceau Hybride avec Modulation d'Indice

La modulation spatiale en réception (RSM) devrait constituer une solution peu complexe pour les futurs récepteurs Internet of Things (IoT), et permettre d'obtenir un taux d'erreurs sur les bits (BER) réduit. De plus, les systèmes mmWave ont ouvert la voie pour atteindre des débits de données de pointe élevés. Dans ce chapitre, nous utilisons les caractéristiques susmentionnées des systèmes mmWave pour concevoir un système RSM-HBF robuste et performant sur le plan spectral, comme illustré à la Figure 6.
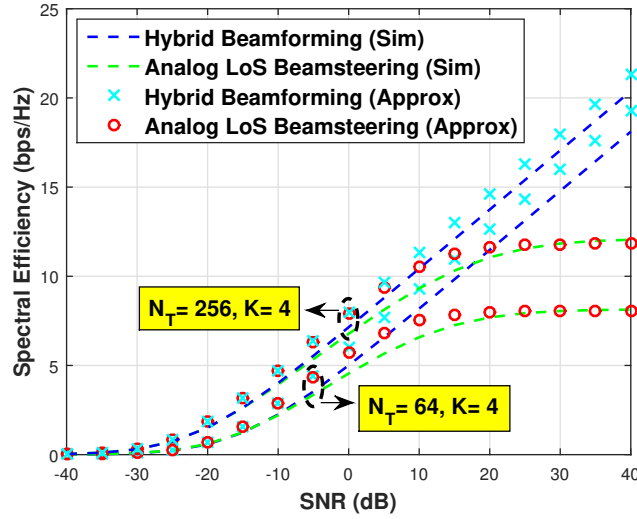
1)Approximations simulées et théoriques de SE par flux pour les systèmes MU-LoS beamsteering et MU-HBF, pour différentes valeurs de N_T et $K = N_b = 4$.
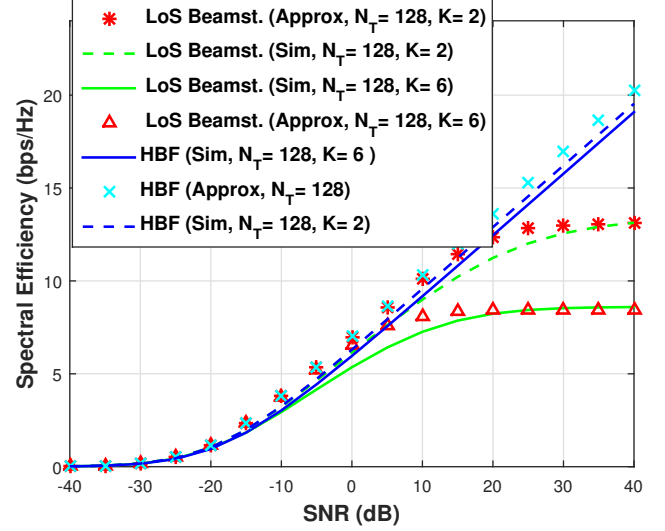
2) Approximations simulées et théoriques de SE par flux pour les systèmes de guidage de faisceau MU-LoS et MU-HBF, pour différents $K = N_b$ étant donné $N_T = 128$.

Figure 3: Approximations simulées et théoriques de SE par flux pour les systèmes de guidage de faisceau MU-LoS et MU-HBF.

De plus, nous dérivons analytiquement la valeur optimale atteinte SE et BER si le récepteur est utilisé avec deux antennes de réception dans un environnement en LoS. En plus, nous calculons de manière analytique le BER obtenu dans un environnement de canal à trajets multiples afin de réaliser une analyse complète. L'analyse analytique et numérique montre que le RSM est pratiquement réalisable en mmWave et peut atteindre de très bonnes performances en appliquant avec soin les techniques de formation de faisceau et de minimisation de corrélation appropriées à l'émetteur et en augmentant l'espacement inter-antenne au niveau du récepteur. Aussi, le gain de conception de récepteur de faible complexité peut être complètement exploité aux bandes millimétriques.

Sondage de Canal pour Analyse Réaliste

Dans le chapitre 6, une implémentation d'un système de transmission sans fil clairsemé (avec peu de multi trajets) à 2,4 GHz sera élaborée en commençant par la plate-forme utilisée pour atteindre notre objectif à l'aide du framework massive MIMO de National Instruments (NI). De plus, nous fournirons une comparaison entre les résultats de la simulation utilisant le modèle de canal statistique utilisé tout au long de la thèse et le modèle réaliste estimé à l'aide de la plateforme NI.

Ensuite, nous décrivons le système de sondage de canal sans fil à 60 GHz et fournissons une comparaison entre les résultats de la simulation utilisant le modèle de canal statistique et le
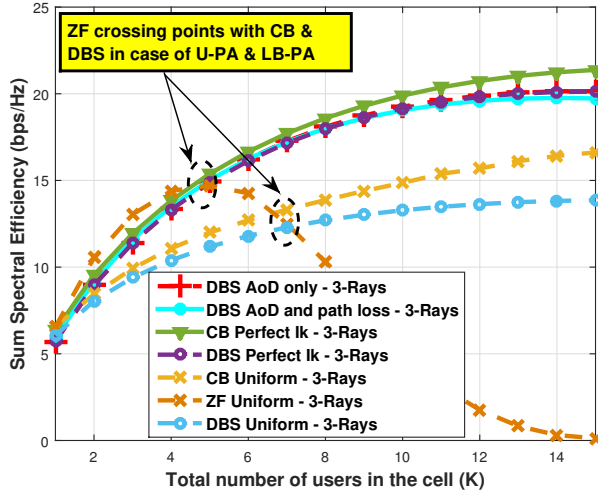
1) Somme SE des précodeurs proposés en supposant un CSI parfait au niveau de l'émetteur dans l'environnement à 3 rayons. La SE est en moyenne sur 500 positions UE aléatoires pour chaque $K \in [1, 15]$ avec $N_T = 16$.
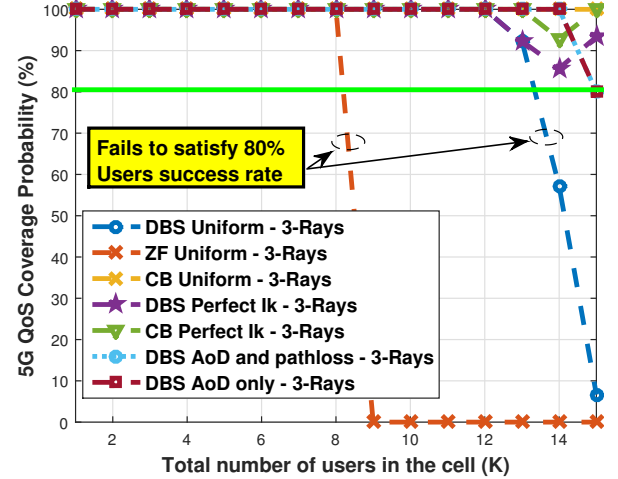
2) Probabilité de couverture des précodeurs proposés en supposant un CSI parfait au niveau de l'émetteur dans l'environnement à 3 rayons. La probabilité de couverture est établie en moyenne sur 500 positions aléatoires d'UE pour chaque $k \in [1, 15]$ avec $N_T = 16$.

Figure 4: SE et probabilité de couverture des précodeurs proposés en supposant un CSI parfait au niveau de l'émetteur dans l'environnement à 3 rayons.

modèle réaliste fourni par notre sondeur de canal proposé à 60 GHz.

Conclusions

Dans cette thèse, nous avons présenté un système MU mmWave massive MIMO. La thèse était basée sur quatre axes pour un tel système qui sont:

- Analyse analytique: Au chapitre 3, nous avons commencé par considérer un canal en LoS pur, puis avons défini la condition pour laquelle HBF et la formation de faisceau entièrement numérique permettent d'obtenir une SE similaire. Ensuite, nous avons fourni une expression analytique de la SE pour la direction de faisceau de LoS analogique et le HBF correspondant dans un canal de LoS pur. Plus tard, nous avons ensuite analysé les performances SE de plusieurs formateurs de faisceaux analogiques dans un canal à trajets multiples clairsemés et leur extension avec systèmes HBF. Nous avons également fourni un nouveau formateur de faisceaux analogiques de faible complexité de type HBF pouvant atteindre des performances SE optimales. Enfin, nous avons validé tous les modèles analytiques en utilisant des résultats de simulation.

- Développement d'algorithmes de faible complexité: Au chapitre 4, nous avons fourni des techniques de traitement du signal de faible complexité afin de permettre la mise en œuvre
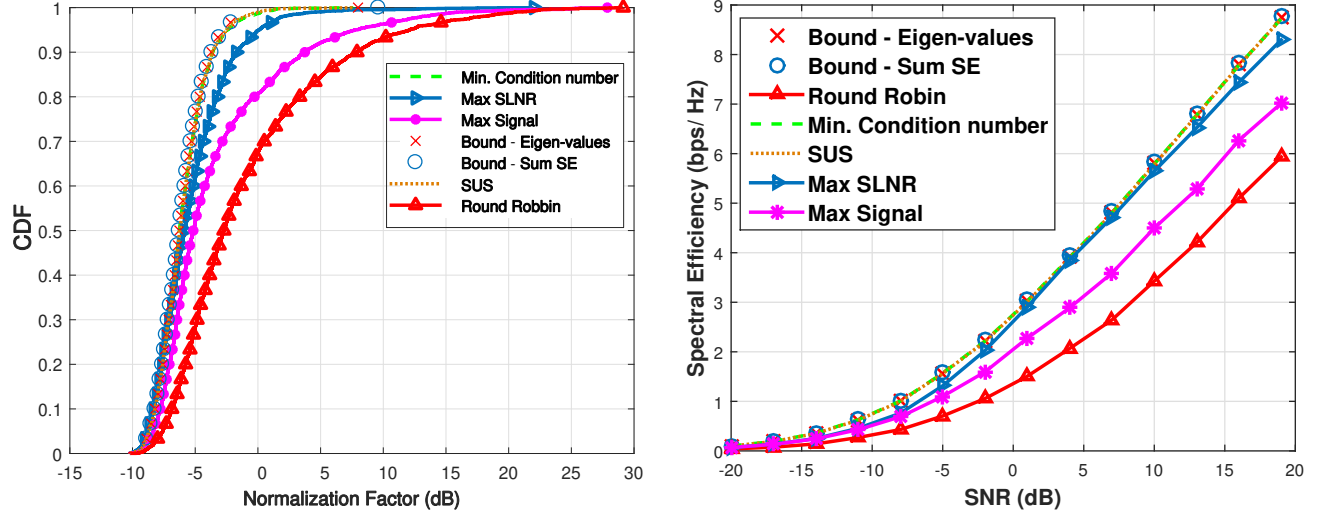
1) Comparaison entre le facteur de normalisation pour les différentes stratégies de sélection d'utilisateurs introduites dans un environnement LoS pur étant donné que $N_T = 16$, $|\mathcal{K}| = 7$, $|\mathcal{C}| = 3$ et $\Delta\phi^t = \frac{\pi}{3}$.

2) Comparaison entre les SE par flux pour les différentes stratégies de sélection d'utilisateurs introduites dans un environnement LoS pur étant donné que $N_T = 16$, $|\mathcal{K}| = 7$, $|\mathcal{C}| = 3$ et $\Delta\phi^t = \frac{\pi}{3}$.

Figure 5: Comparaison entre le facteur de normalisation et le SE par flux pour les différentes stratégies de sélection d'utilisateur introduites dans un environnement LoS pur.
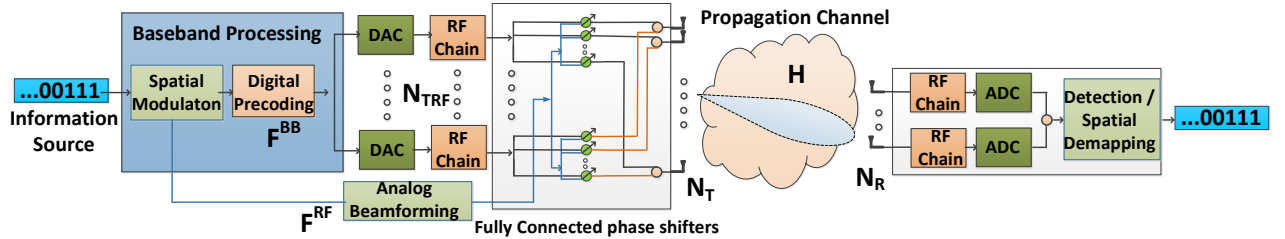

Figure 6: Schéma fonctionnel de RSM avec l'architecture mmWave HBF.

de systèmes mmWave massive MIMO pratiques. Nous avons commencé par examiner une technique de formation de faisceaux et d'allocation de puissance basée sur les angles, faible complexité, pour les canaux mmWave à dominante LoS. Ce cadre angulaire repose sur orientation numérique du faisceau (DBS) pour la formation de faisceau et allocation de puissance basée sur les fuites (LBPA) pour l'allocation de puissance. Ces techniques permettent de répondre aux exigences de faible complexité et de surcharge liées aux systèmes MU mmWave massive MIMO. Enfin, nous avons proposé une nouvelle approche de sélection d'UE de faible complexité appelée sélection d'UE basée sur les fuites et avons

étudié ses performances dans des canaux en LoS purs.

- HBF avec analyse de modulation d'indice: Au chapitre 5, nous avons présenté une étude détaillée d'un système à base de modulation spatiale (SM) en mmWave, couvrant plusieurs les scénarios possibles de manière analytique et numérique, par rapport aux travaux existants dans la littérature. Nous avons dérivé des formulations pour la SE dans le cas d'un canal pur LoS pour plusieurs scénarios de déploiement possibles, avec deux antennes de réception, et avec une optimisation du déploiement du transmetteur obtenu en appliquant la minimisation de la corrélation. De même, nous avons dérivé des formulations pour le BER en canal LoS pur pour tout scénario de déploiement possible, avec deux antennes de réception, et un déploiement optimal du transmetteur appliqué pour minimiser la corrélation. De plus, une formulation pour le BER a été dérivée pour les environnements à trajets multiples ainsi qu'une analyse complète des performances réalisables du RSM avec HBF. Tous les modèles introduits ont été validés par analyse numérique.

- Sondage de canal: Au chapitre 6, nous avons fourni les résultats de sondage de canal pour deux canaux, l'un à 2.4 GHz avec environnement de canal clairsemé et l'autre à 60 GHz. Il a été démontré que le canal 2.4 GHz était sondé dans un environnement clairsemé peut être parfaitement décrit par le modèle statistique de canal clairsemé utilisé tout au long de la thèse. D'autre part, le canal sondé à 60 GHz peut être mieux décrit par la version sans visibilité directe du modèle statistique simple, du fait que cette dernière est largement dominante.

Dans cette thèse, nous avons considéré un modèle de canal à bande étroite pour le canal mmWave MIMO. Nous avons également supposé que le CSI parfait était disponible et supposait des scénarios à cellule unique avec des terminaux de communication stationnaires. De plus, nous n'avons considéré qu'une architecture matérielle analogique, celle des déphaseurs entièrement connectés. Par conséquent, en tant que travail futur, les algorithmes présentés doivent être étendus pour prendre en compte les scénarios suivants:

- Frequency Selective Channels: Dans les systèmes mmWave MIMO avec HBF, l'extension de l'analyse à bande étroite à large bande n'est pas aussi simple que dans les canaux hyperfréquences (¡6 GHz). Cela est dû au fait que dans de tels systèmes, il existe une formation de faisceau analogique, qui est plate sur toute la fréquence et ne peut pas être changée d'une sous-porteuse à l'autre, comme c'est le cas avec la formation de faisceau numérique dans les systèmes à micro-ondes. Par conséquent, il est important d'évaluer l'extension des techniques HBF proposées dans cette thèse pour traiter du scénario de canal sélectif en fréquence.

- CSI imparfait: Dans des scénarios réalistes, l'hypothèse d'un CSI parfait n'est plus valide. Par conséquent, différentes techniques d'estimation de canal doivent être utilisées conjointement avec les algorithmes HBF proposés dans la thèse afin d'évaluer la sensibilité de tels algorithmes avec une erreur d'estimation de canal réaliste.

- Mobilité et cohérence spatiale: Afin de rendre nos algorithmes proposés plus efficaces pour des scénarios réalistes, il est crucial de prendre en compte la mobilité des utilisateurs. Dans ce cas, la cohérence spatiale doit être évaluée pour connaître l'effet de la mobilité sur la dégradation du signal. De plus, des techniques de poursuite de faisceau peuvent être développées en conjonction avec les algorithmes proposés afin d'éviter toute dégradation grave du signal reçu en cas de mobilité.

Acknowledgments

First of all I have to mention that this work would not have been accomplished without this supportive and helpful environment I have experienced from my family and my colleagues in INSA de Rennes which I consider a bless from god and a pride to work in such a place.

I would like to thank my wife Aya for always being there beside me and specially in all the hard and stressful moments. I would like also to thank her for always supporting me and helping me every-time I needed that and always believing in me and motivating me to achieve the best for our small family.

I would like to thank my parents and my sisters for always supporting me in my decisions and providing me the atmosphere to develop myself and always being keen for my success from the beginning. Their continuous sacrifices and support were always motivating me to achieve better and make them proud of me.

I would like to thank Maryline Helard the director of my PhD thesis for being my 'academic mother' being always keen to provide me with all I need in order to enhance myself personally and academically and also being always keen to provide me with a perfect atmosphere to unleash all my research capabilities. I would like also to thank Matthieu Crussiere my co-supervisor who was always helping me to get the best out of myself. Our interesting meetings were always fruitful with lots of ideas and motivation to achieve cutting edge research. I admit that I am going to miss such meetings. Finally, I have to thank Patrice Pajusco who was always keen to add the practical validity part to my work throughout my PhD. Our meetings together specially at the first part of the PhD where always interesting and fruitful. I am really grateful to all my three supervisors and I admit that without their continuous help and support this work wouldn't have been accomplished in that way.

I would like to thank my rapporteurs Prof. Sébastien Roy and Prof. Marie-Laure Boucheret for their thoughtful remarks and their fruitful discussions regarding the thesis subject and future perspectives. I would also like to deeply thank the jury members Prof. Mérouane Debbah, Ing. André Doll and Ing. Claude Desset for their time to attend my defence and for the interesting discussions and opinions they shared with me.

I would like to thank my colleague Dr. Ali Mokh, who participated with me in multiple collaborative tasks regarding index modulation, hence I am really thankful for his time and support. Also, I would like to thank my colleagues Mohammad Alawieh, Marwan El Hajj and Francois Yven whom helped me with the practical validation part of my work. Without their continuous work and support, this part would not have been done.

Finally, I would like to thank all the teams of the M5HESTIA (mmW Multi-user Massive MIMO Hybrid Equipments for Sounding, Transmissions and HW ImplementAtion) project, which I was a part of during my PhD period. Throughout this period I had the opportunity to work in close cooperation with industrial partners from Orange labs and B¡¿com in Rennes and academic partners from IMT atlantique and the university of Rennes 1, where I had the opportunity to work with diverse teams working in the antenna/RF modelling, channel modelling and propagation and hardware prototyping. Henceforth, I have developed deep understanding not only in the signal processing and analytical analysis domains but also in hardware and practical constraints of such systems that need to be considered.

Contents

List of Figures

List of Tables

Abbreviations

3GPP Third Generation Partnership Project. 16, 20, 138

ADC Analog to Digital Converter. 26, 28, 29, 32, 33, 35

AoA Angle of Arrival. 15, 16, 21, 52, 74, 128, 130

AoD Angle of Departure. xvii, 15–18, 21, 23, 28, 30, 52, 74–76, 79–84, 128, 130, 140

APAVSM Analog Precoding-Aided Virtual Space Modulation. 105

AWGN Additive White Gaussian Noise. 9, 27, 107, 129

BB Base Band. 10, 26, 28, 35, 38, 39, 46, 55, 56, 71, 75, 86, 93, 108, 127

BEP Bit Error Probability. 103, 126–129, 133, 135

BER Bit Error Rate. xviii, 5, 103–106, 117–119, 124, 125, 131–133, 135

BIM Beam Index Modulation. xiv, xviii, 3–5, 103–105, 126–133, 135

BS Base Station. xiii, xvii, 2, 9–14, 17, 21–23, 44, 46, 54, 56, 60, 63–65, 77, 79, 80, 84, 85, 92–94, 108, 138, 139

BW Band Width. 2, 4, 19, 21, 26, 32, 38, 51, 53, 77, 78, 81, 135, 138, 139

CB Conjugate Beamforming. 10, 11, 30, 38, 75–77, 82

CSI Channel State Information. xvii, 11, 33, 40, 50, 60, 69, 75, 76, 82, 83, 119, 131, 135, 138

D2D Device to Device. 84

DAC Digital to Analog Converter. 28, 29, 32, 33, 48, 49

DBS Digital Beam Steering. xiv, 3, 5, 30, 73–79, 81–83, 134

DFT Discrete Fourier Transform. xviii, 37, 140, 141

DoA Direction of Arrival. 81

DoF Degree of Freedom. 1, 92

DPC Dirty Paper Code. 9

DSP Digital Signal Processing. 61, 75, 84, 98

EE Energy Efficiency. 1, 33, 49, 51, 75

EGC Equal Gain Combining. 67, 68

EGT Equal Gain Transmission. 3, 5, 28, 38, 62, 67, 68, 74, 84–86, 88–91, 108, 118, 119, 125, 134

FPGA Field Programmable Gate Array. 138

GenSM Generalized Spatial Modulation. 105

GM Geometric Mean. 86, 88, 89

HBF Hybrid Beamforming. xiii, xiv, xvi–xviii, 2–5, 8, 26, 30, 32–34, 38, 39, 43–72, 74, 84–95, 101, 103–136

HPBW Half Power Beam Width. 51

IETR Institute of Electronics and Telecommunications of Rennes. 51

iid independent identically distributed. 7, 14, 16, 18, 40, 41, 59, 118, 130

IM Index Modulation. 5, 126

IoT Internet of Things. 104

ISI Inter Symbol Interference. 21

IUI Inter User Interference. 10, 38, 54–56, 59, 82, 91, 98

KPI Key Performance Indicators. 45

LBPA Leakage Based Power Allocation. xiv, xvii, 3, 5, 73–78, 81–83, 134

LNA Low Noise Amplifier. 35, 36

LoS Line of Sight. xiii, xiv, xvi–xviii, 2–5, 7, 8, 13, 14, 17, 18, 20–22, 24, 25, 28, 30, 38, 43–47, 49–51, 54–64, 66–68, 74–76, 78–86, 88–94, 100, 101, 103–106, 108–111, 113, 114, 117, 120–126, 133–135, 140

LSV Left Singular Vector. 63

LTE Long Term Evolution. 1, 138

MIMO Multiple Input Multiple Output. xii–xiv, xvi, xvii, 1–5, 7–102, 104–107, 126, 127, 130, 134, 135, 138

MISO Multiple Input Single Output. xvi, 24, 25, 28, 31, 32, 45, 46, 53, 55, 56, 62, 67, 68, 76, 85, 88, 92, 93, 108, 139

MMSE Minimum Mean Square Error. 10, 13, 30, 38, 138

mmWave Millimeter Wave. xii–xiv, xvii, xviii, 2–5, 7–102, 104–106, 110, 113, 114, 121–123, 125, 126, 133–135, 143

MRT Maximum Ratio Transmission. 10, 138

MS-STSK Multi-Set Space-Time Shift Keying. 105

MSF-STSK Multi Space-Frequency pace-Time Shift Keying. 105

MU Multi User. xii–xiv, xvi, xvii, 1–3, 7–102, 134, 139

NI National Instruments. 138

OFDM Orthogonal Frequency Division Multiplexing. 23, 45, 77, 138

PA Power Amplifier. 2, 12

PAPR Peak to Average Power Ratio. 12

PCP Pilot Contamination Precoding. 13

PDF Probability Density Function. 38

PEP Pairwise Error Probability. 129

QoS Quality of Service. 82, 83

QRD QR Decomposition. 65

QSM Quadrature Spatial Modulation. 105

RASK Receive Antenna Shift Keying. xvii, 104, 106, 107, 117

RB Resource Block. 12, 14

RF Radio Frequency. iv, xiv, 2, 26–33, 38, 39, 44–51, 54–56, 60, 63, 67–69, 73, 85–87, 93–96, 100, 104, 107–109, 119, 126, 127, 131–133

RMS Root Mean Square. 21

RR Round Robin. 99

RRH Remote Radio Head. 11

RSM Receive Spatial Modulation. xiv, xvii, xviii, 4, 5, 103–110, 113, 114, 118, 119, 121–123, 125, 135

RSV Right Singular Vector. 62

SE Spectral Efficiency. xiii, xvi–xviii, 1–5, 8, 14, 27, 29, 30, 33, 35–38, 40, 41, 43–51, 53–64, 66, 69–71, 74–76, 82–84, 87–95, 98–101, 103–106, 108, 109, 112, 114, 115, 118–121, 123–127, 129–135, 140, 142, 143

SIMO Single Input Multiple Output. 67, 68

SINR Signal to Interference and Noise Ratio. 11, 12, 41, 46

SISO Single Input Single Output. 53

SLNR Signal to Leakage and Noise Ratio. 74, 91, 92, 97–99, 101

SM Spatial Modulation. 3, 104–106, 125, 126, 135

SNR Signal to Noise Ratio. xiii, xviii, 10, 28, 33, 38, 41, 43, 46, 54–57, 59, 61, 62, 64, 68, 86, 98–100, 104, 123, 124, 127, 130–133, 142

SPIM Spatial Path Index Modulation. 126

SSK Space Shift Keying. 104, 105

SSM Spatial Scattering Modulation. xviii, 105, 126, 127, 132, 133

SU Single User. 8, 24, 25, 27–30, 55, 63, 64, 91, 104

SUS Semi-orthogonal User Selection. 91, 92, 96–99

SVD Singular Value Decomposition. xiii, 17, 44, 62–71, 94, 96–98, 109

TDD Time Division Duplex. 12, 138

UE User Equipment. xiv, xvi, xvii, 1–3, 5, 9–14, 17, 18, 21–23, 25, 27, 29–31, 33, 38, 46–48, 50, 53–61, 63, 64, 68, 69, 74–83, 85–88, 91–101, 105, 134–136, 138–141

ULA Uniform Linear Array. xvii, xviii, 14, 15, 17, 18, 23–25, 46, 50, 56, 59, 60, 64, 69, 85, 87, 93, 100, 108, 113, 115, 119–124, 128, 139, 140

UPA Uniform Planar Array. 14–16, 24, 25, 76

USRP Universal Software Radio Peripheral. 139

VNA Vector Network Analyser. 51

WINNER Wireless World Initiative for New Radio. 16, 20

WLAN Wireless Local Area Network. 19

ZF Zero Forcing. xvii, 10, 11, 30, 38, 44–47, 49–51, 54–56, 58, 59, 61, 62, 69–71, 76, 77, 79, 82–84, 86, 88, 89, 91–94, 98, 108, 109, 111, 113, 114, 117, 119, 121–124, 127–130, 138

ZMCSCG Zero Mean Circular Symmetric Complex Gaussian. 39

List of Symbols

$\mathbf{H}_b$ Beamspace channel. xviii, 37, 47, 141

α Complex channel amplitudes vector. 16, 17, 47

b_{DAC} The number of resolution bits of the digital to analog converter. 49

$\mathcal{P}_e$ The average bit error probability conditioned by the channel. 129

b_{PS} The number of resolution bits of the phase shifter. 49, 51

N_{BS} Number of antennas at the base station. 64, 68

f_c . 20

$\mathbf{H}$ Channel matrix. iii, 9, 10, 23–25, 27, 29–32, 37, 39–41, 45–47, 55, 56, 63–68, 76, 85, 93–95, 107–110, 112, 115, 117–119, 127–131

α Channel complex amplitude. iv, 18, 23–26, 28, 46, 47, 52, 53, 56–58, 64–66, 76, 78–80, 85, 86, 93, 94, 108, 128, 130, 131

h Channel scalar. 107, 118

$\mathbf{h}$ Channel vector. iv, 9, 16–18, 23–26, 28, 39, 46, 53, 56–59, 61, 67, 76, 77, 85, 87, 93, 98, 99, 108, 118

ι The condition number. 95, 96

ρ_{corr} The exponential correlation factor. 17

Φ The channel covariance matrix. 16, 17, 39–41

Θ The angular difference between two paths. 111–117, 119–122, 124

$\mathbf{D}$ Diagonal matrix of the singular values. 17, 94, 97, 109

d_t Inter-element distance between adjacent transmit antennas. 15, 16, 56–60, 69, 111–116, 119, 130

D The distance between the transmitter and the receiver. xvii, xviii, 19, 111, 112, 117, 120–124

D_0 The reference distance. 19, 20

d_r Inter-element distance between adjacent receive antennas. xviii, 15, 16, 111, 112, 117, 120–124

$\hat{\mathbf{H}}$ The equivalent channel matrix. xvii, 39, 61, 68, 69, 88–90, 94–97, 108–110, 118, 121–123, 128, 130

$\hat{\mathbf{h}}$ The equivalent channel vector. 39, 94–99

$\hat{\epsilon}$ The expectation of the per stream spectral efficiency. 56–59

$\mathbf{F}^{BB}$ Baseband precoding matrix. iii, iv, 9, 10, 29–33, 38, 39, 45–47, 55, 56, 63, 69, 85, 86, 93, 94, 107–109, 115, 127, 128

$\mathbf{F}^{HBF}$ Hybrid precoding matrix. 39, 47, 69, 107, 108

$\mathbf{F}^{RF}$ Radio frequency precoding matrix. iii, iv, 27, 30–33, 37–39, 45–47, 55, 56, 63, 68, 69, 85, 86, 93, 94, 107–110, 115, 127, 128

F_s The sampling rate. 49

$\mathbf{f}^{BB}$ Baseband precoding vector. 9, 10, 38, 46, 69

$\mathbf{f}^{HBF}$ Hybrid precoding vector. 46

$\mathbf{f}^{RF}$ Radio frequency precoding vector. 38, 39, 55–59, 61, 68, 98, 99, 118, 130, 131

$\mathbf{I}$ Identity matrix. 10, 16, 17, 39–41, 93, 94, 108

I The leakage from one user to the other users. 77, 78, 81, 82

X_σ The log-normal shadowing. 19, 20

$\mathbf{U}$ Matrix of the left singular vectors. 17, 94, 97, 109

N_{BC} Number of subcarriers in the coherence band. 77, 78, 82

N_b Number of spatial transmit beams. vi, xvii, 60, 61, 127–129, 131, 132

$\mathbf{n}$ Additive white Gaussian noise vector. iii, 9, 27, 29–32, 37, 39, 40, 45, 55, 63, 85, 93, 107

n Additive white Gaussian noise. 76, 117, 127, 129

β Normalization factor for a given precoder. xviii, 81, 93–95, 99, 108, 120

N_p Number of channel paths. iv, xvii, xviii, 23–26, 28, 53, 64, 66, 69–71, 76, 78–80, 85–87, 108, 118, 123, 124, 127, 128, 131

N_{FFT} Total number of subcarriers. 77, 78, 82

σ_n^2 Noise variance. 10, 39–41, 46, 98, 99, 117–119, 127, 129

η The efficiency of the power amplifier. 49

L The path loss. 19, 20

κ The path loss exponent. 19, 20

$\mathbf{w}$ Combining vector. 67, 68

P_{DAC} The power consumption of the digital to analog converter. 49

P_{HBF} The power consumption of the hybrid precoding. 49

ϕ^r Azimuth angle of arrival. 15, 16, 24, 25, 52, 64, 65, 68, 128

ϕ^t Azimuth angle of departure. iv, 15–18, 23–26, 28, 30, 46, 47, 52, 53, 56–58, 64, 65, 76, 78–80, 85–87, 93, 108, 111–117, 119, 121, 123, 124, 128, 130

$\Delta\phi^t$ Azimuth angle of departure angular spread. viii, 17, 18, 99–101

ϕ_{rot} The rotation angle of the receiver. 117, 124

P_H The power consumption of the 90 deg hybrid. 48, 49

P_{LO} The power consumption of the local oscillator. 49

P_{LP} The power consumption of the low pass filter. 48, 49

P_M The power consumption of the mixer. 48, 49

P_{out} Outage probability. 82

P Allocated power. 76–80

P_D The power consumption of the digital precoding. 49

P_{PA} The power consumption of the power amplifier. 49

P_{PS} The power consumption of the phase shifter. 49

$\mathbf{f}$ Precoding vector. 28, 39, 46, 67, 68, 76–79, 81, 86, 87, 118

$\mathbf{F}$ Precoding matrix. 30, 39, 76, 79, 81, 85, 94, 107, 121–123

P_{RF} The power consumption of each radio frequency chain. 48, 49

$\mathbf{x}$ The precoded signal. 9, 45, 107, 129

P_T Transmitted power. iii, 9, 27, 29–32, 39, 40, 45, 46, 49, 55, 63, 79, 81, 85, 93

R Rank of the combined digital precoding matrices for all sub-carriers. 45

$\mathbf{r}$ The received signal vector. iii, 9, 27, 29–32, 37, 39, 40, 45, 55, 63, 85, 92, 93, 107, 129

N_{TRF} Number of transmit radio frequency chains. iv, 30–32, 39, 45, 48–50, 55, 60, 69, 86, 92, 95–99, 107, 121–123, 127, 129–133

N_{RRF} Number of receive radio frequency chains. 30, 31, 35, 37

r Received symbol. iii, 31, 76, 77, 92, 117, 127

$\mathbf{V}$ Matrix of the right singular vectors. 94, 97, 109

$\mathbf{a}_r$ Receive steering vector. 15, 16, 24, 25, 64, 65, 68, 128

N_R Receive antennas. iii, xvii, xviii, 9, 15, 16, 24, 25, 27, 29–31, 35–37, 39–41, 64, 65, 67–71, 106–112, 114–124, 127, 128, 130–132

N_R^C Vertical receive antennas. 16

N_R^R Horizontal receive antennas. 16

Λ Scaling factor for a given precoder. 108–112, 115, 117–119, 125, 127, 129, 130

$\mathcal{C}$ The set of selected users. viii, 92–97, 99–101

$\mathbf{s}$ The signal before precoding. iii, 9, 27, 29–32, 37, 39–41, 45, 55, 63, 85, 93, 107, 108, 127–130

χ Signal to interference and noise ratio. 41, 46, 47

ζ Signal to leakage and noise ratio. 98

ρ Signal to noise ratio. xvii, xviii, 40, 41, 46, 47, 56–59, 61, 64, 66, 87, 93, 94, 99–101, 108, 114, 119–121, 125, 127, 129–131

ϵ Spectral efficiency. 39–41, 46, 56–59, 64, 66, 108, 109, 114, 115, 119, 125, 129–131

Δ_r The spatial correlation at the receive side. 64–66

Δ_t The spatial correlation at the transmit side. 64–66, 109–113, 115, 116, 118

c The speed of light. 20

N_S Number of spatial streams. 29, 30, 45, 47–49, 64, 67

$N_{S,sub}$ Total number of streams over all the sub-carriers. 45

θ^r Elevation angle of arrival. 16, 25

θ^t Elevation angle of departure. 15, 16, 23–25, 30, 76, 78–80

s Transmitted symbol. 76

$\mathbf{A}_t$ Transmit steering matrix. 30, 47, 79

$\mathbf{a}_t$ Transmit steering vector. iv, 15, 17, 18, 23–26, 28, 30, 46, 47, 53, 56–58, 64, 65, 76, 78–80, 85–87, 93, 108, 111, 112, 116, 117, 128, 130

K Total number of user equipments. iii–vi, xvi, xvii, 9, 10, 23–25, 30–32, 38, 39, 46–50, 53, 54, 56–61, 69–71, 76–80, 82, 85, 93

N_T Transmit antennas. iii–viii, xvi–xviii, 9, 10, 15–18, 23–32, 39–41, 45–51, 53–61, 64, 65, 67–71, 77, 78, 82, 83, 85–87, 93, 94, 99–101, 106–123, 127, 128, 130–132

N_T^C Vertical transmit antennas. 15, 16

N_T^R Horizontal transmit antennas. 15, 16

N_{UE} Number of antennas at the user equipment. 64, 68

$\mathcal{K}$ The set of all user equipments in the system. viii, 92, 96–101

λ The wavelength. xvii, xviii, 15, 23, 69, 81, 87, 100, 119–124, 130, 139, 140

$\mathbf{W}^{BB}$ Baseband combining matrix. 29, 30, 33

$\mathbf{W}^{RF}$ Radio frequency combining matrix. 27, 30, 31, 33, 37, 63, 68, 128

$\mathbf{w}^{RF}$ Radio frequency combining vector. 31, 68, 127, 129–131

Mathematical Notations

x	Scalar
$\mathbf{x}$	Vector
$\mathbf{X}$	Matrix
$\mathbf{X}^{-1}$	Inverse of matrix $\mathbf{X}$
$\mathbf{X}^*$	Complex conjugate of matrix $\mathbf{X}$
$\mathbf{X}^T$	Transpose of matrix $\mathbf{X}$
$\mathbf{X}^H$	Conjugate transpose of matrix $\mathbf{X}$
$Tr(\mathbf{X})$	Trace of matrix $\mathbf{X}$
$det(\mathbf{X})$	Determinant of matrix $\mathbf{X}$
$\|\mathbf{X}\|$	L-2 norm of matrix $\mathbf{X}$
$\|\mathbf{X}\|_F$	Frobenius norm of matrix $\mathbf{X}$
$\mathbb{E}(\mathbf{x})$	Expectation of random variable $\mathbf{x}$
$\mathbb{C}$	Complex field
$\mathbb{R}$	Real field
$\mathcal{P}$	A set
$|\mathcal{P}|$	Cardinality of the set $\mathcal{P}$
$[\mathbf{X}]_{\mathcal{P},:}$	A submatrix of matrix $\mathbf{X}$ indexed by the row indices in $\mathcal{P}$
$[\mathbf{X}]_{:,\mathcal{P}}$	A submatrix of matrix $\mathbf{X}$ indexed by the column indices in $\mathcal{P}$
$[\mathbf{X}]_{\mathcal{P},\mathcal{Q}}$	A submatrix of matrix $\mathbf{X}$ indexed by the row indices in $\mathcal{P}$ and column indices in $\mathcal{Q}$
$\odot$	Hadamard product
$\backslash$	Set difference
$\otimes$	Kronecker product
$\mathcal{O}(.)$	The order of computations
$|x|$	The amplitude of complex number x
$\angle x$	The phase of complex number x
$\mathcal{U}[a,b]$	Uniform distribution with parameters a and b
e^x	Exponential function of x
$\ln(.)$	Natural logarithm
$\log_x(.)$	Logarithmic function of base x
$\mathcal{CN}(\mu,\sigma^2)$	Complex normal distribution with mean μ and variance σ^2
$\prod$	Product of a sequence
$\sum$	Summation of a sequence
$\mathbf{argmax}$	Argument of the maximum

argmin   Argument of the minimum

$Diag(\mathbf{x})$ Diagonal matrix with diagonal entries $\mathbf{x}$

$\mathbb{P}(x)$ Probability of x

$|\mathbf{X}|$ Determinant of matrix $\mathbf{X}$

$\mathbf{X}^{\ddagger}$ Pseudo-inverse of matrix $\mathbf{X}$

$\lambda_{\max}(\mathbf{X})$ The largest eigenvalue of matrix $\mathbf{X}$

$\lambda_{\min}(\mathbf{X})$ The smallest eigenvalue of matrix $\mathbf{X}$

$\mathbf{Re}(x)$ The real value of x

$\mathcal{J}(.)$ The Bessel function

Chapter 1

Introduction

Contents

Recently, the demand for higher data rates and better coverage has been urgently reported in order to satisfy the requirements of the fifth generation of mobile networks (5G) [10]. More specifically both Spectral Efficiency and Energy Efficiency (EE) are on the top of these improvement requirements by the 5G. MIMO systems have emerged as one of the key enablers that can enhance both EE and SE [11] and have been extensively used in many recent standards such as in Long Term Evolution (LTE) releases 8-16 and also in Wifi 802.11n, 802.11ac,..etc. MIMO can achieve such gains thanks to exploiting the spatial domain in addition to the time and frequency ones, therefore, providing an extra Degree of Freedom (DoF) for conveying and processing the information.

In the early 2010's the massive MIMO terminology appeared [12, 13] in order to maximize the achievable gains of MIMO by increasing the number of antennas massively. A concrete mathematical modelling was presented for characterizing the massive MIMO systems in the following years. These theoretical studies relied on many theories such as the random matrix theory and the central limit theorem. Driven by the fact that many random behaviors tend to deterministic ones when their dimensions tend to infinity [14], massive MIMO with asymptotic assumptions that the number of antennas tend to infinity was extensively studied in the recent literature [1, 15, 16].

Moreover, massive MIMO was considered as a key player for MU transmissions [1] driven by the fact that with large number of antennas quasi-orthogonal beams can be formed to serve multiple UEs. Therefore, allowing multiple UEs to be served on the same time and frequency resources and differentiating between them in space, which significantly enhances the SE and the coverage of the network.

In order to consider the practical implementation of MU massive MIMO, two main factors need to be taken into account. The first factor is the size of the array, as the theoretical studies consider very large number of antennas, this is practically infeasible specifically at the conventional microwave frequencies (sub-6 GHz band). Moreover, even if the BS can deploy a considerably large massive MIMO array at sub-6 GHz ($\approx$ 100 [2]), deploying massive number of antennas at the UE side at such frequencies is not possible. The second limiting factor for MU massive MIMO is the hardware complexity and power consumption. Given the fact that in order to support MU scenarios with massive MIMO, digital precoding needs to be considered. In this case, a dedicated RF chain is needed per transmit antenna, which is an extensively high hardware complexity and also consumes power extensively since the Power Amplifiers (PAs) are not perfect in realistic scenarios.

In order to unleash the potentials of the MU massive MIMO systems, such systems exploit the mmWave frequencies for a candidate frequency band [17]. Unlike the conventional microwave systems (< 6 GHz), the mmWave systems exploit the band from 28 GHz to 300 GHz. Driven by such vast and splendid spectrum resources, mmWave systems along side with massive MIMO is considered one of the main key enablers for the 5G. Although, mmWave systems can provide large Band Width transmissions allowing for high achievable data rates, they suffer from multiple practical challenges. The first one is that at such frequencies the propagation wave suffers from high path loss compared to the microwave ones. This leads to low range transmissions and also leads to a sparse LoS dominated propagation channel [18]. The second one is that at such frequencies the hardware components are complex, costly and power hungry [3]. Therefore, in order to tackle the challenges of both the MU massive MIMO systems and the mmWave systems both are combined together in single transmission scheme refereed to as MU massive MIMO mmWave systems.

In MU massive MIMO mmWave systems, the path-loss problem at mmWave frequencies is solved using the transmit array gain offered by the massive transmit array. Also, the array size problem of massive MIMO is solved at mmWave frequencies, since at such frequencies, thanks to the small wavelength the massive antenna array can be deployed in an acceptable form factor at both the BS and the UE sides. Moreover, the hardware and power consumption problems for MU massive MIMO mmWave systems can be solved using a recently proposed beamforming technique referred to as HBF [4, 5]. Unlike the conventional digital precoding used for massive MIMO systems that need a dedicated RF chain per antenna, the HBF only needs a small number of RF chains compared to the number of transmit antennas. Despite, the significant lower hardware complexity and power consumption, HBF can still achieve close SE compared to fully digital precoding solutions at mmWave frequencies [5, 6]. This is due to the fact that, at mmWave frequencies the channel is sparse, thus a few RF chains are enough to fully control the channel dominant paths [7, 8].

Throughout the thesis we consider HBF in MU massive MIMO mmWave systems. We provide analytical analysis for some linear analog and digital precoders in LoS dominated mmWave channels with massive transmit antenna array. Also, we provide some low complexity signal

processing techniques such as power allocation, UEs selection, and Spatial Modulation (SM) to ease the realistic implementation of such MU massive MIMO mmWave systems. Finally, we tackle some of the main challenges of HBF massive MIMO mmWave systems such as the LoS blockage.

1.1 Objectives and Contribution

The aim of this thesis is to study low complexity signal processing techniques for HBF. Also, throughout the thesis we aim at providing analytical analysis for conventional HBF techniques in realistic mmWave massive MIMO channels. Moreover, we tackle some of the challenges of mmWave channels such as the blockage by proposing novel HBF structures to deal with such limitation.

Indeed, considering mmWave massive MIMO channels, a lot hardware, propagation and power consumption limitations exist. In order to consider such challenges, within this thesis we provide novel low complexity signal processing techniques to overcome such challenges imposed. The proposed techniques cover low complexity analog beamforming, digital precoding, stream allocation, power allocation, Spatial Modulation, Beam Index Modulation and consider low channel estimation overhead.

First, we consider a low complexity low overhead power allocation technique that aims at decreasing the inter-user interference power (leakage power) between the multiple UEs served simultaneously within the same cell. This Leakage Based Power Allocation is used in conjunction with an angular based precoder refered to as Digital Beam Steering in a joint framework. This framework has low complexity and low overhead since it only relies on estimating the angular information of the channel which are frequency flat and only change with mobility. This study led to:

- The publication of a conference paper in June 2018 entitled "Angular based Beamforming and Power Allocation Framework in a Multi-user Millimeter-Wave Massive MIMO System" [19].

Then, we present a robust HBF against blockage effect in sparse mmWave channels depending on Equal Gain Transmission (EGT) analog precoder and it has been compared to the previously proposed precoders in the literature that consider the blockage effect for sparse mmWave channels. This study led to:

- The publication of a conference paper in June 2018 entitled "Hybrid Beamforming for Multi-User MISO Channels with Equal Gain Transmission: A Robust and Spectral Efficient Approach" [20].

Again, aiming at providing low complexity and low overhead signal processing techniques for hybrid analog-digital mmWave MIMO systems, we consider a low complexity leakage based UEs selection and stream allocation approach and show that it can achieve sub-optimal SE performance with low complexity and low overhead requirements. This study led to:

- The publication of a conference paper in September 2018 entitled "Leakage based Users Selection for HBF in MillimeterWave MIMO" [21]

Later, we study the gap between the SE of the HBF and the full digital beamforming and investigate the condition for which both can achieve the same SE. Indeed, when these conditions occur, the HBF is more favourable compared to the full digital solution because it has lower hardware complexity and power consumption. This study led to:

- The publication of a conference paper in April 2019 entitled "On The Equivalence between Hybrid and Full Digital Beamforming in mmWave Communications" [6]

The other part of the thesis was dedicated to the theoretical analysis for HBF systems in LoS dominated mmWave massive MIMO channels. Moreover, we considered analytical analysis of HBF in conjunction with low complexity Receive Spatial Modulation and Beam Index Modulation systems. These studies led to:

- The publication of a conference paper in September 2019 entitled "On the Theoretical Limits of Beam Steering in mmWave Massive MIMO Channels" [22].

- The submission of a journal paper entitled "Analytical Performance of Hybrid Beam Index Modulation" to IEEE WCL.

- The preparation of a journal paper entitled "On The Performance of LoS Beamsteering in Sparse mmWave Channels" to be submitted to IEEE Access.

- The preparation of a journal paper entitled "Hybrid Beamforming for Receive Spatial Modulation" to be submitted to IEEE TWC.

1.2   Organization of The Thesis

The thesis is organized as follows: in Chapter 2, we cover the main concepts of MIMO, massive MIMO, mmWave systems, beamforming techniques and HBF architectures. We start by describing briefly the existing MIMO signal processing techniques. Then, we give a detailed introduction about the massive MIMO terminology, signal processing techniques and its theoretical limits. Later, we move to describing the mmWave systems and highlight their potentials in terms of the large Band Width (BW) and splendid throughput. Also, we show the challenges that limit the practical deployment of mmWave systems. Moreover, we show how the combination of massive MIMO and mmWave systems can be beneficial for both. Finally, we give a detailed analysis of the currently existing channel models and beamforming/precoding techniques for the massive MIMO mmWave systems.

In Chapter 3, we work on analytically describing the achievable Spectral Efficiency of the proposed HBF techniques throughout the thesis. Also, we aim at quantifying the performance gap between the full digital beamforming and the HBF. Moreover, we highlight the conditions for which the Hybrid Beamforming can achieve the exact Spectral Efficiency of the full digital beamforming scenario and we provide a fair comparison in terms of the energy and hardware efficiency for both architectures.

In Chapter 4, we describe the proposed low complexity signal processing techniques for HBF to allow for practical implementation feasibility in mmWave massive MIMO systems. We start by applying a low complexity power allocation technique (LBPA) in a joint framework with angular based precoder (DBS) that only depends on the angular information of the channel's LoS component. Thus, providing a low complexity-low overhead paradigm for mmWave MIMO systems. After that, we consider the sensitivity to the blockage of the LoS propagation path in mmWave channels. We propose a robust HBF architecture that relies on EGT in the analog layer to exploit the multipath channel components gains and add them constructively at the receiver. Later, we propose a novel low complexity UEs selection technique which again depends on minimizing the leakage between the selected UEs in a pure LoS channel.

In Chapter 5, we consider HBF system together with the recently emerging Index Modulation (IM). More specifically we start by considering HBF with Receive Spatial Modulation and analytically characterize the SE and the BER of the proposed system. Moreover, we extend our analysis to a more recent IM technique, yet more suitable to mmWave sparse channels that suffer from high path-loss, which is the Beam Index Modulation.

In the appendix, in order to proof the practical validity of our analysis and simulations which rely on statistical channel models, we implement some of the proposed algorithms on the National Instruments massive MIMO platform in order to verify the practical validity of these algorithms on realistic sounded channels.

Finally, we draw the conclusions and highlight the future research directions and perspectives that can extend based on our work throughout this thesis.

Chapter 2

Background for Hybrid **MU** Massive **MIMO mmWave** Systems

Contents

2.1   Key Aspects of Massive MIMO

In this section we present a detailed review on several key aspects of research in massive MIMO. We first present a system model for the MU massive MIMO systems for the ease of analysis in Subsection 2.1.1. Then we describe the designs of linear precoders in Subsection 2.1.2. Later, we focus on the issue of pilot contamination, and introduce decontamination methods in
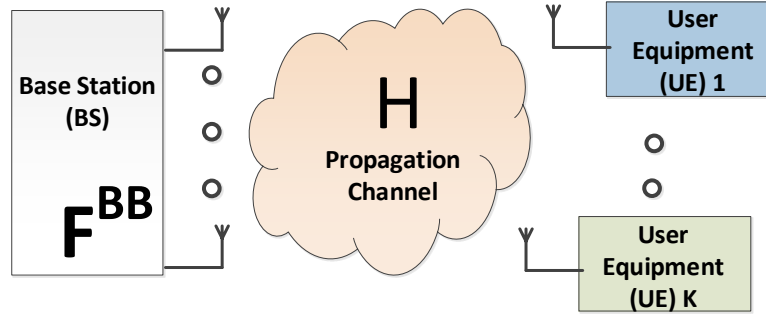
Figure 2.1: Full digital MU massive MIMO system.

Subsection 2.1.3. Finally, in Subsection 2.1.4, we will briefly introduce some field measurement campaigns for massive MIMO systems.

2.1.1 System Model

In this subsection we present a traditional single cell MU massive MIMO system as shown in Figure 2.1. In the downlink scenario, the transmitter (BS) is deployed with large (massive) number of transmit antennas ($N_T \rightarrow \infty$), while the K receivers (UEs) are equipped with a single receive antenna each ($N_R = 1$). Hence, the received signal vector for all the K UEs can be expressed as follows:

$$\mathbf{r} = \sqrt{P_T}\mathbf{H}\mathbf{x} + \mathbf{n} \tag{2.1}$$

where P_T is the transmit power, $\mathbf{H} \in \mathbb{C}^{K \times N_T}$ is the MU channel matrix, with columns $\mathbf{h}_k$ representing the channel vectors for each UE k. $\mathbf{x} = \mathbf{F}^{BB}\mathbf{s}$ represents the precoded transmit signal, given that $\mathbf{s}$ of dimensions $K \times 1$ is the transmit signal vector before precoding and $\mathbf{F}^{BB} \in \mathbb{C}^{N_T \times K}$ is the MU precoding matrix with columns $\mathbf{f}^{BB}$ representing the precoding vectors for each UE k. Finally, $\mathbf{n} \in \mathbb{C}^{K \times 1}$ represents the Additive White Gaussian Noise (AWGN) noise vector.

2.1.2 Precoding Techniques

In this subsection, we focus on linear precoders for massive MIMO systems,because they are less complex and more practical than the non-linear precoders, such as the Dirty Paper Code (DPC) precoding. Also, Simulations show that with a large number of antennas, the achievable rate of linear precoding approaches the channel capacity bound [14] and henceforth non linear precoders no longer have a significant advantage.

Single-cell precoding

We start with the single-cell precoding. A given BS designs the precoders to its K served UEs, based on the MU channel matrix $\mathbf{H}$ whose k-th column is given as $\mathbf{h}_k$. For the downlink

precoding, let $\mathbf{F}^{BB}$ be the Base Band (BB) digital precoding matrix for the BS where its k-th column $\mathbf{f}^{BB}$ is the precoding vector for UE k. A Conjugate Beamforming (CB) precoder, also known as Maximum Ratio Transmission (MRT) precoder, aiming at maximizing the received SNR for each UE can be calculated in terms of the MU channel as follows [23] :

$$\mathbf{F}^{BB}{}_{CB} = \mathbf{H}^H \tag{2.2}$$

The aim of the CB is to constructively add the linear combinations of the signal. This summation grows proportionally with the number of transmit antennas N_T. This CB precoder offers maximum beamforming gain at each UE side but it also leads to Inter User Interference (IUI). Therefore, a more complex linear precoding technique named ZF precoder was proposed in [24] to mitigate the IUI. In this case the precoding matrix $\mathbf{F}^{BB}$ with columns $\mathbf{f}^{BB}{}_k$ for each UE k, aims at suppressing the IUI. The ZF condition is defined as follows:

$$\mathbf{H}\mathbf{f}^{BB}{}_i = \left\{ \begin{array}{l} 1, k = i \\ 0, k \neq i \end{array} \right. \tag{2.3}$$

The precoding vectors $\mathbf{f}^{BB}{}_k$ which form the precoding matrix $\mathbf{F}^{BB}$ are chosen to satisfy the above-mentioned zero interference condition. The solution to this problem, is to get the pseudo-inverse of the MU channel matrix $\mathbf{H}$ between the BS and the set of active K UEs [25], which can be done as follows:

$$\mathbf{F}^{BB}{}_{ZF} = \mathbf{H}^{\ddagger} = \mathbf{H}^H(\mathbf{H}\mathbf{H}^H)^{-1} \tag{2.4}$$

where $\mathbf{H}^{\ddagger}$ is the Moore-Penrose pseudoinverse of the MU channel matrix $\mathbf{H}$. However, ZF has a drawback, which is noise enhancement that occur at low SNR [25]. Noise enhancement leads to a degradation in the performance of the overall system. Minimum Mean Square Error (MMSE) precoding solves the problem of noise enhancement suffered ZF [25].

As ZF precoding tends to mitigate the interference caused by the streams sent by the BS to the other UEs to zero, the MMSE precoding eases this constraint, hence, allowing for some IUI to occur while at the same time providing better performance than the ZF [26]. The MMSE precoding calculation is defined as follows:

$$\mathbf{F}^{BB}{}_{MMSE} = \mathbf{H}^H(\mathbf{H}\mathbf{H}^H + \sigma_n^2\mathbf{I}_K)^{-1} \tag{2.5}$$

where σ_n^2 is the noise variance and $\mathbf{I}_K$ is a $K \times K$ identity matrix, such that K is the total number of UEs. MMSE provides better performance than ZF especially for single receive antenna UEs in downlink transmissions [26].

In [27], the performance of linear precoding techniques was evaluated in a single cell massive MIMO scenario. Also, derivations of lower bounds for the channel capacity of ZF and CB were given. Moreover, The authors showed by simulation results that ZF precoder achieves higher data rate than the CB one in the high SNR regime, while in the low SNR regime, the CB achieves higher data rate. In [28] the authors provided an approximation to the boundary SNR to switch between CB and ZF.

In [29], the rate performance for both the uplink and downlink transmissions was studied in a multi cell scenario. The analysis showed that both ZF and CB can achieve asymptotically the

same Signal to Interference and Noise Ratio (SINR) assuming that both the signal and interference have the same covariance matrix. Moreover, the analysis for the finite number of BS antennas case, shows that ZF precoding converges faster to the asymptotic limit than the CB one.

Multi-cell precoding

Multi-cell coordinated transmission has been recently considered for MIMO and massive MIMO networks. In traditional MIMO cellular networks multi-cell coordinated transmission mainly aimed at reducing the interference level [30]. However, in massive MIMO cellular networks coordinated transmission can also be leveraged in order to reduce the number of antennas per BS by installing antennas in multiple positions and coordinating their transmissions. Henceforth, overcoming the form factor limitation of massive MIMO systems. For example, a network MIMO architecture presented in [31], was shown to achieve similar performance of a massive MIMO system with fewer antennas at each BS.

Distributed massive MIMO architectures were presented in [32, 33], where the massive antennas are no longer co located. Instead, they are distributed over multiple Remote Radio Heads (RRHs) and are coordinated together to perform joint transmission.

Another application for multi-cell coordination is the mitigation of pilot contamination as shown in [34, 35]. Moreover, it can also be applied in order to decrease the total transmission power of the network as shown in [36].

However, in order to apply multi-cell coordination, the CSI needs to be shared between all the BSs in the network, which needs a lot of signaling overhead [37]. Therefore, in order to overcome such a challenge, one solution is to reduce the overhead due to CSI. This can be achieved by designing coordinated precoding techniques based on long-term channel statistics instead of instantaneous CSI [36, 34, 35]. Also, decentralized precoding techniques can be used to reduce the overhead of distributed massive MIMO systems as shown in [33].

Non-ideal hardware constraints

In order to consider realistic implementation issues, massive MIMO arrays are mainly built with low cost components. These components suffer from hardware imperfections that need to be taken into consideration. Therefore, hardware imperfection constraints need to be considered during the design of massive MIMO systems.

In [38], the authors presented a general framework to model the additive distortions arising from the hardware imperfections in massive MIMO systems. Moreover, in [39] an extension for the framework was proposed in order to model the multiplicative phase drifts and noise amplification effects.

In [38], the authors showed that the hardware impairments at the UE side are the main limiting factor of the capacity. On the other hand, the effect of the hardware impairments at the BS side vanishes asymptotically. Also, in [38, 39] it was shown that, for massive MIMO systems with large number of antennas, the hardware impairments have less effect. Therefore, the BSs with massive antenna arrays can deploy low-cost antenna elements without a notable degradation in performance.

Another issue for massive MIMO systems is the efficiency of PAs. One solution for this issue is to use low Peak to Average Power Ratio (PAPR) precoding designs such as the ones presented in [40, 41].

Massive MIMO systems mainly depend on the channel reciprocity for channel estimation (Time Division Duplex (TDD)). However, in realistic scenarios, this channel reciprocity is not straightforward, since the transmitter and the receiver have different circuit gains. Therefore, in order to restore the channel reciprocity, calibration methods have been proposed, in [42, 43, 44], in order to compensate for the mismatches between the transmitter and the receiver.

2.1.3 Pilot Contamination

In multi-cell massive MIMO systems, pilot sequences are often reused in multiple cells causing what is known as pilot contamination. Therefore, in such systems, when a given BS estimates the channel by correlating the received pilot signal with the corresponding pilot sequence, the estimated channel is contaminated by a combination of interference from the UEs that share the same pilot in the other cells [45]. Pilot contamination is known to be one of the main limiting factors for massive MIMO systems, since it limits the SINR performance scaling with infinite antennas [12].

Therefore, in order to deal with pilot contamination and reduce/mitigate its effect, several techniques have been proposed in the literature and will be summarized in this subsection as follows.

Reducing pilot reuse in a resource block

The first approach to limit the pilot contamination effect is to reduce the number of UEs that use the same pilot sequence for a given Resource Block (RB) in the massive MIMO network. This can be achieved by increasing the number of orthogonal pilots in the network in order to avoid the need for pilot sequences sharing. However, increasing the number of orthogonal pilot sequences is not straightforward, since it requires longer pilot sequences and thus leading to higher training overhead. Moreover, the maximum number of orthogonal pilots depends ob the coherence time of the massive MIMO system.

Another approach, is to apply a fractional pilot reuse technique introduced in [46], which has similar idea to the well known fractional frequency reuse paradigm. This fractional reuse technique achieves higher throughput compared to the full pilot reuse in [12], since the cell edge UEs become more immune to pilot contamination.

One more approach called asynchronous pilot transmission was proposed in [47], to avoid synchronous pilot transmission which maximizes the effect of pilot contamination [12]. This proposed asynchronous pilot transmission, applies a shifted-frame protocol, such that the BS in the network are clustered into multiple groups, where the channel training in each group is done in disjoint and shifted time periods within a frame. The authors in [47], showed that this asynchronous pilot transmission achieves better asymptotic rate performance compared to the synchronous one.

Coordinating between multiple cells

In order to reduce the effect of pilot contamination, without changing the pilot sequence design, coordination between multiple cells can be leveraged.

One approach is to use a coordinated scheduling algorithm, such as the one proposed in [48] for minimizing the estimation error that arise from pilot contamination. This algorithm can acquire an interference-free channel estimate of the signal utilizing an MMSE channel estimator, given that the eigenvectors of the covariance matrices of the signal and interference are orthogonal.

Another approach to mitigate the pilot contamination, is a coordinated precoding method called Pilot Contamination Precoding (PCP), which was was presented in [34, 35]. This PCP aims at relaxing the overhead requirements for the exchange of information between the BSs, as it only requires the exchange of the large scale path losses and the information symbols.

Developing blind estimation algorithm

Recently, some research work started to avoid using the pilot sequences for training to avoid the pilot contamination effect utilizing what is known as blind channel estimation algorithms [49, 50]. These blind estimation algorithms depend on the assumption that the signal subspace is asymptotically orthogonal to the interference one, when the number of antennas is infinite [49, 50].

In [50], the covariance matrix of the received signal is utilized to estimate the channel matrix. However, in practical scenarios, the covariance matrix of the received signal is unknown at the BS and can only be approximated by the empirical covariance matrix of the uplink data samples. Therefore, in [50] the authors showed by simulations that the performance of the proposed blind algorithm mainly depends on the accuracy of the covariance matrix estimation. Hence, utilizing a large number of uplink data symbols for the covariance matrix estimation allows blind channel estimation techniques to outperform the original pilot-aided channel estimation in terms of symbol error probability.

2.1.4   Field Measurements

Recently, many prototypes and field measurements have emerged to characterize the massive MIMO channel environment and realistic implementation issues [51, 52, 53, 54, 55].

In [55], a prototype named Argos was proposed to model a massive MIMO BS with 64 transmit antennas, and can serve up to 15 UEs at the same time. It was shown by experiments in [55], that Argos can achieve ≈ 6.7 fold gain in capacity compared to a single antenna BS with using $\approx \frac{1}{64}$-th of the transmission power.

In [52], a measurement campaign at Lund's university campus in Sweden was performed at 2.6 GHz with 128 transmit antennas at the BS. The experiments carried out in [52], showed that increasing the number of antenna elements in the transmit array, achieves better orthogonality between the channels of the served UEs, in case the UEs are in non LoS channel scenario or LoS scenario with sufficient angular separation. However, in case the served UEs are in a pure LoS channel scenario with small angular separation, the orthogonality between the UEs' channels can

not be achieved. Therefore, in case UEs have LoS dominated channels, scheduling algorithms need to be developed to guarantee a minimum angular separation between UEs scheduled on the same RB.

Moreover, in [54], a measurement campaign was presented in order to characterize the spatial correlation between the antennas at the BS. The measurement setup included a virtual ULA with 128 antennas, half-wavelength spaced, at 2.6 GHz. It was shown that, non LoS links generally have less variations in the correlation level compared to the LoS links.

Although, both the sounded massive MIMO channels and the theoretical iid Rayleigh channels differ, many work in the literature assured the fact that the iid Rayleigh channel model is a valid approximation for the realistic massive MIMO channels at the sub 6 GHz frequencies [51, 52, 53, 54]. Moreover, in [52], the authors showed that for their measurement scenario with 128 antennas at the BS, the sounded channels achieves $\approx 90\%$ of the channel capacity in iid fading channels in case non LoS propagation environment exists. However, in case the UEs are in LoS environment with small angular separation, the measured channels achieve $\approx 50\%$ of the channel capacity in iid fading channels.

2.2 Channel Models

In this section we present a detailed review on several channel models proposed for massive MIMO and mmWave systems. We first describe the commonly used antenna array architectures for Massive MIMO and mmWave systems in Subsection 2.2.1. Then, in Subsection 2.2.2, we present a summary for the classical models used to characterize the massive MIMO channels systems specifically in sub-6 GHz frequencies. Later in Subsection 2.2.3, we describe the mmWave channel characteristics, which differ substantially from the sub-6 GHz channels. In Subsections 2.2.4 and 2.2.5, we will present the two methods used throughout the thesis for modelling the mmWave massive MIMO channel. These two models are a deterministic ray tracing based model and a stochastic physical ray based one. We consider the ray tracing tool as a deterministic channel model to benchmark the performance of our proposed algorithms. However, throughout the thesis we mainly consider the stochastic ray based model for our theoretical and numerical analysis to obtain closed form models for the SE of the proposed beamforming algorithms. Finally, in Subsection 2.2.6 define the multiple channel scenarios that we use throughout the thesis based on the two models in Subsections 2.2.4 and 2.2.5.

2.2.1 Antenna Array Architectures

In this subsection we briefly introduce the proposed antenna array architectures as shown in Figure 2.2. Throughout the thesis we consider both the ULA and the Uniform Planar Array (UPA) architectures, where the antenna element can be generic (omni directional, directive, etc.). However, since in this thesis our aim is to analytically analyse and develop beamforming and signal processing techniques, we only use arrays of omni directional antennas for tractability and simplicity of analysis. However, in realistic mmWave deployment scenarios directional antennas are more favourable, considering omni directional antennas for simulations and com-
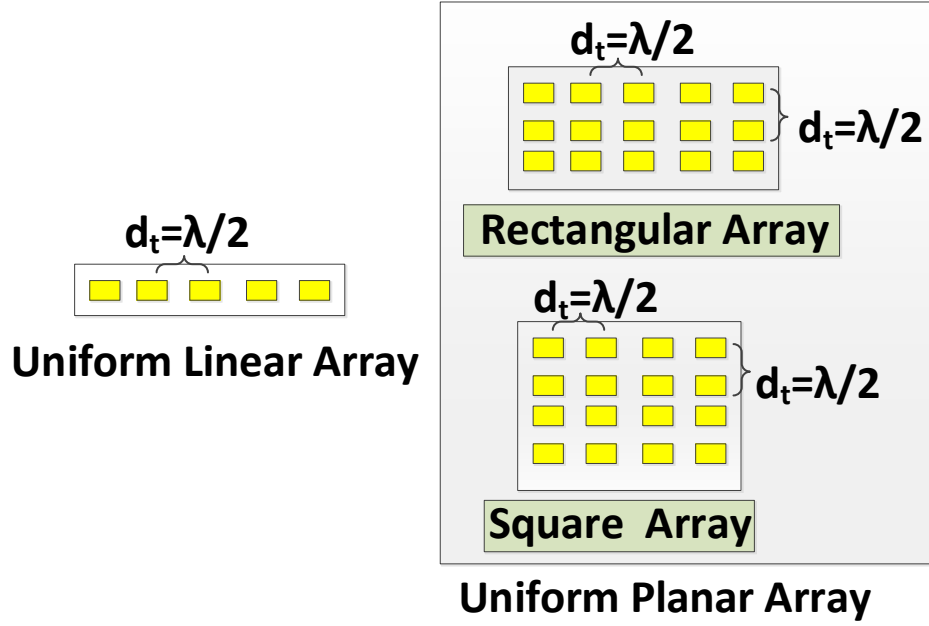
Figure 2.2: The proposed antenna array architectures.

parison between multiple signal processing techniques is an acceptable and accurate approach [5, 56]. Moreover, although we only consider arrays of omni directional antennas, our proposed framework is generic to consider the radiation pattern of any proposed antenna element.

In case a ULA with omni directional antennas is used, the steering vector at the transmitter side can be defined as follows:

$$\mathbf{a}_t(\phi^t) = \frac{1}{\sqrt{N_T}}[1, e^{j\beta(\phi^t)}, ..., e^{j(N_T-1)\beta(\phi^t)}]^T \tag{2.6}$$

where ϕ^t is the azimuth AoD, N_T is the number of transmit antennas, and $\beta(\phi^t)$ is given as

$$\beta(\phi^t) = \frac{2\pi}{\lambda}d_t\sin(\phi^t) \tag{2.7}$$

such that d_t is the inter-antenna element spacing at the transmitter and λ is the wavelength. Similarly, for a ULA of omni directional antennas, the steering vector at the receiver side $\mathbf{a}_r(\phi^r)$ can be calculated similar to Equation (2.6), with replacing ϕ^t, d_t, N_T by ϕ^r, d_r, N_R respectively, such that ϕ^r is the azimuth Angle of Arrival (AoA), d_r is the inter-antenna element spacing at the receiver and N_R is the number of receive antennas.

In case UPA with omni directional antennas is used, the steering vector at the transmitter side can be defined as follows:

$$\mathbf{a}_t(\phi^t, \theta^t) = \frac{1}{\sqrt{N_T}}[1, ..., e^{j(N_T^C-1)\frac{2\pi}{\lambda}d_t\cos(\phi^t)\sin(\theta^t)}, ..., e^{j\frac{2\pi}{\lambda}d_t\left((N_T^C-1)\cos(\phi^t)\sin(\theta^t)+(N_T^R-1)\sin(\phi^t)\right)}]^T,$$

$$\tag{2.8}$$

15

where N_T^C and N_T^R represent the number of columns and rows of the transmit array respectively, while θ^t represents the elevation AoD. Again, for a UPA of omni directional antennas, the steering vector at the receiver side $\mathbf{a}_r(\phi^r, \theta^r)$ can be calculated similar to Equation (2.8), with replacing $\phi^t, \theta^t, d_t, N_T, N_T^C, N_T^R$ by $\phi^r, \theta^r, d_r, N_R, N_R^C, N_R^R$ respectively, such that θ^r is the elevation AoA. N_R^C and N_R^R represent the number of columns and rows of the receive array respectively.

2.2.2 Historical Massive MIMO Channel Models

Based on the discussion in Subsection 2.1.4 regarding the channel measurement campaigns, we can conclude that channel modeling for massive MIMO systems, needs to consider trade offs between the tractability and practical accuracy issues.

In this subsection, we will discuss the analytical channel models that are used in the massive MIMO literature to define the performance bounds and asymptotic limits thanks to the tractability in analysis. On the other hand, other channel models based on measurement campaigns for industrial applications can be found in [57] for the Wireless World Initiative for New Radio (WINNER)+ model, [58] for the COST 2000 model, [59] for the Third Generation Partnership Project (3GPP) 3D MIMO channel model.

The main characteristic that analytical massive MIMO channel models consider, is the asymptotic orthogonality, also known as favourable propagation, which we can be defined as follows.

Definition: Channel vectors $\mathbf{h}_1 \in \mathbb{C}^{1 \times N_T}$ and $\mathbf{h}_2 \in \mathbb{C}^{1 \times N_T}$ are asymptotically orthogonal, if the following limit holds

$$\lim_{N_T \to \infty} \frac{\mathbf{h}_1^H \mathbf{h}_2}{|\mathbf{h}_1||\mathbf{h}_2|} = 0 \tag{2.9}$$

iid fading channel model

The most commonly used model for the analysis of massive MIMO channels in the sub-6 GHz band is the iid Rayleigh channel model [60]. In this model, the channel vector $\mathbf{h} \in \mathbb{C}^{1 \times N_T}$ follows the complex Gaussian distribution $\mathcal{CN}(0, \mathbf{I}_{N_T})$. In [1], it was shown that the iid Rayleigh fading channel satisfies the favourable propagation property of massive MIMO (asymptotic orthogonality). The main drawback of the iid fading channel model is that it does not consider the spatial correlation effects. Therefore, a model that considers the spatial correlation was proposed as follows.

Correlated fading channel model

In order to consider the spatial correlation and mutual coupling effects on the propagation channel, a Kronecker model was proposed to model such effects [29], such that the vector $\mathbf{h}$ is modeled as follows

$$\mathbf{h} = \sqrt{\Phi}\alpha \tag{2.10}$$

where Φ is the small-scale fading covariance matrix, and α is a vector following the distribution $\mathcal{CN}(0, \mathbf{I}_{N_T})$. The SVD of the Φ can be denoted as follows

$$\Phi = \mathbf{U}_\Phi^H \mathbf{D}_\Phi \mathbf{U}_\Phi \tag{2.11}$$

where $\mathbf{D}_\Phi$ is a diagonal matrix containing the singular values, and the m-th singular value is denoted as $\sqrt{\lambda_m} \geq 0$. Moreover, the matrix Φ is normalized as to satisfy the following condition

$$Tr(\Phi) = \sum_{m=1}^{N_T} \sqrt{\lambda_m} = N_T \tag{2.12}$$

This covariance matrix Φ can be modelled using different models, for example, it can be modelled using the exponential correlation model in [61]. using this exponential correlation model, for $m, k \in [1, N_T]$, the (m, k)-th of the matrix Φ is defined as follows

$$\Phi\mathsf{m,k} = \rho_{corr}^{|m-k|}, \tag{2.13}$$

such that ρ_{corr} represents the correlation coefficient between the adjacent antennas, and $|\rho_{corr}| \in [0, 1)$.

Another model that can be used to model the covariance matrix Φ based on the angular spread was presented in [48, 62]. In this case the covariance matrix Φ is defined as follows

$$\Phi = \mathbb{E}_{\phi^t}[\mathbf{a}_t(\phi^t)\mathbf{a}_t(\phi^t)^H], \tag{2.14}$$

such that $\mathbf{a}_t(\phi^t)$ represents the steering vector of the BS antenna array, ϕ^t is the AoD for a given UE, and the expectation is taken over the angular power spectrum in order to consider the angular spread.

In [48, 62] a special case of this model was considered, in which a ULAs with a pure LoS channel: Thus, the steering vector $\mathbf{a}_t(\phi^t)$ is defined as in Equation (2.6). The angular power spectrum is assumed to have a uniform distribution in the interval $[\phi^t - \frac{\Delta\phi^t}{2}, \phi^t + \frac{\Delta\phi^t}{2}] \subset [0, \pi]$, such that $\Delta\phi^t$ represents the maximum azimuth angular spread.

The correlated fading channels in Equation (2.10) do not guarantee the satisfaction of the asymptotic orthogonality property, since it depends on the structure of the covariance matrix. However, a sufficient condition in order to guarantee that the asymptotic orthogonality property is satisfied is defined in the following theorem.

Theorem 1. *For $k = 1, 2$, if the channel vector $\mathbf{h}_k$ is modelled as in Equation (2.10) and the mean square of the eigenvalues of Φ is uniformly bounded as follows:*

$$\lim_{N_T \to \infty} sup \sum_{m=1}^{N_T} \frac{\lambda_m}{N_T} < \infty, \tag{2.15}$$

then, in this case, the asymptotic orthogonality property in Equation (2.9) is satisfied, as follows

$$\lim_{N_T \to \infty} \mathbf{h}_1^H \mathbf{h}_2 = 0, \tag{2.16}$$

and

$$\lim_{N_T \to \infty} \mathbf{h}_k^H \mathbf{h}_k = 1. \tag{2.17}$$

The constraint in Equation (2.15) is satisfied by the exponential correlation model in Equation (2.13) [63], and the angular spread model in Equation (2.14) with certain constraints on the range of the angular spread $\Delta\phi^t$ [62].

LoS channel model

In case only single LoS path exist for each UE, with no reflected paths, the channel can be modelled as a pure LoS one, as in [1, 64]. In this case, the channel vector $\mathbf{h}$ is modelled by its steering vector as follows

$$\mathbf{h} = \alpha\mathbf{a}_t(\phi^t) \tag{2.18}$$

where $\mathbf{a}_t(\phi^t)$ is often assumed to be the steering vector of a ULA as defined in Equation (2.6) [1, 64]. For pure LoS channels with ULAs, one condition in order to fulfil the asymptotic orthogonality property is defined in the following theorem.

Theorem 2. *From [1], let $\mathbf{a}_t(\phi^t)$ be the steering vector of a ULA defined in Equation (2.6), and for $k = 1, 2$, $\phi^t{}_k$ is the AoD of the k-th UE. If $\sin(\phi^t)$ is iid uniformly distributed in $[-1, 1]$ then, the asymptotic orthogonality is achieved as follows*

$$\lim_{N_T \to \infty} \mathbf{a}_t(\phi^t{}_1)\mathbf{a}_t(\phi^t{}_2) = 0. \tag{2.19}$$

Hint: The asymptotic orthogonality is not always guaranteed in LoS channels. For example, in [1], one counter example was given: when $|\sin(\phi^t{}_1) - \sin(\phi^t{}_2)| = \frac{1}{N_T}$

$$\lim_{N_T \to \infty} \mathbf{a}_t(\phi^t{}_1)\mathbf{a}_t(\phi^t{}_2) = \frac{2j}{\pi}. \tag{2.20}$$

Non-stationary channel models

In massive MIMO systems, specifically the ones operating in the sub-6 GHz frequencies, the dimension of the array is usually large. Therefore, in this case, the assumption that the dimension of the array is negligible compared to the link length between the transmitter and the receiver is no longer an accurate one. In order to capture the near field effects of the channel, non-stationary channel models have been presented in [65, 66, 67].

For example, the authors in [65, 66], modelled the spherical wavefront at the massive antenna array by an ellipse model, where the clusters' dynamics were modelled by birth and death processes. While in [67], the visible region concept was applied in order to model the fact that some clusters are only visible for a fraction of the antennas in the massive array, while they are not visible for the rest. Moreover, in [32] the concept of channel aging (the non-stationarity in time domain) was defined and its impact was examined, such that an autoregressive series was used to model the dynamics of the channel, and also some channel prediction algorithms were proposed to deal with the channel aging.

2.2.3   mmWave Channel Characteristics

After discussing some channel models used for the sub-6 GHz band, now we move to discussing the characteristics of the channels in the mmWave band (from 30 GHz to 300 GHz) which have been studied extensively in the recent literature [68, 69, 70, 71]. Unlike the traditional sub-6 GHz channels which are band limited, mmWave channels offer splendid spectrum resources, with BWs up to multiple gigahertz [68, 69].

A lot of measurement campaigns have been carried out in the last few years, in order to develop a clear understanding of the main characteristics of the mmWave channels, for example, the work in [69, 72, 73, 74] and the references therein. Although, mmWave channels depends on the site-specific effects and may differ from one environment to another, still many important insights and statistics about the mmWave channel have been extracted from the measurement campaigns [69, 73]. Henceforth, in this subsection, we will summarize the main characteristics of the mmWave channels obtained from the measurement campaigns. These characteristics help to develop a solid understanding of the mmWave channels and help to develop analytical models that can describe such channel environments accurately.

Penetration Loss

In early mmWave channel measurement campaigns, the penetration loss for mmWave signals through different materials was examined for the 60 GHz in [75, 76], for the the 40 GHz in [72, 77] and for the 28 GHz in [72].

These measurements show that the penetration loss vary significantly based on the material. For example, for materials used in the outer walls of buildings, the mmWave signals suffer from > 170 dB loss through only 10 cm thick brick or concrete walls [77]. This means that, in this case both the indoor and the outdoor environments can be assumed as separate isolated systems. On the other hand, for materials used in the inner walls of buildings, the mmWave signals suffer from approximately similar penetration loss compared to that in the sub-6 GHz. For example, the penetration loss through a 2.5 cm inner wall changes from 5.4 dB at 2.5 GHz to 6.0 dB at 60 GHz [68]. This result motivates the application of mmWave systems for indoor Wireless Local Area Networks (WLANs).

Another issue, is that mmWave signals suffer from high penetration losses due to human bodies and trees. For example, the penetration loss due to human body for mmWave signals can range from 20 to 40 dB [72]. In [78], the authors showed how these losses can cause link blockage and hence, increase the outage probability in mmWave cellular networks. Also, in [79, 80] examined the effect of foliage losses, which can reach several dB, and hence degrading the link budget for mmWave transmissions.

Large-scale Path Loss

The path loss for a link of length D can be modeled using the log-distance model as:

$$L(D) = L(D_0) + 10\kappa \log_{10}\left(\frac{D}{D_0}\right) + X_\sigma, \qquad (2.21)$$

such that $L(D_0)$ is the close-in free space path loss, κ represents the path loss exponent, and X_σ is a random variable that models the log-normal shadowing. The close-in path loss $L(D_0)$ can be calculated using the Frii's equation as follows:

$$L(D_0) = 10 \log_{10} \left(\frac{4\pi D_0 f_c}{c} \right) \tag{2.22}$$

such that f_c is the carrier frequency, c is the speed of light, and the close-in distance is chosen as in [74] $L(D_0) = 1m$. From Equation (2.22), it is clear that the close-in path loss $L(D_0)$ is directly proportional to the carrier frequency. This means that, assuming isotropic antennas are deployed at both the transmitter and the receiver, a given mmWave signal transmitted at 30 GHz will suffer a 20 dB free space path loss more than that at 3 GHz. This large difference in path loss between the mmWave signals and the sub-6 GHz ones can be compensated by the antenna directivity gains offered by massive MIMO arrays [18, 68].

Given that blockages exist in the LoS path due to the high penetration losses, the measurement campaigns results show that the LoS links and the non LoS ones have different path loss laws. In [72, 73, 74], the authors defined the path loss exponent for a LoS link κ_L to be $\kappa_L = 2$ using the extensive measurements results with directional antennas. This can be explained as follows: In mmWave band; the Fresnel zone is small, hence the direct path is not likely to get affected by the nearby obstacles and therefore, the LoS mmWave transmissions are approximately similar to the free space ones.

The non LoS links always have a path loss exponent κ_n greater than the LoS ones, but the value of κ_n is not deterministic and varies with the measurement environment. For example, in [74], measurements in the New York and Austin city were performed and the results show that, the non LoS path loss exponent was found to be $\kappa_n = 4.5$ in Manhattan at 28 GHz, $\kappa_n = 3.3$ in Manhattan at 38 GHz, and $\kappa_n = 4.7$ in Manhattan at 73 GHz.

Moreover, the exponent κ_n is not only dependable on the scattering environment, but also it depends on the antenna beam width [73, 18, 81].

Finally, considering the shadowing effect X_σ, the variance of the shadowing also differs in the LoS and non LoS links. For example, the variance of the shadowing is 1.1 dB for LoS links, and 10 dB for non LoS ones, in the 28 GHz Manhattan measurements [74].

Multi-path Effect and Small-scale Fading

According to all the aforementioned channel measurement campaigns, it was shown that the mmWave channel have significantly less multi-path components, compared to the sub-6 GHz channels. This phenomena is called channel sparsity. In [74], it was shown that the average number of multi-path components is approximately 5 at 28 GHz and 3 at 73 GHz in the Manhattan area. On the other hand, for the sub-6 GHz channel in urban areas an average of 15 clusters of components are assumed in the 3GPP and the WINNER models [57].

Given that the mmWave channels are sparse, compressed sensing techniques can be efficiently used to estimate the mmWave channels and to design efficient precoders as shown in [82, 83]. Additionally, because of the sparsity of mmWave channels, small-scale fading has a minor effect on the mmWave signals, compared to the Rayleigh fading in the sub-6 GHz channels. One consequence of this sparsity property, is the high spatial correlation in the mmWave

channels. Also, the effect of small-scale fading is minor, when highly directional antennas at both the receiver and transmitter are deployed, pointing towards the boresight direction [18].

The sparse multi-path components of the channel arrive at the receiver side at different time delays and different angles. Therefore, We will briefly discuss the temporal and spatial statistics of the multi-path components of the mmWave channels as follows:

Delay spread: Delay spread is known to be a metric to evaluate the difference in the arrival time of the multi-path components of the channel. Moreover, Root Mean Square (RMS) delay spread defines the standard deviation of the delays for the measured multi-path components. Given the fact that mmWave signals suffer from high path loss, mmWave signals have smaller delay spread compared to the sub-6 GHz signals. Additionally, the symbol period for mmWave signals is much smaller compared to the sub-6 GHz signals, due to the large BW at the mmWave systems. Therefore, the smaller delay spread at mmWave may still create Inter Symbol Interference (ISI) that needs to be equalized at the receiver side.

The delay spread is highly dependent on the scattering environment and the positions of scattering objects. For example, in [74], it was shown that the delay spread in New York city is larger than in Austin, because of the more reflective environment. Moreover, utilizing directional beamforming and combining at the transmitter and the receiver sides further reduces the effect of the delay spread, since in this case, the energy is focused on fewer paths that are captured within the narrow beamwidth.

For a LoS link with perfect beam alignment on the boresight direction, the delay spread is almost negligible. Even, For a LoS link with beam misalignment, the delay spread is low ≈ 50 ns [73, 74]. On the other hand, for non LoS links, the delay spread is lager. For example, an average of ≈ 10 ns at 73 GHz, even when the beams are aligned towards the strongest channel path. Moreover, in [73], it was shown that the delay spread may decrease with increasing the distance between the transmitter and the receiver, which is expected, since for higher distance less paths will survive because of the high path loss at mmWave frequencies.

Angular spread: As mentioned before, mmWave channels are sparse, which means that they are composed from a few dominant paths. Therefore, in the angular domain the energy of the mmWave signals is concentrated in a few principle AoDs and AoAs directions [74]. Also, scattering happens at the surface of the reflectors (since at mmWave, the wavelength is very small such that the reflecting surfaces are seen to be rough ones with irregularities). This leads to spreading of the energy around those principle directions with a certain spread, measured by the RMS angular spread [76]. Henceforth, the in the angular space, the energy of the received signal is distributed as a set of spatial lobes, where the center of each lobe defines the principle AoA and the width of the lobe depends on the angular spread [74, 18]. For example, in [74], the average angular spread for a spatial lobe was measured to be 6.8° at 28 GHz and 3.7° at 73 GHz in the New York city measurement campaign. Additionally, it was shown in [73, 18] that when the height of the receiver decreases, the angular spread increases. Hence in [73], the authors proposed to use an adaptive array composed of a massive number of antennas with narrow beamwidths at the BS side due to the small angular spread. On the other hand, in [72], the authors proposed to deploy a wider beam antenna at the UE side to capture more power, because of the larger angular spread at the UE side.

Implications on mmWave System Design

Based on the aforementioned channel characteristics of mmWave channels, the following implications for the design and the analysis of mmWave cellular systems can be concluded:

- Indoor-outdoor penetration: Given that the penetration loss for outer walls of a building is $\approx$ 170 dB, hence, the outer walls can be assumed impenetrable for mmWave signals. Therefore, one main issue for mmWave signals is to design fast handover algorithms between the indoor and outdoor BSs for a smooth coverage experience for the UEs.

- Body and foliage blocking: The human body and foliage blocking are crucial for mmWave transmissions, and need to be considered in the network architecture and/or signal processing techniques for mmWave systems. For example, one signal processing solution can be to apply diversity beamforming, where the power is divided over multiple channel paths instead of focusing the power on the most dominant channel path. Another solution is the macro-diversity, where each UE can be connected to multiple BSs to allow fast switching between the links in case of blockage.

- Path loss: The high pathloss is one of the bottlenecks of the mmWave channels. Also, different path loss models should be considered for the LoS and non LoS paths. In order to compensate for this severe path loss, the deployment of massive antenna arrays with high directivity is crucial for mmWave systems.

- Channel sparsity: One of the main characteristics of mmWave channels is the sparsity of the multi-paths. This sparsity can be utilized in the design of channel estimation and precoding algorithms. Additionally, it can be leveraged to design some analytical tools, such as the physical ray based virtual representation of the channel that will be introduced in Subsection 2.2.4 in order to evaluate the performance of mmWave transmissions.

- Small-scale fading: In mmWave systems utilizing directional beamforming, the Rayleigh fading model is no longer applicable. It is even acceptable to neglect the small-scale fading effects when directional antenna arrays at both the BS and the UEs sides are appropriately aligned. Additionally, one acceptable assumption to model the mmWave channel, is to use a general Nakagami small-scale fading model with environment specific parameters tuning.

- Angular spread: As aforementioned, the angular spread depends on the hieght of the receiver, hence it is shown to be larger at the UEs side compared to the BSs side. Therefore, it is suggested to use a wider beam antenna array at the UEs side to capture more energy. This suggestion is even practically reasonable, since at the UEs side, due to hardware constraints, it is more realistic to deploy a small or intermediate number of antennas at the array, therefore having wider beams compared to the BS which is expected to have massive antenna array with very narrow (pencil) beams.

2.2.4 Physical Ray Based Model

Now, we move to describing the channel model used the most throughout our work. As aforementioned, early channel sounding campaigns in mmWave bands show that the mmWave channel has limitations imposed on the signal propagation, starting from the severe pathloss, limited scattering [18], limited diffraction effects [84] and high probability of blocking [85] due to the small wavelengths at such frequencies. Thus, only few paths can survive to the receiver and thus the sparsity of the mmWave channel is obvious. Henceforth, we use the sparse geometric channel model in [86, 56] with limited number of scatterers that contribute by one propagation path each, to model the mmWave channel. We assume a perfect downlink Orthogonal Frequency Division Multiplexing (OFDM) system. Thus, the channel is represented by one different matrix for each sub-carrier. The downlink narrowband channel vector for each UE k with single receive antenna $\mathbf{h}_k$ is represented as follows:

$$\mathbf{h}_k = \sqrt{\frac{N_T}{N_p{}^k}} \sum_{p=1}^{N_p{}^k} \alpha_{k,p} \mathbf{a}_t(\phi^t{}_{k,p})^H \tag{2.23}$$

where N_T is the number of transmit antennas, $\alpha_{k,p}$ is the complex amplitude of propagation path p which is one of the received $N_p{}^k$ paths by UE k, such that $\alpha_{k,p} \sim \mathcal{CN}(0,1)$. While $\phi^t{}_{k,p}$ represents the AoD for path p of UE k, such that $\phi^t{}_{k,p} \in [0, 2\pi]$. Finally, $\mathbf{a}_t(\phi^t{}_{k,p})$ is the transmit array steering vector which depends on the array geometry. In case ULA array is deployed then $\mathbf{a}_t(\phi^t{}_{k,p})$ can be calculated according to Equation (2.6). Thus, the MU channel $\mathbf{H} \in \mathbb{C}^{K \times N_T}$ can be expressed as $\mathbf{H} = [\mathbf{h}_1^T, \mathbf{h}_2^T, ..., \mathbf{h}_K^T]^T$.

2.2.5 Ray Tracing Model

In this thesis we consider a practical and simple ray tracing scenario shown in Figure 2.3. This scenario is a street canyon environment, with antenna array located on a building wall at the height of h = 10 m. The street is 15 m wide and we assume the cell covers a section of 30 m of the street in length. We consider only 2 multi-path components, the one reflected on the opposite building and the one on the ground, both considered as perfect reflectors. All users are placed on a line so that elevation angle is the same for all. System performance is simulated with up to 10 UEs by fixing the distance between them as 3 m.

In our proposed ray tracing scenario where all the reflectors are perfect. Hence the channel gain $\alpha_{k,p}$ for UE K over path p only depends on the large scale pathloss and is given as follows:

$$\alpha_{k,p} = \left(\frac{\lambda}{4\pi d_{k,p}} \right), \tag{2.24}$$

such that λ is the wavelength, and $d_{k,p}$ is the distance covered by path p for UE k. The channel vector between UE k with single receive antenna and the N_T antennas of the BS can be written on a flat channel with perfect reflectors as follows:

$$\mathbf{h}_k = \sum_{p=1}^{N_p{}^k} \alpha_{k,p} \mathbf{a}_t(\phi^t{}_{k,p}, \theta^t{}_{k,p}), \tag{2.25}$$
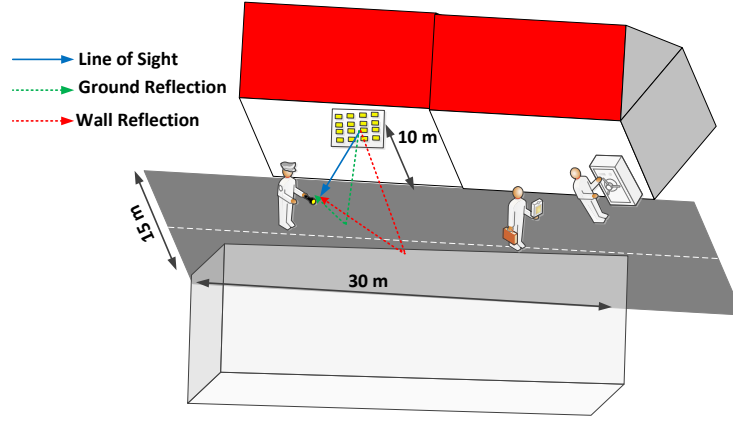
Figure 2.3: Street canyon environment with illustrating both the 1-Ray Scenario (LoS only) and the 3-Rays scenario (LoS and 2 perfect reflections from the ground and the opposite wall)

with $\mathbf{a}_t(\phi^t, \theta^t)$ is the transmit steering vector in case UPA with omni-directional antennas is considered in the transmit side and is calculated as in Equation (2.8). Therefore, we can see that both the physical ray based model in Equation (2.23) and the ray tracing based model in Equation (2.25) are similar in structure, while the only difference is that the channel parameters α, ϕ^t, θ^t are deterministic in the ray tracing model instead of being statistical as in the physical ray based model. In case we consider ULA with omni-directional antennas at the transmitter side we replace $\mathbf{a}_t(\phi^t, \theta^t)$ by $\mathbf{a}_t(\phi^t)$ which is calculated in Equation (2.6). The MU channel $\mathbf{H} \in \mathbb{C}^{K \times N_T}$ can be expressed as

$$\mathbf{H} = [\mathbf{h}_1^T, \mathbf{h}_2^T, ..., \mathbf{h}_K^T]^T \tag{2.26}$$

2.2.6 Different Channel Scenarios

Throughout Subsections 2.2.4 and 2.2.5, we considered a MU MISO channel with sparse multi path components and no blockage effect. However, in the next chapters we will tackle some scenarios where the channel is SU MIMO and/or pure LoS and/or suffer from blockage. Therefore, in this subsection we will define these scenarios and show their effects on the proposed channel model in Subsection 2.2.4. Extending the channel model in Subsection 2.2.5 to consider these special cases is quite similar and straightforward, hence we omit it for the sake of readability.

SU MIMO Channel Scenario

In this case, the channel model in Equation 2.23 can be modified as follows:

$$\mathbf{H} = \sqrt{\frac{N_R N_T}{N_p}} \sum_{p=1}^{N_p} \alpha_p \mathbf{a}_r(\phi^r_p) \mathbf{a}_t(\phi^t_p)^H \tag{2.27}$$

where N_R represents the number of receive antennas, and $\mathbf{H}$ is the SU MIMO channel. In case UPAs are considered at the transmitter and the receiver sides instead of ULAs, then $\mathbf{a}_r(\phi^r{}_p), \mathbf{a}_t(\phi^t{}_p)$ need to be replaced by $\mathbf{a}_r(\phi^r{}_p, \theta^r{}_p), \mathbf{a}_t(\phi^t{}_p, \theta^t{}_p)$ which can be calculated according to Equation (2.8).

Pure LoS Channel Scenario

In case the channel is pure LoS and no multipath components exist, then Equation (2.23) can be simplified as follows:

$$\mathbf{h}_k = \sqrt{N_T}\alpha_k \mathbf{a}_t(\phi^t{}_k)^H \tag{2.28}$$

since for each UE k only a single path is available, the path index p is omitted, and the summation over paths does not exist anymore. Then, the MU MISO channel can be reconstructed as $\mathbf{H} = [\mathbf{h}_1^T, \mathbf{h}_2^T, ..., \mathbf{h}_K^T]^T$. In case the channel is a pure LoS SU MIMO one, then Equation (2.27) can be simplified as follows:

$$\mathbf{H} = \sqrt{N_R N_T}\alpha \mathbf{a}_r(\phi^r)\mathbf{a}_t(\phi^t)^H \tag{2.29}$$

Blockage Effect

For the propagation paths blocking we adopt the model in [85], which considers the effect of human bodies. It is modeled as a log normal random variable of mean -55.1 dB and standard deviation 7.9 dB and represented by the log-normal loss variable $\zeta \sim \mathcal{N}(-55.1, 7.9)$. Then linearizing the blocking factor to be $B = 10^{\frac{\zeta}{10}}$. We consider two blockage scenarios of the channel model throughout the thesis as follows:

- **Scenario 1 (LoS Blockage)**: In this scenario the blockage factor is applied to the channel path with highest gain (LoS path) for each UE k in Equation (2.23):

$$p_{LoS} = \underset{p}{\operatorname{argmax}}|\alpha_p| \tag{2.30}$$

  Then the channel vector for each UE k is calculated as follows:

$$\mathbf{h}_{k,LoS} = \sqrt{\frac{N_T}{N_p{}^k}}\left(B\alpha_{k,p_{los}}\mathbf{a}_t(\phi^t{}_{k,p_{los}})^H\right) \tag{2.31}$$

$$\mathbf{h}_{k,nLoS} = \sqrt{\frac{N_T}{N_p{}^k}}\left(\sum_{p=1,p\neq p_{LoS}}^{N_{pk}}\alpha_{k,p}\mathbf{a}_t(\phi^t{}_{k,p})^H\right) \tag{2.32}$$

$$\mathbf{h}_k = \mathbf{h}_{k,LoS} + \mathbf{h}_{k,nLoS} \tag{2.33}$$

- **Scenario 2 (Random Path Blockage)**: In this scenario the blockage model is applied to a random channel path p_{rand} for each UE k in each channel realization in Equation (2.23), hence the channel vector for each UE k is calculated as follows:

$$\mathbf{h}_{k,rand} = \sqrt{\frac{N_T}{N_p{}^k}}\left(B\alpha_{k,p_{rand}}\mathbf{a}_t(\phi^t{}_{k,p_{rand}})^H\right) \tag{2.34}$$

$$\mathbf{h}_{k,nrand} = \sqrt{\frac{N_T}{N_p{}^k}} \left(\sum_{p=1,p\neq p_{rand}}^{N_p{}^k} \alpha_{k,p} \mathbf{a}_t(\phi^t{}_{k,p})^H \right) \tag{2.35}$$

$$\mathbf{h}_k = \mathbf{h}_{k,rand} + \mathbf{h}_{k,nrand} \tag{2.36}$$

2.3 Beamforming for **mmWave** Massive **MIMO** Systems

In this section, we provide a detailed description for the beamforming techniques and architectures that are used for mmWave massive MIMO systems. In Subsection 2.3.1, the constraints for mmWave architectures are stressed. Then, in Subsections 2.3.2, 2.3.3 and 2.3.4, the analog, digital and hybrid beamforming architectures are described respectively, with emphasizing the advantages and disadvantages of each one and highlighting the beamforming algorithms that are used throughout the thesis.

2.3.1 Constraints for **mmWave** Architectures

In sub-6 GHz cellular systems, the MIMO precoding is conventionally done in the BB (digital layer), for example, the massive MIMO system introduced in Subsection 2.1.1. This is because digital signal processing allows to have a full access to modify both the amplitudes and phases of the entries in the precoding/combining matrices. Unlike, in analog processing (RF part), due to hardware limitations, only the phases of the precoding/combining matrices can be modified. However, as shown in Figure 2.5, fully digital MIMO processing requires that the transceiver dedicates an RF chain per antenna element. Additionally, sub-6 GHz cellular systems, high resolution Analog to Digital Converters (ADCs) are conventionally used, thus, the ADC quantization error is a minor problem for such systems.

However, in mmWave cellular systems, these assumptions are no longer practical, since such systems can not afford to utilize the full digital processing architectures, due to the high cost and power consumption of mixed-signal components in the RF chains [4, 87]. Therefore, in the recent literature [4, 87, 88, 89, 90], another alternative architectures were proposed for practical mmWave systems. For example, one solution for the hardware and power constraints imposed by the mmWave systems is to apply an analog beamforming/Hybrid Beamforming architecture that requires less RF chains than the antennas. Thus, performing full/part of the MIMO processing using cost-efficient and power-efficient analog components [4, 89, 90]. Another solution that can be used in parallel with the analog beamforming/Hybrid Beamforming architectures, is to use low-resolution ADCs to reduce the power consumption due to the high sampling rate required by the large mmWave BW [87, 88].

In this section we will focus on describing the mmWave systems' beamforming architectures as follows.

2.3.2 Analog Beamforming

The analog beamforming architecture consists of a phase shifting network that can be implemented either using active or passive phase shifters or analog beamforming networks such
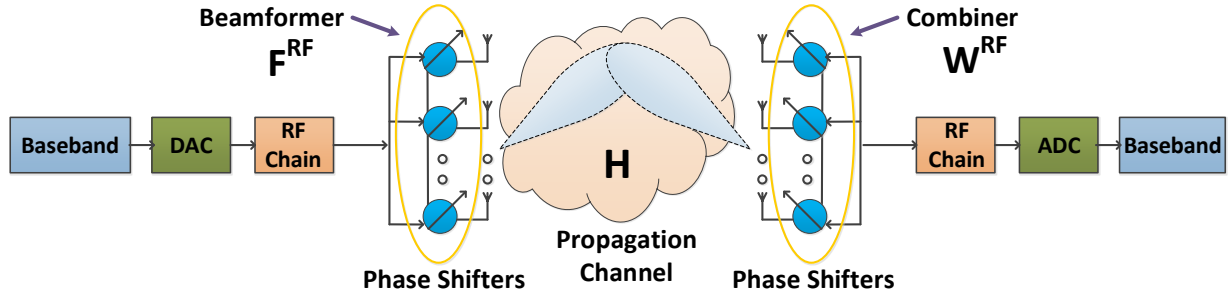
Figure 2.4: The Analog Beamforming Architecture

as: lens array, buttler matrix, etc. The basic architecture of analog beamforming using phase shifters is shown in Figure 2.4. For phased array based analog beamforming, the phase shifters deployed have constant amplitude and quantized angles. The power consumption of the phase shifters depends on its angular resolution. Moreover, the phase shifters apply for entire band.

SU System Model

In case analog beamforming is applied at the transmitter side and analog combining is applied at the receiver side, the received signal can be expressed as follows:

$$\mathbf{r} = \sqrt{P_T} \, (\mathbf{W}^{RF})^H \mathbf{H} \mathbf{F}^{RF} \mathbf{s} + (\mathbf{W}^{RF})^H \mathbf{n} \tag{2.37}$$

such that P_T is a scalar defining the transmit power, $\mathbf{W}^{RF}$ and $\mathbf{F}^{RF}$ denote the analog combiner of dimension $N_R \times 1$ and the analog beamformer of dimension $N_T \times 1$ respectively. $\mathbf{H}$ represents the propagation channel of dimensions $N_R \times N_T$. Finally, $\mathbf{n}$ the AWGN vector of dimension $N_R \times 1$.

The Advantages and Disadvantages of Analog Beamforming

The advantages of analog beamforming can be summarized as follows:

- Low hardware complexity (1 RF chain is required).

- Low power consumption (1 RF chain is required).

- Can increase the link budget.

- Low overhead (1 UE is supported per time/frequency resource).

However, the disadvantages of analog beamforming can be summarized as follows:

- Limited to single stream and SU MIMO.

- Not favourable from SE and coverage perspectives due to the limitation of serving 1 UE per time/frequency resource.

Analog Beamforming Algorithms

In this subsubsection the analog beamforming algorithms considered within the thesis which are the LoS beamsteering algoritm and the EGT algorithm are detailed.

LoS Beamsteering: This is the most straightforward approach in which the beam steering is done to the path with the highest magnitude (LoS path or the best non LoS path in case no LoS path exist). This approach achieves high SNR in case no blockage occurs due to the sparse nature of the mmWave channel and the LoS dominance. The beamforming vector is calculated based on the knowledge of the best path AoD $\phi^t_{k,pLoS}$ as follows:

$$\mathbf{f}_{LoS} = \mathbf{a}_t(\phi^t_{pLoS}) \tag{2.38}$$

Therefore, it is clear that it has low overhead since it only needs estimating the angles of the departure of the LoS path and also has low computational complexity. However, in case there exist other dominant paths in the channel, it will lead to SNR degradation. Moreover, if the best path is blocked the SNR degrades severely and it can suffer from outage.

Equal Gain Transmission: Here we introduce EGT as a promising candidate for solving the SNR maximization together with achieving high robustness. In EGT we formulate the problem in a more efficient way in order to achieve all the potential gains of the system as follows:

$$\mathbf{f} = \underset{\mathbf{f}}{\operatorname{argmax}} \sum_{p=1}^{N_p} |\alpha_p|^2 \mathbf{a}_t(\phi^t_p)^H \mathbf{f}\mathbf{f}^H \mathbf{a}_t(\phi^t_p) \tag{2.39}$$
$$\text{s.t. } \|\mathbf{f}\| = 1$$

Here, we aim at maximizing the SNR over all the transmission paths and do not limit the maximization problem to the maximum eigenvector of the SNR only as in the LoS beamsteering. The problem in Equation (2.39) takes into account the constant gain constraint for realistic implementation in analog RF networks based on phased arrays. The closed form solution for this problem is the EGT technique [91, 92], in which the beamforming vector for MISO systems is given as:

$$\mathbf{f}_{EGT} = \frac{e^{j\angle \mathbf{h}^H}}{\sqrt{N_T}} \tag{2.40}$$

thus, EGT gives a closed form non-iterative solution that maximizes the SNR, together with distributing the energy efficiently on the propagation paths with considering constructively adding them up.

2.3.3   Digital Beamforming

In case digital beamforming is adopted, all the signal processing is done in the digital domain (Base Band). Digital beamforming needs a dedicated RF chain per antenna. Moreover, a dedicated mixed analog/digital device is needed per antenna (ADC per receive antenna and Digital to Analog Converter (DAC) per transmit antenna). In this subsection, we will only define the SU system model, since the MU digital beamforming model was previously introduced in Subsection 2.1.1.
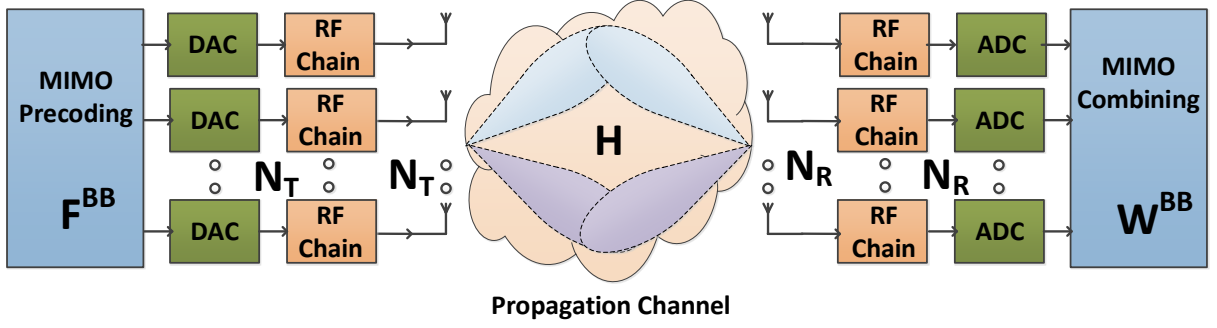
Figure 2.5: The Digital Beamforming Architecture

SU System Model

In case digital beamforming and combining are applied in a SU MIMO scenario as shown in Figure 2.5, the received signal can be expressed as follows:

$$\mathbf{r} = \sqrt{P_T}(\mathbf{W}^{BB})^H \mathbf{H} \mathbf{F}^{BB} \mathbf{s} + (\mathbf{W}^{BB})^H \mathbf{n} \tag{2.41}$$

where $\mathbf{W}^{BB}$ and $\mathbf{F}^{BB}$ are the digital combiner of dimensions $N_R \times N_S$ and the digital beamformer of dimensions $N_T \times N_S$ respectively, such that N_S is the number of spatially multiplexed data streams.

The Advantages and Disadvantages of Digital Beamforming

The advantages of digital beamforming can be summarized as follows:

- Can provide interference free MU MIMO scenario with number of UEs up to N_T.

- Favourable in terms of enhancing the network's SE.

- A lot of existing digital precoding techniques exist in the current literature as shown in the previous subsection.

However, the main disadvantages of digital beamforming can be summarized as:

- One RF chain and ADC/DAC is required per antenna.

- Thus, there exist limitations in terms of hardware complexity, power consumption and overhead in massive MIMO mmWave systems.

Digital Beamforming Algorithms

Given that we already described the CB, ZF and MMSE linear precoders in Subsection 2.1.2, here we will only describe a new linear low complexity-low overhead digital linear precoder named DBS [19]. Althourgh, DBS is not suitable for sub-6 GHz massive MIMO systems which have rich scattering channels, it is suitable for sparse LoS dominated mmWave massive MIMO channels as will be explained later in this subsection.

DBS Precoding: DBS is the MU version of the LoS beamsteering and uses the AoD of each UE to steer a beam in their direction. Therefore, it can be seen as a promising approach for mmWave channels which are sparse and LoS dominated. The hardware needed for its implementation is the same as any digital beamforming one, but what changes radically is the information needed to precode the signal. Indeed, for a 3D environment where AoD of one UE is described with two angles (ϕ^t and θ^t) which means that the number of coefficients for the DBS is 2 per UE. Therefore, the precoding matrix in this case for K UEs $\mathbf{F}$ is defined as:

$$\mathbf{F} = \mathbf{A}_t(\phi^t, \theta^t) \tag{2.42}$$

where $\mathbf{A}_t(\phi^t, \theta^t) = [\mathbf{a}_t(\phi^t{}_{1,LoS}, \theta^t{}_{1,LoS}), ..., \mathbf{a}_t(\phi^t{}_{K,LoS}, \theta^t{}_{K,LoS})]$ is a matrix with k-th column representing the steering vector for the LoS path for UE k represented as $\mathbf{a}_t(\phi^t{}_{k,LoS}, \theta^t{}_{k,LoS})$.

2.3.4 Hybrid Beamforming

Driven by the disadvantages of both analog and digital beamforming for MU massive MIMO mmWave systems, the HBF emergence became a necessity for such systems to work efficiently [8]. The main idea of HBF is to strike a balance between the high SE offered by digital beamforming and the low hardware complexity and power consumption offered by analog beamforming. As shown in Figure 2.6, the HBF architecture is flexible one, in which the signal processing is split between the analog and digital domains. In the analog domain a network of phase shifters [5] or fixed analog beamforming network [9] can be used to preform physical beams in the UEs directions. Then, the channel dimensions are compressed in the analog domain through projecting the propagation channel on the analog beamforming and combining basis leading to compressing the $N_R \times N_T$ dimensions into $N_{RRF} \times N_{TRF}$, where N_{RRF} and N_{TRF} represent the number of the RF chains at the receiver and the transmitter respectively and given that $N_T >> N_{TRF}$ and $N_R >> N_{RRF}$.

SU System Model

In case hybrid beamformer and combiner are applied in a SU MIMO system as shown in Figure 2.6, the received signal can be expressed as follows:

$$\mathbf{r} = \sqrt{P_T}(\mathbf{W}^{BB})^H(\mathbf{W}^{RF})^H\mathbf{H}\mathbf{F}^{RF}\mathbf{F}^{BB}\mathbf{s} + (\mathbf{W}^{BB})^H(\mathbf{W}^{RF})^H\mathbf{n} \tag{2.43}$$

where the hybrid combiner consists of an analog part $\mathbf{W}^{RF}$ of dimensions $N_R \times N_{RRF}$ and a digital part $\mathbf{W}^{BB}$ of dimensions $N_{RRF} \times N_S$. Similarly, the hybrid precoder consists of an analog part $\mathbf{F}^{RF}$ of dimensions $N_T \times N_{TRF}$ and a digital part $\mathbf{F}^{BB}$ of dimensions $N_{TRF} \times N_S$.
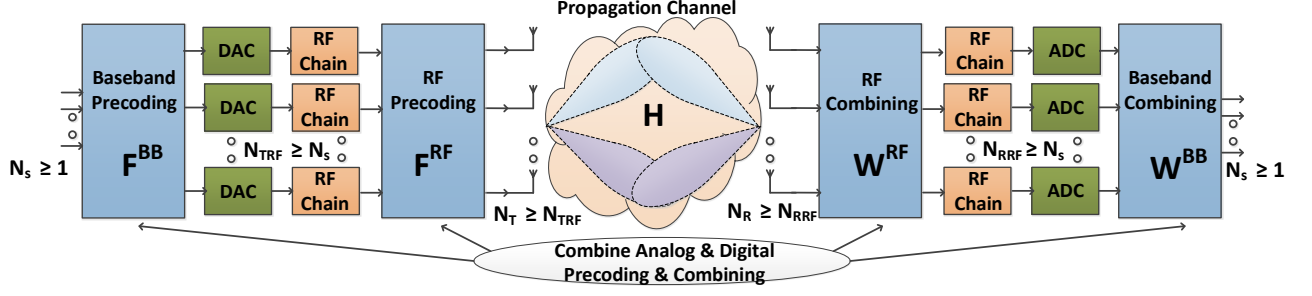
Figure 2.6: The Hybrid Beamforming Architecture

MU System Model
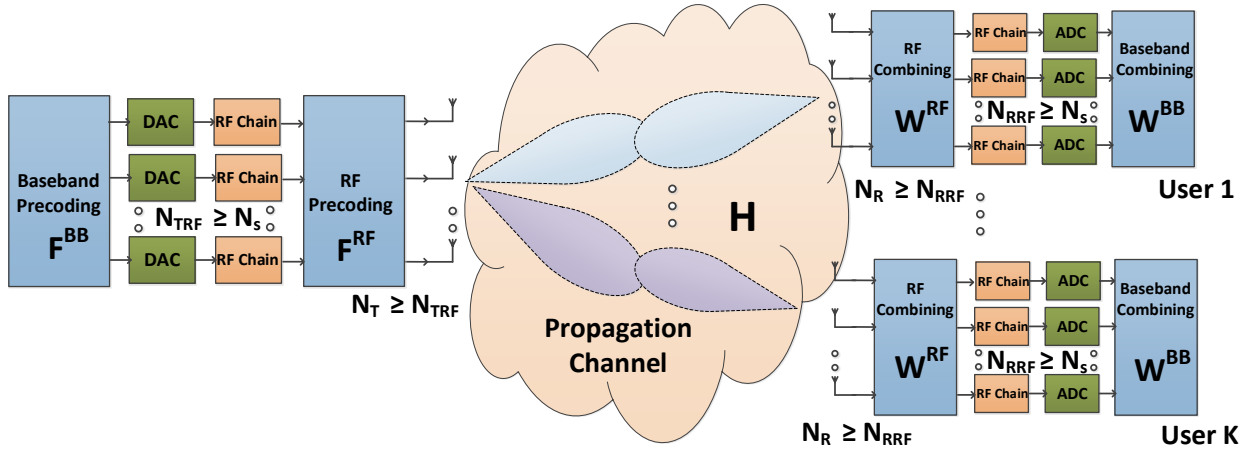
Figure 2.7: The MU MIMO Hybrid Beamforming Architecture

In case hybrid beamformers and combiners are applied in a MU MIMO downlink system as shown in Figure 2.7, where each UE is equipped with a single RF chain $N_{RRF} = 1$ and can only receive a single stream, the received signal vector $\mathbf{r} = [r_1, r_2, ..., r_K]$ can be expressed as follows:

$$\mathbf{r} = \sqrt{P_T}(\mathbf{W}^{RF})^H \mathbf{H} \mathbf{F}^{RF} \mathbf{F}^{BB} \mathbf{s} + (\mathbf{W}^{RF})^H \mathbf{n} \tag{2.44}$$

In this case the hybrid combiner consists of only an analog part $\mathbf{W}^{RF} = [\mathbf{w}^{RF}_1, ..., \mathbf{w}^{RF}_K]$, with each RF combining vector $\mathbf{w}^{RF}$ of dimensions $N_R \times 1$. On the other hand, the hybrid precoder consists of an analog part $\mathbf{F}^{RF}$ of dimensions $N_T \times N_{TRF}$ and a digital part $\mathbf{F}^{BB}$ of dimensions $N_{TRF} \times K$.

In case hybrid beamformers are applied in a MU MISO downlink system as shown in Figure 2.8, where each UE is equipped with a single receive antenna $N_R = 1$ and can only receive a single stream, the received signal vector $\mathbf{r} = [r_1, r_2, ..., r_K]$ can be expressed as follows:
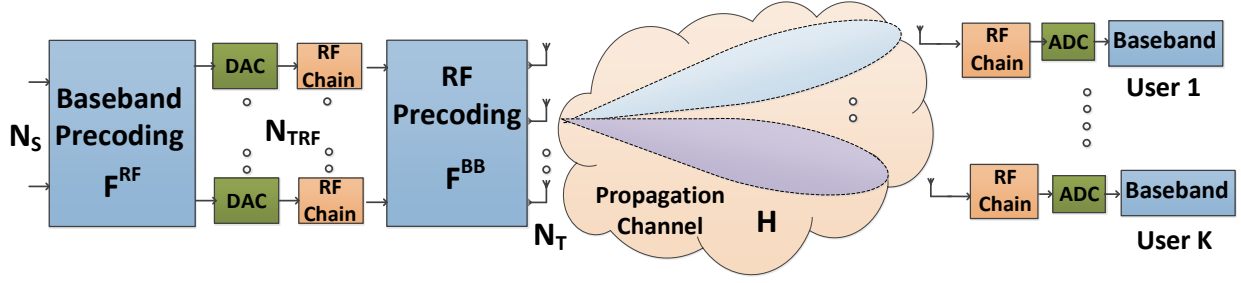
Figure 2.8: The MU MISO Hybrid Beamforming Architecture

$$\mathbf{r} = \sqrt{P_T}\mathbf{H}\mathbf{F}^{RF}\mathbf{F}^{BB}\mathbf{s} + \mathbf{n} \tag{2.45}$$

In this case the hybrid precoder consists of an analog part $\mathbf{F}^{RF}$ of dimensions $N_T \times N_{TRF}$ and a digital part $\mathbf{F}^{BB}$ of dimensions $N_{TRF} \times K$.

The Potentials and Challenges of HBF

Given the fact that HBF has flexible architecture, instead of defining the advantages and disadvantages of it, we will reformulate this definition as the potentials and challenges of HBF.

The potentials of HBF can be summarized as follows:

- Can support MU multi-stream MIMO scenario with flexible hardware and power constraints.

- Can employ much more transmit antennas than the RF chains. Henceforth, it can achieve high array gains without requiring high number of RF chains or DACs/ADCs.

- Can achieve higher transmit array gain compared to the digital systems with same number of RF chains (approximately the same hardware complexity).

On the other hand, the challenges of HBF can be summarized as follows:

- High resolution power hungry phase shifters in the analog domain cause high power consumption.

- The high power consumption and the complexity of RF chains at high frequencies and ADCs/DACs at high BW (in comparison with the analog beamforming, where only one RF chain and ADC/DAC is required).

Therefore, in order to overcome the challenges of HBF, some primary solutions emerged in the literature [93, 90, 3, 94, 95] that aim at:

- Implementing less complex, power efficient RF chains and ADCs/DACs for high frequencies and large BW.

- Use low number of RF chains and ADCs/DACs encouraged by the propagation channel sparsity.

- Use low resolution ADCs/DACs and compensate for the quantization error in the digital domain.

- Use low resolution phase shifters.

- Use lower complexity analog components instead of the phase shifters such as the lens array and switches.

HBF Signal Processing Architectures

Here, we compare between the existing signal processing architectures in the literature for HBF and highlight the advantages and disadvantages for each one.

- **Fully Joint Architecture**: In this architecture the analog and digital beamformers and combiners are calculated globally in order to maximize a certain objective such as the SE or the EE. Although, these kinds of algorithms are favourable in terms of SE maximization and can achieve optimal performance, they are iterative and computationally complex. Also, they need training over the channel which leads to extensive overhead and affects the throughput of the system. Moreover, this kind of iterative algorithms can result in outdated CSI. Therefore, in order to relax these complexity and overhead constraints, the two following architectures emerged in which the transmitter and the receiver are decoupled and/or the analog and the digital parts are decoupled. Although, this decoupling does not achieve globally optimal solution, it is less complex, and more practical.

- **Transmitter/Receiver Decoupling HBF**: In this architecture, the hybrid beamformer $\mathbf{F}^{RF}\mathbf{F}^{BB}$ and the analog combiner $\mathbf{W}^{BB}\mathbf{W}^{RF}$ are calculated separately. However, the analog and digital parts can still be calculated jointly or decoupled [96]. This architecture is better in terms of complexity and overhead compared to the case of fully joint architecture, since it avoids the feedback of the beamformer and combiner over the channel over multiple iterations. However, on the other hand it has sub-optimal SE performance compared to the fully joint one because in each side (transmitter or receiver), the other side is assumed to be constant which leads to SE performance loss.

- **Analog/Digital Decoupling HBF**: Again in order to relax the complexity, overhead and delay constraints arising from the fully joint structure, work in the literature [97] further decoupled the analog and digital parts for further simplified implementation. In this scenario, first the analog beamformer and combiner are calculated in order to maximize a certain objective (for example the received SNR) for each UE separately or jointly solving the global SE maximization problem in analog domain jointly for multiple UEs with taking into account the hardware constraints imposed by the analog layer, namely
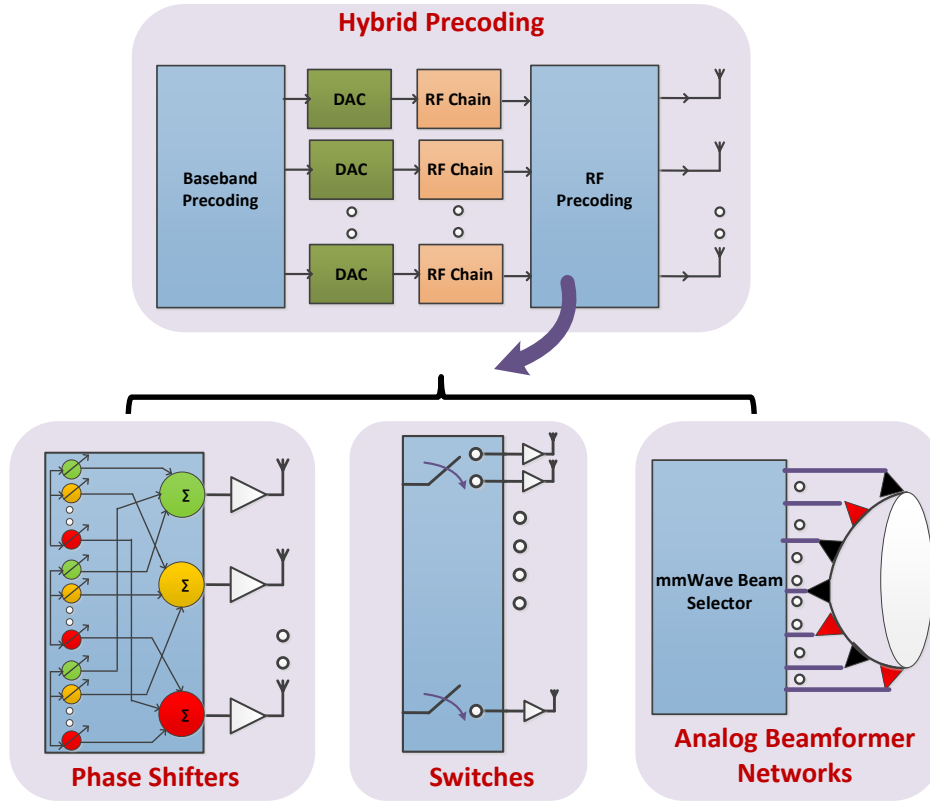
Figure 2.9: Possible Analog Architectures for HBF

the constant amplitude and quantized phases constraints. Then in the digital layer, the digital beamforer and combiner are calculated based on the reduced dimensions equivalent channel that encompasses the propagation channel together with both the analog beamformer and combiner. Thus, dividing the beamforming and combining problems into two consecutive steps as explained in details in [56].

HBF Physical Architectures

Here, we provide an introduction to a variety of analog network architectures found in the literature and shown in Figure 2.9. Recently many work in the literature considered fully connected and sub-connected architectures of phase shifters and switches as potential candidates for the analog layer design in hybrid beamforming [93, 90]. Moreover, some work considered fixed analog beamforming networks such as the lens array [98] and the buttler matrix [99] to be contenders to phased arrays and switch based arrays. Therefore, the question that arise is, which analog beamforming architecture is favourable in which scenario. The answer of this question will be introduced in this part.

- **Fully Connected Architectures**: Fully connected analog architectures were considered

1) Fully Connected Analog Architecture
with Phase Shifters

2) Fully Connected Analog Architecture
with Switches
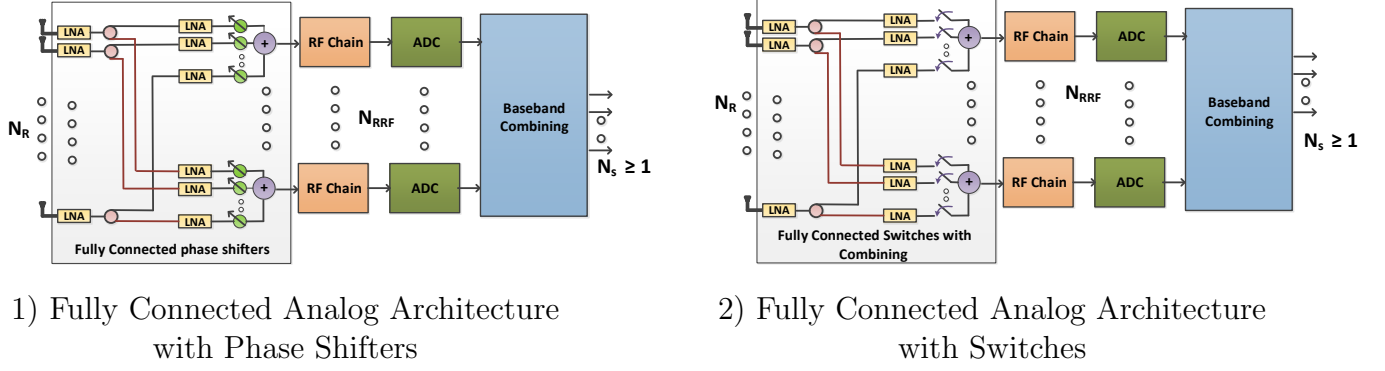
Figure 2.10: Illustration of the Fully Connected Analog Architectures

in the literature as the default analog networks, since they provide full control on the analog processing and calculations [90] and is favourable in terms of SE maximization. However, driven by the fact that fully connected architectures whether based on phase shifters or even switches have high hardware complexity and high power consumption, therefore it is not favourable in terms of practical implementation.

First we start by describing the fully connected analog architecture with phase shifters shown in Figure 2.10-1. In this architecture, in order to assess the hardware complexity we define the number of hardware elements needed at the receiver side (given the fact that due to the duality the hardware elements required at the transmitter have the same behaviour) in such architecture as follows:

- Low Noise Amplifiers (LNAs): $N_R + N_R N_{RRF}$
- Phase Shifters: $N_R N_{RRF}$
- Combiners: N_{RRF}
- Splitters: N_R

Moreover, the receiver power consumption model can be defined as in [90] as follows:

$$P_{FP} = N_R(N_{RRF} + 1)P_{LNA} + N_R N_{RRF} P_{PS} + N_{RRF}(P_{RFC} + P_{ADC}) + P_{BB} \qquad (2.46)$$

where P_{LNA} represents the power per LNA, P_{PS} denotes the power per phase shifter. P_{RFC} represents the power per RF chain and P_{ADC} denotes the power per ADC. Finally, P_{BB} represents the power consumed in the digital part (BB).

The mathematical model for the set of possible analog combiners $\mathcal{A}_{FP}$ in such architecture is expressed as:

$$\mathcal{A}_{FP} = \left\{ \mathbf{x} \in \mathbb{C}^{N_R \times 1} \big| |x_i| = 1, \forall i \right\} \qquad (2.47)$$

Therefore, the main advantage of this architecture is that it can achieve the highest SE compared to the other architectures. However, this gain is accompanied by some disadvantages, which can be summarized as follows:

1) Sub-Connected Analog Architecture with Phase Shifters

2) Sub-Connected Analog Architecture with Switches
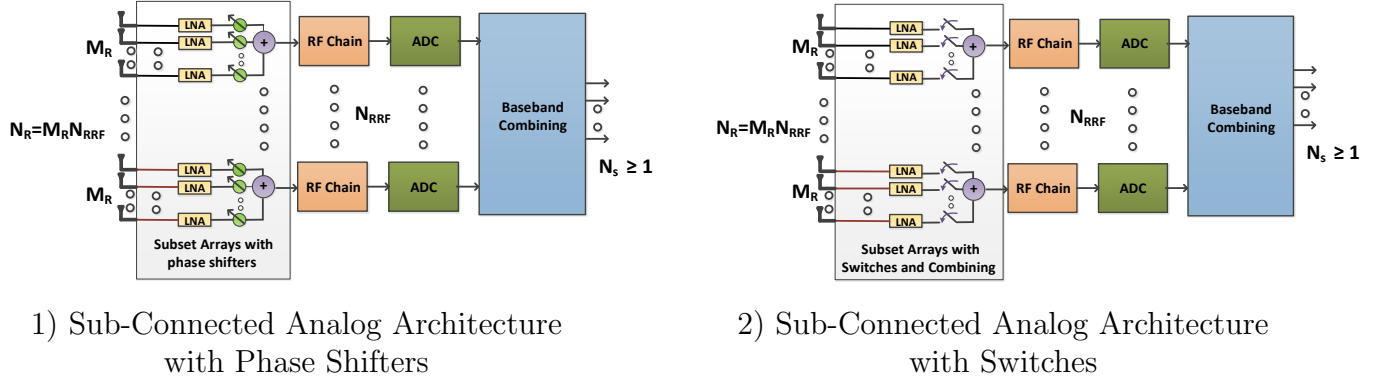
Figure 2.11: Illustration of the Sub-Connected Analog Architectures

– This architecture has the highest hardware complexity.

– It has the highest hardware cost.

– It has the highest power consumption.

Another, fully connected architecture adopted in the literature is the one shown in Figure 2.10-2, with switches replacing the phase shifters. This architecture has less hardware complexity, however this is done on the cost of reduced SE, since in this case not all the antennas are active. Thus, the antenna array gain is not maximized as in the case of phase shifters.

The number of hardware elements at the receiver is similar to the previous architecture, with replacing the phase shifters by switches. Again, the receiver power consumption model is similar to the one in Equation (2.46) but with replacing P_{PS} by the power wasted by the switch P_S. Finally, the mathematical model for the set of possible analog combiners $\mathcal{A}_{FS}$ in such architecture is expressed as:

$$\mathcal{A}_{FS} = \{\mathbf{x} \in \mathcal{B}^{N_R \times 1}\} \tag{2.48}$$

where $\mathcal{B}$ is the set of binary numbers $\{0, 1\}$.

- **Sub-Connected Architectures**: In order to relax the hardware complexity and the power consumption constraints in the fully connected architectures, the sub connected architectures emerged as an alternative solution, however achieving less SE compared to fully connected one. First we describe the sub-connected architecture based on phase shifters as shown in Figure 2.11-1. The number of hardware elements at the receiver in this case can be represented as:

  – LNAs: N_R

  – Phase Shifters: N_R

    – Combiners: N_{RRF}

Therefore, it is clear that a massive reduction in the hardware components can be achieved by the sub-connected architecture compared to the fully connected one. Similarly the receiver power consumption can be described in this case as follows:

$$P_{SP} = N_R P_{LNA} + N_R P_{PS} + N_{RRF}(P_{RFC} + P_{ADC}) + P_{BB} \tag{2.49}$$

Therefore, compared to Equation (2.46) the power consumption is significantly reduced. The advantages of this architecture are as follows:

    – Lower hardware complexity than the fully connected one.

    – Lower hardware cost than the fully connected one.

    – Lower power consumption than the fully connected one.

However, the main disadvantage of this architecture is that the array gain is reduced by $\frac{1}{N_{RRF}}$ leading to a reduction is the achieved SE. Similar to the fully connected approach, the phase shifters in the sub-connected architecture can be replaced by switches as shown in Figure 2.11-2.

- **Analog Beamforming Networks with Beam Selection**: Finally, the authors in [98] proposed using the lens array for analog beamforming and/or combining as shown in Figure 2.12. The main advantages of the lens array is that, it computes the spatial DFT directly in the analog domain. Henceforth, it is equivalent to setting the analog precoders and/or combiners to DFT matrices. Therefore, it is favourable in terms of complexity, power consumption and overhead compared to the architectures based on phase shifters and switches, which need some signal processing calculations for the analog beamformers and combiners. The received signal in this case before applying the digital precoding part, can be expressed as follows:

$$\mathbf{r} = (\mathbf{W}^{RF})^H \mathbf{H} \mathbf{F}^{RF} \mathbf{s} + (\mathbf{W}^{RF})^H \mathbf{n} \tag{2.50}$$

Given that the lens array is used at both the transmitter and the receiver, then

$$\mathbf{F}^{RF} = \mathbf{W}^{RF} = \mathbf{U} \tag{2.51}$$

where $\mathbf{U}$ is the unitary DFT matrix. Given the fact that the mmWave sparse propagation channel can be expressed in terms of the beamspace channel $\mathbf{H}_b$ as follows [100]:

$$\mathbf{H} = \mathbf{U} \mathbf{H}_b \mathbf{U}^H \tag{2.52}$$

Therefore, from Equations (2.51) and (2.52), we can have direct access to the beamspace channel using the lens array and thus the received signal vector can be expressed as:

$$\mathbf{r} = \mathbf{H}_b \mathbf{s} + (\mathbf{W}^{RF})^H \mathbf{n} \tag{2.53}$$
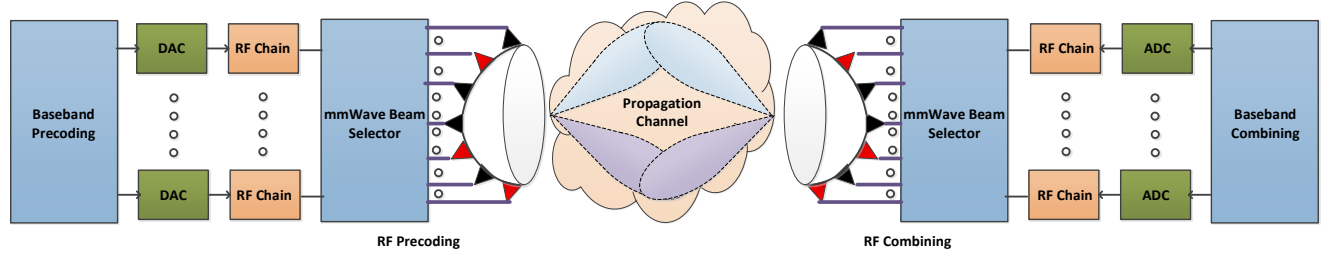
Figure 2.12: Lens Array for HBF with Beam Selection

Hybrid Beamforming Algorithm

Two Stage HBF: Throughout the thesis we will use the two stage decoupled HBF due to its low computational and hardware complexity and thus practical feasibility [56]. Also, we will assume a fully connected phase shifters network available in the analog layer. The proposed HBF framework can be divided into two main stages which are the RF (analog) stage and the BB (digital) one. In the first stage (analog), for the precoding matrix $\mathbf{F}^{RF} = [\mathbf{f}^{RF}{}_1, ..., \mathbf{f}^{RF}{}_K]$ we choose to apply either LoS beamsteering in case the channel is LoS dominated and can be approximated as a pure LoS or EGT in case the channel multi path components are significant and need to be captured, where both algorithms are described in Subsection 2.3.2.

Then, in the second stage (digital) precoding $\mathbf{F}^{BB} = [\mathbf{f}^{BB}{}_1, ..., \mathbf{f}^{BB}{}_K]$, we choose one of the digital beamforming techniques (CB - ZF - MMSE) in Subsection 2.1.2. Throughout the thesis we mainly choose ZF for the digital layer since it is widely adopted as the digital layer for HBF in the recent literature [5, 56]. This is due to the fact that both LoS beamsteering and EGT aim at maximizing the received SNR for each UE seperately but they do not consider the IUI between the UEs. Therefore, using the ZF in the digital layer is crucial to mitigate the IUI. After applying the digital stage, the HBF precoder is normalized as follows:

$$\mathbf{f}^{BB}{}_k = \frac{\mathbf{f}^{BB}{}_k}{\|\mathbf{F}^{RF}\mathbf{f}^{BB}{}_k\|_F} \tag{2.54}$$

2.4 Spectral Efficiency

In this section, we we will focus on defining the SE of the MU MIMO channel, since it is the main performance metric that we consider throughout the thesis to evaluate the performance of the proposed signal processing algorithms. We will derive the deterministic and ergodic SE, also known as the normalized channel capacity (the BW effect is normalized) of such a system.

2.4.1 Deterministic SE

For a given MIMO channel, the SE (normalized capacity) is defined as the maximum mutual information that can be achieved through the variation of the Probability Density Function (PDF)

Algorithm 1 Two Stage Decoupled HBF

---

1) **First Stage:** RF Analog Beamforming **such that**
$$\mathbf{F}^{RF} = [\mathbf{f}^{RF}{}_1, ..., \mathbf{f}^{RF}{}_K]$$
$\mathbf{f}^{RF}{}_k$ can be chosen from $\{\mathbf{f}_{LoS,k}, \mathbf{f}_{EGT,k}\}$

2) Calculate the equivalent channel $\hat{\mathbf{H}}$ as:
$$\hat{\mathbf{H}} = [\hat{\mathbf{h}}_1^T, ..., \hat{\mathbf{h}}_K^T]$$
$\hat{\mathbf{h}}_k = \mathbf{h}_k \mathbf{F}^{RF}, (\mathbf{h}_k \in \mathbb{C}^{1 \times N_T}, \mathbf{F}^{RF} \in \mathbb{C}^{N_T \times N_{TRF}}, \hat{\mathbf{h}}_k \in \mathbb{C}^{1 \times N_{TRF}})$

3) **Second Stage:** Digital Precoding such that
$\mathbf{F}^{BB}$ can be chosen as any BB technique. Here we choose ZF, hence$\mathbf{F}^{BB} = \mathbf{F}_{ZF}$

4) Here the digital beamforming $\mathbf{F}^{BB}$ is applied on the equivalent channel $\hat{\mathbf{H}}$ instead of the propagation channel $\mathbf{H}$. Hence, replacing $\mathbf{H}$ by $\hat{\mathbf{H}}$, the beamformer is calculated as:
$$\mathbf{F}_{ZF} = \hat{\mathbf{H}}^H (\hat{\mathbf{H}}\hat{\mathbf{H}}^H)^{-1}$$

5) The digital beamformers are normalized to satisfy the total power constraint using the scaling factors in Equation (2.54)

6) Finally the hybrid beamformer is calculated as:
$$\mathbf{F}^{HBF} = \mathbf{F}^{RF}\mathbf{F}^{BB}$$

---

of the transmit signal vector and is represented, according to [101], as follows:

$$\epsilon = \max_{Tr(\Phi_{\mathbf{s},\mathbf{s}}) < P_T} I(\mathbf{s}; \mathbf{r}) \qquad \text{bits/channel use,} \tag{2.55}$$

such that $I(\mathbf{s}; \mathbf{r})$ represents the mutual information of the random transmitted and received signal vectors $\mathbf{s}$ and $\mathbf{r}$, while $Tr(\Phi_{\mathbf{s},\mathbf{s}}) < P_T$ defines the maximum transmit power constraint. Then, $I(\mathbf{s}; \mathbf{r})$ can be further represented as:

$$\begin{aligned} I(\mathbf{s}; \mathbf{r}) &= h(\mathbf{r}) - h(\mathbf{r}|\mathbf{s}) \\ &= h(\mathbf{r}) - h(\mathbf{Hs} + \mathbf{n}|\mathbf{s}) \\ &= h(\mathbf{r}) - h(\mathbf{n}) \end{aligned} \tag{2.56}$$

where the differential entropy of the received signal $h(\mathbf{r})$ is maximized if $\mathbf{r}$ is Zero Mean Circular Symmetric Complex Gaussian (ZMCSCG), which also needs that the transmit signal $\mathbf{s}$ is ZMCSCG. Henceforth, the differential entropy of $\mathbf{r}$ and $\mathbf{n}$ can be defined as follows:

$$h(\mathbf{r}) = \log_2(\det(\pi e \Phi_{\mathbf{r},\mathbf{r}})) \tag{2.57}$$

$$h(\mathbf{n}) = \log_2(\det(\pi e \sigma_n^2 \mathbf{I}_{N_R})) \tag{2.58}$$

such that $e = 2.71828$ represents the Euler number and $\Phi_{\mathbf{r},\mathbf{r}}$ represents the covariance matrix of the received signal $\mathbf{r}$ which is calculated as follows:

$$\begin{aligned}
\Phi_{\mathbf{r},\mathbf{r}} &= \mathbb{E}[\mathbf{r}\mathbf{r}^H] \\
&= \mathbb{E}[(\sqrt{P_T}\mathbf{H}\mathbf{s}+\mathbf{n})(\sqrt{P_T}\mathbf{H}\mathbf{s}+\mathbf{n})^H] \\
&= \mathbb{E}[(\sqrt{P_T}\mathbf{H}\mathbf{s}\mathbf{s}^H\mathbf{H}^H)] + \mathbb{E}[\mathbf{n}\mathbf{n}^H] \\
&= P_T\mathbf{H}\mathbb{E}[\mathbf{s}\mathbf{s}^H]\mathbf{H}^H + \sigma_n^2\mathbf{I}_{N_R} \\
&= P_T\mathbf{H}\Phi_{\mathbf{s},\mathbf{s}}\mathbf{H}^H + \sigma_n^2\mathbf{I}_{N_R}
\end{aligned} \tag{2.59}$$

such that $\Phi_{\mathbf{s},\mathbf{s}}$ is the covariance matrix of transmitted signal $\mathbf{s}$. Thus, from Equations (2.56) - (2.59), the mutual information can be expressed as follows:

$$\begin{aligned}
I(\mathbf{s};\mathbf{r}) &= \log_2(\det(\pi e \Phi_{\mathbf{r},\mathbf{r}})) - \log_2(\det(\pi e \sigma_n^2\mathbf{I}_{N_R})) \\
&= \log_2\left(\det\left(\mathbf{I}_{N_R} + \frac{1}{\sigma_n^2}\mathbf{H}\Phi_{\mathbf{s},\mathbf{s}}\mathbf{H}^H\right)\right)
\end{aligned} \tag{2.60}$$

Correspondingly, for a deterministic MIMO channel, the SE (normalized capacity) can be defined as follows:

$$\epsilon = \max_{Tr(\Phi_{\mathbf{s},\mathbf{s}})<P_T} \log_2\left(\det\left(\mathbf{I}_{N_R} + \frac{1}{\sigma_n^2}\mathbf{H}\Phi_{\mathbf{s},\mathbf{s}}\mathbf{H}^H\right)\right) \qquad \text{bits/channel use} \tag{2.61}$$

It is worth noting that the aforementioned analysis for the capacity relies on full Channel State Information knowledge. Consequently, if full CSI is available at the transmitter, optimal transmission can be achieved through allocating more power to the subchannels with more gains using the waterfilling algorithm [101]. On the other hand, if the CSI knowledge is not available at the transmitter side, the optimal transmission is achieved by allocating equal power over all the transmit antennas. In this case the SE of the MIMO channel is expressed as follows:

$$\epsilon = \log_2\left(\det\left(\mathbf{I}_{N_R} + \frac{\rho}{N_T}\mathbf{H}\mathbf{H}^H\right)\right) \tag{2.62}$$

2.4.2 Ergodic SE

MIMO channels often vary randomly due to the channel fading effects. In this case, the channel $\mathbf{H}$ has a time-variant behaviour and and can be modelled as a random matrix. Consequently, the SE of the MIMO channel can be obtained by averaging over all the channel realizations as follows:

$$\epsilon = \max_{Tr(\Phi_{\mathbf{s},\mathbf{s}})<P_T} \mathbb{E}_{\mathbf{H}}\left[\log_2\left(\det\left(\mathbf{I}_{N_R} + \frac{1}{\sigma_n^2}\mathbf{H}\Phi_{\mathbf{s},\mathbf{s}}\mathbf{H}^H\right)\right)\right] \qquad \text{bits/channel use} \tag{2.63}$$

In case an iid Rayleigh fading channel model is assumed, the optimal transmission can be achieved through allocating power equally over all the transmit antennas. Then, the transmit

signal covariance matrix can be expressed as $\Phi_{\mathbf{s,s}} = \frac{\rho}{N_T}\mathbf{I}$, where $\rho = \frac{pw}{\sigma_n^2}$ is the transmit SNR. The resulting SE is then expressed as follows:

$$
\begin{aligned}
\epsilon &= \mathbb{E}_{\mathbf{H}}\left[\log_2\left(\det\left(\mathbf{I}_{N_R} + \frac{\rho}{N_T}\mathbf{H}\mathbf{H}^H\right)\right)\right] \\
&= \mathbb{E}\left[\log_2\left(\prod_{i=1}^{N}\left(1 + \frac{\rho}{N_T}\lambda_i\right)\right)\right] \\
&= \sum_{i=1}^{N}\mathbb{E}\left[\log_2\left(1 + \frac{\rho}{N_T}\lambda_i\right)\right] \qquad \text{bits/channel use}
\end{aligned}
\tag{2.64}
$$

such that $N = \min(N_T, N_R)$ is the rank of the channel, which represents the total number of the channel eigenmodes. $\lambda_1, \lambda_2, , ..., \lambda_N$ represent the eigenvalues of channel. Moreover, considering iid Gaussian input signaling, the achievable sum SE of the system can be expressed as follows:

$$
\epsilon = \sum_{i=1}^{N}\mathbb{E}[\log_2(1+\chi_i)] \qquad \text{bits/transmission}
\tag{2.65}
$$

where χ_i represents the received SINR per spatial sub-channel (channel eigenmode). For a given wireless communication system, the received SINR χ_i depends on multiple factors such as: channel statistics, signal processing techniques used, number of antennas, correlation between the antennas, etc. Therefore, χ_i and accordingly the sum SE will be considered the main metric to evaluate the system performance throughout the thesis.

Chapter 3

Analytical Analysis for **HBF** in **MU** Massive **MIMO mmWave** Channels

Contents

In this chapter we will provide analytical analysis for Hybrid Beamforming (HBF) in mmWave massive MIMO channels. We start by considering a pure LoS channel, and define the condition for which both HBF and full digital beamforming achieve similar SE. Then, we analytically provide a closed form expression for the SE of the analog LoS beamsteering and the corresponding HBF extension in pure LoS channel. Finally, we analyze the SE performance of multiple analog beamformers in sparse multipath channel and their corresponding HBF extension, and we provide a novel low complexity analog beamforming and HBF that can achieve sub-optimal Spectral Efficiency (SE) performance.

3.1 Comparison Between Full Digital Beamforming And HBF

As aforementioned, practically implementing MU massive MIMO mmWave systems with full digital beamforming is challenging. Therefore, analog beamforming can be seen as an appropriate solution for such systems, since it does not impose the same hardware and power consumption constraints as the full digital case. Hybrid Beamforming (HBF) is even more efficient, since it can capture the trade-off between the high SE performance of full digital beamforming and the low power consumption and hardware complexity of analog beamforming. In this section we prove mathematically that both HBF and full digital beamforming can achieve exactly the same SE in case pure LoS channel is assumed, and ZF is used in the digital layer of the HBF. Moreover, we show that this equivalence is fulfilled with the minimum possible hardware requirements for HBF (number of transmit RF chains equals the number of served spatial streams). Finally we validate our propositions by simulation results.

3.1.1 Background

HBF emerged as one of the best candidates for the MU massive MIMO mmWave systems, since it strikes a balance between the high SE gains and the low power consumption and hardware complexity. Therefore, recently, a lot of work in the literature started to inspect the possibility to achieve exactly the same SE of full digital beamforming with HBF in sparse mmWave channels [8, 102, 103]. This is motivated by the fact that HBF has less hardware and power consumption

requirements compared to the full digital ones. Accordingly, in case both can achieve similar SE in some specific conditions, than HBF is clearly a better solution with respect to all the system Key Performance Indicatorss (KPIs).

In [5, 56] it was shown that the SE difference between the digital beamforming and HBF is minimal in massive MIMO mmWave channels with only small number of RF chains. This is because at such sparse channels, a small number of RF chains is enough to fully control the channel dominant paths.

In [8, 102, 103], the authors showed that both HBF and digital beamforming can have the same SE performance in case one of these conditions exist:

- For narrow band channels with analog layer composed of a network of fully connected phase shifters: The number of RF chains is larger than or equal double the number of the served spatial streams $N_{TRF} \geq 2N_S$ [8, 102].

- For wide band channels with analog layer composed of phase shifters: R RF chains and $2R(N_T - R + 1)$ phase shifters should be used, such that $R \leq N_T$ is the rank of the combined digital precoder matrices of all sub-carriers (with OFDM) [103].

- For narrow band channels with analog layer composed of phase shifters together with variable gain amplifiers: The number of served spatial streams N_S is smaller than or equal the number of RF chains N_{TRF}, ($N_S \leq N_{TRF}$) [8, 102].

- For wide band channels with analog layer composed of phase shifters together with variable gain amplifiers: The number of RF chains is larger than or equal $\min(N_T, N_{S,sub})$, such that $N_{S,sub}$ denotes the total number of streams over all the sub-carriers (with OFDM) [8, 102].

In this section, we consider only the narrow band channels with analog layer composed of a network of fully connected phase shifters case. We analytically show that we can further achieve the equivalence in SE between HBF and digital beamforming with only $N_{TRF} = N_S$ under two conditions: the channel is pure LoS and the digital layer of HBF is ZF and similarly the digital beamforming is ZF based.

3.1.2 System and Channel Model

The proposed system is a downlink MU MISO system for both digital beamforming and HBF. The received signal for the digital beamforming case was given in Equation (2.1) and represented here for readability as follows:

$$\mathbf{r} = \sqrt{P_T}\mathbf{H}\mathbf{x} + \mathbf{n} \tag{3.1}$$

while for the HBF case, the received signal was given in Equation (2.45) and represented here for readability as follows:

$$\mathbf{r} = \sqrt{P_T}\mathbf{H}\mathbf{F}^{RF}\mathbf{F}^{BB}\mathbf{s} + \mathbf{n} \tag{3.2}$$

The channel model considered in this section, is the sparse physical ray based model introduced in Subsection 2.2.4. Given that we consider MU MISO pure LoS channel with ULA at the BS and a single receive antenna at each UE k, the channel vector for each UE k was given in Equation (2.28) and represented here for readability as follows:

$$\mathbf{h}_k = \sqrt{N_T}\alpha_k\mathbf{a}_t(\phi^t_k)^H \tag{3.3}$$

Then, the MU channel $\mathbf{H}$ can be calculated as $\mathbf{H} = [\mathbf{h}_1^T, \mathbf{h}_2^T, ..., \mathbf{h}_K^T]^T$.

3.1.3 Beamforming Techniques

In this section, we consider both digital and HBF techniques. For the digital beamformer, we utilize the ZF precoder given in Equation (2.4). While for HBF we utilize the two stage HBF algorithm described in Algorithm 1 in Subsection 2.3.4, with using ZF for the BB precoder $\mathbf{F}^{BB}$ and LoS beamsteering for the RF precoder $\mathbf{F}^{RF}$.

3.1.4 SE Analytical Analysis

The per stream SE is expressed according to Equation (2.65) as follows:

$$\epsilon_k = \log_2(1 + \chi_k) \tag{3.4}$$

where χ_k is the received SINR for UE k. In case fully digital ZF beamforming is applied, the SINR for UE k is expressed as follows [104, 28]:

$$\chi_k^{ZF} = \frac{\rho}{\|\mathbf{f}_k^{ZF}\|^2} \tag{3.5}$$

where $\rho = \frac{P_T}{\sigma_n^2}$ is the transmit SNR. According to ([28]), $\|\mathbf{f}_k^{ZF}\|^2$ can be represented as:

$$\|\mathbf{f}_k^{ZF}\|^2 = ((\mathbf{H}\mathbf{H}^H)^{-1})_{k,k} \tag{3.6}$$

substituting Equation (3.6) in (3.5), then χ_k^{ZF} is expressed as:

$$\chi_k^{ZF} = \frac{\rho}{((\mathbf{H}\mathbf{H}^H)^{-1})_{k,k}} \tag{3.7}$$

Similarly, in case HBF with ZF digital layer is applied, the SINR for UE k is expressed as follows:

$$\chi_k^{HBF} = \frac{\rho}{\|\mathbf{f}^{HBF}_k\|^2} \tag{3.8}$$

where $\|\mathbf{f}^{HBF}_k\|^2$ can be expressed as:

$$\|\mathbf{f}^{HBF}_k\|^2 = \|\mathbf{F}^{RF}\mathbf{f}^{BB}_k\|^2 = (\mathbf{F}^{RF}\mathbf{f}^{BB}_k)^H(\mathbf{F}^{RF}\mathbf{f}^{BB}_k) \tag{3.9}$$

Given that the channel is a pure LoS channel, the MU channel with K UEs can be reformulated as follows:

$$\mathbf{H} = \sqrt{N_T}\mathbf{H}_b\mathbf{A}_t^H \tag{3.10}$$

where $\mathbf{H}_b = \text{Diag}(\alpha)$ is the beamspace channel (a diagonal matrix with the diagonal entries corresponding to α_k). $\mathbf{A}_t$ is the transmit steering matrix, with columns representing the transmit steering vectors $\mathbf{a}_t(\phi^t_k)$. Moreover, since we consider LoS beamsteering as the analog beamformer, it can be expressed as $\mathbf{F}^{RF} = \mathbf{A}_t$. Therefore, in this case the hybrid beamformer $\mathbf{F}^{HBF} = \mathbf{F}^{RF}\mathbf{F}^{BB}$ can be represented as follows:

$$\begin{aligned}
\mathbf{F}^{RF}\mathbf{F}^{BB} &= \mathbf{F}^{RF}(\mathbf{F}^{RF})^H\mathbf{H}^H(\mathbf{H}\mathbf{F}^{RF}(\mathbf{F}^{RF})^H\mathbf{H}^H)^{-1} \\
&= \frac{1}{\sqrt{N_T}}\mathbf{A}_t\mathbf{A}_t^H\mathbf{A}_t\mathbf{H}_b^H(\mathbf{H}_b\mathbf{A}_t^H\mathbf{A}_t\mathbf{A}_t^H\mathbf{A}_t\mathbf{H}_b^H)^{-1} \\
&= (\sqrt{N_T}\mathbf{H}_b\mathbf{A}_t^H)^{-1} = (\mathbf{H})^{-1}
\end{aligned} \tag{3.11}$$

Similarly $(\mathbf{F}^{RF}\mathbf{F}^{BB})^H$ can be represented as:

$$(\mathbf{F}^{RF}\mathbf{F}^{BB})^H = ((\mathbf{H})^{-1})^H = (\mathbf{H}^H)^{-1} \tag{3.12}$$

Substituting Equations (3.11) and (3.12) in Equation (3.9), then $\|\mathbf{F}^{HBF}_k\|^2$ can be denoted as:

$$\|\mathbf{F}^{HBF}_k\|^2 = ((\mathbf{H}^H)^{-1}(\mathbf{H})^{-1})_{k,k} = ((\mathbf{H}\mathbf{H}^H)^{-1})_{k,k} \tag{3.13}$$

Finally, substituting Equation (3.13) in (3.8), then χ_k^{HBF} is expressed as:

$$\chi_k^{HBF} = \frac{\rho}{((\mathbf{H}\mathbf{H}^H)^{-1})_{k,k}} \tag{3.14}$$

Therefore, from Equations (3.7) and (3.14) we prove that both fully digital ZF and HBF based on ZF achieve the same SE in pure LoS channels with applying LoS beamsteering analog beamforming in the HBF case. This is valid as long the the number of RF chains is at least equal to the number of data streams N_S. Hence achieving the same SE of ZF digital beamforming with massive complexity and power consumption reduction. In this section, the total number of data streams N_S is equal to the number of UEs K, since each UE has a single receive antenna and thus served by a single stream.

3.1.5 Hardware Architectures

In this subsection, we discuss the hardware complexity of the two architectures adopted in this section which are the fully digital beamforming and the HBF, illustrated in Figure 3.1.

As we already proved in the previous subsection, that both architectures can achieve the same SE in case ZF is used as the full digital beamformer and in case the HBF is applied in pure LoS channel with ZF digital layer, and LoS beamsteering in the analog layer. Therefore, here we aim at evaluating the hardware efficiency of both architectures. Hardware efficiency is defined as the achieved SE relative to the hardware complexity. Therefore, given that both architectures

1) The fully digital beamforming transmitter architecture.

2) The fully connected HBF transmitter architecture.
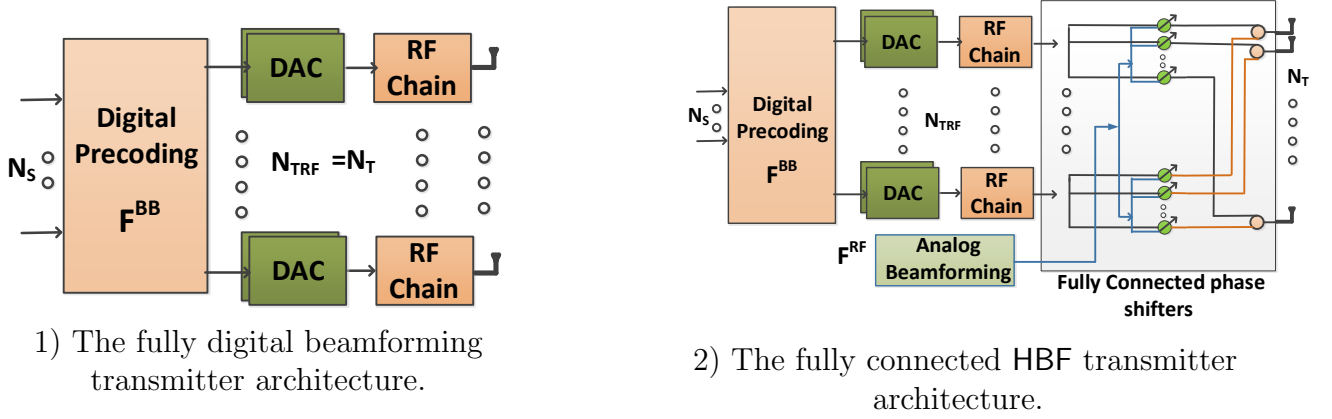
Figure 3.1: Illustration of the Full Digital Beamforming and HBF Architectures

Table 3.1: Hardware Complexity Comparison

Component	Digital Beamforming	HBF
Power Amplifier	1	1
Phase Shifter	0	$N_{TRF}N_T$
Local Oscillator	1	1
RF Chain	N_T	N_{TRF}
DAC	$2N_T$	$2N_{TRF}$

achieve the same SE, the hardware efficiency is inversely proportional to the number of complex hardware components used.

According to Figure 3.1 the number of hardware elements for each architecture can be deduced and it is summarized in Table 3.1.

Indeed in massive MIMO systems, the number of transmit antennas N_T is much more than the number of UEs ($N_T >> K$). Also, in our proposed HBF system, we use $N_{TRF} = N_S$, where $N_S = K$ in our scenario, since each UE is served by a single spatial stream. Accordingly, in order to summarize, in the fully connected HBF architecture we need $N_{TRF} = N_S = K << N_T$. On the other hand, in the fully digital one we need $N_{TRF} = N_T >> K$. Therefore, it is clear that in our proposed scenario, HBF is much more hardware efficient compared to the full digital one since it requires less number of RF chains and DACs.

3.1.6 Power Consumption Models

In this subsection, we will present the power consumption models that we consider for the two architectures proposed. The power consumption for each RF chain P_{RF} is modelled as follows:

$$P_{RF} = 2P_{LP} + 2P_M + P_H \tag{3.15}$$

Table 3.2: Power Consumption of the Analog Components [3]

Component	Value
Power Amplifier (P_{PA})	$\frac{P_T}{\eta}, \eta = 27\%$
Phase Shifter (P_{PS})	for $b_{PS} = 4, 21.6$ mW
Local Oscillator (P_{LO})	22.5 mW
90° hybrid with buffers (P_H)	3 mW
Mixer (P_M)	0.3 mW
Low Pass Filter (P_{LP})	14 mW
RF Chain (P_{RF})	31.6 mW
DAC (P_{DAC})	Equation (3.17)

such that P_{LP}, P_M and P_H denote the power consumed by the low pass filter, the mixer, and the 90° hybrid respectively. Therefore, the power consumption of the full digital ZF architecture can be defined as follows:

$$P_D = P_T + P_{LO} + P_{PA} + N_T(2P_{DAC} + P_{RF}) \tag{3.16}$$

such that P_T represents the transmit power, P_{LO} denotes the power consumed by the local oscillator, P_{PA} represents the power consumed by all the power amplifiers which can be expressed as $P_{PA} = \frac{P_T}{\eta}$ such that η represents the power amplifiers efficiency. The power consumed by the DAC P_{DAC} is defined as follows:

$$P_{DAC} = 1.5(10^{-5})(2^{b_{DAC}}) + 9(10^{-12})(b_{DAC})(F_s) \tag{3.17}$$

such that b_{DAC} represents resolution of the DAC in bits. F_s represents the sampling rate in Hertz. The power consumption of the HBF architecture with fully connected phase shifters can be defines as follows:

$$P_{HBF} = P_T + P_{LO} + P_{PA} + N_{TRF}(2P_{DAC} + P_{RF} + N_T P_{PS}) \tag{3.18}$$

such that the power consumption of the phase shifter is denoted as P_{PS} which depends on the number of resolution bits b_{PS}. In order to give a quantitative analysis for the power consumption of the proposed architectures, we use practical values for all the aforementioned components at 28 GHz, given in [3] and summarized in Table 3.2.

3.1.7 Numerical Analysis

In this subsection, we aim at validating the aforementioned SE analytical analysis for fully digital ZF and the HBF based on ZF digital layer and LoS beamsteering analog layer in a pure LoS channel. Also, we aim at comparing between both architectures in terms of Energy Efficiency (EE), together with the HBF architecture proposed in the literature [8, 102] with the constraint $N_{TRF} = 2N_S = 2K$.

The simulation parameters used within this subsection are as follows:
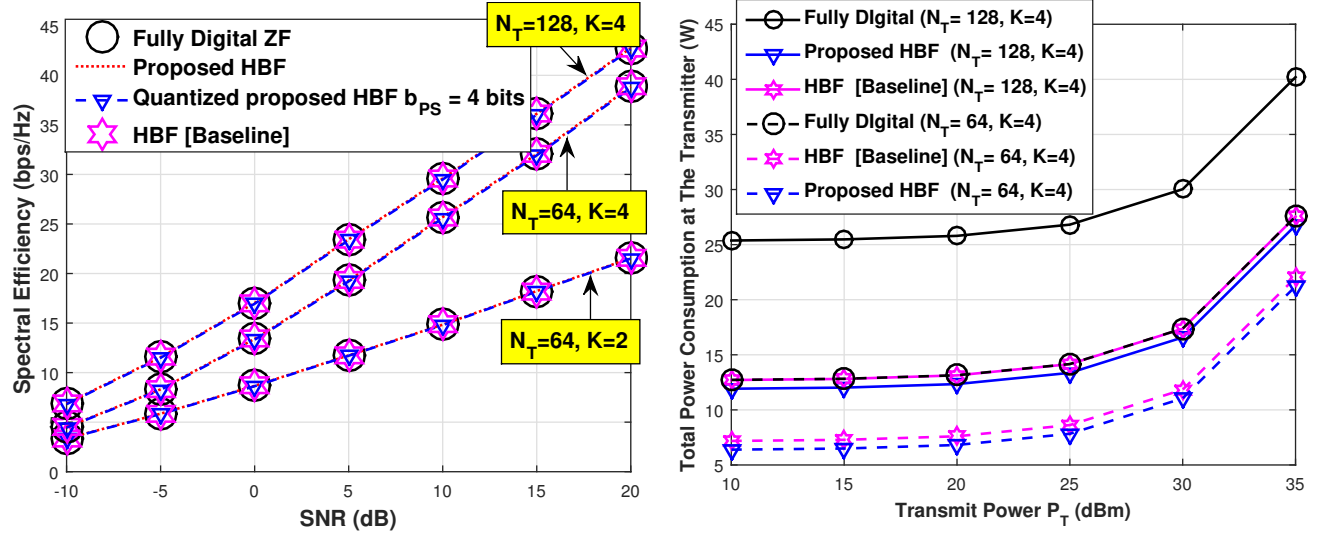
1) SE comparison for the proposed beamforming architectures for different N_T and K.

2) Transmitter power consumption comparison for the proposed beamforming architectures for different N_T and K.

Figure 3.2: SE and power consumption comparisons for the proposed beamforming architectures for different N_T and K.

- The transmit antenna array is ULA with half wavelength spacing.

- Each UE is equipped with a single receive antenna and served by a single stream.

- In full digital ZF scenario: the number of transmit RF chains N_{TRF} equals the number of transmit antennas ($N_{TRF}{}^{ZF} = N_T$).

- In our proposed HBF scenario: the number of transmit RF chains N_{TRF} equals the number of UEs ($N_{TRF}{}^{HBF,1} = K$).

- In the HBF scenario in the literature [8, 102]: the number of transmit RF chains N_{TRF} equals double the number of UEs ($N_{TRF}{}^{HBF,2} = 2K$).

- The simulations are done in a Monte Carlo fashion with 1000 realizations.

- Perfect CSI is assumed at the transmitter.

In Figure 3.2-1, we can observe that all the beamforming architectures achieve similar SE performance for different simulation setups. Thus, showing that the SE of our proposed HBF with the condition $N_{TRF} = K$, achieves the same SE as the fully digital architecture ($N_{TRF} = N_T$) and as the HBF in [8, 102] with the condition $N_{TRF} = 2K$. Therefore, validating our analytical SE analysis in Subsection 3.1.4. This result stresses the privilege of our proposed HBF for ZF precoding in LoS channels.

In order to have more realistic assumptions and consider the hardware impairments in our analysis, we consider limited resolution quantized phase shifters ($b_{PS} = 4$ bits). Again, in Figure 3.2-1, we can observe that even with $b_{PS} = 4$ bits, the SE degradation is negligible when the number of transmit antennas N_T is large.

In Figure 3.2-2, the power consumption for the introduced beamforming scenarios is compared for different simulation setups. Given that all the proposed scenarios achieve similar SE, the power consumption metric is enough to compare the EE of the proposed scenarios. It is clear in Figure 3.2-2, that our proposed HBF achieves the lowest power consumption and hence it has the best EE compared to the fully digital beamforming and the HBF architecture proposed in [8, 102].

3.1.8 Sparse Channel Sounding at 60 GHz

After showing the equivalence between the proposed HBF and the full digital ZF using the simulation results in the previous subsection based on pure LoS channels. In this subsection we evaluate how far this approximation is, compared to realistic mmWave channels. In order to do this, we use channel sounding measurements done at 60 GHz through a cooperation with PhD student Marwan El Hajj who is working in the IETR lab at INSA de Rennes, in the channel measurements and propagation team. Throughout the collaborative work with Marwan, data acquisition of the channel sounding measurements at 60 GHz was done. The channel sounder description was already introduced in [105]. For the sake of clarity, we will explain briefly the channel sounder and then calculate the SE of both the proposed HBF and the full digital ZF in order to evaluate the SE difference with a realistic sounded mmWave channel.

The measurement system includes a Vector Network Analyser operating at center frequency of 3.5 GHz with 2 GHz BW over 401 sub-carriers sequentially with 5 MHz frequency spacing. The transposition to 60 GHz is provided by the RF modules (up and down converters) using standard components such as multipliers and mixers. The antenna at the transmitter side is a horn one with 100° at 6 dB beam width in both E and H planes with 7.3 dBi gain. The antenna used is vertically polarized and operating between 58 and 62 GHz.

At the receiver side, a 22.5 dBi gain horn antenna was used with 10° and 13° Half Power Beam Widths (HPBWs) in E and H planes respectively, and with 22.5 dBi gain. Before starting measurements, a calibration was made to remove the losses of the cables, and a back to back test, to remove the influence of the up/down converters from the frequency response channel. The transmitted power at 60 GHz was 0 dBm.

All the measurements considered in this subsection have been carried out in a typical meeting room (6.58×3.18×2.48 m) in the Institute of Electronics and Telecommunications of Rennes (IETR) laboratory (Figure 3.3). The channel sounder configuration was as follows: the transmitter's horn antenna was raised to 1.9 m height in one corner of the room (Figure 3.3). The receiver's antenna is a horn one with 13° narrow beam width, set at 1 m height. Rotations by 6° azimuth steps on the receiver side using a positioner were done, and the channel frequency response for each 6° step was collected.

At the receiver side, 3 positions were chosen around the table (Figure 3.4). The transmitter's central axis was pointed towards the main diagonal of the room without tilt, as shown in Figure
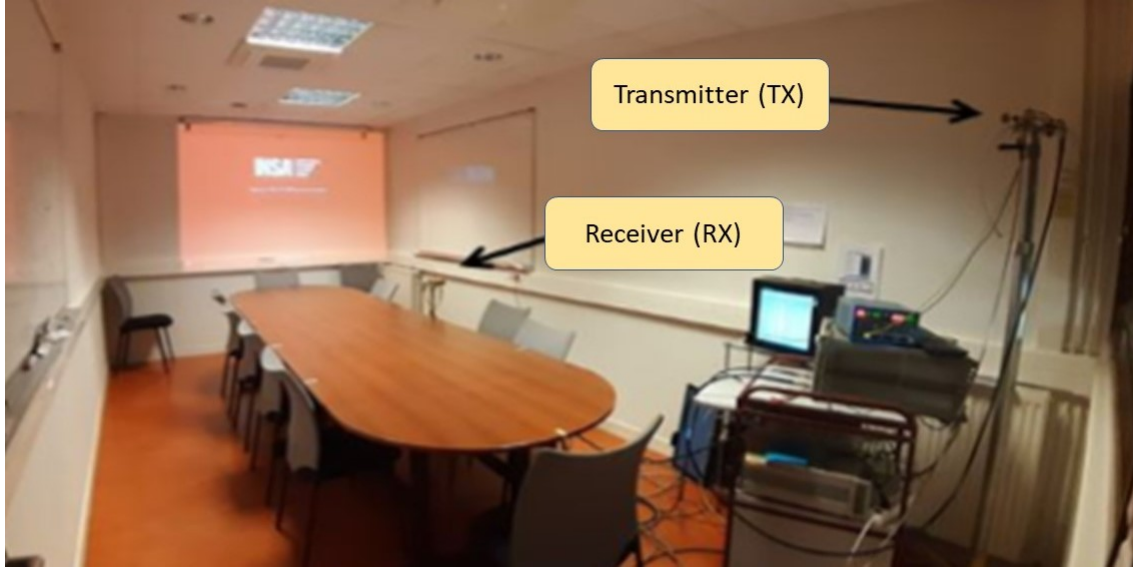
Figure 3.3: Measurement campaign in a meeting room.
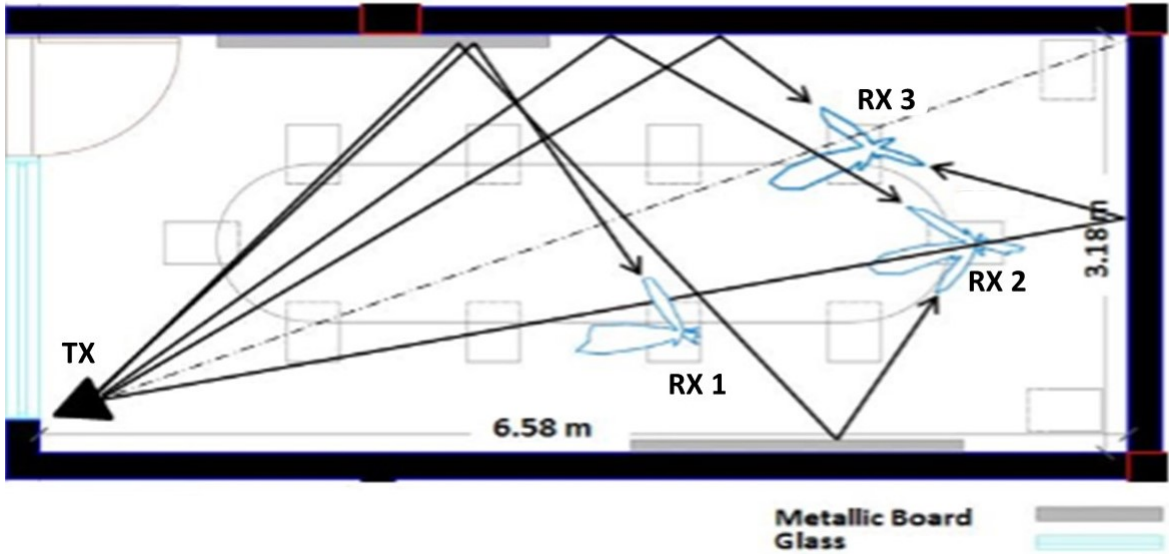
Figure 3.4: Meeting room plane with applying ray tracing.

3.4. All the measurements have been made in an empty environment (no people), with typical furniture (table, chairs,two metallic boards) and closed wooden door.

As aforementioned, at the receiver side a directive antenna is employed, which is mounted over a positioner that rotates with 6° steps in order to resolve the angles of the received paths and determine their complex amplitudes (α) and their azimuth AoAs (ϕ^r). Then, using ray tracing as shown in Figure 3.4, the azimuth AoDs can be calculated for different paths (ϕ^t).
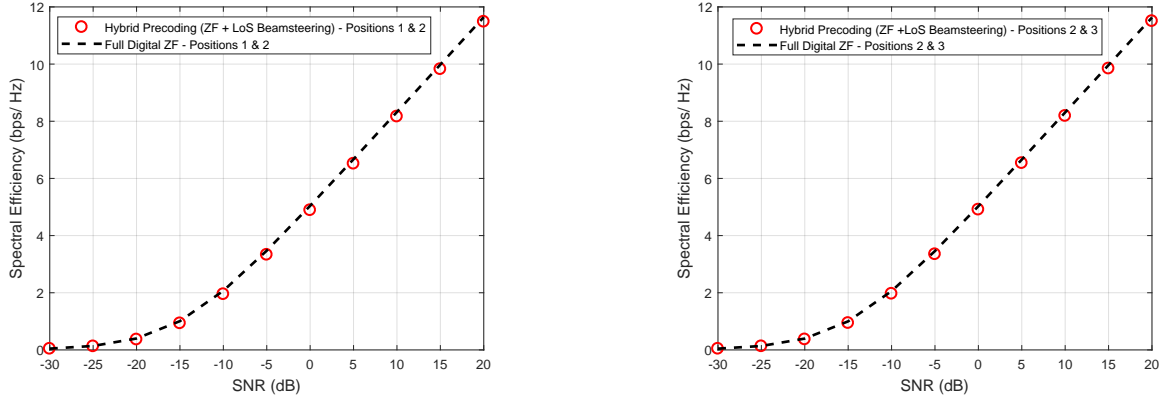
1) RX Positions 1 and 2 as shown in Figure 3.4.

2) RX Positions 2 and 3 as shown in Figure 3.4.

Figure 3.5: Per stream SE comparison for the proposed beamforming architectures for $N_T = 64$ and $K = 2$ with different UEs' positions.

Table 3.3: Parameters of the measurement campaign in the meeting room.

Node	Antenna Type	Height
TX	Horn (100° (E-plane) - 100° (H-plane))	1.9 m
RX	Horn (10.1° (E-plane) - 13.1° (H-plane))	1 m

Measurements are done for all the BW, however in this section we will only consider narrowband channel measurements (only the measurements at the center frequency (60 GHz)). Then we normalize the path-loss and transmitted power effects from the complex amplitudes of the sounded channel as follows:

$$\hat{\alpha} = \sum_{j=1}^{N_p} \alpha_j^2 \tag{3.19}$$

$$\alpha_j^2 = \frac{\alpha_j^2}{\hat{\alpha}} \tag{3.20}$$

Then we can virtually construct a MISO $\mathbf{h}_k$ channel from the Single Input Single Output (SISO) sounded channel (with parameters α and ϕ^t measured and calculated for each path) for any number of transmit antennas N_T as follows:

$$\mathbf{h}_k = \sqrt{N_T} \sum_{j=1}^{N_p} \alpha_j \mathbf{a}_t(\phi^t_{k,j})^H, \tag{3.21}$$

53

In order to calculate the SE, we define a scenario where $N_T = 64$ and $K = 2$ with single receive antenna for each UE. Two deployments for the UEs positions were considered, the first one considering positions RX 1 and RX 2 shown in Figure 3.4. While the second deployment considers positions RX 2 and RX 3 also shown in Figure 3.4.

In Figure 3.5, we can observe that for both deployments the per stream SE of both the proposed HBF and the full digital ZF are approximately the same. This validates the practical relevance of the previous analysis and simulation results in the previous subsections. Therefore, it is clear that in some realistic mmWave transmission scenarios which are LoS dominated, the proposed HBF can accurately approximate the full digital ZF with lower hardware complexity and lower power consumption.

3.1.9 Conclusion

In this section, we relaxed the constraint for equity between the HBF with fully connected phase shifters and the full digital beamforming for narrow band channels in the literature. We proved mathematically and verified by simulation results that with RF chains equal to the number of the served spatial streams, this equity can hold under specific conditions. Henceforth, our proposed HBF architecture is considered hardware, power and spectral efficient compared to the full digital ZF beamforming in pure LoS mmWave channels.Moreover, we validated using realistic sounded mmWave channel, that this equivalence can approximately hold in practical LoS dominated scenarios. The work in this section has been published in [6].

3.2 HBF in Pure LoS MU Massive MIMO mmWave Channel

As previously mentioned analog LoS beamsteering can be considered a low complex solution for massive MIMO mmWave systems. Given the fact that massive MIMO systems allow for low spatial correlation between the UEs when a high number of transmit antennas is available at the BS. This fact enables analog LoS beamsteering with multiple RF chains at the transmitter to serve MU scenarios, since in such case the IUI is minimal.

In this section, we provide a closed form analytical model for the SE of the MU analog LoS beamsteering in pure LoS channels. Also, we theoretically analyze the saturation level of the SE of MU analog LoS beamsteering at high SNR. Moreover, we show that HBF relying on ZF in the digital layer and LoS beamsteering in the analog layer is a better option for MU massive MIMO mmWave systems at high SNR regime, since the SE in this case scales with the SNR and does not saturate as in the case of MU analog LoS beamsteering. Finally, we provide a closed form analytical model for the SE of the proposed HBF for MU scenarios in pure LoS channels.

3.2.1 Background

It is well known that at mmWave frequencies, massive MIMO systems can be deployed with reasonable form factors. Henceforth, the recent studies concerning the favourable propagation

1) The MU analog beamforming architecture.

2) The HBF architecture.
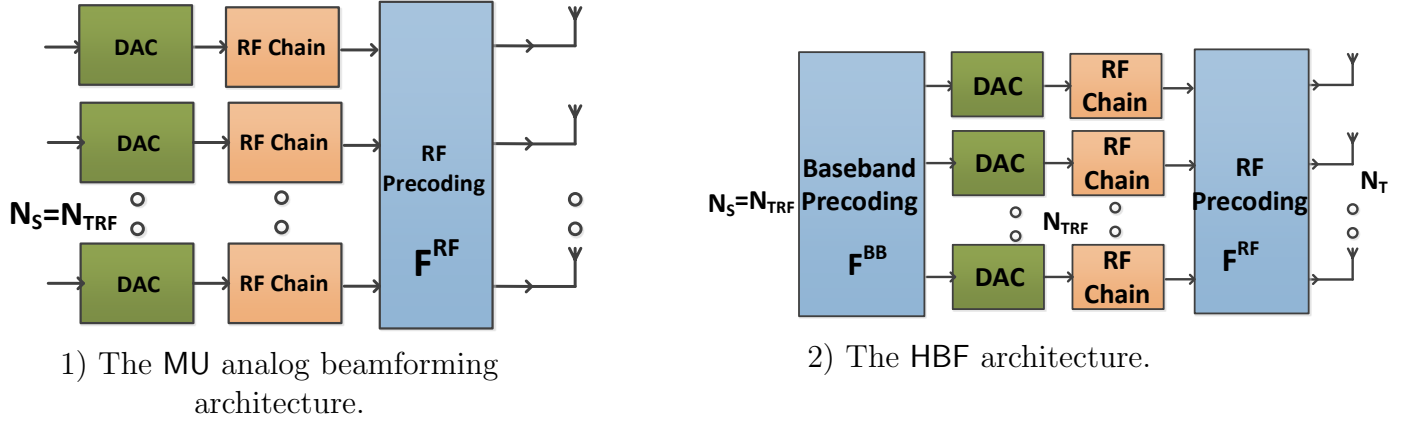
Figure 3.6: Illustration of the MU Analog Beamforming and HBF Architectures.

scenario and the channel hardening [106, 107, 108, 1] became more realistic assumptions to approximate the system performance when the number of antennas is large enough.

These asymptotic approximations motivate considering the analog LoS beamsteering as a promising candidate for MU scenarios given the low residual IUI level obtained at large-scale antenna regime. Therefore, is this section we will provide a closed form approximation for the SE achieved by MU analog LoS beamsteering in pure LoS channels.

Also, it was shown in the current literature that the SE of the MU LoS beamsteering system saturates at high SNR regime. However, up till now, no closed form approximation for this SE saturation bound has been offered yet. Henceforth, in this section we provide an analytical analysis for this saturation bound at high SNR regime for MU analog LoS beamsteering in pure LoS channels. Moreover, we provide an analytical approximation for the SE achieved by MU HBF with ZF digital layer and LoS beamsteering analog layer in pure LoS channels. Finally, all the introduced models are validated by simulation results.

3.2.2 System and Channel Model

The proposed system is a downlink MU MISO system for both analog beamforming and HBF. The MU analog beamforming system shown in Figure 3.6-1 can be seen as an extension of the SU analog beamforming in Subsection 2.3.2, with having multiple RF chains but without Base Band signal processing included. The received signal for the MU analog beamforming case can be expressed as follows:

$$\mathbf{r} = \sqrt{P_T}\mathbf{H}\mathbf{F}^{RF}\mathbf{s} + \mathbf{n} \tag{3.22}$$

where $\mathbf{F}^{RF}$ of dimensions $N_T \times N_{TRF}$ is the analog beamforming matrix with each column $\mathbf{f}^{RF}{}_k$ of dimension $1 \times N_T$ representing the RF beamforming vector for each UE k.

While for the HBF case, the received signal was given in Equation (2.45) and represented here for readability as follows:

$$\mathbf{r} = \sqrt{P_T}\mathbf{H}\mathbf{F}^{RF}\mathbf{F}^{BB}\mathbf{s} + \mathbf{n} \tag{3.23}$$

The channel model considered in this section, is the sparse physical ray based model introduced in Subsection 2.2.4. Given that we consider MU MISO pure LoS channel with ULA at the BS and a single receive antenna at each UE k, the channel vector for each UE k was given in Equation (2.28) and represented here for readability as follows:

$$\mathbf{h}_k = \sqrt{N_T}\alpha_k \mathbf{a}_t(\phi^t{}_k)^H \tag{3.24}$$

Then, the MU channel $\mathbf{H}$ can be calculated as $\mathbf{H} = [\mathbf{h}_1^T, \mathbf{h}_2^T, ..., \mathbf{h}_K^T]^T$.

3.2.3 Beamforming Techniques

In this section, we consider both analog beamforming and HBF techniques. For the MU analog beamformer, we utilize the LoS beamsteering precoder for each UE k given in Equation (2.38). While for HBF we utilize the two stage HBF algorithm described in Algorithm 1 in Subsection 2.3.4, with using ZF for the BB precoder $\mathbf{F}^{BB}$ and LoS beamsteering for the RF precoder $\mathbf{F}^{RF}$.

3.2.4 SE Analytical Analysis for MU Analog LoS Beamsteering

Let us consider the MU analog LoS beamsteering case, where multiple UEs are served simultaneously in the same time-frequency resource using LoS beamsteering. In this situation, the IUI is not tackled by any digital signal processing operation. The expectation of the per stream SE $\hat{\epsilon} = \mathbb{E}[\epsilon_k]$ can hence be expressed according to Equation (2.65) as follows:

$$\hat{\epsilon} = \mathbb{E}\left\{\log_2\left(1 + \frac{\rho|\mathbf{h}_k\mathbf{f}^{RF}{}_k|^2}{\rho\sum_{i=1,i\neq k}^{K}|\mathbf{h}_k\mathbf{f}^{RF}{}_i|^2 + 1}\right)\right\} \tag{3.25}$$

where ρ represents the per UE transmit SNR. Utilizing Equation (3.25), we will define two propositions that characterize the SE performance of the MU analog LoS beamsteering system.

Proposition 1. *For $K = 2$ UEs, served by MU analog LoS beamsteering in pure LoS channel, the expected per stream SE $\hat{\epsilon} = \mathbb{E}[\epsilon_k]$ can be approximated as:*

$$\hat{\epsilon} \approx \log_2\left(1 + \frac{N_T}{\frac{1+\rho}{\rho} + 2\sum_{i=1}^{N_T-1}\left(1 - \frac{i}{N_T}\right)\mathcal{J}_0^2(2\pi d_t i)}\right) \tag{3.26}$$

where $\mathcal{J}_0$ represents the zero order Bessel function.

Proof. Here we use the approximation that $\mathbb{E}\left[\log_2\left(1 + \frac{\mathbf{X}}{\mathbf{Y}}\right)\right] \approx \log_2\left(1 + \frac{\mathbb{E}[\mathbf{X}]}{\mathbb{E}[\mathbf{Y}]}\right)$ in [109], if $\mathbf{X} = \sum \mathbf{X}_i$ and $\mathbf{Y} = \sum \mathbf{Y}_i$ represent the summation of non negative random variables. $\mathbf{X}$ and $\mathbf{Y}$ independency is not required for this approximation to hold, and the approximation accuracy increases with the number of the summation terms included in $\mathbf{X}$ and $\mathbf{Y}$ [110, 109]. Therefore, Equation (3.25) can now be approximated (given that $K = 2$ UEs) as follows:

$$\hat{\epsilon} \approx \log_2\left(1 + \frac{\rho\mathbb{E}[|\mathbf{h}_k\mathbf{f}^{RF}{}_k|^2]}{\rho\mathbb{E}[|\mathbf{h}_k\mathbf{f}^{RF}{}_{\hat{k}}|^2] + 1}\right) \tag{3.27}$$

where $\mathbf{f}^{RF}_{\hat{k}}$ is the analog LoS beamsteering beamformer of the interfering UE $\hat{k}$. In order to evaluate Equation (3.27), we evaluate $\mathbb{E}[|\mathbf{h}_k\mathbf{f}^{RF}_k|^2]$ and $\mathbb{E}[|\mathbf{h}_k\mathbf{f}^{RF}_{\hat{k}}|^2]$ separately as follows:

$$
\begin{aligned}
\mathbb{E}[|\mathbf{h}_k\mathbf{f}^{RF}_k|^2] &= \mathbb{E}[|\sqrt{N_T}\,\alpha_k\mathbf{a}_t^H(\phi^t_k)\mathbf{a}_t(\phi^t_k)|^2] \\
&= N_T\mathbb{E}[|\alpha_k|^2] = N_T
\end{aligned}
\tag{3.28}
$$

where $|\alpha_k|^2$ has a chi-squared distribution. Then evaluating the interference part $\mathbb{E}[|\mathbf{h}_k\mathbf{f}^{RF}_{\hat{k}}|^2]$ as follows:

$$
\begin{aligned}
\mathbb{E}[|\mathbf{h}_k\mathbf{f}^{RF}_{\hat{k}}|^2] &= \mathbb{E}[|\sqrt{N_T}\,\alpha_k\mathbf{a}_t^H(\phi^t_k)\mathbf{a}_t(\phi^t_{\hat{k}})|^2] \\
&= N_T\mathbb{E}[|\alpha_k|^2]\mathbb{E}[|\mathbf{a}_t^H(\phi^t_k)\mathbf{a}_t(\phi^t_{\hat{k}})|^2]
\end{aligned}
\tag{3.29}
$$

where α and ϕ^t are statistically independent which explains the second line in Equation (3.29) and as aforementioned $\mathbb{E}[|\alpha_k|^2] = 1$. For readability, we define $\upsilon = |\mathbf{a}_t^H(\phi^t_k)\mathbf{a}_t(\phi^t_{\hat{k}})|^2$. According to [106], given that $\phi^t \sim \mathcal{U}[0, 2\pi]$, $\mathbb{E}[\upsilon]$ can be expressed as follows:

$$
\mathbb{E}[\upsilon] = \frac{1 + 2\sum_{i=1}^{N_T-1}\left(1 - \frac{i}{N_T}\right)\mathcal{J}_0^2(2\pi d_t i)}{N_T}
\tag{3.30}
$$

Therefore, $\mathbb{E}[|\mathbf{h}_k\mathbf{f}^{RF}_{\hat{k}}|^2]$ can be expressed as:

$$
\mathbb{E}[|\mathbf{h}_k\mathbf{f}^{RF}_{\hat{k}}|^2] = 1 + 2\sum_{i=1}^{N_T-1}\left(1 - \frac{i}{N_T}\right)\mathcal{J}_0^2(2\pi d_t i)
\tag{3.31}
$$

substituting Equations (3.28) and (3.31) in Equation (3.27), the expected per stream SE $\mathbb{E}[\epsilon_k]$ for $K = 2$ UEs using MU analog LoS beamsteering at high SNR regime can be approximated as follows:

$$
\hat{\epsilon} \approx \log_2\left(1 + \frac{N_T}{\frac{1+\rho}{\rho} + 2\sum_{i=1}^{N_T-1}\left(1 - \frac{i}{N_T}\right)\mathcal{J}_0^2(2\pi d_t i)}\right)
\tag{3.32}
$$

$\blacksquare$

Proposition 2. *For $K > 2$ UEs, served by MU analog LoS beamsteering in pure LoS channel, the expected achieved per stream SE $\hat{\epsilon} = \mathbb{E}[\epsilon_k]$ can be approximated by:*

$$
\hat{\epsilon} \approx \log_2\left(1 + \frac{\frac{N_T}{(K-1)^2}}{\frac{1+\rho}{\rho} + 2\sum_{i=1}^{N_T-1}\left(1 - \frac{i}{N_T}\right)\mathcal{J}_0^2(2\pi d_t i)}\right)
\tag{3.33}
$$

Proof. The difference between this case and the previous proposition is only in the interference term, since here we have $K - 1$ interference terms instead of only one. Therefore, similar to the analysis in the previous proposition, the average per stream SE $\hat{\epsilon} = \mathbb{E}[\epsilon_k]$ can be approximated as follows:

$$
\hat{\epsilon} \approx \log_2\left(1 + \frac{\rho\mathbb{E}[|\mathbf{h}_k\mathbf{f}^{RF}_k|^2]}{\rho\mathbb{E}[\sum_{i=1,i\neq k}^{K}|\mathbf{h}_k\mathbf{f}^{RF}_i|^2] + 1}\right)
\tag{3.34}
$$

where $\mathbb{E}[|\mathbf{h}_k\mathbf{f}^{RF}{}_k|^2] = N_T$ as shown in Equation (3.28).

While $\mathbb{E}[\sum_{i=1,i\neq k}^{K}|\mathbf{h}_k\mathbf{f}^{RF}{}_i|^2] = \mathbb{E}[\sum_{i=1,i\neq k}^{K}|\sqrt{N_T}\,\alpha_k\mathbf{a}_t{}^H(\phi^t{}_k)\mathbf{a}_t(\phi^t{}_i)|^2]$ can be expanded as follows:

$$\mathbb{E}\left[\sum_{i=1,i\neq k}^{K}|\mathbf{h}_k\mathbf{f}^{RF}{}_i|^2\right] = N_T\mathbb{E}[|\alpha_k|^2]\mathbb{E}\left[\sum_{i=1,i\neq k}^{K}\upsilon_{k,i}\right] \tag{3.35}$$

where $\upsilon_{k,i} = |\mathbf{a}_t{}^H(\phi^t{}_k)\mathbf{a}_t(\phi^t{}_i)|^2$. Given the fact that $\sum_{i=1}^{n}x_i^2 \leq (\sum_{i=1}^{n}x_i)^2$, therefore, here we use the upper bound approximation $\sum_{i=1,i\neq k}^{K}|\mathbf{a}_t{}^H(\phi^t{}_k)\mathbf{a}_t(\phi^t{}_i)|^2 \approx (\sum_{i=1,i\neq k}^{K}|\mathbf{a}_t{}^H(\phi^t{}_k)\mathbf{a}_t(\phi^t{}_i)|)^2$ for tractability issues, given that the approximation error is minimal for high number of transmit antennas N_T since the correlation terms $|\mathbf{a}_t{}^H(\phi^t{}_k)\mathbf{a}_t(\phi^t{}_i)|$ will have values that tend to zero. Therefore, according to [111], $\mathbb{E}[(\sum_{i=1,i\neq k}^{K}|\mathbf{a}_t{}^H(\phi^t{}_k)\mathbf{a}_t(\phi^t{}_i)|)^2]$ can be approximated by its upper bound as follows:

$$\mathbb{E}[\left(\sum_{i=1,i\neq k}^{K}|\mathbf{a}_t{}^H(\phi^t{}_k)\mathbf{a}_t(\phi^t{}_i)|\right)^2] \approx (K-1)\sum_{i=1,i\neq k}^{K}\mathbb{E}[\upsilon_{k,i}] \tag{3.36}$$

with approximation error $\frac{1}{2}\Gamma$ where Γ is given as follows:

$$\Gamma = \sum_{i=1,i\neq k}^{K}\sum_{j=1,j\neq k}^{K}(|\mathbf{a}_t{}^H(\phi^t{}_k)\mathbf{a}_t(\phi^t{}_i)| - |\mathbf{a}_t{}^H(\phi^t{}_k)\mathbf{a}_t(\phi^t{}_j)|)^2 \tag{3.37}$$

where $\Gamma \rightarrow 0$ when the number of transmit antennas is large ($N_T \rightarrow \infty$). Therefore, similar to Equation (3.30) and according to [106], $\Upsilon = (K-1)\sum_{i=1,i\neq k}^{K}\mathbb{E}[|\mathbf{a}_t{}^H(\phi^t{}_k)\mathbf{a}_t(\phi^t{}_i)|^2]$ can be expressed as follows:

$$\Upsilon = (K-1)^2\frac{1 + 2\sum_{i=1}^{N_T-1}\left(1 - \frac{i}{N_T}\right)\mathcal{J}_0^2(2\pi d_t i)}{N_T} \tag{3.38}$$

Finally, from Equations (3.38), (3.35) and (3.34), the expected per stream SE $\hat{\epsilon} = \mathbb{E}[\epsilon_k]$ for $K > 2$ UEs using MU analog LoS beamsteering with large number of transmit antennas can be approximated as follows:

$$\hat{\epsilon} \approx \log_2\left(1 + \frac{\frac{N_T}{(K-1)^2}}{\frac{1+\rho}{\rho} + 2\sum_{i=1}^{N_T-1}\left(1 - \frac{i}{N_T}\right)\mathcal{J}_0^2(2\pi d_t i)}\right) \tag{3.39}$$

We can observe that at $K = 2$ the expected per stream SE $\hat{\epsilon} = \mathbb{E}[\epsilon_k]$ in Equation (3.39) converges to the same expression in Equation (3.32) which validates the generalization of our approximation in this proposition for MU analog LoS beamsteering with any number of UEs K. ∎

3.2.5 SE Analytical Analysis for HBF

In this subsection, the tight upper bound approximation of the achievable per stream SE $\mathbb{E}[\epsilon_k]$ for MU HBF that relies on LoS beamsteering in the analog layer and ZF in the digital layer, with large number of transmit antennas, is analyzed in the following proposition.

Proposition 3. *For K UEs, served by MU HBF that relies on LoS beamsteering in the analog layer and ZF in the digital layer, in pure LoS channel with large number of transmit antennas, the expected achieved per stream SE $\hat{\epsilon} = \mathbb{E}[\epsilon_k]$ is approximated as follows:*

$$\hat{\epsilon} \approx \log_2(1 + \rho N_T) \tag{3.40}$$

Proof. Given that ZF is applied in the digital layer of the HBF, the IUI term $\sum_{i=1,i\neq k}^{K} |\mathbf{h}_k \mathbf{f}^{RF}_i|^2$ in Equation (3.25) is forced to zero. Moreover, the signal term $|\mathbf{h}_k \mathbf{f}^{RF}_k|^2$ is down scaled in order to mitigate the interference. However, it is shown in [106, 108] that the interference term in case of ULA transmit arrays is negligible for large number of transmit antennas. Therefore, the assumption in [112] that the interference term is negligible compared to the signal term for iid Rayleigh channels when ZF is applied in the HBF and the number of transmit antennas is large can be reused here in our case with ULA correlated sparse channel. Thus, we use this assumption to derive a tight upper bound for the SE of the MU HBF. This implies that at large number of transmit antennas with applying ZF in the digital domain, the following approximation holds:

$$\frac{\rho |\mathbf{h}_k \mathbf{f}^{RF}_k|^2}{\rho \sum_{i=1,i\neq k}^{K} |\mathbf{h}_k \mathbf{f}^{RF}_i|^2 + 1} \approx \rho |\mathbf{h}_k \mathbf{f}^{RF}_k|^2 \tag{3.41}$$

Given that $\mathbb{E}[|\mathbf{h}_k \mathbf{f}^{RF}_k|^2] = N_T$ as aforementioned in proposition 1. Using Jensen inequality, the tight upper bound approximation for the expected per stream SE $\hat{\epsilon} = \mathbb{E}[\epsilon_k]$ with large number of transmit antennas can be given as follows:

$$\hat{\epsilon} \approx \log_2(1 + \rho N_T) \tag{3.42}$$

$\blacksquare$

3.2.6 Asymptotic SE Analysis at high SNR Regime

In this subsection, we theoretically define the saturation level of the expected per stream SE ϵ for MU analog LoS beamsteering for high transmit SNR scenarios in pure LoS channel. Given that the transmit SNR ρ is large, the assumption $\rho \sum_{i=1,i\neq k}^{K} |\mathbf{h}_k \mathbf{f}^{RF}_i|^2 >> 1$ holds, which leads to the approximation $1 + \rho \sum_{i=1,i\neq k}^{K} |\mathbf{h}_k \mathbf{f}^{RF}_i|^2 \approx \rho \sum_{i=1,i\neq k}^{K} |\mathbf{h}_k \mathbf{f}^{RF}_i|^2$ (interference limited scenario). Therefore, in such case the expected per stream SE can approximated according to Equation (3.33) as:

$$\hat{\epsilon} \approx \log_2 \left(1 + \frac{\frac{N_T}{(K-1)^2}}{1 + 2\sum_{i=1}^{N_T-1} \left(1 - \frac{i}{N_T}\right) \mathcal{J}_0^2(2\pi d_t i)} \right) \tag{3.43}$$

where $\hat{\epsilon}$ saturates and does not scale with ρ anymore. This is not the case with the HBF, thanks to the ZF digital layer, the interference is totally mitigated (no interference limited scenario) and the expected per stream SE $\hat{\epsilon}$ scales logarithmically with ρ as shown in Equation (3.40).
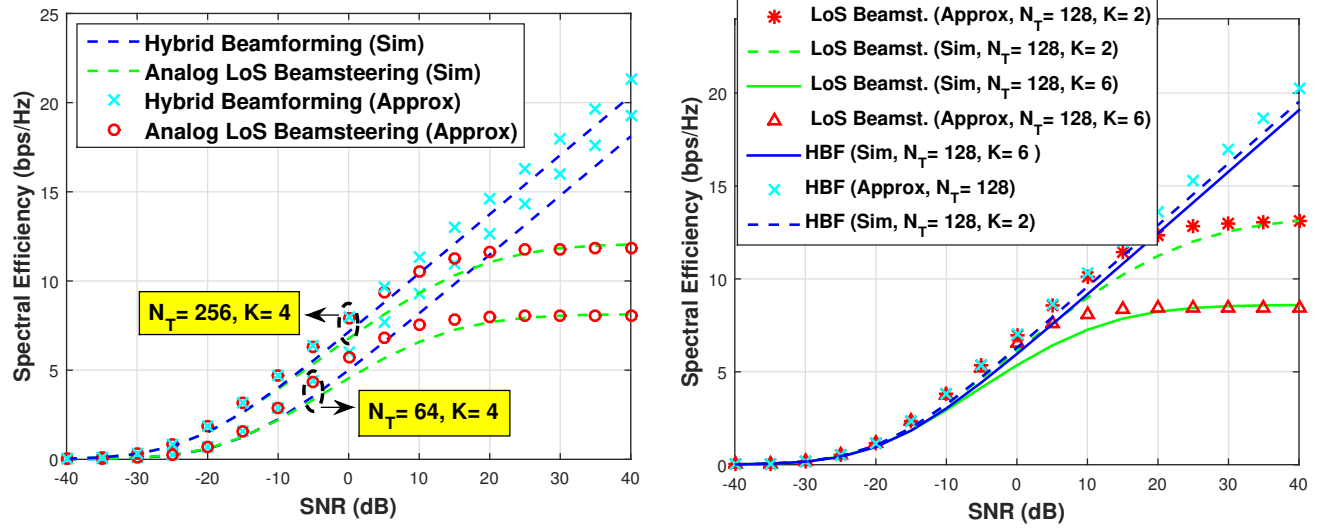
1) Simulated and theoretical approximations of per stream SE for MU-LoS beamsteering and MU-HBF systems, for different values of N_T and $K = N_b = 4$.

2) Simulated and theoretical approximations of per stream SE for MU-LoS beamsteering and MU-HBF systems, for different $K = N_b$ given $N_T = 128$.

Figure 3.7: Simulated and theoretical approximations of per stream SE for MU-LoS beamsteering and MU-HBF systems.

3.2.7   Numerical Analysis

In this subsection, we validate the aforementioned SE models for both MU LoS beamsteering and MU HBF in pure LoS channels. The transmit antenna array is ULA with half wavelength spacing $d_t = \frac{\lambda}{2}$. The number of transmit RF chains N_{TRF} equals the number of UEs and thus equals the number of the steered beams N_b by the BS $N_{TRF} = K = N_b$ for both MU LoS beamsteering and MU HBF. The simulations are carried out in a Monte Carlo fashion with 10000 realizations. Perfect CSI at the transmitter is assumed.

In Figure 3.7-1, the simulated per stream SE of the MU LoS beamsteering and MU HBF systems, together with the theoretical approximations given in Equations (3.33) and (3.40) are evaluated for different values of N_T, given $K = N_b = 4$ for validation purposes. We can observe that the proposed theoretical approximations are tight enough with ≈ 1.2 bps/Hz approximation error at 0 dB for MU LoS beamsteering for both $N_T = 64$ and $N_T = 256$. For MU HBF the approximation error at 0 dB for $N_T = 64$ is ≈ 1 bps/Hz and for $N_T = 256$ is ≈ 0.8 bps/Hz. This is expected because as N_T increases the approximation for HBF in Equation (3.40) becomes more accurate since the interference term tends to zero.

In Figure 3.7-2, the simulated per stream SE for MU LoS beamsteering and MU HBF systems, together with the theoretical approximations given in Equations (3.33) and (3.40) are evaluated for different values of N_b, given $N_T = 128$ for validation purposes. Again, we can observe that the proposed theoretical approximations are tight enough with ≈ 1 bps/Hz approximation
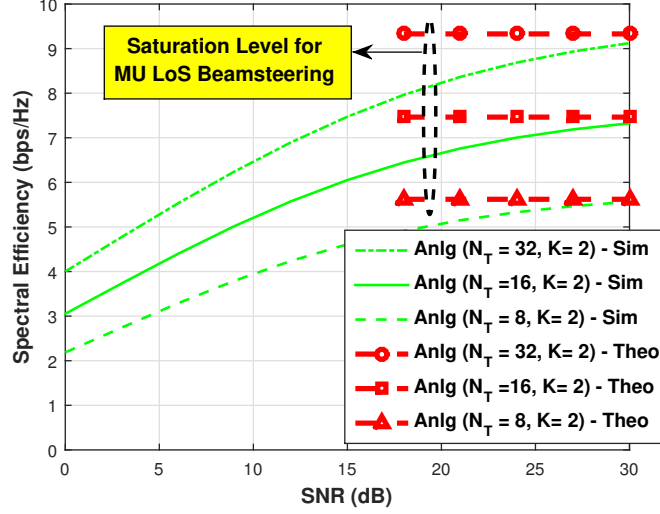
Figure 3.8: Simulated and theoretical saturation bound of per stream SE for MU LoS beam-steering, for different values of N_T and $N_b = 2$.

error at 0 dB for MU LoS beamsteering for $N_b = 6$ and ≈ 0.8 bps/Hz for $N_b = 2$. This is easily explained because as N_b decreases, the approximation error in Equation (3.37) decreases for fixed N_T. In the MU HBF case the approximation error is ≈ 1 bps/Hz for $N_b = 6$ and ≈ 0.7 bps/Hz for $N_b = 2$. Since decreasing the number of beams $K = N_b$ decreases the total interference term $\sum_{i=1,i\neq k}^{K} |\mathbf{h}_k \mathbf{f}^{RF}{}_i|^2$, hence the approximation in Equation (3.40) becomes more accurate.

From both Figures 3.7-1 and 3.7-2, we can observe that depending on the three parameters ρ, N_T and N_b, the SE performance gap between MU LoS beamsteering and MU HBF can be quantified. It is clear that when both MU LoS beamsteering and MU HBF can achieve approximately similar SE performance (at low SNR, high number of transmit antennas and small number of UEs), MU LoS beamsteering is more favourable because it avoids the Digital Signal Processing (DSP) complexity of the ZF. Also, it has lower overhead and channel estimation complexity, since it only needs estimating the LoS angular information, while MU HBF needs full estimation of the equivalent channel $\hat{\mathbf{H}}$. Otherwise, MU HBF is more favourable as it achieves significantly higher SE than MU LoS beamsteering, even if it is on the cost of the extra DSP processing complexity and channel estimation overhead.

Finally, in Figure 3.8, the simulated per stream SE for MU LoS beamsteering, together with the theoretical saturation bound given in Equation (3.43) are evaluated for different values of N_T, given $K = N_b = 2$ for validation purposes. We can observe that for different N_T, the SE for MU LoS beamsteering saturates to its corresponding analytical saturation upper bound at high SNR which validates our SE model in Equation (3.43).

3.2.8   Conclusion

In this section, we proposed an analytical closed form approximation for the expected achievable SE of MU analog LoS beamsteering in massive MIMO pure LoS channels. Also, we provided a

theoretical approximation for the SE saturation level of these systems at high SNR regime.

Moreover, we proposed a closed form approximation for the expected SE performance of the MU HBF system with ZF digital layer and LoS beamsteering analog layer in massive MIMO pure LoS channels. Finally, all the proposed models were validated by simulation results. The work in this section has been published in [22].

3.3   HBF in Sparse MU Massive MIMO mmWave Channel

In this section we analyze the problem of capturing the sparse multi-path channel components' gains by using hardware constrained analog phase shifters in sparse mmWave MIMO channels. Equal Gain Transmission was proposed in the literature as a closed form non complex solution for the MISO case that utilize analog phase shifters in sparse mmWave channels [91]. However, in case of a full MIMO scenario, the optimal solution is the SVD precoding which can not be implemented using analog phase shifters. Therefore, a sub-optimal solution was proposed that rely on applying a phase approximation of the SVD precoding to adapt with analog phase shifters used for mmWave beamforming/precoding [91, 113, 114].

In this section, we propose a novel closed form suboptimal algorithm for approximating the SVD precoding using phase shifters in sparse mmWave MIMO channels. Our proposed algorithm does not need SVD decompositions, henceforth decreasing the computational complexity significantly compared to the SVD based algorithms in the literature. Moreover, we prove by the simulation results that our proposed algorithm can achieve better SE compared to the SVD approximations provided in the literature.

3.3.1   Background

Analog LoS beamsteering [115] has emerged as a low complexity, low overhead solution [19] for mmWave MIMO channels. However, in case multiple paths exist in the channel which is still familiar in mmWave channels (since mainly they are sparse channels and not exactly pure LoS), LoS beamsteering is no longer an optimal solution, since the channel gains of the sparse multipath components are no longer exploited. In the case of MISO multipath channels, the optimal beamforming solution with analog phase shifters was already proposed in [91] namely EGT. However, in case of multipath MIMO channels, the optimal solution, in case a full digital system exists, is well known as the SVD precoding [5]. In an analog system with phase shifters no optimal closed form solution exist while sub-optimum solutions exist in the literature [91, 113, 114].

In [91] the authors proposed an iterative analog approximation for the SVD while in [113] the authors proposed a closed form analog approximation for the SVD without iterations as in [91] and showed that the performance gap between their closed form solution and the iterative (cyclic) one is negligible and not worth the additional complexity. Moreover, recently in [114] the authors again proposed the closed form solution in [113] for analog mmWave MIMO beamforming. In [114], the proposed algorithm extracts the phases of the most dominant Right Singular Vector (RSV) to design the analog beamformer and the same approach can applied at
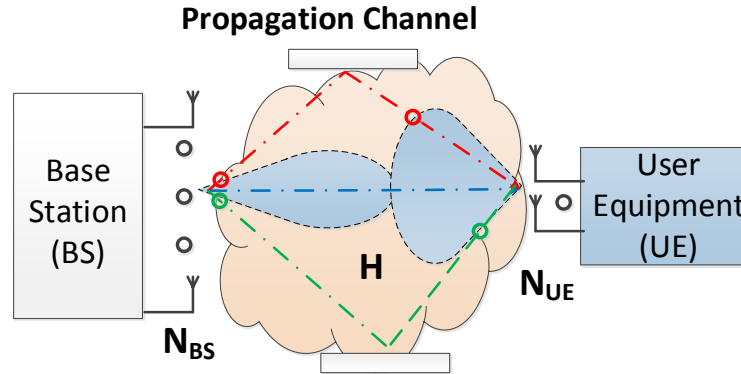
Figure 3.9: Illustrative figure of the proposed massive MIMO mmWave system in a sparse channel.

the receiver by extracting the phases of the most dominant Left Singular Vector (LSV) to design the analog combiner. The authors showed that using such an approximation they can approach the optimal full digital SVD SE in sparse channels even when deploying this analog strategy in a Hybrid Beamforming framework.

In this section, we propose a novel low complexity analog beamforming for mmWave MIMO sparse channels that can capture the gains of the multipath components of the channel. Hence, ensuring a better SE performance compared to the LoS beamsteering in such channels. Also, since our proposed algorithm does not rely on SVD computations it has significantly lower complexity compared to the SVD approximations in the literature [113, 114]. Moreover, we show by simulation results that our proposed algorithm achieves better SE compared to the more complex SVD approximations in the literature [113, 114] in realistic mmWave MIMO scenarios.

3.3.2 System and Channel Model

The proposed system for analog beamforming is a SU MIMO system described in Subsection 2.3.2 and shown in Figure 2.4 with single RF chain at both the BS and the UE. In this case, the received signal was already given in Equation (2.37) and represented here for readability as follows:

$$\mathbf{r} = \sqrt{P_T}\,(\mathbf{W}^{RF})^H \mathbf{H} \mathbf{F}^{RF} \mathbf{s} + (\mathbf{W}^{RF})^H \mathbf{n} \tag{3.44}$$

While for the HBF case, the system considered is a MU MIMO one described in Subsection 2.3.4 and shown in Figure 2.7 with multiple RF chains at the BS and single RF chain at each UE side. In this case, the received signal was given in Equation (2.44) and represented here for readability as follows:

$$\mathbf{r} = \sqrt{P_T}(\mathbf{W}^{RF})^H \mathbf{H} \mathbf{F}^{RF} \mathbf{F}^{BB} \mathbf{s} + (\mathbf{W}^{RF})^H \mathbf{n} \tag{3.45}$$

The channel model considered in this section, is the sparse physical ray based model introduced in Subsection 2.2.4. Given that we consider SU MIMO and MU MIMO multipath channels with

ULAs at the BS and the UEs side, the channel matrix for each UE k was given in Equation (2.27) and represented here for readability as follows:

$$\mathbf{H}_k = \sqrt{\frac{N_R N_T}{N_p{}^k}} \sum_{p=1}^{N_p{}^k} \alpha_{k,p} \mathbf{a}_r(\phi^r{}_{k,p}) \mathbf{a}_t(\phi^t{}_{k,p})^H \tag{3.46}$$

3.3.3 Analytical Analysis for the SVD Precoding in 2 Paths Channel

As aforementioned, it is well known that the optimal precoder for SU MIMO channel is the SVD one since it allows direct access to the channel eigenvalues. It is also well known that for LoS channels, the MIMO channel has a unity rank and the singular value of the channel is simply the channel gain of the LoS path α_{LoS}. Therefore, in mmWave channels which are LoS dominated, LoS beamsteering was seen as low complexity hardware feasible approximation for the SVD precoding.

However, as we previously mentioned that mmWave channels are sparse in nature which means that some additional multipath components exist. This means that in case LoS Beamsteering is used, it can no longer properly capture the channel gains offered by the multiple channel paths. Correspondingly, a performance gap starts to arise between the LoS beamsteering precoding and the optimal SVD precoding. Therefore, here in this section we derive a closed form model for this gap in the SE between the LoS beamsteering and the SVD for the simplest multipath case (when 2 channel paths exist), which is considered the baseline for both algorithms to start deviating in terms of SE. We highlight later by simulation results how this performance gap expands when the number of channel paths further increases.

In case the channel has only 2 paths and given that typically in mmWave MIMO systems the number of BS antennas $N_{BS} >> 2$ and the number of the UE antennas $N_{UE} > 2$, therefore the channel rank is limited by the number of paths $N_p = 2$. In case a single stream will be served by the system $N_S = 1$, and LoS beamsteering is applied for transmit precoding and receive combining, and $\alpha_1 > \alpha_2$ the SE, according to Equation (2.65), is given as follows:

$$\epsilon = \log_2(1 + \rho(|\alpha_1| + |\alpha_2||\Delta_r||\Delta_t|)^2) \tag{3.47}$$

where ρ represents the transmit SNR and $\Delta_r = \mathbf{a}_r{}^H(\phi^r{}_1)\mathbf{a}_r(\phi^r{}_2)$ represents the spatial correlation between the two paths at the receiver side. Similarly, $\Delta_t = \mathbf{a}_t{}^H(\phi^t{}_1)\mathbf{a}_t(\phi^t{}_2)$ represents the spatial correlation between the two paths at the transmitter side. On the other hand the SE given that SVD precoding and combining is applied, will be given as follows:

$$\epsilon = \log_2(1 + \rho\lambda_{max}(\mathbf{H})) \tag{3.48}$$

where $\lambda_{max}(\mathbf{H})$ is the maximum eigenvalue of the MIMO channel $\mathbf{H}$. Given that both N_R and N_T have large values, finding a closed form model for $\lambda_{max}(\mathbf{H})$ is not feasible for rich scattering channels and SVD computations need to be done using numerical software analysis. However, in case the channel is sparse which is the case in mmWave frequencies, the MIMO channel $\mathbf{H}$ can have an equivalent lower dimension matrix with the same eigenvalues [116]. Therefore,

in this section we will tackle the case when only 2 paths exist in a system with $N_R > 2$ and $N_T > 2$. Therefore, in such a case, the real channel rank is 2. In this section we will use the analysis in [116], for decreasing the dimension of the channel using QR Decomposition (QRD). We will also generalize this analysis for any value of the channel paths' complex gains α_1 and α_2. Moreover, we will provide a closed form expression for the channel eigenvalues λ_1 and λ_2. The sparse channel matrix $\mathbf{H}$ can be expanded as follows:

$$\mathbf{H} = \begin{bmatrix} \mathbf{a}_r(\phi^r{}_1) & \mathbf{a}_r(\phi^r{}_2) \end{bmatrix} \begin{bmatrix} \alpha_1 & \\ & \alpha_2 \end{bmatrix} \begin{bmatrix} \mathbf{a}_t{}^H(\phi^t{}_1) \\ \mathbf{a}_t{}^H(\phi^t{}_2) \end{bmatrix} \tag{3.49}$$

Applying QRD on both the transmit and receive steering matrices and using similar analysis as in [116, Eqs. 7-11] an equivalent matrix with reduced dimensions (2×2) with the same singular values can be calculated as follows:

$$\bar{\mathbf{H}} = \begin{bmatrix} \alpha_1 + \alpha_2 \Delta_r \Delta_t{}^H & \alpha_2 \Delta_r \sqrt{1 - |\Delta_t|^2} \\ \alpha_2 \Delta_t{}^H \sqrt{1 - |\Delta_r|^2} & \alpha_2 \sqrt{1 - |\Delta_r|^2} \sqrt{1 - |\Delta_t|^2} \end{bmatrix} \tag{3.50}$$

Therefore, in order to calculate the eigenvalues λ_1 and λ_2 we need to define the matrix $\mathbf{G} = \bar{\mathbf{H}}\bar{\mathbf{H}}^H = \{g_{i,j}\}_{2\times 2}$ with entries given as follows:

$$\begin{aligned} g_{11} &= |\alpha_1|^2 + \alpha_1 \alpha_2^H \Delta_r{}^H \Delta_t + \alpha_1^H \alpha_2 \Delta_r \Delta_t{}^H + |\alpha_2|^2 |\Delta_r|^2 \\ g_{22} &= |\alpha_2|^2 (1 - |\Delta_r|^2) \\ g_{12} &= \alpha_1 \alpha_2^H \Delta_t \sqrt{1 - \Delta_r{}^2} + |\alpha_2|^2 \Delta_r \sqrt{1 - \Delta_r{}^2} \\ g_{21} &= g_{12}^H \end{aligned} \tag{3.51}$$

Moreover, given that $\mathbf{G}$ is a Hermitian matrix, the eigenvalues λ_1 and λ_2 can be given according to [117] as follows:

$$\begin{aligned} \lambda_1 &= \frac{1}{2}(g_{11} + g_{22} + \delta) \\ \lambda_2 &= \frac{1}{2}(g_{11} + g_{22} - \delta) \end{aligned} \tag{3.52}$$

where δ is given as follows:

$$\delta = \sqrt{4|g_{12}|^2 + (g_{11} - g_{22})^2} \tag{3.53}$$

3.3.4 Analytical Analysis for the SVD Precoding in 2 Paths Channel with Massive Array at the BS

Given the fact that in realistic mmWave MIMO systems, the BS has a massive antenna array, Henceforth, the approximation $\Delta_r \approx 0$ can hold for up-link scenarios and the approximation $\Delta_t \approx 0$ can hold for down-link scenarios. Moreover, driven by the fact that the propagation channel $\mathbf{H}$ is reciprocal, evaluating the eigenvalues of the channel in the up-link scenario will yield similar values for the down-link one. Therefore, in this section we will analyze the two eigenvalues of the channel λ_1 and λ_2 in the up-link scenario, given that the BS has a massive

antenna array ($\Delta_r \approx 0$). In this scenario, the entries of the matrix **G** in Equation (3.51) can be simplified as follows:

$$g_{11} \approx |\alpha_1|^2, \quad g_{22} \approx |\alpha_2|^2, \quad g_{12} \approx \alpha_1 \alpha_2^H \Delta_t, \quad g_{21} \approx g_{12}^H \tag{3.54}$$

Similarly, λ_1, λ_2 and δ in Equations (3.52) and (3.53) can be approximated as follows:

$$\begin{aligned} \lambda_1 &\approx \frac{1}{2}(|\alpha_1|^2 + |\alpha_2|^2 + \delta) \\ \lambda_2 &\approx \frac{1}{2}(|\alpha_1|^2 + |\alpha_2|^2 - \delta) \\ \delta &\approx \sqrt{4|\alpha_1|^2|\alpha_2|^2\Delta_t^2 + (|\alpha_1|^2 - |\alpha_2|^2)^2} \end{aligned} \tag{3.55}$$

Therefore, from Equation (3.55), we can define two extreme cases:

- Case 1: when the paths are fully orthogonal ($\Delta_t = 0$), in this case: $\lambda_1 = |\alpha_1|^2$ and $\lambda_2 = |\alpha_2|^2$.

- Case 2: when the paths are fully correlated (represent one equivalent path, $\Delta_t = 1$), in this case: $\lambda_1 = |\alpha_1|^2 + |\alpha_2|^2$ and $\lambda_2 = 0$.

The realistic scenario $0 \leq \Delta_t \leq 1$ is bounded between these two extreme cases, and thus given that $\alpha_1 > \alpha_2$, the maximum eigenvalue $\lambda_{max}(\mathbf{H}) = \lambda_1$ can be represented as follows:

$$\lambda_1 = |\alpha_1|^2 + \kappa \tag{3.56}$$

where $0 \leq \kappa \leq |\alpha_2|^2$ is defined as follows:

$$\kappa \approx -\frac{|\alpha_1|^2}{2} + \frac{|\alpha_2|^2}{2} + \frac{\delta}{2} \tag{3.57}$$

Therefore, according to Equation (3.48), the achievable SE of the SVD precoding and combining for a single stream transmission in a channel with 2 paths can be expressed as follows:

$$\epsilon = \log_2(1 + \rho(|\alpha_1|^2 + \kappa)) \tag{3.58}$$

while in case LoS beamsteering is applied for beamforming and combining in such scenario ($\Delta_r \approx 0$), the SE according to Equation (3.47) can be calculated as follows:

$$\epsilon = \log_2(1 + \rho|\alpha_1|^2) \tag{3.59}$$

From both Equations (3.58) and (3.59), it is clear that the LoS beamsteering SE performance deviation from the optimal SVD performance is due to the factor κ. Moreover, it is straightforward to observe that this deviation factor κ increases with the number of channel paths N_p. Therefore, as the number of channel paths increases, the LoS beamsteering is no longer an efficient approximation for SVD and other approximations should be considered to efficiently capture the channel gains of the multipath components of the sparse channel.

3.3.5 Novel Analog and HBF for MU Massive MIMO mmWave

As aforementioned, given that the mmWave MIMO channels are sparse, typically multiple channel components exist together with the LoS component. In order to capture such gains with low hardware complexity some analog beamforming techniques were proposed in the literature that require only a single RF chain and a network of phase shifters. In this subsection we will present such algorithms proposed in the literature. Moreover, we will provide a novel analog beamforming algorithm that does not require SVD decomposition and hence has a reduced computational complexity compared to the the baseline algorithms in the literature.

Baseline Algorithms

In [118], the authors provided an algorithm called cyclic EGT, on which they aim at solving the following optimization problem, given that analog system exist ($N_S = 1$ and unit norm phase shifters exist):

$$\operatorname*{argmax}_{\mathbf{f},\mathbf{w}} |\mathbf{w}^H \mathbf{H} \mathbf{f}|^2$$
$$s.t. |\mathbf{w}_i|^2 = \frac{1}{N_R}, \quad i = 1, 2, ..., N_R, \tag{3.60}$$
$$|\mathbf{f}_j|^2 = \frac{1}{N_T}, \quad j = 1, 2, ..., N_T.$$

Given that this problem is non convex with no existing closed form solution, the cyclic iterative methodology was considered in [118] to solve this problem, such that their proposed algorithm can be summarized as follows:

- Step 0: The combiner vector $\mathbf{w}$ is initialized as the most dominant left singular vector of the channel $\mathbf{H}$ ($\mathbf{w} = \mathbf{U}_{:,1}$)

- Step 1: Calculate $\mathbf{f}$ as the EGT precoder for the MISO equivalent channel $\mathbf{h}_{MISO} = \mathbf{w}^H \mathbf{H}$, then $\mathbf{f}$ is calculated as: $\mathbf{f} = \frac{e^{j\angle \mathbf{H}^H \mathbf{w}}}{\sqrt{N_T}}$

- Step 2: Calculate $\mathbf{w}$ as the Equal Gain Combining (EGC) combiner for the Single Input Multiple Output (SIMO) equivalent channel $\mathbf{h}_{SIMO} = \mathbf{H}\mathbf{f}$, then $\mathbf{w}$ is calculated as: $\mathbf{w} = \frac{e^{j\angle \mathbf{H}\mathbf{f}}}{\sqrt{N_R}}$

Then both steps 1 and 2 are repeated in an iterative manner to form an alternating minimization approach for solving the previously mentioned optimization problem until a stopping criteria is reached, since the convergence of this approach is only valid for specific conditions [118].

It is clear that this approach suffers from two main limitations that make it less favourable for massive MIMO mmWave systems. The first limitation is the complex SVD computation needed at step 0, considering that the massive MIMO channel with large number of N_T and N_R. The second limitation is the iterative process between steps 1 and 2 which again adds complexity and delay constraints.

In [113] the authors relaxed the second limitation, by proposing another algorithm in which the beamforming and combining vectors are simply calculated as the phase of the most dominant right and left singular vectors respectively as follows: $\mathbf{w} = \mathbf{U}_{:,1}$ and $\mathbf{f} = \mathbf{V}_{:,1}$. They showed that the received SNR performance gap between the cyclic (iterative) EGT in [118] and their proposed algorithm is approximately in the range of $0.01 - 0.035$ dB and henceforth not worth the additional complexity and delay arising from iterations. Moreover, recently in [114], the authors reconsidered the same criteria in [113] for designing the analog layer of their proposed hybrid beamforming.

Proposed algorithm

Here we go further and relax the two limitations of the cyclic EGT by proposing a novel low complexity analog beamforming and combining technique. The mechanism of our proposed technique in case downlink scenario is considered ($N_T = N_{BS}, N_R = N_{UE}, N_T > N_R$) can be summarized as follows:

- Step 0: The combiner vector $\mathbf{w}$ is initialized as the LoS receive steering vector $\mathbf{w} = \mathbf{a}_r(\phi^r{}_{LoS})$. According to Figure 3.9, it is shown that $\mathbf{a}_r(\phi^r{}_{LoS})$ is able to capture the full gain of the LoS path together with considerable amount of the gain from the other multiple paths, since it has a wider beam compared to the transmit steering vector. However, here no SVD decomposition is needed which massively reduces the computational complexity.

- Step 1: This step is similar to step 1 in the cyclic EGT, where transmit EGT is applied to the equivalent MISO channel as follows: $\mathbf{f} = \frac{e^{j\angle\mathbf{H}^H\mathbf{w}}}{\sqrt{N_T}}$.

- Step 2: Again, this step is similar to step 2 in the cyclic EGT algorithm, where receive EGC is applied to the equivalent SIMO channel as follows: $\mathbf{w} = \frac{e^{j\angle\mathbf{Hf}}}{\sqrt{N_R}}$.

Henceforth, our proposed algorithm does not require any SVD decomposition or iterative steps compared to the baseline algorithms in the literature, yet it is able to capture the gains of the multiple channel paths. Later, we extend our discussion to the HBF scenario, where a digital processing layer is added. In this case multiple interference free spatial streams can be served simultaneously thanks to having multiple RF chains and using the digital processing layer, the optimal SVD precoding can be better approximated compared to using hardware limited analog beamforming with unit norm phase shifters only.

In order to apply the HBF, we first need to calculate the equivalent channel $\hat{\mathbf{H}}$ as follows: $\hat{\mathbf{H}} = \mathbf{W}^{RF}\mathbf{H}\mathbf{F}^{RF}$, where $\mathbf{H}$ is the MU channel encompassing the MIMO channels $\mathbf{H}_k$ for each UE k. Similarly, $\mathbf{F}^{RF}$ is the analog precoding matrix encompassing the precoding vectors $\mathbf{f}^{RF}{}_k$ for UE k and $\mathbf{W}^{RF}$ is the analog combining matrix encompassing the combining vectors $\mathbf{w}^{RF}{}_k$ for UE k given that each UE k is served by a single stream and equipped with a single RF chain.
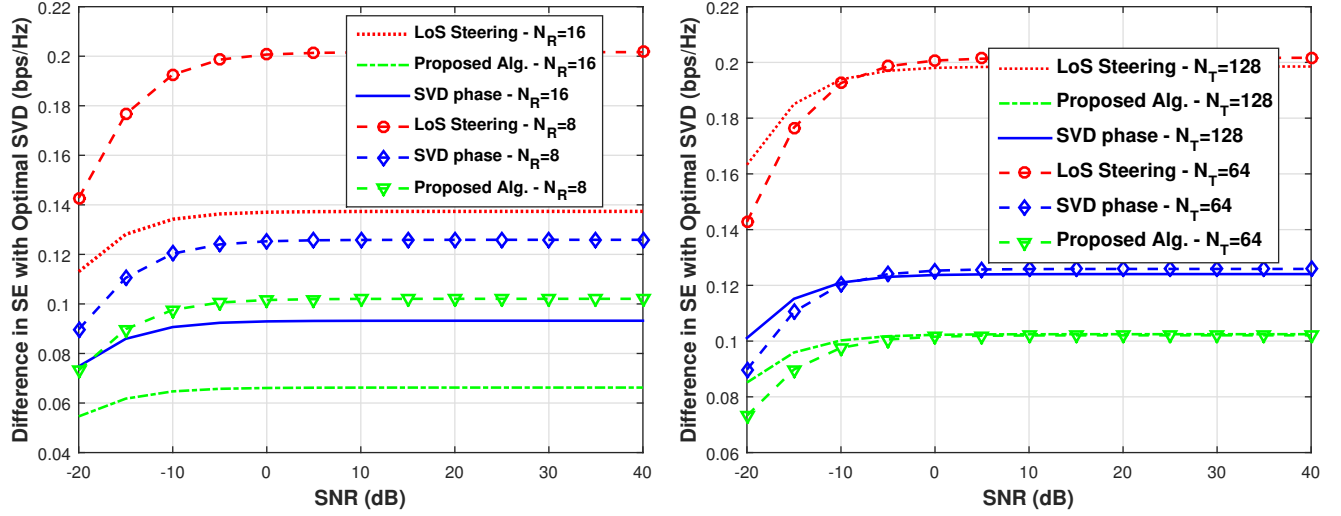
1) SE comparison between the proposed algorithm and the baseline ones for $N_T = 64, N_p = 3$ and variable N_R.

2) SE comparison between the proposed algorithm and the baseline ones for $N_R = 8, N_p = 3$ and variable N_T.

Figure 3.10: SE comparisons for the proposed analog beamforming techniques for different N_T and N_R.

Then the second stage of the HBF is done by applying ZF on the equivalent channel as follows:

$$\mathbf{F}^{BB}{}_{ZF} = \hat{\mathbf{H}}^H(\hat{\mathbf{H}}\hat{\mathbf{H}}^H)^{-1} \tag{3.61}$$

Then the digital precoder is normalized as follows:

$$\mathbf{f}^{BB}{}_k = \mathbf{f}^{BB}{}_k \|\mathbf{F}^{RF}\mathbf{f}^{BB}{}_k\|_F \tag{3.62}$$

Finally the hybrid beamformer can be constructed as follows: $\mathbf{F}^{HBF} = \mathbf{F}^{RF}\mathbf{F}^{BB}$.

3.3.6 Numerical Analysis

In this subsection, we evaluate the performance of the proposed algoritms and compare them with the baseline ones in the literature for both analog beamforming and HBF.

The transmit antenna array is ULA with half wavelength spacing $d_t = \frac{\lambda}{2}$. The number of transmit RF chains N_{TRF} equals the number of UEs $N_{TRF} = K$ for the MU HBF case. The simulations are carried out in a Monte Carlo fashion with 10000 realizations. Perfect CSI at the transmitter is assumed.

In Figure 3.10-1, SE comparison between the proposed algorithm and the baseline ones for $N_T = 64, N_p = 3$ and variable N_R is given. We can see that our proposed algorithm achieves suboptimal SE with a minimal gap compared to the optimal SVD precoding and it overperforms the baseline analog precoding techniques. In Figure 3.10-2, SE comparison between the proposed algorithm and the baseline ones for $N_R = 8, N_p = 3$ and variable N_T
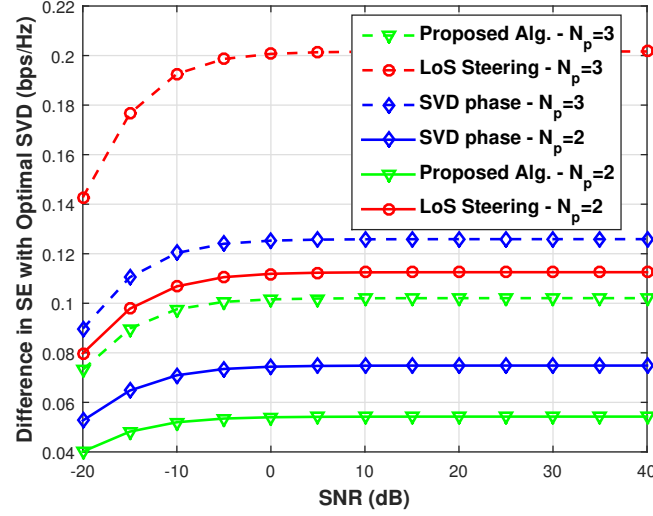
Figure 3.11: SE comparison between the proposed algorithm and the baseline ones for $N_T = 64, N_R = 8$ and variable N_p.
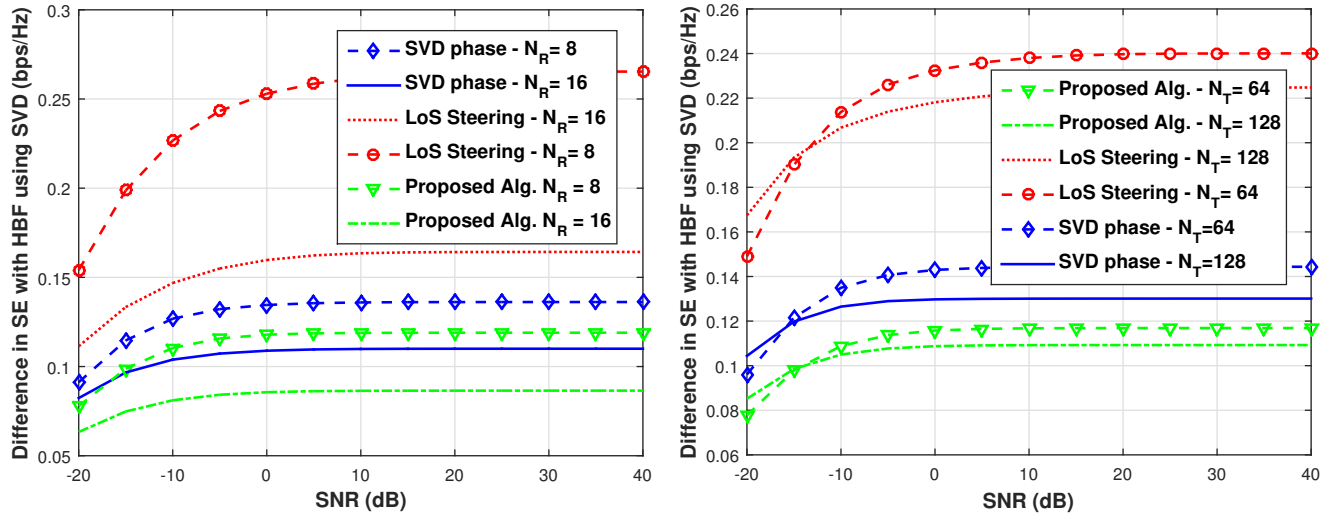
1) SE comparison between the proposed algorithm and the baseline ones in a HBF framework with ZF digital layer, for $K = 2, N_T = 64, N_p = 3$ and variable N_R.

2) SE comparison between the proposed algorithm and the baseline ones in a HBF framework with ZF digital layer, for $K = 2, N_R = 8, N_p = 3$ and variable N_T.

Figure 3.12: SE comparisons for the proposed HBF techniques for different N_T and N_R.

is given. Again, we can observe that our proposed algorithm achieves suboptimal SE with a minimal gap compared to the optimal SVD precoding and also overperforms the baseline analog precoding algorithms. Finally, in Figure 3.11, both $N_T = 64$ and $N_R = 8$ are fixed, while the number of paths N_p is varied. Similarly, our proposed algorithm achieves the most close SE
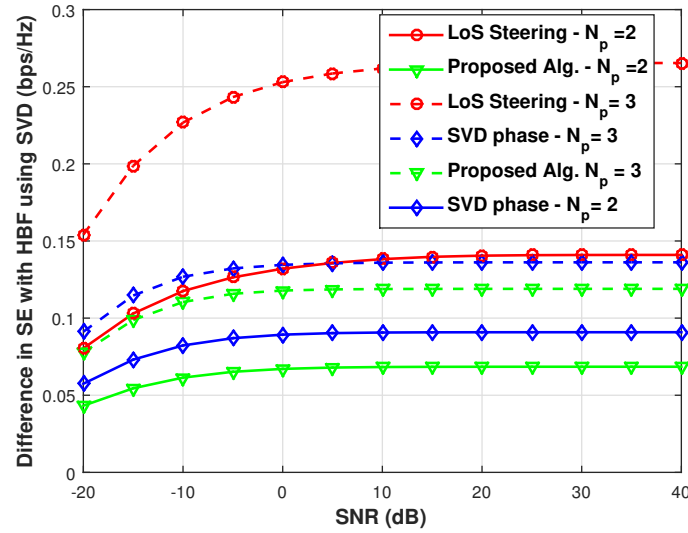
Figure 3.13: SE comparison between the proposed algorithm and the baseline ones in a HBF framework with ZF digital layer, for $K = 2, N_T = 64, N_R = 8$ and variable N_p.

performance to the optimum SVD one.

Now moving to the HBF extension of our proposed algorithm. In Figures 3.12 and 3.13 we can observe that for different scenarios (variable N_p or N_T or N_R) the HBF extension of our proposed algorithm with ZF digital layer achieves higher SE performance compared to the HBF extension of the baseline analog precoders with ZF digital layer.

3.3.7 Conclusion

In this section, we proposed a novel low complexity analog beamforming for mmWave MIMO sparse channels that can capture the gains of the multipath components of the channel. Then, we extended the proposed algorithm to the Hybrid Beamforming scenario to support MU transmissions by adding a Zero Forcing digital layer in the Base Band. We showed by analysis how our proposed agorithm relaxes the complexity of the baseline algorithms in the literature, thus being more suitable for mmWave massive MIMO deployments. Moreover, we showed by simulation results that our proposed algorithm achieves higher SE compared to the baseline analog algorithms. Finally we showed that the HBF extension of our proposed algorithm with ZF digital layer also achieves higher SE compared to the HBF extension of the baseline analog precoding techniques in the literature.

Chapter 4

Low Complexity **MU** Massive **MIMO** **mmWave** Systems

Contents

In this chapter we will provide low complexity signal processing techniques in order to enable practical MU massive MIMO mmWave systems. We start by considering a low complexity angular based beamforming and power allocation framework for LoS dominated mmWave channels. This angular framework relies on Digital Beam Steering for beamforming and Leakage Based Power Allocation for power allocation. Henceforth ensuring low-complexity and low overhead requirements needed for MU massive MIMO mmWave systems. Later, we introduce a Hybrid Beamforming framework that captures the diversity of the multipath sparse channel in the analog domain using the Equal Gain Transmission spatial precoding scheme to allow for robustness against link blockages. Finally, we propose a novel low complexity UEs selection approach named leakage based UEs selection and studied its performance in pure LoS channels.

4.1 Angular Based Beamforming and Power Allocation Framework for MU Massive MIMO mmWave Systems

Many beamforming and power allocation techniques have recently emerged to leverage the sparse channel characteristics of mmWave systems in order to enhance the sum capacity and the coverage for MU transmissions. However, most of the existing algorithms are practically limited due to full channel knowledge and high complexity requirements. In this section we introduce a novel, low complexity, angular based beamforming and power allocation framework, that requires the knowledge of the main contributing AoAs/AoDs of the propagation channel only. Exploiting the fact that the propagation conditions are highly driven by the geometrical structure of the channel in mmWave scenarios, our method relies on the estimation of the leakage caused by each UE on all the other UEs, approximated from the AoDs contributions. We prove with the simulation results that this approach, in addition to be practically plausible, can enhance the network SE alongside with maintaining acceptable data rates for the cell edge UEs.

4.1.1 Background

From a Base Band signal processing point of view, efficient usage of large antenna arrays through digital beamforming techniques attracts huge interest in the perspective of improved EE and SE using smart MU separation in the spatial domain. However, a central issue is to ensure the availability of the CSI of the MU MIMO channel at the transmitter upon which digital beamforming strategies are based.

Many optimization algorithms have highlighted that power allocation in MU MIMO [119, 120] and MU massive MIMO [121] systems, is an additional processing layer which can lead to substantial improvements of the system's SE and EE. However, these algorithms focus only on optimizing the objective function, without considering the computational complexity, latency and overhead constraints. Complexity problems have partially been addressed in [122, 123] where the authors focus their effort on improving the performance of low complexity linear precoders such as the CB. It is interestingly shown that such simple precoders can achieve considerable gains in SE and EE when coupled together with an interference wise power allocation. Though, the proposed iterative algorithms can not scale with massive MIMO ultra dense networks' low latency-low overhead requirements.

Contrary to the aforementioned algorithms, some other interesting perspectives appeared with introducing the LBPA [124] solution. Such approach is a low complexity, closed form non iterative one. It aims at minimizing the interference each UE generates to all the other UEs which is referred to as leakage. Such an approach is interesting to pursue together with finding an answer to the channel estimation overhead minimization.

In previous work [125, 126], we introduced the DBS precoding concept as a simple frequency flat - angle based beamforming technique which can be viewed as the MU extension of the analog LoS beamsteering. It is considered an interesting paradigm for the mmWave massive MIMO systems due to its low complexity and low overhead. In the case of a propagation scenario strongly conditioned by the LoS component of the channel, as is the case in mmWave and/or in the small-cell environment, it is favorable to implement a precoder such as DBS which maximizes the emitted power only in the main direction of each UE. In this section, we investigate the potentials of DBS precoding through coupling it with an interference wise power allocation in a hierarchical framework. More precisely, we propose to couple DBS with LBPA in order to ensure the low complexity of our scheme. Moreover, we derive closed form simplifications for the LBPA to adapt it to the DBS low overhead. Thus, in our introduced approach the AoDs information is only required and the full CSI at the transmitter requirement is relaxed.

Therefore, the contribution of the introduced framework in this section compared to the previous massive MIMO beamforming and power allocation algorithms in the literature can be summarized as follows:

- **Angular Analysis**: We present a DBS - LBPA framework that depends only on the AoD information with multiple simplifications and evaluate the performance in each case. Thus, relaxing the full CSI knowledge requirement.

- **Scalability**: Due to the low complexity of our solution, it can scale with increasing the number of antennas and it can be implemented at sophisticated mmWave DSP. Also, due

to the low overhead, our solution can be used for coordination between cells in multi-cell environments through relaxing the backhaul constraints.

- **Coverage and Outage Analysis**: In this section we provide analysis for the coverage achieved by the DBS - LBPA framework. We prove by simulation results that it achieves low outage probability together with enhancing the sum SE.

For baseline scenarios, we decouple the beamforming and power allocation problems in order to ensure a flexible framework. We consider two classical precoding techniques as a baseline which are the ZF and the CB precoders. Then we consider the DBS as our contribution. For the power allocation problem we consider the LBPA approach. First we utilize LBPA based on full CSI. Afterwards, we relax the full CSI requirement and derive a simpler power allocation strategy that relies only on the AoD information. Then we show by simulation results how our proposed angular frequency flat framework (DBS - LBPA with AoD information) can achieve high data rates in highly LoS environments with low overhead and low complexity requirements.

4.1.2   System and Channel Model

The proposed system is a downlink MU MISO system with digital beamforming described in Subsection 2.1.1 and shown in Figure 2.1. The received signal for each UE k be expressed as follows:

$$r_k = \mathbf{h}_k^T \mathbf{f}_k s_k + \sum_{i=1 \neq k}^{K} \mathbf{h}_k^T \mathbf{f}_i s_i + n_k, \tag{4.1}$$

where UE k is allocated power $\mathbb{E}\left[|s_k|^2\right] = P_k$. $\mathbf{f}_k$ is the kth column of the precoding matrix $\mathbf{F}$.

The channel model considered in this section, is the ray tracing based model introduced in Subsection 2.2.5. Given that we consider MU MISO multipath channel with UPA at the transmitter and a single receive antenna at each UE k, the channel vector for each UE k was given in Equation (2.25) and represented here for readability as follows:

$$\mathbf{h}_k = \sum_{p=1}^{N_p{}^k} \alpha_{k,p} \mathbf{a}_t(\phi^t{}_{k,p}, \theta^t{}_{k,p}), \tag{4.2}$$

Then, the MU channel $\mathbf{H}$ can be calculated as $\mathbf{H} = [\mathbf{h}_1^T, \mathbf{h}_2^T, ..., \mathbf{h}_K^T]^T$.

4.1.3   Beamforming Techniques

In this section, we consider three digital beamforming techniques namely ZF, CB and DBS. Both ZF and CB are described in Subsection 2.1.2 in Equations (2.4) and (2.2) respectively. While DBS is explained in Subsection 2.3.3 in Equation (2.42). DBS is introduced in this section as a promising low complexity-low overhead linear precoder suitable for sparse channels such as the mmWave one compared to the classical linear precoders (ZF and CB).

4.1.4   Interference and Leakage Analysis

High directivity beamforming techniques with narrow beams can achieve high beamforming gains, however they are very sensitive to channel knowledge inaccuracies at the transmitter. In techniques like ZF for instance, the nulling positions are very sensitive to channel estimation errors in high directivity cases. Henceforth, other beamforming techniques like CB and DBS can become more favorable than ZF in practical massive MIMO mmWave regime due to the less sensitivity to estimation errors with high directivity. However, due to the fact that CB and DBS do not consider minimizing the interference between the UEs, we focus on adding an extra processing layer for suppressing it.

In this section we utilize the LBPA for suppressing the interference through power allocation processing for precoders that do not consider interference as an objective. In order to utilize the LBPA we have first to define the leakage metric which will be considered the main building block of the algorithm. If we analyze the symbol r_k received by the UE k in Equation (4.1), we notice that the interfering part is the sum of the $K - 1$ signals destined for the other UEs and weighted by their respective precoders ($\mathbf{f}_i, \forall i \neq k \in [1, K]$).

From the BS's perspective, it is relevant to know how the formation of a beam to a new UE will harm its neighbors (i.e. the leakage that will be caused). We denote the leakage created by the transmission to UE k as I_k. OFDM transmission is assumed with N_{FFT} subcarriers. In the general case of N_T transmit antennas and N_{FFT} subcarriers, the leakage resulting from the transmission to UE k is calculated as follows:

$$I_k = \frac{P_k}{N_{FFT}} \sum_{n=1}^{N_{FFT}} \sum_{j \neq k=1}^{K} |\mathbf{h}_j[n]^T \mathbf{f}_k[n]|^2, \tag{4.3}$$

where $\mathbf{h}_j[n]$ is the vector comprising, for the subcarrier n, the N_T frequency attenuating coefficients associated with the N_T antenna-to-antenna links between the transmitter and the jth receiver. Similarly, $\mathbf{f}_k[n]$ is the precoding vector constructed from the attenuation coefficients for the subcarrier n of the channels between the UE k and the BS.

From this expression, it is clear that the calculation of *Leakage* requires a complete knowledge of the channel response constructed from the frequency responses of the set of links (i.e. $N_T \times K$ links), for all the subcarriers. The number of subcarriers to be estimated depends closely on the BW and the coherence band. Let N_{BC} be the number of subcarriers in the coherence band, then, the number of coefficients to be estimated to obtain the channel frequency response is $\frac{N_T \times K \times N_{FFT}}{N_{BC}}$.

The constraint of complete knowledge of the channel response becomes problematic in MU massive MIMO mmWave systems, since the number of channel coefficients to be estimated increases linearly with the number of transmit antennas.

Henceforth, the solution described in [124], which is based on complete knowledge of the propagation channel response, is not suitable for MU massive MIMO mmWave systems.

Since the leakage is an evaluation of the power emitted in the direction of the other UEs, so it is possible to avoid the averaging on all the subcarriers by exploiting the angular model of
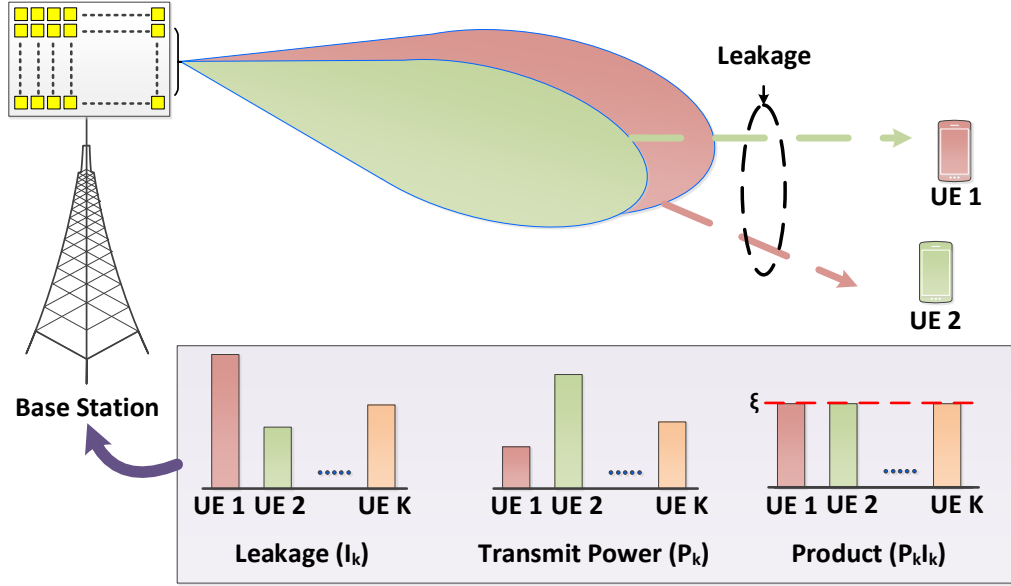
Figure 4.1: Illustrating the mechanism for the LBPA

the channel as follows:

$$I_k = P_k \sum_{j \neq k}^{K} \sum_{l=1}^{N_p{}^j} \alpha_{j,l} |\mathbf{a}_t(\phi^t{}_{j,l}, \theta^t{}_{j,l})^T \mathbf{f}_k|^2 \tag{4.4}$$

Note that if we consider the pure LoS scenario, the dependence on the subcarrier index disappears. Then $N_{FFT} = N_{BC}$ and thus only $N_T \times K$ coefficients are needed per estimation. This is due to the fact that the 1-Ray channel response is frequency flat over the BW.

Hence, an angle based precoder only needs $2K$ coefficients (as many azimuth and elevation angles as there are UEs) and also has optimal performance in such an ideal configuration.

4.1.5 LBPA-DBS Hierarchical Framework

In this subsection we will firstly describe the LBPA whose aim is to act on the individual power weights per UE in order to minimize the effects of *Leakage* between the UEs. Later we will apply the LBPA together with its simplifications on the DBS precoder.

Overview

A situation of equity between the UEs in terms of level of mutually produced *Leakage* is achieved by guaranteeing the following equality:

$$P_k I_k = \xi \quad \forall k \in [1, K] \tag{4.5}$$

78

1) AoD + path loss of the $N_p{}^j$ paths.
2) AoD of the $N_p{}^j$ paths.
3) AoD + path loss of the LoS.
4) AoD of the LoS.
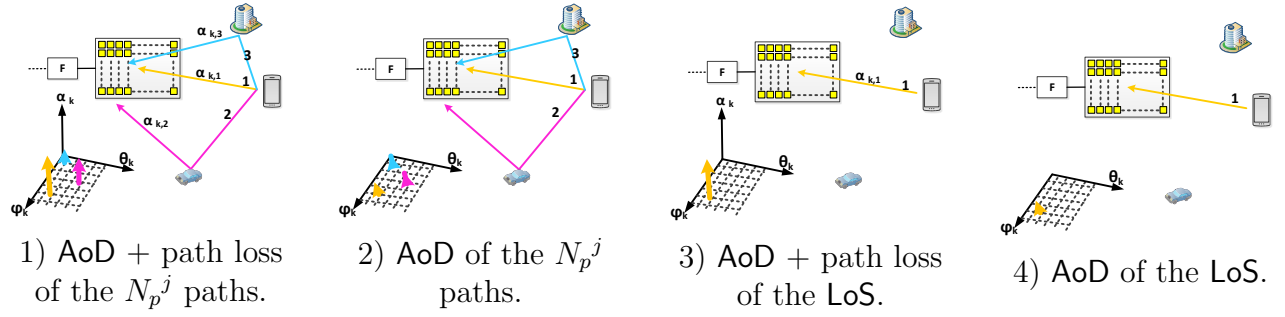
Figure 4.2: Illustration of the amount of information available at the BS, concerning one UE from the K terminals of the cell, for the calculation of the power to be allocated.

where ξ is a constant as shown in Figure 4.1. This equality is easily achieved by applying the following power per UE:

$$P_k = \frac{\xi}{\sum_{j\neq k}^{K} \sum_{l=1}^{N_p{}^j} \alpha_{j,l} |\mathbf{a}_t(\phi^t{}_{j,l}, \theta^t{}_{j,l})^T \mathbf{f}_k|^2} \tag{4.6}$$

Remark: The value of ξ is chosen so as to ensure the total power constraint P_T, as follows:

$$\sum_{k=1}^{K} P_k = P_T \longrightarrow \xi = \frac{P_T}{\sum_{k=1}^{K} \Lambda} \tag{4.7}$$

$$\text{, with } \Lambda = \frac{1}{\sum_{j\neq k}^{K} \sum_{l=1}^{N_p{}^j} \alpha_{j,l} |\mathbf{a}_t(\phi^t{}_{j,l}, \theta^t{}_{j,l})^T \mathbf{f}_k|^2} \tag{4.8}$$

Simplifying the allocation

Here we will describe several simplified expressions of the allocated power P_k as a function of the amount of angular information available at the BS. The simulations performed, presented later, show that the performance degradation remains minimal in practical situations. Nevertheless, the underlying overhead reduction is worth interest.

In all the simplified expressions which follow, we will consider the DBS precoder due to its low overhead which is suitable for the future dense networks of small cells. Thus, P_k can be expressed as follows:

$$P_k = \frac{1}{\sum_{j\neq k}^{K} \sum_{l=1}^{N_p{}^j} \alpha_{j,l} |\mathbf{a}_t(\phi^t{}_{j,l}, \theta^t{}_{j,l})^T \mathbf{a}_t(\phi^t{}_{k,l}, \theta^t{}_{k,l})^*|^2} \tag{4.9}$$

Remark: Note that using complex precoders is quite possible. The only challenge is how to be formed from the geometric knowledge available. For example, it would be quite possible to form a geometric version of the ZF which would be expressed as $\mathbf{F} = \mathbf{A}_t{}^H (\mathbf{A}_t \mathbf{A}_t{}^H)^{-1}$.

Simplification 1: AoD + Attenuation of direct and secondary paths

Figure 4.2 - 1) Illustrates the amount of information known to the BS as the number of AoDs and the paths attenuation for each UE. Each UE j returns back to the BS the information about $T_j \leq L_j$ paths detected during the estimation process. The expression of the power allocated to the UE k is then:

$$P_k = \frac{1}{\sum_{j \neq k}^{K} \sum_{l=1}^{T_j} \alpha_{j,l} |\mathbf{a}_t(\phi^t_{j,l}, \theta^t_{j,l})^T \mathbf{a}_t(\phi^t_{k,l}, \theta^t_{k,l})^*|^2} \tag{4.10}$$

Simplification 2: AoD of direct and secondary paths

Now, if only the AoDs of $T_j \leq L_j$ paths are known to the BS for each UE $j \in [1, K]$, see Figure 4.2- 2), the power to be allocated to UE k is expressed as:

$$P_k = \frac{1}{\sum_{j \neq k}^{K} \sum_{l=1}^{T_j} |\mathbf{a}_t(\phi^t_{j,l}, \theta^t_{j,l})^T \mathbf{a}_t(\phi^t_{k,l}, \theta^t_{k,l})^*|^2} \tag{4.11}$$

Simplification 3 : AoD + Direct path attenuation only

Our interest in such angular solutions is based on the use of mmWave channels, the losses in free space are therefore very high and therefore the ratio $\frac{\alpha_{j,i}}{\alpha_{j,1}}$, with $j \in [1, K]$ and $i \in [2, N_p{}^j]$, is very small. Therefore, it seems logical to proceed with an additional simplification. This simplification considers only the direct path for each UE, estimating its AoD and its attenuation, as illustrated in Figure 4.2- 3). The power to be allocated to the UE k then becomes:

$$P_k = \frac{1}{\sum_{j \neq k}^{K} \alpha_{j,1} |\mathbf{a}_t(\phi^t_{j,1}, \theta^t_{j,1})^T \mathbf{a}_t(\phi^t_{k,1}, \theta^t_{k,1})^*|^2} \tag{4.12}$$

Simplification 4: AoD for direct path only

The expression of the allocated power only requires an estimate of the AoD from the BS as shown in Figure 4.2 - 4), and thus P_K is calculated as follows:

$$P_k = \frac{1}{\sum_{j \neq k}^{K} |\mathbf{a}_t(\phi^t_{j,1}, \theta^t_{j,1})^T \mathbf{a}_t(\phi^t_{k,1}, \theta^t_{k,1})^*|^2} \tag{4.13}$$

4.1.6 Numerical Analysis

System parameters

In order to realistically evaluate the performance of the proposed algorithms we develop two specific configurations in a street canyon environment, described in more details in Subsection 2.2.5. The first one, called 1-Ray scenario, which only takes into account the LoS path between each UE and the BS. The second one, called 3-Rays, adds two perfect reflections as shown in Figure 2.3. The simulation parameters are summarized in Table 4.1.

Table 4.1: Simulation Parameters

Parameter	Value
Channel Model	Ray Tracing based
Propagation, Scenario	1-Ray & 3-Rays, Street Canyon
Simulation Type	Monte Carlo (500 realizations)
Center Frequency, BW	60 GHz, 100 MHz
Transmit Antennas, Architecture	16, Square
Antennas Inter-element spacing	$\frac{\lambda}{2}$
Transmitter height, Receiver height	10 m, 1.5 m
Receive Antennas, UEs' positions	1, Random

Representing simplified power allocation techniques

The notations used in the legend of Figure 4.3, displaying the simulation results are as follows:

- *Uniform*: refers to the uniform power allocation.

- *Perfect I_k*: corresponds to the LBPA allocation with the *Leakage* known perfectly (i.e. the case in Figure 4.2 - 1)).

- *DBS Direction of Arrival (DoA) and pathloss*: corresponds to the DBS precoder with LBPA allocation given that the *Leakage* expression is simplified based on the LoS AoD and path loss information only as shown in Figure 4.2 - 3).

- *DBS DoA only*: corresponds to the DBS precoder with LBPA allocation given that the *Leakage* expression is simplified based on the LoS AoD information only as shown in Figure 4.2 - 4).

Precoders

The power allocation coefficients obtained in Equation (4.9) and its simplifications are applied at the precoding stage, pondering each UE coefficient by its leakage energy as follows:

$$\mathbf{F} = \sqrt{P_T} \left[\frac{\mathbf{f}_1}{\sqrt{I_1}}, \frac{\mathbf{f}_2}{\sqrt{I_2}}, ..., \frac{\mathbf{f}_K}{\sqrt{I_K}} \right]. \tag{4.14}$$

To ensure the global transmitted power P_T remains unchanged, a normalization factor β needs to be applied to form a normalized precoding vector $\mathbf{F} = \frac{\mathbf{F}}{\sqrt{\beta}}$. This factor is expressed as follows:

$$\beta = \mathbb{E}[Tr(\mathbf{F}^H \mathbf{F})]. \tag{4.15}$$

We analyze and compare the performance of the 3 aforementioned linear precoders, described in more details in Subsection 2.1.2.

Table 4.2: Computational Complexity and Overhead

Algorithm	Complexity	Coefficients
ZF [127]	$K(24(K-1)N_T{}^2$ $+48(K-1)^2N_T + 54(K-1)^3 + 6N_T)$	$\frac{N_T K N_{FFT}}{N_{BC}}$
CB [127]	$K(6N_T + 2(N_T-1) + 6N_T)$	$\frac{N_T K N_{FFT}}{N_{BC}}$
DBS	$K(6N_T + 2(N_T-1) + 6N_T)$	LoS AoD based $= 2K$
LBPA [124]	$K(12N_T + 4)$	LoS AoD based $= 2K$

Figure 4.3-1 shows how the LBPA improves the sum SE obtained by the precoders that does not consider minimizing the interference (CB and DBS) in the 3-Rays environment. The LBPA is not applied to the ZF SE analysis, since the role of LBPA in single cell scenario is to cancel the IUI, which is already canceled by ZF in this case leading to $I_k = 0$, $\forall k \in [1, K]$. The results in Figure 4.3-1 show that low complexity precoders (CB and DBS) can achieve almost the same sum SE as ZF, and they can even achieve higher SE when the number of the UEs increases in dense environments. This result shows that with the low complexity-low overhead framework based on the DBS, together with LBPA we can achieve better SE performance compared to the ZF with less complexity, less overhead, and without matrix inversion limitations. Table 4.2 shows that our proposed DBS - LBPA solution has much less complexity and less overhead compared to the ZF. Moreover, it requires only $2K$ channel coefficients against $\frac{N_T \times K \times N_{FFT}}{N_{BC}}$ in case of CB - LBPA solution.

Impact of the LBPA on the system performance

The CB benefits from the diversity of the channel as it forms a beam adapted to it, while the DBS knows only the direction of the UEs and not their channels. However, according to Figure 4.3-1 with LBPA the gap between DBS and CB decreases. Moreover, LBPA succeeds in decreasing the gap significantly between CB and ZF. These results unleash the main advantage of LBPA, which is reducing the benefit of using high complexity-high overhead signal processing techniques.

For the DBS precoder, simplifications 1,3 and 4 respectively as described in Subsection 4.1.5, are intertwined with the curve which shows the CB performance with LBPA based on perfect CSI at the transmitter. Therefore, we can conclude that, by knowing the directions of the direct paths for each UE, we can achieve high SE with low overhead.

Comparing the results to the ZF baseline precoder we can see that the crossing point (number of UEs above which the CB and DBS outperforms the ZF) is quite higher with uniform power allocation (U-PA) than with LBPA (~ 7 UEs with U-PA against ~ 5 UEs with LBPA).

In order to evaluate the coverage probability and the Quality of Service (QoS) satisfaction for all the UEs in the cell, we first define a QoS constraint on per UE data rate. According to [128] the average UE data rate in 5G should be at least 0.1 Gbps. In our simulations we define the acceptable outage probability to be $P_{out} = 20\%$. Thus the cell coverage probability
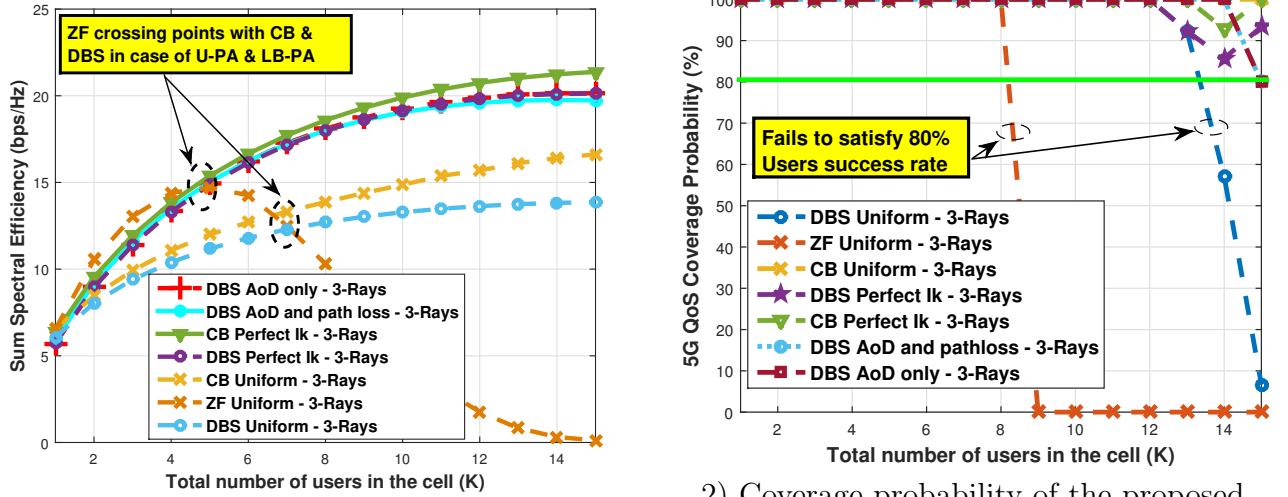
1) Sum SE of the proposed precoders assuming perfect CSI at the transmitter or AoD knowledge in the 3-Rays environment. The SE is averaged over 500 random UEs' positions for each $K \in [1, 15]$ with $N_T = 16$.

2) Coverage probability of the proposed precoders assuming perfect CSI at the transmitter or AoD knowledge in the 3-Rays environment. The coverage probability is averaged over 500 random UEs' positions for each $k \in [1, 15]$ with $N_T = 16$.

Figure 4.3: SE and coverage probability of the proposed precoders assuming perfect CSI at the transmitter or AoD knowledge in the 3-Rays environment.

should be at least 80%. Figure 4.3-2 gives more insights in terms of coverage and cell edge UEs' performance. We can observe that for all the precoders based on the LBPA the 5G per UE QoS constraint is satisfied for at least 80%. However, for the ZF, DBS precoders with uniform power allocation, the 5G per UE QoS constraint is not satisfied with increasing the number of simultaneously served UEs per cell ($\sim$ 9 UEs in the case of ZF and $\sim$ 14 in the case of DBS). Henceforth, the results reinforce our assumption that LBPA applies some sort of fairness between the served UEs. This is due to forcing the total leakage emitted by each UE to be constant as shown in Equation (4.6) and Figure 4.1. Thus, LBPA increases the system sum SE in a non greedy behavior, by considering the constant leakage per UE linear constraint.

4.1.7 Conclusion

In this section, we have demonstrated how the AoD information makes an assessment of the interference in a MU transmission. We have derived simple interference-wise power allocation solutions based on the angular channel structure to relax the overhead requirements. Henceforth, the advantages of our DBS - LBPA framework can be summarized as follows:

- It is more suitable for MU MIMO LoS dominated systems with partial channel knowledge compared to traditional complex solutions (such as the ZF).

- It ensures a relative threshold of fairness between the UEs, due to minimizing the leakage.

- In realistic mmWave LoS channel scenarios, knowing only the AoD still allows an effective SE performance gain.

The work in this section was published in [19].

4.2   Blockage in mmWave Channels

Transmissions at mmWave frequencies is obstructed by the frequent propagation ray blockage due to the small wavelength. Recently, a lot of research has thus been dedicated to HBF solutions to adapt with hardware limitations, and also trying to solve the ray blockage problem.

In this section we introduce a novel HBF framework that captures the diversity of the multipath sparse channel in the analog domain using the EGT spatial precoding scheme. We first highlight how such beamformer can enhance both the SE and the robustness of the communication system. Then, we unleash the potentials of the DSP layer to suppress the MU interference using the ZF approach. We introduce a generic and realistic channel blockage model to evaluate the robustness of our solution. We show through simulations that our algorithm achieves higher performance in terms of SE and robustness to blockage compared to the existing techniques in the literature.

4.2.1   Background

As mentioned before, modeling the propagation channel at mmWave systems is a challenge, as it has different characteristics compared to lower frequencies. At mmWaves, the propagation channel suffers from very high path-loss which can be tackled by using very large (massive) antenna arrays with very high directivity and hence very large array gains. This, can compensate the high path-loss effect. Also, one of the main challenges of mmWave channels is that they are LoS dominated channels, driven by the fact of the high path-loss, limited scattering and shadowing characteristics, only a small number of multipath components can survive their way to the receiver side. This fact makes the mmWave channel very sensitive to LoS blockages, which is one of the crucial issues that needs to be tackled for having a reliable and robust mmWave communication system [129].

In order to solve the blockage issue experienced at mmWave range, specifically the LoS component blockage, a lot of research has recently been conducted from different approaches. The previous works can be classified into four main directions. The first direction is to detect/expect the blockage and hence the transmitter can estimate the blockage interval and can adapt to it using signal processing techniques. In this direction, the work in [130] introduced a camera assisted proactive BS selection in order to detect the human body blockage and adapt the network. In [131] instead of using cameras, the authors utilize the radars to detect the blockage. The second direction is to adjust the network architecture to adapt for LoS blocking. In [132] the authors show how the relays can be used to aid the mmWave network to cope with LoS blockages through multi-hop transmissions. In [133] the authors proposed to use the Device to Device (D2D) technology to extend the coverage in case of link blockage. The third direction is to tackle the blockage in higher layers than the physical such as the work in [134].

Finally, the fourth direction, which we focus on in this section is to utilize the signal processing tools in leveraging the channel multipath and diversity properties in order to avoid severe signal degradation due to blockages. Driven by the fact that the mmWave channels are sparse and LoS dominated, the main idea in this direction is to introduce algorithms to distribute the energy efficiently over the propagation paths. This helps in achieving robust mmWave propagation links that can survive LoS blockages without severe degradation in the achieved data rates. The work in [135] adopted this idea, extending and enhancing the work in [136, 137] by introducing a novel RF diversity beamforming scheme and evaluating its robustness against LoS blockages in mmWave regime. However, all of the work in the literature did not consider constructively adding the multipath components which results in non efficient full utilization of the channel diversity. Moreover, all of the previous work only considered solving the problem in the analog domain for single user scenario, henceforth ignoring the scalability of these algorithms for MU scenarios in which the interference aspects have also to be considered.

In this section, we present a novel framework that unleash the channel diversity in the analog domain, then utilize the signal processing tools in the digital layer to cancel the inter-user interference. Up to the author's knowledge, this work is the first to address the idea of exploiting the channel diversity in HBF through using analog RF EGT [92], while most of the existing HBF literature focus on LoS beamsteering approach [5, 56]. Also, this work is the first which tackles the blockage issue by using HBF for MU scenarios. Finally, this work is the first to consider the constructive addition of the propagation paths during exploiting the channel diversity for robustness against blockage.

4.2.2 System and Channel Model

The proposed system is a downlink MU MISO system. In case analog beamforming is applied, the UEs are multiplexed in time and/or frequency, while in case HBF is applied, all the K served UEs are multiplexed in space. The received signal vector can be expressed as follows:

$$\mathbf{r} = \sqrt{P_T}\mathbf{HFs} + \mathbf{n} \tag{4.16}$$

where $\mathbf{F} = \mathbf{F}^{RF}$ in case analog beamforming is applied and $\mathbf{F} = \mathbf{F}^{RF}\mathbf{F}^{BB}$ in case HBF is applied.

The channel model considered in this section, is the sparse physical ray based model introduced in Subsection 2.2.4. Given that we consider MU MISO multipath channel with ULA at the BS and a single receive antenna at each UE k, the channel vector for each UE k was given in Equation (2.23) and represented here for readability as follows:

$$\mathbf{h}_k = \sqrt{\frac{N_T}{N_p{}^k}} \sum_{p=1}^{N_p{}^k} \alpha_{k,p}\mathbf{a}_t(\phi^t{}_{k,p})^H \tag{4.17}$$

Moreover, in this section we consider two special cases when blockage occurs to the channel, namely the LoS blockage case and the random blockage case which are explained in details in Subsection 2.2.6 and defined in Equations (2.33) and (2.36). Then, the MU channel $\mathbf{H}$ can be calculated as $\mathbf{H} = [\mathbf{h}_1^T, \mathbf{h}_2^T, ..., \mathbf{h}_K^T]^T$.

4.2.3 Beamforming Techniques

In this section, we consider both analog and HBF techniques. For the analog beamformer, we utilize both the LoS beamsteering and EGT techniques described in Subsection 2.3.2 in Equations (2.38) and (2.40) respectively. A baseline RF precoder introduced in [135] referred to as geometric mean maximization RF precoder will be considered to benchmark our results and will be described in details in the next subsection.

While for HBF we utilize the two stage HBF algorithm described in Algorithm 1, with using ZF for the BB precoder $\mathbf{F}^{BB}$ and LoS beamsteering or EGT or the geometric mean maximization baseline algorithm alternatively for the RF precoder $\mathbf{F}^{RF}$.

4.2.4 Geometric Mean Maximization RF Beamsteering

In this approach introduced in [135], the objective is to maximize the receive SNR, however, with distributing the energy more efficiently on the channel multiple paths to consider the spatial diversity required for the beamforming robustness. The work in [135] is considered an extension to the work in [136, 137], which considered also enhancing the diversity of the analog beamfromers, but without taking into account the SNR maximization objective. Assigning $\mathbf{G}_p = |\alpha_p|^2 \mathbf{a}_t(\phi^t{}_{k,p})^H \mathbf{f}\mathbf{f}^H \mathbf{a}_t(\phi^t{}_{k,p})$ for a given path p and UE k for readability and utilizing the lower bound of that rank one Hermitian matrix, we can have the following lower bound for the receive SNR:

$$\lambda_{max}\left\{\sum_{p=1}^{N_p}\mathbf{G}_p\right\} \geq \frac{1}{N_{TRF}}\sum_{d=1}^{N_p}\lambda_{max}\left\{\mathbf{G}_d\right\} \tag{4.18}$$

After obtaining the lower bound for the SNR maximum eigenvalue, the inequality of the arithmetic and geometric means is exploited to address the spatial diversity issue to the problem so the lower bound is reformulated as:

$$\lambda_{max}\left\{\sum_{p=1}^{N_p}\mathbf{G}_p\right\} \geq \sqrt[N_p]{\prod_{d=1}^{N_p}\mathbf{G}_d} \tag{4.19}$$

Then, the optimization problem was reformulated based on maximizing the geometric mean (lower bound) to distribute the power efficiently on the propagation paths as follows

$$\mathbf{f} = \underset{\mathbf{f}}{\operatorname{argmax}} \sum_{p=1}^{N_p} \log(|\mathbf{a}_t(\phi^t{}_p)^H\mathbf{f}|^2)$$
$$\text{s.t. } \|\mathbf{f}\| = 1 \tag{4.20}$$

which ensures maximizing the fairness of the energy distribution over the channel paths, together with maximizing the lower bound of the achievable receive SNR. This approach has more potential to ensure an acceptable trade-off between SNR maximization and link robustness against blockage compared to the LoS beamsteering. The Geometric Mean (GM) based beamformer $\mathbf{f}_{GM}$ calculation is described into details in Algorithm (2) with computational complexity $\mathcal{O}(N_T N_p \varrho)$, where ϱ is the number of iterations, and it is proved to converge after few iterations ($\varrho \leq 10$).

Algorithm 2 Robust RF precoder gradient ascent algorithm [135]

---

1) **Initialization :** $\mathbf{f}_0 = \frac{\sum_{p=1}^{N_p} \mathbf{a}_t(\phi^t{}_p)}{\| \sum_{p=1}^{N_p} \mathbf{a}_t(\phi^t{}_p) \|}$ (Superposition)

2) **for** $i = 0$ to $\varrho - 1$ (Iterations)

3)   Calculate the gradient : $\nabla_{f,i} = \sum_{p=1}^{N_p} \frac{\mathbf{a}_t(\phi^t{}_p)}{\mathbf{f}_i^H \mathbf{a}_t(\phi^t{}_p)}$

4)   Calculate the normalized rejection:

         $\Psi_i = \frac{\nabla_{f,i} - \mathbf{f}_i^H \nabla_{f,i} \mathbf{f}_i}{\| \nabla_{f,i} - \mathbf{f}_i^H \nabla_{f,i} \mathbf{f}_i \|}$

5)   Calculate the optimal step Φ_i by one-dimensional search over $[0, 2\pi)$:

$$\Phi_i = \underset{\Phi_i}{\arg\max} \sum_{p=1}^{N_p} \log(|\mathbf{a}_t(\phi^t{}_p)^H (\mathbf{f}_i \cos \Phi_i + \Psi_i \sin \Phi_i)|^2),$$

6)   Updating rule: $\mathbf{f}_{i+1} = \mathbf{f}_i \cos \Phi_i + \Psi_i \sin \Phi_i$

7) $\mathbf{f}_{i+1} = \frac{1}{\sqrt{N_T}} e^{j\angle \mathbf{f}_{i+1}}$ (for equal gain beamforming)

8) **end**

4.2.5 Numerical Analysis

Table 4.3: Simulation Parameters

Parameter	Value
Channel Model	Sparse Statistical Model [86]
Number of Propagation Paths	8-Rays
Simulation Type	Monte Carlo (500 realizations)
Transmit Antennas, Architecture	64, ULA
Transmit Antennas Inter-element spacing	$\frac{\lambda}{2}$
Number of Transmit RF Chains	4
Number of UEs, Receive Antennas	4, 1

Here, we evaluate the performance of the introduced analog beamforming and HBF algorithms in terms of SE and robustness based on the simulation parameters summarized in Table (4.3). First we compare between the analog beamforming algorithms using the ς outage capacity to capture the robustness against blockage, given that the ς outage capacity is defined as

$$\varsigma = \mathbb{P}(\log_2(1 + \rho |\mathbf{h}\mathbf{f}|^2) < R) \tag{4.21}$$

where ς represents the outage percentage for a given data rate R, here we use $\varsigma = 1\%$. We assume that in case of analog beamforming the UEs are multiplexed in time/frequency, thus no MU interference exists and thus we omit the UEs index k for readability.
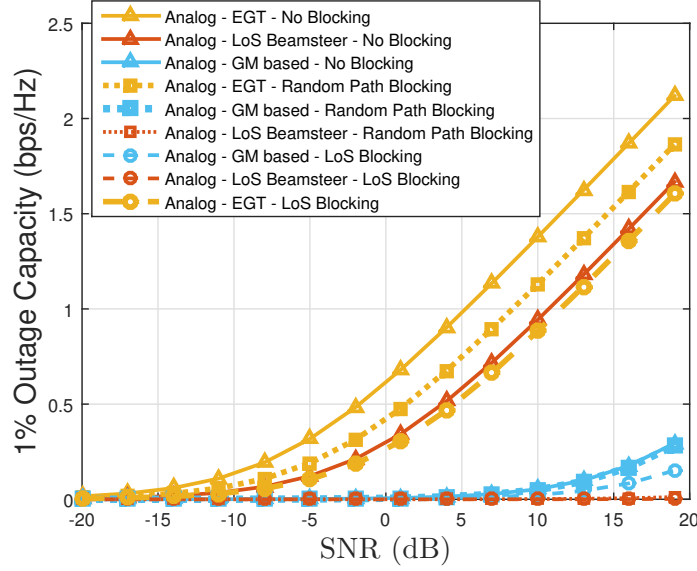
Figure 4.4: Comparison between the 1% outage capacity for different analog beamsteering approaches with and without blockage.

In Figure 4.4 we observe that the LoS beamsteering can achieve high outage capacity in case no blockage occurs. However, in case of LoS blockage or even random path blockage, the 1% outage capacity degrades severely. Thus, LoS beamsteering is not robust against blockage. Then, moving to the GM beamsteering algorithm, we can observe that in case of no blockage it has the worst performance, but in case of LoS or random blockages, it has more robust performance compared to the LoS beamsteering due to the fact that it distributes the energy over the multiple propagation paths. Finally, the EGT achieves the highest outage capacity in case no blockage occurs due to the constructive addition of all the channel paths. Moreover, EGT achieves also the highest performance in case of LoS or random path blockages. Henceforth, EGT achieves the highest robustness compared to the other proposed analog beamformers.

Moving forward to evaluate the SE of different analog beamformers (where multiple UEs are multiplexed in time/frequency) and their extension to MU-MISO systems using HBF architectures in Figures 4.5a, 4.5b and 4.6. In Figure 4.5a in case no blockage occurs, we can observe that for analog algorithms EGT achieves the best average per UE SE followed by the LoS beamsteering, and finally the GM beamsteering achieves the worst average per UE SE. In case ZF is applied in the digital domain for hybrid architectures, again we achieve the same order of performance for the different algorithms applied at the analog part. However, the performance gap increases in case of EGT compared to the other algorithms. This can be explained in more details in Figure 4.7. As we can see in Figure 4.7 the condition number of the equivalent channel $\hat{\mathbf{H}}$ in case of EGT is much smaller compared to the LoS beamsteering and GM beamsteering due to the fact that EGT captures the multipath components of the channel coherently, thus resulting in a less correlated well conditioned equivalent channel matrix compared to the LoS and GM beamsteering.
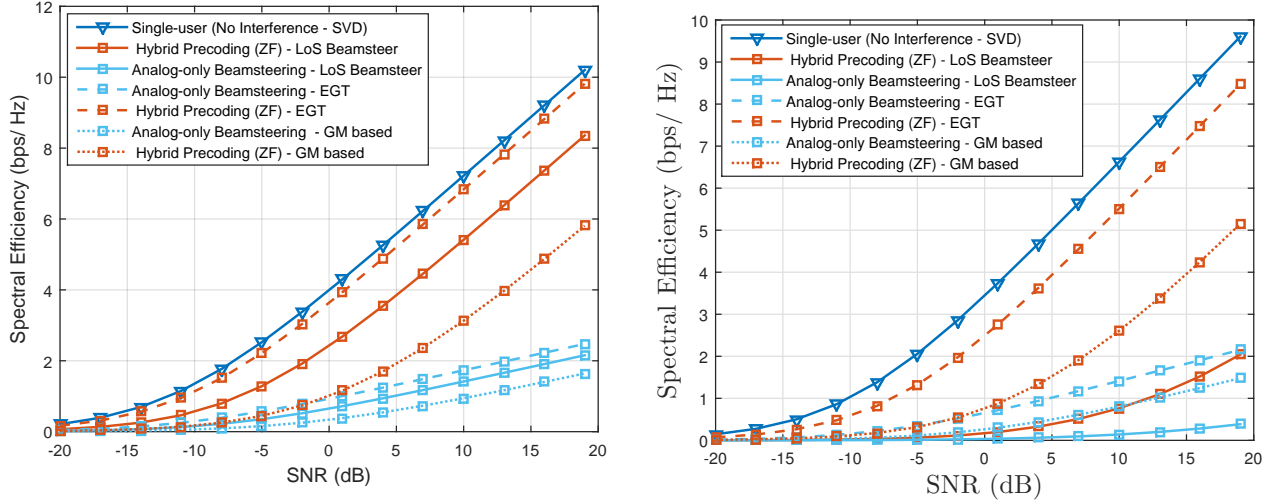
(a) Comparison between different analog and hybrid beamforming approaches without blockage in terms of the SE.

(b) The effect of the LoS path blockage on different analog and hybrid beamforming approaches in terms of the SE.

Figure 4.5: Comparison between different analog and hybrid beamforming approaches in terms of the SE.

Henceforth, applying ZF on $\hat{\mathbf{H}}$ based on EGT analog layer achieves higher SE compared to the case of LoS or GM beamsteering analog layer. Then in Figure 4.5b in case LoS blockage occurs, we can observe that for analog beamformers EGT is the most robust one followed by GM beamsteering and finally the LoS beamsteering. Similarly after applying the ZF for MU HBF, the same order exists, however with an obvious gap between the EGT and the other algorithms which is again explained by the condition number reduction with EGT shown in Figure 4.7.

Finally in Figure 4.6, in case a random path is blocked, we observe that again EGT achieves the highest average SE, followed by LoS beamsteering and finally the GM beamsteering achieves the worst SE on average, and their HBF extensions have the same order. This contradicts the outage capacity results in Figure 4.4 in which the GM beamsteering has higher outage capacity than the LoS beamsteering. This is due to the fact that on average in case of random path blockage LoS beamsteering achieves higher SE, specially in the realizations in which the blocked path is not the LoS path. However, considering the 1% outage capacity, which is a measure of the robustness of the algorithms and considers the worst case scenarios, we observe that GM beamsteering achieves higher outage capacity than the LoS beamsteering in case of random path blockage, because in case the random blocked path is the LoS path, the LoS beamsteering capacity drops significantly.

4.2.6 Conclusion

In this section we introduced EGT precoding as a potential robust and spectral efficient algorithm in the analog domain for mmWave systems that utilize HBF architectures. Given different
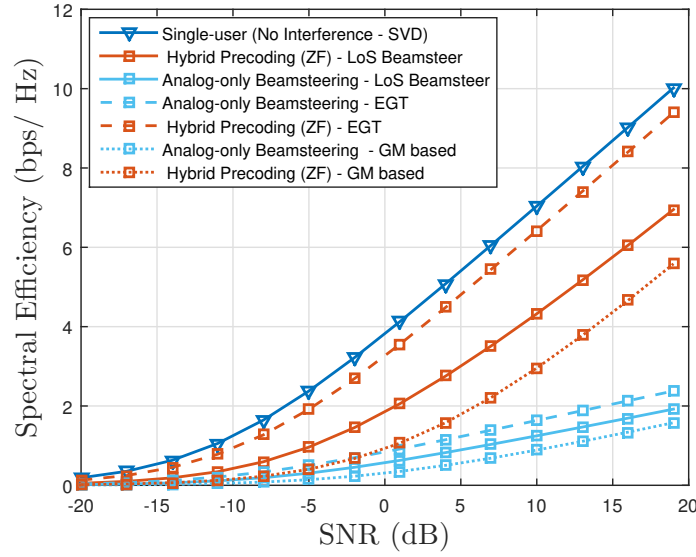
Figure 4.6: The effect of the random path blockage on different analog and hybrid beamforming approaches in terms of the SE
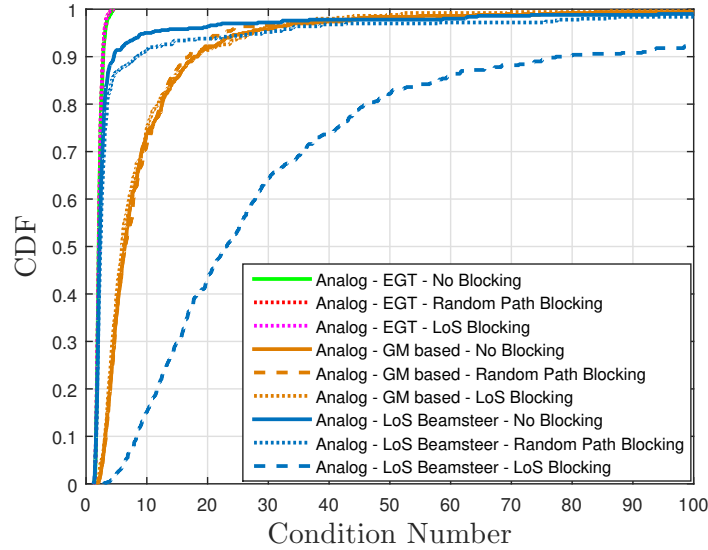
Figure 4.7: Comparison between the condition number of the equivalent channel $\hat{\mathbf{H}}$ after using different analog beamforming strategies in different blocking scenarios.

blockage scenarios, we showed that using EGT not only yields higher SE than traditional LoS beamsteering approaches, but also provides higher robustness against blockage compared to the already existing techniques of the literature. Moreover, integrating EGT in HBF architec-

tures with ZF digital processing layer is proved to be advantageous, since EGT achieves lower condition number for the equivalent channel matrix, thus producing well conditioned matrices for inversion compared to LoS beamsteering strategies generally adopted in the literature. The work in this section was published in [20].

4.3   Leakage based UEs Selection

As mentioned before, applying HBF in mmWave systems guarantees MU transmission with low hardware requirements. ZF precoding can be utilized at the digital layer of the HBF to mitigate the IUI. However, due to the sparse nature of the mmWave channels, a ZF precoder may provide limited performance due to the highly correlated MU channel matrix. Thus, the aim of this section is to address the interference mitigation problem in the analog domain before handling it at the ZF digital level. SLNR based UEs selection algorithm is introduced for maximizing the SE of the system with low complexity requirements. We finally highlight by simulations the potential gains achieved by the introduced interference aware UEs selection approach.

4.3.1   Background

HBF focus mainly on serving multiple streams for SU or MU scenarios in the spatial domain. Many work in the literature recently focused on MU HBF [138, 139, 56] by decoupling the beamforming design problem into two problems in the analog and digital domains that can be addressed separately or jointly. In [56], the authors decouple the two problems and solve the analog problem using the LoS beamsteering to maximize the received signal by each UE. Then, in the digital part the MU interference is tackled through applying the ZF digital beamforming. This framework is crucial to consider at mmWave frequencies, due to the high LoS dominated channels and clustered UEs deployments planned for mmWave small cells leading to high spatial correlation of the MU channel. These high spatially correlated channel matrices turns out to be ill-conditioned for inversion, thus limiting the performance of the ZF beamforming.

It is then understood that UEs selection algorithms are crucial for mmWave HBF techniques that rely on ZF at the digital layer. A lot of works have been dedicated to UEs selection for fully digital ZF precoding [140, 141, 142]. In most of the contributions, the selection was mainly done based on the orthogonality of the channels of the selected UEs using linear algebraic approaches for the 'orthogonality' terminology. Other works translated the orthogonality metric into other simpler, yet similar metrics to relax the complexity constraints imposed in the orthogonality based algorithms such as: the angle between the subspaces [143, 144], also based on the chordal distance in [145] and based on the matrix determinant for representing the orthogonality in [146]. Complementary to 'orthogonality' based approaches, the authors in [147] introduced a statistical based terminology which is the 'spatial correlation' expressed by the condition number of the MU channel matrix. In this work, it was shown that imposing the condition number as the constraint in the Semi-orthogonal User Selection (SUS) algorithm [140] could improve the performance of the ZF beamformer. However, they didn't analyze analytically or even consider how to utilize the condition number probably as a UEs selection metric through

deriving a new algorithm instead of just imposing it as constraint in the SUS algorithm [140].

In this section, we introduce a novel UEs' selection algorithm for HBF systems relying on the condition number as a UEs selection metric. The condition number is chosen as our metric for evaluating the correlation between the UEs. The main idea of the proposed algorithm is to decrease the correlation of the MU channel matrix by choosing the UEs which have the lowest condition number of their mutual MU channel matrix. The introduced algorithm is derived analytically and compared with the baseline SUS technique [140]. We show that our approach is particularly adequate when applied to sparse channels such as mmWave channels, since the condition number can in that case be easily approximated. Accordingly, as proposed in this section, it is then possible to design a suboptimal yet efficient UEs selection algorithm based on maximizing the SLNR of the selected UEs. We show with complexity analysis and simulation results, the potentials of this sub-optimum approach in mmWave LoS dominated environments.

The contribution of this section can be summarized as follows:

- Interference aware analog layer: The main objective in this section is to involve the analog layer in HBF, in tackling the interference, unlike [56]. Due to the analog constraints forced on the analog domain, (specifically constant amplitude phase-shifters), the analog beamforming and/or power allocation solutions are not capable of taking into account the interference mitigation in the analog part. Henceforth, we choose the interference aware UEs selection approaches to address that problem in the analog domain, since it is not affected by the analog hardware constraints, yet it enhances the performance of the ZF precoding in the digital layer significantly as will be shown later in the simulation results.

- Analytically deriving novel condition number based UEs selection.

- Introducing a low complexity sub-optimum UEs selection algorithm based on the SLNR metric: Maximizing the SLNR has been utilized before for precoding [148] and power allocation [124] [19], serving as a low complexity approach for maximizing the SE of the system. However, up to the authors knowledge, it was not utilized for UEs selection before. Thus, in this section, we apply this metric for the UEs selection, since it acts as an attractive candidate for mmWave systems UEs selection problem.

4.3.2 System and Channel Model

In this section we consider a downlink MU MISO system with applying HBF at the BS side. The BS has a set of available UEs to serve denoted as $\mathcal{K}$, however it can serve a maximum number of UEs $|\mathcal{C}|$, where $\mathcal{C}$ is the set of the selected UEs to be served. The cardinality of the served set of UEs is limited to the number of RF chains available at the BS, such that $|\mathcal{C}| \leq N_{TRF}$. In the sequel, we assume $|\mathcal{C}| = N_{TRF}$, to achieve the maximum multiplexing and coverage gains (DoFs).

At the transmitter side HBF is applied, while at the receiver side each UE $k \in \mathcal{K}$ has only a single receive antenna and thus it can not apply combining schemes and can be served only by a single stream. The streams received by the set of selected UEs $\mathcal{C}$, $\mathbf{r} = [r_1, r_2, ..., r_{|\mathcal{C}|}]^T \in \mathbb{C}^{|\mathcal{C}| \times 1}$

are expressed as in Equation (2.45) and represented for readability as follows:

$$\mathbf{r} = \sqrt{P_T}\mathbf{H}\mathbf{F}^{RF}\mathbf{F}^{BB}\mathbf{s} + \mathbf{n} \tag{4.22}$$

The channel model considered in this section, is the sparse physical ray based model introduced in Subsection 2.2.4. Given that we consider MU MISO pure LoS channel with ULA at the BS and a single receive antenna at each UE k, the channel vector for each UE k was given in Equation (2.28) and represented here for readability as follows:

$$\mathbf{h}_k = \sqrt{N_T}\alpha_k\mathbf{a}_t(\phi^t{}_k)^H \tag{4.23}$$

Then, the MU channel $\mathbf{H}$ can be calculated as $\mathbf{H} = [\mathbf{h}_1^T, \mathbf{h}_2^T, ..., \mathbf{h}_K^T]^T$.

4.3.3 Beamforming Technique

In this section, we only consider HBF. We utilize the two stage HBF algorithm described in Algorithm 1, with using ZF for the BB precoder $\mathbf{F}^{BB}$ and LoS beamsteering for the RF precoder $\mathbf{F}^{RF}$.

4.3.4 UEs Grouping Strategies and Our Proposed Algorithm

Problem Formulation and Analytical Analysis

In this section we try to involve the analog domain in considering the interference/correlation between the selected UEs, since the analog beamforming do not handle this task and relies on the digital precoding stage. This is achieved through applying spatial correlation minimization (interference aware) UEs selection.

Problem Formulation for Digital ZF:
Given a digital ZF precoding system is considered, the sum SE maximization problem is formulated as follows:

$$\mathcal{C} = \underset{\mathcal{C}}{\arg\max} \log_2 \left(\det \left(\mathbf{I}_{|\mathcal{C}|} + \frac{\rho}{|\mathcal{C}|\beta_{\mathcal{C}}} |\mathbf{H}_{\mathcal{C}}\mathbf{F}^{BB}{}_{\mathcal{C}}|^2 \right) \right) \tag{4.24}$$

where $\beta_{\mathcal{C}}$ represents the ZF normalization factor for the subset of selected UEs $\mathcal{C}$. Applying ZF as the digital precoding ensures that $|\mathbf{H}_{\mathcal{C}}\mathbf{F}^{BB}{}_{\mathcal{C}}| = \mathbf{I}_{|\mathcal{C}|}$. Thus, the problem can be dually approached as choosing the optimal set of UEs $\mathcal{C}$ that minimizes the normalization factor $\beta_{\mathcal{C}}$.

The normalization factor for digital ZF precoder $\beta_{\mathcal{C}}$ is calculated as follows [149]:

$$\beta_{\mathcal{C}} = \sum_{k=1}^{|\mathcal{C}|} \frac{1}{\lambda_k} \tag{4.25}$$

where λ_k represent the $k-$th eigenvalue of the propagation channel $\mathbf{H}_{\mathcal{C}}$.

Problem Formulation for HBF (LoS Beamsteering - ZF):
Here we reformulate the problem of the sum SE maximization given the analog beamformers

are already calculated and the equivalent channel $\hat{\mathbf{h}}_k$ is available at the BS for each UE k. Then formulating the problem as in Equation (4.24), with expressing the constraint $\|\mathbf{F}^{RF}\mathbf{F}^{BB}\|_F^2 = |\mathcal{C}|$ in the objective function and solving it for the best UEs set to be selected for maximizing the SE can be written as:

$$\mathcal{C} = \underset{\mathcal{C}}{\operatorname{argmax}} \ \log_2 \left(\det \left(\mathbf{I}_{|\mathcal{C}|} + \frac{\rho}{|\mathcal{C}|\beta_{\mathcal{C}}} |\hat{\mathbf{H}}_{\mathcal{C}}\mathbf{F}_{\mathcal{C}}|^2 \right) \right) \tag{4.26}$$

Lemma 3. *The normalization factor for HBF based on LoS beamsteering in the analog domain and ZF precoder in the digital domain in a pure LoS channel, with assuming that the channel amplitudes α are normalized, $\beta_{\mathcal{C}}$ is calculated as follows:*

$$\beta_{\mathcal{C}} = \sum_{k=1}^{|\mathcal{C}|} \frac{1}{\lambda_k} \tag{4.27}$$

Proof. The assumption that α is normalized is just taken into account in the derivation, since in pure LoS it just applies linear scaling for the steering vectors of the UEs. The normalization factor for HBF (LoS beamsteering - ZF) can be analyzed as follows:

$$\beta_{\mathcal{C}} = \mathbb{E}(Tr((\mathbf{F}^{RF}{}_{\mathcal{C}})^H (\mathbf{F}^{BB}{}_{\mathcal{C}})^H \mathbf{F}^{RF}{}_{\mathcal{C}}\mathbf{F}^{BB}{}_{\mathcal{C}})) \tag{4.28}$$

Given the fact that the ZF precoder $\mathbf{F}^{BB}{}_{\mathcal{C}}$ is applied on the equivalent channel $\hat{\mathbf{H}}$, and given that the SVD of the equivalent channel is $\hat{\mathbf{H}} = \mathbf{U}_e\mathbf{D}_e\mathbf{V}_e^H$. Henceforth, it can be deduced that:

$$\beta_{\mathcal{C}} = \mathbb{E}(Tr((\mathbf{F}^{RF}{}_{\mathcal{C}})^H \mathbf{F}^{RF}{}_{\mathcal{C}}\mathbf{D}_e^{-2})) \tag{4.29}$$

Again, due to the fact that the SVD of the propagation channel is $\mathbf{H} = \mathbf{U}\mathbf{D}\mathbf{V}^H$, and that the RF beamforming matrix in this specific case (pure LoS channel with the LoS beamsteering approach and normalizing α) $\mathbf{F}^{RF} = \frac{\mathbf{H}^H}{\sqrt{N_T}}$. Thus,

$$\begin{aligned} \mathbb{E}\{Tr((\mathbf{F}^{RF})^H \mathbf{F}^{RF}\mathbf{D}_e^{-2}) &= \mathbb{E}\left\{ Tr\left(\frac{1}{N_T}\mathbf{H}\mathbf{H}^H\mathbf{D}_e^{-2} \right) \right\} \\ &= \mathbb{E}\left\{ Tr\left(\frac{1}{N_T}\mathbf{D}^2\mathbf{D}_e^{-2} \right) \right\} \\ &= \frac{\sum_{k=1}^{|\mathcal{C}|} \frac{\lambda_k^{\mathbf{H}}}{\lambda_k^{\hat{\mathbf{H}}}}}{N_T} \end{aligned} \tag{4.30}$$

Where $\lambda_k^{\mathbf{H}}$ and $\lambda_k^{\hat{\mathbf{H}}}$ represent the $k-$th eigenvalue of the channel and the equivalent channel respectively. In this specific scenario (pure LoS environment with LoS beamsteering) the eigenvalues of the equivalent channel are related to the eigenvalues of the channel as follows:

$$\lambda_k^{\hat{\mathbf{H}}} = \frac{(\lambda_k^{\mathbf{H}})^2}{N_T} \tag{4.31}$$

Thus, substituting Equation (4.31) in (4.30), the normalization factor is represented as follows:

$$\beta_{\mathcal{C}} = \sum_{k=1}^{|\mathcal{C}|} \frac{1}{(\lambda_k^{\mathbf{H}})} = \sum_{k=1}^{|\mathcal{C}|} \frac{1}{\lambda_k} \tag{4.32}$$

∎

Thus, it is clear that in both digital and HBF cases, the sum SE is controlled by the propagation channel's eigenvalues. Therefore, the sum SE maximization problem can be reformulated, for a constant number of selected UEs $|\mathcal{C}| = N_{TRF}$ as follows:

$$\mathcal{C} = \underset{\mathcal{C}}{\operatorname{argmin}}\ \beta_{\mathcal{C}} \tag{4.33}$$

Condition Number based UEs Selection

The normalization factor of the HBF $\beta_{\mathcal{C}}$ is limited by the minimum eigenvalue of the propagation channel matrix $\mathbf{H}_{\mathcal{C}}$ or equivalently the minimum eigenvalue of the equivalent channel $\hat{\mathbf{H}}_{\mathcal{C}}$ from Equations (4.27) and (4.31). Therefore, the problem in Equation (4.33) can be reformulated again as maximizing the minimum eigenvalue of the equivalent channel as follows:

$$\mathcal{C} = \underset{\mathcal{C}}{\operatorname{argmax}}\ \lambda_{min} \tag{4.34}$$

where λ_{min} is calculated as $\lambda_{min} = \min\{\lambda_1, ..., \lambda_{|\mathcal{C}|}\}$. Consequently, this can be directly translated to minimizing the condition number ι of the MU equivalent channel $\hat{\mathbf{H}}_{\mathcal{C}}$ as follows:

$$\mathcal{C} = \underset{\mathcal{C}}{\operatorname{argmin}}\ \iota(\hat{\mathbf{H}}_{\mathcal{C}}) \tag{4.35}$$

such that the condition number $\iota(\hat{\mathbf{H}}_{\mathcal{C}})$ is calculated as:

$$\iota(\hat{\mathbf{H}}_{\mathcal{C}}) = \sqrt{\frac{\lambda_{max}}{\lambda_{min}}} \tag{4.36}$$

where λ_{max} is the maximum eigenvalue of the equivalent channel and is calculated as $\lambda_{max} = \max\{\lambda_1, ..., \lambda_{|\mathcal{C}|}\}$

Proposed Algorithm:

After formulating the problem to minimizing the condition number of the MU equivalent channel $\iota(\hat{\mathbf{H}}_{\mathcal{C}})$, here we propose an algorithm to select the UEs based on this objective.

Initially, the first selected UE in the set $\mathcal{C}$ is the UE that has the maximum equivalent channel norm $\left\|\hat{\mathbf{h}}_k\right\|$. Then the algorithm iterates with maximum number of iterations (maximum number of UEs selected) equals to the number of the RF chains N_{TRF}.

Within each iteration i a filtration process is done to filter the UEs and find the candidate set $\mathcal{T}_i$ based on a certain correlation threshold, defined by a threshold condition number $\gamma \geq 1$.

This threshold γ represents a trade-off parameter between the UEs diversity gain which can be maximized in case $\gamma \to \inf$ and the low MU correlation gain maximized in case $\gamma \to 1$. In this section we consider serving $|\mathcal{C}| = N_{TRF}$ UEs, thus we set $\gamma \to \inf$. However, we introduce the threshold β here for completeness and generic introduction of the algorithm. Then, in each iteration the selected UE k is selected such that to minimize the condition number of the UE equivalent channel together with the previously selected UEs in the previous iterations $\mathcal{C}_{i-1}$ as follows:

$$k = \operatorname*{argmin}_{k \in \mathcal{T}_{i-1}} \iota(\hat{\mathbf{H}}_{\mathcal{C}_{i-1} \cup k}) \tag{4.37}$$

The proposed algorithm is summarized in Algorithm (3).

Algorithm 3 Condition Number Based Selection

---

1) **Initialize** $i = 1$, $\mathcal{C}_0 = []$, $\mathcal{T}_0 = \mathcal{K}$, $\gamma \geq 1$
2)   **While** $(i \leq \min(|\mathcal{T}_{i-1}|,\ N_{TRF}))$ **do**
3)   **if** (i=1)
4)   **find**

$$k = \operatorname*{argmax}_{k \in \mathcal{T}_{i-1}} \left\| \hat{\mathbf{h}}_k \right\|$$

5)   **else**
        find

$$k = \operatorname*{argmin}_{k \in \mathcal{T}_{i-1}} \iota(\hat{\mathbf{H}}_{\mathcal{C}_{i-1} \cup k})$$

6)   **end if**
7) $\mathcal{C}_i = \mathcal{C}_{i-1} \cup k$
8) $\mathcal{T}_i = \{j \in \mathcal{T}_{i-1},\ j \notin \mathcal{C}_i,\ \iota(\hat{\mathbf{H}}_{j \cup \mathcal{C}_i}) < \gamma \}$
9) $i = i + 1$
10) **end**

Complexity Analysis

In order to evaluate the proposed algorithm and have a fair comparison with the other UEs selection algorithms, we analyze the worst case (upper bound) computational complexity. The computational complexity analysis is based on the maximum number of SVDs needed in our algorithm, since SVD is the most complex operation applied in the proposed algorithm with a complexity of $\mathcal{O}(nm^2 + n^3)$ for an $m \times n$ matrix. Henceforth, the computational complexity in the worst case (in case $\gamma \to \inf$) is of the order $\mathcal{O}(|\mathcal{K}| N_{TRF}{}^3)$, given that $\mathcal{K}$ is the set of all the UEs and N_{TRF} is the number of the transmit RF chains.

Semi-Orthogonal UEs Selection

Algorithm Description:

In this subsection we briefly describe the SUS algorithm proposed in [140, 141], which we use as a baseline for our introduced UEs selection algorithms.

Table 4.4: Computational Complexity of the proposed Algorithms

Condition Number	SUS [140]	Simple SUS [141]	SLNR [124]
$\mathcal{O}(|\mathcal{K}|L^3)$	$\mathcal{O}(|\mathcal{K}|N_{TRF}{}^3)$	$\mathcal{O}(|\mathcal{K}|N_{TRF}{}^2)$	$\mathcal{O}(|\mathcal{K}|N_{TRF})$

Initially, the first UE selected in the set $\mathcal{C}$ is the one with the maximum equivalent channel norm $\left\|\hat{\mathbf{h}}_k\right\|$. Within each iteration i a filtration process is done to filter the UEs and find the candidate set $\mathcal{T}_i$ based on a certain orthogonality threshold $\Omega \in [0, 1]$ as follows:

$$\mathcal{T}_i = \left\{ j \in \mathcal{T}_{i-1}, j \notin \mathcal{C}_i, \frac{|\hat{\mathbf{h}}_j \mathbf{V}_{i-1}^0 (\mathbf{V}_{i-1}^0)^H \hat{\mathbf{h}}_k^H|}{\|\hat{\mathbf{h}}_j\| \|\hat{\mathbf{h}}_k \mathbf{V}_{i-1}^0\|} \right\} < \Omega \tag{4.38}$$

where $\mathbf{V}_{i-1}^0$ is a matrix, which its columns form an orthonormal basis for the null space of the equivalent channel $\hat{\mathbf{H}}_{\mathcal{C}_{i-1}}$ at the iteration $i-1$ and is obtained from the SVD of $\hat{\mathbf{H}}_{\mathcal{C}_{i-1}}$ as follows:

$$\hat{\mathbf{H}}_{\mathcal{C}_{i-1}} = \mathbf{U}_{i-1} \mathbf{D}_{i-1} [\mathbf{V}_{i-1}^1 \mathbf{V}_{i-1}^0]^H \tag{4.39}$$

In case $\Omega = 0$, this represents full (strict) channel orthogonality scenario, and increasing Ω relaxes the channel orthogonality constraint. Again, throughout the section we use only the full multiplexing case ($\Omega = 1$). Then, in each iteration the selected UE k is the one with the maximum channel component orthogonal on the subspace spanned by the interference (previously selected UEs $\mathcal{C}_{i-1}$) as follows:

$$k = \underset{k \in \mathcal{T}_{i-1}}{\operatorname{argmax}} \left\|\hat{\mathbf{h}}_k \mathbf{V}_{i-1}^0\right\| \tag{4.40}$$

The SUS algorithm is summarized in Algorithm (4).

Algorithm 4 Semi-Orthogonal Users Selection [140, 141]

---

1) **Initialize** $i = 1$, $\mathbf{V}_0^0 = \mathbf{I}$, $\mathcal{C}_0 = []$, $\mathcal{T}_0 = \mathcal{K}$, $\Omega \in [0, 1]$
2) **While** $(i \leq \min(|\mathcal{T}_{i-1}|, N_{TRF}))$ **do**
3)   **find**

$$k = \underset{k \in \mathcal{T}_{i-1}}{\operatorname{argmax}} \left\|\hat{\mathbf{h}}_k \mathbf{V}_{i-1}^0\right\|$$

4) $\mathcal{C}_i = \mathcal{C}_{i-1} \cup k$
5) $\mathbf{V}_i^0 = \mathcal{P}_\perp(\hat{\mathbf{H}}_{\mathcal{C}_i})$ as in Equation (4.39)
6) $\mathcal{T}_i = \left\{ j \in \mathcal{T}_{i-1}, \ j \notin \mathcal{C}_i, \ \frac{|\hat{\mathbf{h}}_j \mathbf{V}_{i-1}^0 (\mathbf{V}_{i-1}^0)^H \hat{\mathbf{h}}_k^H|}{\|\hat{\mathbf{h}}_j\| \|\hat{\mathbf{h}}_k \mathbf{V}_{i-1}^0\|} \right\} < \Omega$
7) $i = i + 1$
8) **end**

Complexity Analysis:

Similar to the aforementioned condition number based UEs selection algorithm, here we also analyze the computational complexity of the SUS algorithm based on the number of SVDs needed in the worst case scenario (upper bound - in case $\Omega = 1$). In this case the computational complexity is also of order $\mathcal{O}(|\mathcal{K}|N_{TRF}{}^3)$ [141]. However, in [141] a simplified, yet equivalent, SUS algorithm was introduced that avoids applying SVD decomposition and requires an upper bound total number of flops expressed as $12|\mathcal{K}|N_{TRF}{}^2 + 8N_{TRF}{}^3 + 7|\mathcal{K}|N_{TRF} - |\mathcal{K}| - 17N_{TRF}{}^2$, henceforth the computational complexity for the simplified SUS in [141] can be represented of order $\mathcal{O}(|\mathcal{K}|N_{TRF}{}^2)$.

Maximum SLNR Based Selection

Given the fact that all the previously studied algorithms have high computational complexity, which limits the practical implementation of such algorithms in a realistic mmWave system, specifically in the analog part which has limited DSP resources. Henceforth, the SLNR metric can be utilized as a sub-optimum low complexity approximation of the condition number UEs selection, since it encounters both maximizing the signal and minimizing the leakage (correlation) objectives.

Proposed Algorithm:

The SLNR metric ζ for a given UE k in the analog domain is defined as follows:

$$\zeta_k = \frac{|\mathbf{h}_k \mathbf{f}^{RF}{}_k|^2}{\sum_{i \neq k}|\mathbf{h}_i \mathbf{f}^{RF}{}_k|^2 + \sigma_n^2} \tag{4.41}$$

Then, the SLNR maximization UEs selection is explained in Algorithm (5), and the computational complexity of this algorithm can be determined in analogy with [124] and [19] of order $\mathcal{O}(|\mathcal{K}|N_{TRF})$.

Maximum Received Signal Based Selection

This maximum received signal UEs selection is considered the basic baseline UEs selection approach throughout the section. In this approach, the UEs with the highest received signal power are selected without considering the interference (leakage/correlation) between the selected UEs. Thus, decoupling the UEs selection from the interference management problem and relying on ZF for nulling the IUI at the digital layer. Therefore, this strategy aims at maximizing the SNR of the selected UEs. Thus, the maximum received signal algorithm is similar to the maximum SLNR one explained in Algorithm (5) with replacing Step (5) to be similar to Step (4), which is:

$$k = \operatorname*{argmax}_{k \in \mathcal{T}_{i-1}} \left\| \hat{\mathbf{h}}_k \right\| \tag{4.42}$$

4.3.5   Numerical Analysis

In this subsection, we evaluate the performance of the introduced UEs selection algorithms in terms of the SE based on the simulation parameters summarized in Table (4.5).

Algorithm 5 SLNR Based Selection
---
1) **Initialize** $i = 1, \mathcal{C}_0 = [], \mathcal{T}_0 = \mathcal{K}$

2)   **While** $(i \leq N_{TRF})$ **do**

3)   **if** (i=1)

4)   **find**

$$k = \operatorname*{argmax}_{k \in \mathcal{T}_{i-1}} \left\| \hat{\mathbf{h}}_k \right\|$$

5)   **else**

      find

$$k = \operatorname*{argmax}_{k \in \mathcal{T}_{i-1}} \frac{|\mathbf{h}_k \mathbf{f}^{RF}{}_k|^2}{\sum_{i \in \mathcal{C}_{i-1}} |\mathbf{h}_i \mathbf{f}^{RF}{}_k|^2 + \sigma_n^2}$$

6)   **end if**

7) $\mathcal{C}_i = \mathcal{C}_{i-1} \cup k$

8) $\mathcal{T}_i = \{ j \in \mathcal{T}_{i-1}, j \notin \mathcal{C}_i \}$

9) $i = i + 1$

10) **end**

We compare between the different introduced UEs selection algorithms in terms of SE and complexity. As we observe in Table 4.4 that maximum SLNR algorithm has the lowest computational complexity in the introduced interference aware UEs selection algorithms. Thus, it is the most favorable one in terms of complexity and realistic implementation.

In Figure 4.8-1, we evaluate the normalization factor $\beta_\mathcal{C}$ in a given scenario ($N_T = 16$, and angular spread $\Delta\phi^t = \frac{\pi}{3}$). It is shown that both SUS and condition number based UEs selection achieve the lower bound of the normalization factor. This normalization factor's lower bound is calculated twice, once using the exhaustive search on the sum SE in Equation (4.26) and another time using the exhaustive search on the eigenvalues equivalent bound in Equation (4.27). Also, we can observe that the SLNR algorithm achieves sub-optimal normalization factor with median difference of ≈ 0.5 dB with the lower bound, while the maximum signal algorithm and the Round Robin (RR) ones have a significant performance degradation.

In Figure 4.8-2, we realize the effect of the normalization factor on the per stream SE in the same scenario ($N_T = 16$, $\Delta\phi^t = \frac{\pi}{3}$), we can observe again that, both SUS and condition number UEs selection achieve the upper bound of the SE, while maximum SLNR achieves suboptimal SE with only 0.5 bps/Hz difference to the SE upper bound at SNR $\rho = 19$ dB. However, interference non-aware algorithms such as maximum signal and RR suffer from a significant SE loss.

In Figures 4.9-1 and 4.9-2, we generalize the simulation scenarios to have generic insights about the performance of the introduced algorithms in various channel environments. In Figure 4.9-1, the SNR is fixed $\rho = 10$ dB and the angular spread $\Delta\phi^t = \frac{\pi}{3}$, while the number of transmit antennas is varied $N_T = \{16, 32, 64, 128\}$. It is shown that, with increasing the number of transmit antennas, the spatial correlation/interference decreases, due to the higher spatial resolution at the transmitter side. Thus, enhancing the performance of non-interference aware algorithm (Maximum received signal algorithm) significantly, from 1.5 bps/Hz difference

Table 4.5: Simulation Parameters

Parameter	Value
Number of Propagation Paths	1 Ray (Pure LoS)
Simulation Type	Monte Carlo (1000 realizations)
Transmit Array Architecture	ULA
Inter-antenna spacing	$\frac{\lambda}{2}$
Number of Transmit RF Chains	3
Total UEs, Receive Antennas	7, 1
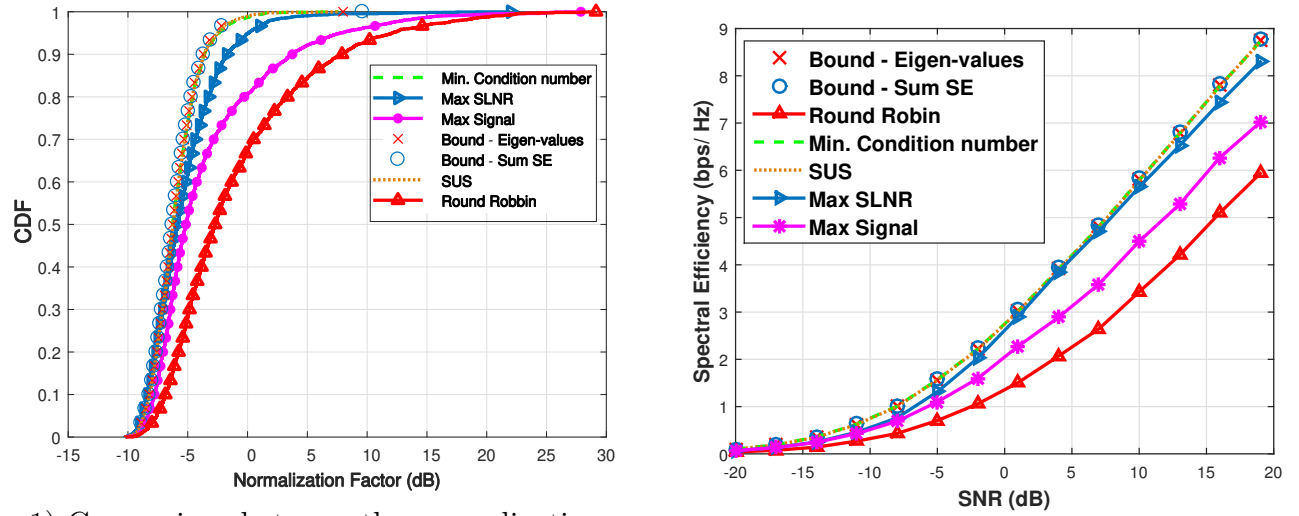
1) Comparison between the normalization factor for the different UEs selection strategies introduced in a pure LoS environment given that $N_T = 16$, $|\mathcal{K}| = 7$, $|\mathcal{C}| = 3$, and $\Delta\phi^t = \frac{\pi}{3}$.

2) Comparison between the per stream SE for the different user selection strategies introduced in a pure LoS environment given that $N_T = 16$, $|\mathcal{K}| = 7$, $|\mathcal{C}| = 3$, and $\Delta\phi^t = \frac{\pi}{3}$.

Figure 4.8: Comparison between the normalization factor and the per stream SE for the different UEs selection strategies introduced in a pure LoS environment.

with the SE upper bound at $N_T = 16$ to 0.2 bps/Hz difference at $N_T = 128$.

In Figure 4.9-2, the SNR is fixed $\rho = 10$ dB and the number of transmit antennas $N_T = 16$, while the angular spread is varied $\Delta\phi^t = \{\frac{\pi}{3}, \frac{\pi}{2}, \frac{3\pi}{2}, 2\pi\}$. It is shown that, with increasing the angular spread, the spatial correlation/interference decreases, due to the higher angular separation between the UEs. Thus, enhancing the SE performance of non-interference aware algorithm (Maximum received signal algorithm) significantly, from 1.5 bps/Hz difference with the SE upper bound at $\Delta\phi^t = \frac{\pi}{3}$ to 0.4 bps/Hz difference at $\Delta\phi^t = 2\pi$.
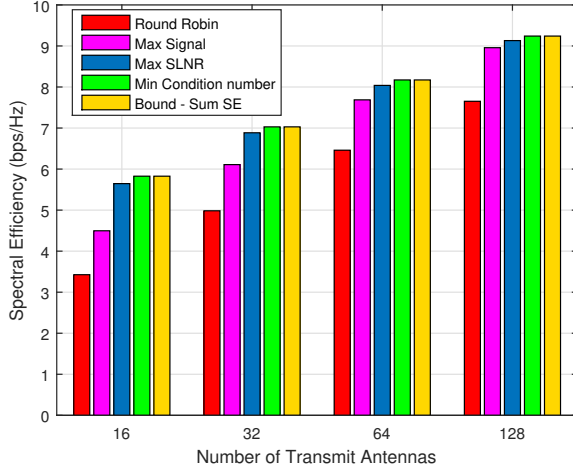
1) Comparison between the per stream SE for the different user selection strategies introduced in a pure LoS environment with different spatial correlation given different number of transmit antennas with fixed angular spread
$\Delta\phi^t = \frac{\pi}{3}, \rho = 10\text{dB}, |\mathcal{K}| = 7, |\mathcal{C}| = 3.$
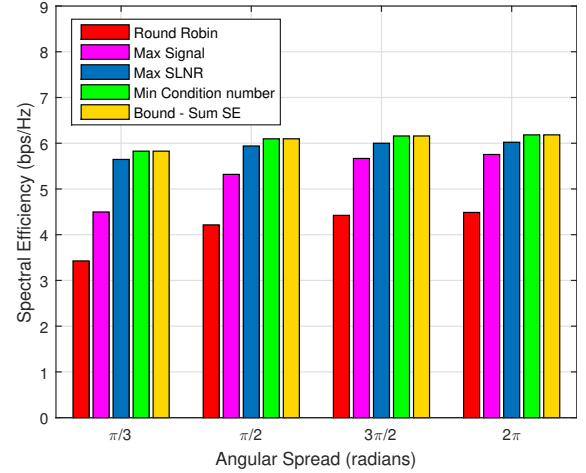
2) Comparison between the per stream SE for the different UEs selection strategies introduced in a pure LoS environment with different spatial correlation given different angular spread with fixed number of transmit antennas
$N_T = 16, \rho = 10\text{dB}, |\mathcal{K}| = 7, |\mathcal{C}| = 3.$

Figure 4.9: Comparison between the per stream SE for the different user selection strategies introduced in a pure LoS environment.

4.3.6 Conclusion

In this section we provided a detailed study on the UEs selection topic with HBF in mmWave systems. We proved that in highly correlated environments, due to clustered UEs deployments and average number of transmit antennas, interference aware UEs selection is crucial and achieves considerable gains over non aware UEs selection approach based on maximizing the received signals. However, in perfect channel conditions (massive transmit antennas and large angular spreads), selecting the UEs based on their received signal strength can be sufficient.

We derived analytically an optimum interference aware UEs selection based on the condition number of the MU channel and then we provided a sub-optimal low complexity (realistic) UEs selection approach based on SLNR maximization. We proved with simulation results that the maximum SLNR algorithm is a potential candidate for the future mmWave systems achieving a trade-off between high SE performance and low complexity. The work in this section was published in [21].

Chapter 5

HBF with Index Modulation

Contents

5.1 HBF with Receive Spatial Modulation

Receive Spatial Modulation(RSM) is expected to be a low complexity solution for the future Internet of Things (IoT) receivers, that achieve reduced BER. Also, mmWave frequencies have paved the road to achieve high peak data rates. mmWave channels are characterized by being LoS dominated. Moreover, due to the high carrier frequencies at mmWave systems, massive antenna arrays can be deployed at the transmitter or the receiver with much less RF chains through Hybrid Beamforming.

In this section we utilize the aforementioned characteristics of mmWave systems to design a robust and spectral efficient RSM system. Moreover, we analytically derive the optimal achieved SE and BER in case the receiver is employed with two receive antennas in a LoS environment. Also, we analytically derive the achieved BER in a general multi-path channel environment for the sake of complete analysis. The analysis are done for a SU MIMO system, with HBF at the transmitter utilizing massive MIMO array with only two RF chains, thus unleashing the gains that can be achieved by RSM in realistic mmWave system with minimal hardware complexity.

5.1.1 Background

Spatial Modulation(SM) is a recent low complexity-energy efficient paradigm that evolved to support communication nodes with limitations on power consumption and complexity [150] such as IoT. SM deals with the index of the transmit or receive antennas to transmit spatial information bits additional to classical IQ modulated signal [151].

Space Shift Keying (SSK) [152] has evolved as one of the primary SM techniques at the transmitter side, that aims at leveraging the multi-path propagation of the channel associated to the different antennas [153]. SSK is combined with single-stream transmission which decreases the hardware complexity and power consumption significantly at the transmitter [154]. In this technique, the information is mapped to the index of transmit antenna. On the other side, when the information is mapped to the index of receive antenna, the technique is called RSM.

A specific RSM approach was introduced in [155] named RASK. The transmitted information is mapped to the index of the receive antenna. In this approach the signal energy is focused towards a targeted antenna, thus a single antenna is targeted at a time, while no useful information are transmitted in the IQ mapping stage. The RASK detection is simply done by comparing the real part of the received signal power for each receive antenna, henceforth, decreasing the complexity significantly at the receiver side [156]. Note that for other RSM techniques, additional IQ symbols could be transmitted with the transmitted signal.

Henceforth, due to all the aforementioned characteristics of RSM, it is shown that combining RSM with HBF in mmWave systems is a win-win approach. Given the fact that mmWave systems suffer from high power consumption, high hardware cost and sensitivity to complex computations, RSM is crucial for mmWave mobile receivers in the downlink scenario in order to achieve high SE with low BER and low energy consumption/hardware complexity. Henceforth, providing a solution for practical mmWave based Mobile UEs at low cost and low power consumption.

Recently, a lot of work started to consider a framework combining both SM and mmWaves for the aforementioned reasons [157]. In [158, 159, 160, 161, 162] the authors considered SM in mmWave systems with non beamforming schemes. Hence, the array gains were not leveraged and the path-loss effect at mmWave frequencies were dominant. In [160], capacity analysis for Quadrature Spatial Modulation (QSM) in mmWave MIMO system was carried out. In [158], SSK is evaluated in LoS conditions. Moreover, in [159, 162] SM and Generalized Spatial Modulation (GenSM) were utilized for indoor LoS mmWave environment. In [161] Variable N_u GenSM was presented as an extension for GenSM with fixed N_u which uses less number of transmit antennas to achieve the same data rate and thus beneficial for mmWave LoS systems. All of the aforementioned work did not consider beamforming and just focused on the proof of concept that SM can work in mmWave channels.

More recent analysis for SM in mmWave [163, 164, 165, 149, 166, 167] started to take into account beamforming aided solutions to cope with the high path-loss at such frequencies. As a first step, analog beamforming was considered, since it is a practical solution for mmWave MIMO systems due to its low power consumption and low hardware complexity. In [163, 164] the authors introduced the Multi-Set Space-Time Shift Keying (MS-STSK) and Multi Space-Frequency pace-Time Shift Keying (MSF-STSK) paradigms for space-time and space-frequency shift keying in mmWave MIMO channels with analog beamsteering. In [165] GenSM based mmWave MIMO is introduced with leveraging the gains of analog beamforming. In [166] adaptive SM with spatial signature design was introduced for up-link mmWave communication. Also, in [149] the performance of the RSM in mmWave scenario was studied in a special deployment scenario in which no interference exists between the spatial streams targeting different receive antennas. Thus, only analog beamforming is utilized. Finally, in [167] BIM was presented as a novel paradigm that aims to map each symbol to a beam instead of the antenna index, this paradigm will be extensively explained in the next section of this chapter.

More recent work in the literature of SM mmWave systems [168, 169, 170, 171, 172] started to consider hybrid beamforming over analog one, driven by the fact that it can mitigate the correlation/interference between the spatial streams together with achieving acceptable hardware complexity and power consumption. In [168] the authors introduced Analog Precoding-Aided Virtual Space Modulation (APAVSM) and further extended their design for HBF by presenting multimode hybrid precoder designs. HBF extension for GenSM was proposed in [169, 171]. SSM [170] was introduced to map each symbol to a scatterer index instead of the antenna index for sparse multi-path mmWave channels with utilizing HBF. Finally in [172], the BIM paradigm was extended to utilize HBF.

Apart from the previous exhaustive list of references, where most of them consider transmit SM, in which the transmit array gain is not leveraged completely, we consider RSM in this
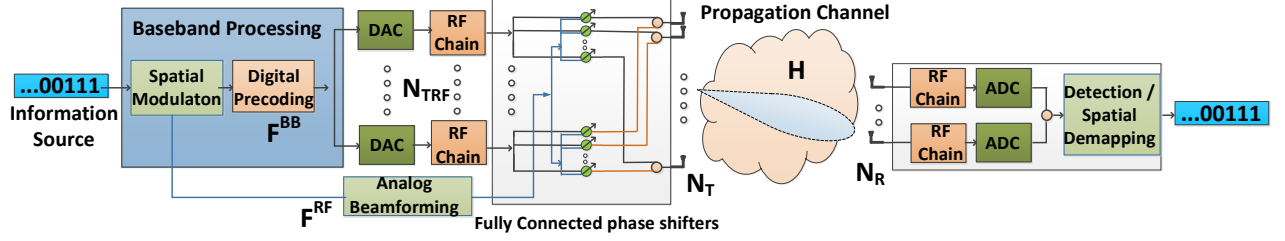
Figure 5.1: Block diagram of RASK with mmWave HBF architecture.

section in order to fully utilize the transmit array gain. Mainly the work in [149] is considered a valuable reference that considered the RSM system in a mmWave channel which is a pure deterministic LoS one, (not rician or sparse) which is considered bottle neck scenario for SM in general, which depends on the richness of the channel. The authors in [149] proved that under specific deployment conditions RSM mmWave MIMO system can work in pure LoS channel even with analog beamforming only. Therefore, we focus on extending the work in [149] which is considered up to our knowledge the main baseline for RSM with transmit beamforming in mmWave MIMO channels in the current literature.

In this section, we present a novel framework considering the RASK RSM technique with transmit HBF at mmWave pure LoS propagation environment. In [149] the results are considered impractical and incomplete, since they consider a specific deployment scenario for interference mitigation. However, in realistic deployments, this condition is less likely to hold. Therefore, in this section in order to be more complete, we cover all possible deployment scenarios in deterministic pure LoS channel. Also, we extend the analog beamforming to be a hybrid one, in order to consider mitigating the interference (cross-talk) between the spatial streams in practical deployments to avoid wrong beam detection at the receiver side. Moreover, we consider the general multi-path channel environment for the RSM together with the LoS only analysis in order to have a complete and practical framework for HBF RSM system that can hold for the mmWave systems or even the microwave ones as well. The achievable SE is analytically and numerically studied for pure LoS channels and for multipath channels. Moreover, the BER performance of the proposed framework is analytically and numerically studied with maximum likelihood detector.

5.1.2 System Model

In this subsection, we first set up the model for a communication system utilizing the RASK scheme over a flat fading channel. Then, we introduce the precoding scheme carried out to form the spatial symbols and transmit the IQ symbols, together with introducing the beamforming architectures used within our framework.

In our framework a MIMO system equipped with N_T transmit antennas and N_R receive antennas is considered. According to the $N_T \times N_R$ multiple-antenna system architecture, the

RASK system can be modeled using the following matrix based input-output signal expression

$$\mathbf{r} = \mathbf{\Upsilon} \mathbf{H} \underbrace{\mathbf{F s}}_{\mathbf{x}} + \mathbf{n}, \tag{5.1}$$

where $\mathbf{H} \in \mathbb{C}^{N_R \times N_T}$ is the MIMO flat fading channel matrix with elements $h_{j,i}$ representing the complex channel gain between the ith transmit antenna, denoted T_i, and the jth receive antenna, denoted R_j. $\mathbf{x} \in \mathbb{R}^{N_T \times 1}$ is the vector of samples transmitted through the N_T transmit antennas and intended to focus the signal towards the receive antenna R_k. $\mathbf{r} \in \mathbb{C}^{N_R \times 1}$ is the vector of the received signals on all receive antennas and $\mathbf{n} \in \mathbb{C}^{N_R \times 1}$ is the vector of AWGN) samples. Spatial focusing is obtained through the beamforming matrix $\mathbf{F} \in \mathbb{C}^{N_T \times N_R}$ which will be explained into more details later. The beamforming matrix $\mathbf{F}$ transforms the vector of spatial symbols $\mathbf{s}$ into the vector of transmitted samples $\mathbf{x}$. Finally, $\mathbf{\Upsilon} = \mathrm{diag}(\mathbf{\Upsilon}_1, ..., \mathbf{\Upsilon}_{N_R})$ is a diagonal scaling matrix.

Receive Spatial Modulation

The spatial symbols accompanied with the IQ symbol $\mathbf{s}_{IQ,k}$ where k is the index of the antenna that should be targeted according to the spatial mapping, are formed such that the entries $\mathbf{s}_k(j)$ of $\mathbf{s}_k$ verify $\mathbf{s}_k(j) = \mathbf{s}_{IQ,k}$ for $j = k$ and $\mathbf{s}_k(j) = 0$, $\forall j \neq k$,

The block diagram of the RASK system is depicted in Figure 5.1. A group of $m = \log_2(N_R)$ bits are additionally mapped to a spatial symbol $\mathbf{s}_k$ which is written as

$$\mathbf{s}_k = \begin{bmatrix} 0 & ... & \underbrace{\mathbf{s}_{IQ,k}}_{k-thposition} & ... & 0 \end{bmatrix}^T$$

given that k is the position of the targeted antenna related to the symbol that should be transmitted as aforementioned. Then, the beamforming matrix $\mathbf{F}$ transforms the vector of symbols $\mathbf{s}$ into a vector of transmitted signals denoted as $\mathbf{x} \in \mathbb{C}^{N_T \times 1}$. At the receiver side, the RASK receiver has to detect the targeted antenna among the N_R receive antennas in order to estimate the transmitted spatial symbol.

Scaling Factor

The framework presented and studied in this section is based on HBF architecture. The hybrid beamformer is represented as: $\mathbf{F}^{HBF} = \mathbf{F}^{RF}\mathbf{F}^{BB}$, where $\mathbf{F}^{BB} \in \mathbb{C}^{N_{TRF} \times N_R}$ represents the digital precoder and $\mathbf{F}^{RF} \in \mathbb{C}^{N_T \times N_{TRF}}$ denotes the analog beamformer, given that N_{TRF} represents the number of available RF chains at the transmitter. The number of the spatial streams to be supported equals the number of receive antennas N_R.

The power normalization is insured for the average transmit power for fairness of detection for RSM, given that the scaling factor is calculated as follows:

$$\Upsilon_i = \frac{1}{\sqrt{\mathbb{E}_{\mathbf{s}} \left\{ \mathrm{Tr} \left(\left(\mathbf{F}^{RF} \mathbf{F}^{BB} \mathbf{s}_i \right)^H \mathbf{F}^{RF} \mathbf{F}^{BB} \mathbf{s}_i \right) \right\}}} \tag{5.2}$$

where $\mathbb{E}_\mathbf{s}$ stands for the expectation over $\mathbf{s}$. For such normalization, all the entries are equal and the normalization matrix $\mathbf{\Upsilon}$ is reduced to a scalar Λ.

5.1.3   Channel Model

The channel model considered in this section, is the sparse physical ray based model introduced in Subsection 2.2.4. Given that a ULA transmit array is deployed at the BS, the channel vector for each receive antenna R_k can be expressed as in Equation (2.23) as follows:

$$\mathbf{h}_k = \sqrt{\frac{N_T}{N_p^{\,k}}} \sum_{p=1}^{N_p^{\,k}} \alpha_{k,p} \mathbf{a}_t(\phi^t_{\,k,p})^H \tag{5.3}$$

In this section we initially consider a specific scenario illustrated in Figure 5.2-1 in which we have a pure LoS channel between the transmitter and each receive antenna $N_p^{\,k} = 1$. Also, since the receive antennas are closely spaced we assume they approximately have the same channel gain $\alpha_k = 1$. For the general multipath channel scenario we consider $N_p^{\,k} >> 1$.

5.1.4   Beamforming Techniques

In this section, we consider both analog and HBF techniques. For the analog beamformer, we utilize both the LoS beamsteering and EGT techniques described in Subsection 2.3.2 in Equations (2.38) and (2.40) respectively. Based on the channel scenario, we choose the analog precoder as follows: In case the channel is pure LoS $N_p = 1$ we apply the LoS beamsteering, while in case the channel is a multipath one we apply the EGT to capture the multipath gains. While for HBF we utilize the two stage HBF algorithm described in Algorithm 1, with using ZF for the BB precoder $\mathbf{F}^{BB}$ and LoS beamsteering or EGT alternatively for the RF precoder $\mathbf{F}^{RF}$.

5.1.5   HBF with RSM for Pure LoS Channels

Analytical SE Performance

Here, we consider spatial modulation at the receiver (RSM). Thus, only one receive antenna is targeted at a symbol duration, so the system is considered as a MISO system with interference (cross-talk) arising from the correlation between the streams. Also, in this section we only consider the SE of the IQ transmitted symbols since the extra $m = \log_2(N_r)$ bits that are added by the spatial symbols do not rely on the channel statistics and can be considered as a constant gain for the IQ SE. Henceforth, the SE of the channel using the HBF and RSM can be represented according to Equation (2.62) as:

$$\epsilon = \frac{1}{N_R} \log_2 \left(\det \left[\mathbf{I}_{N_R} + \rho \Lambda \mathbf{H} \mathbf{F}^{HBF} (\mathbf{F}^{HBF})^H \mathbf{H}^H \right] \right) \tag{5.4}$$

where $\Lambda = \frac{1}{\beta}$ is the scaling factor for the hybrid precoder. In case ZF is used as a digital precoder $\mathbf{F}^{BB} = \hat{\mathbf{H}}^H (\hat{\mathbf{H}} \hat{\mathbf{H}}^H)^{-1}$, then $\mathbf{H} \mathbf{F}^{HBF} = \mathbf{I}_{N_R}$ and the SE can be represented as:

$$\epsilon = \frac{1}{N_R} \log_2 \left(\det \left[\mathbf{I}_{N_R} + \rho \Lambda \mathbf{I}_{N_R} \right] \right) \tag{5.5}$$

In the following part of this subsection, we provide closed form analytic solutions for the SE of the RSM system with HBF in a pure LoS scenario for two receive antennas $N_R = 2$. In this scenario a deterministic LoS path between the transmitter and each receive antenna R_k is considered. For $N_R = 2$, two deterministic LoS paths exist between the transmitter and the receiver. In Equation (5.5), it is clear that maximizing the SE ϵ is equivalent to maximizing the scaling factor Λ.

Proposition 4. *In a pure LoS environment, the HBF with ZF digital precoder has a scaling factor for two receive antennas $N_R = 2$, that is calculated as follows:*

$$\Lambda = N_T(1 - |\Delta_t|^2) \tag{5.6}$$

where $|\Delta_t|$ is the absolute value of the transmit spatial correlation between the two paths.

Proof. The scaling factor for the two receive antennas Λ can be represented as follows:

$$\Lambda = \frac{1}{\mathbb{E}\left\{\text{Tr}\left(\left(\mathbf{F}^{RF}\mathbf{F}^{BB}\right)^H \mathbf{F}^{RF}\mathbf{F}^{BB}\right)\right\}} \tag{5.7}$$

given that the SVD of the equivalent channel $\hat{\mathbf{H}} = \mathbf{H}\mathbf{F}^{RF}$ is $\hat{\mathbf{H}} = \mathbf{U}_e\mathbf{D}_e\mathbf{V}_e^H$. Henceforth:

$$\mathbb{E}\left\{\text{Tr}\left(\left(\mathbf{F}^{RF}\mathbf{F}^{BB}\right)^H \mathbf{F}^{RF}\mathbf{F}^{BB}\right)\right\} = \mathbb{E}\{Tr((\mathbf{F}^{RF})^H\mathbf{F}^{RF}\mathbf{D}_e^{-2})\} \tag{5.8}$$

Given the fact that the SVD of the propagation channel $\mathbf{H}$ is $\mathbf{H} = \mathbf{U}\mathbf{D}\mathbf{V}^H$, and that the RF beamforming matrix in this specific case (pure LoS) is $\mathbf{F}^{RF} = \frac{\mathbf{H}^H}{\sqrt{N_T}}$. Thus,

$$
\begin{aligned}
\mathbb{E}\{Tr((\mathbf{F}^{RF})^H\mathbf{F}^{RF}\mathbf{D}_e^{-2})\} &= \mathbb{E}\left\{Tr\left(\frac{1}{N_T}\mathbf{H}\mathbf{H}^H\mathbf{D}_e^{-2}\right)\right\} \\
&= \mathbb{E}\left\{Tr\left(\frac{1}{N_T}\mathbf{D}^2\mathbf{D}_e^{-2}\right)\right\} \\
&= \frac{1}{N_T}\sum_{i=1}^{N_R}\frac{\lambda_i^{\mathbf{H}}}{\lambda_i^{\hat{\mathbf{H}}}}
\end{aligned}
\tag{5.9}
$$

Then from Equations (5.8) and (5.9), the scaling factor in Equation (5.7) is calculated as follows:

$$\Lambda = \frac{N_T}{\sum_{i=1}^{N_R}\frac{\lambda_i^{\mathbf{H}}}{\lambda_i^{\hat{\mathbf{H}}}}} \tag{5.10}$$

If only two receive antennas are considered at the receiver ($N_R = 2$), in a pure LoS environment, the two eigenvalues $\lambda_i^{\mathbf{H}}$ of the propagation channel $\mathbf{H}$ satisfy the following characteristics:

$$\lambda_1^{\mathbf{H}} + \lambda_2^{\mathbf{H}} = N_T N_R = 2N_T \tag{5.11}$$

$$\lambda_1^{\mathbf{H}}\lambda_2^{\mathbf{H}} = (1 - |\Delta_t|^2)N_T^2 \tag{5.12}$$

1) LoS RSM before deployment
optimization.

2) LoS RSM after deployment
optimization.
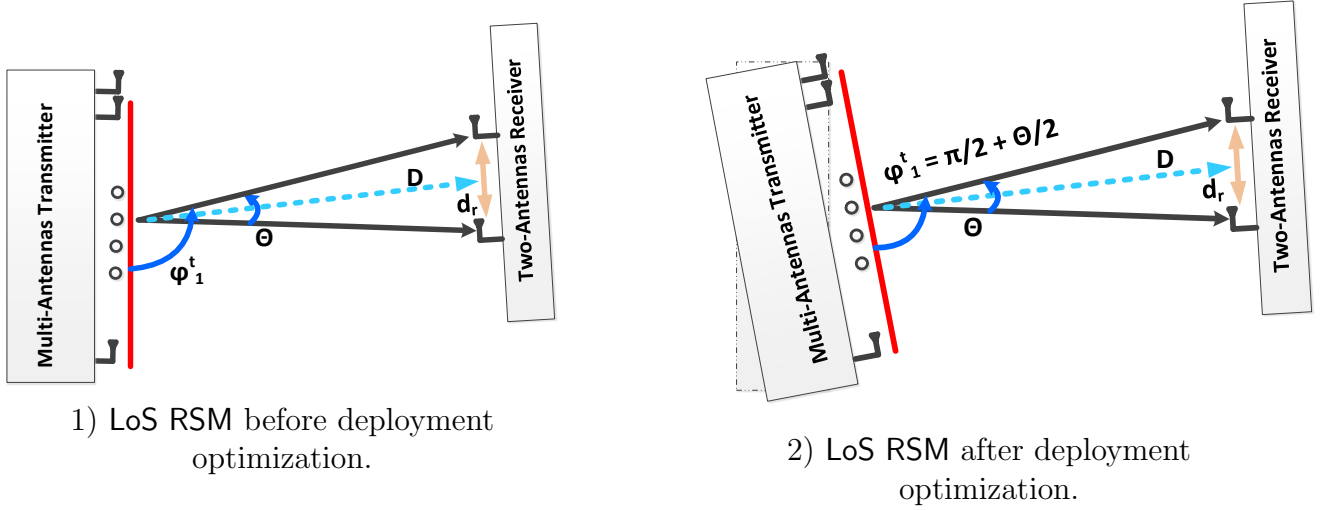
Figure 5.2: Illustration of the correlation minimization approach adopted for the RSM mmWave framework for two paths.

where the addition property in Equation (5.11) is illustrated in [149] and the multiplication property Equation (5.12) is illustrated in [116]. Then, solving Equations (5.11) and (5.12) simultaneously, the channel $\mathbf{H}$ eigenvalues are calculated as follows:

$$\lambda_1^{\mathbf{H}} = (1 - |\Delta_t|)N_T \text{ and } \lambda_2^{\mathbf{H}} = (1 + |\Delta_t|)N_T \tag{5.13}$$

Moreover, the two eigenvalues $\lambda_i^{\hat{\mathbf{H}}}$ of the equivalent channel $\hat{\mathbf{H}}$, can be calculated utilizing the fact that the analog beamformer (LoS Beamsteering) in this case (LoS scenario) can be represented as $\mathbf{F}^{RF} = \frac{\mathbf{H}^H}{\sqrt{N_T}}$. Thus, the eigenvalues of the equivalent channel $\hat{\mathbf{H}} = \mathbf{H}\mathbf{F}^{RF}$ can be related using Equations (5.11) and (5.12) in case $N_R = 2$ as follows:

$$\sqrt{\lambda_1^{\hat{\mathbf{H}}}} + \sqrt{\lambda_2^{\hat{\mathbf{H}}}} = \sqrt{N_T}N_R = 2\sqrt{N_T} \tag{5.14}$$

$$\sqrt{\lambda_1^{\hat{\mathbf{H}}}\lambda_2^{\hat{\mathbf{H}}}} = (1 - |\Delta_t|^2)N_T \tag{5.15}$$

Henceforth, solving Equations (5.14) and (5.15) simultaneously, the eigenvalues of the equivalent channel $\hat{\mathbf{H}}$ can be obtained as follows:

$$\lambda_1^{\hat{\mathbf{H}}} = (1 - |\Delta_t|)^2 N_T \text{ and } \lambda_2^{\hat{\mathbf{H}}} = (1 + |\Delta_t|)^2 N_T \tag{5.16}$$

Therefore, for two receive antennas ($N_R = 2$), the scaling factor can be expressed as:

$$\begin{aligned}
\Lambda &= \frac{N_T}{\sum_{i=1}^{N_R} \frac{\lambda_i^{\mathbf{H}}}{\lambda_i^{\hat{\mathbf{H}}}}} \\
&= \frac{N_T}{\frac{(1-|\Delta_t|)N_T}{(1-|\Delta_t|)^2 N_T} + \frac{(1+|\Delta_t|)N_T}{(1+|\Delta_t|)^2 N_T}} \\
&= N_T(1 - |\Delta_t|^2)
\end{aligned} \tag{5.17}$$

110

∎

Proposition 5. *The HBF with ZF digital precoder has an average scaling factor for two receive antennas $N_R = 2$ in pure LoS scenario as shown in Figure 5.2-1, that is calculated as follows:*

$$\mathbb{E}[\Lambda] \approx N_T - \left(1 + 2 \sum_{i=1}^{N_T - 1} \left(1 - \frac{i}{N_T}\right) \mathcal{J}_0(4\pi d_t \sin(\frac{\Theta}{2})i)\right) \tag{5.18}$$

where $\mathcal{J}_0$ is the zero order Bessel function.

Proof. It is clear from Equation (5.6) that the scaling factor Λ depends on the square of the absolute value of the transmit spatial correlation between the two paths $|\Delta_t|^2$. Therefore:

$$\mathbb{E}[\Lambda] = N_T(1 - \mathbb{E}[|\Delta_t|^2]) \tag{5.19}$$

Given that $\mathbb{E}[|\Delta_t|^2]$ can be expanded as follows:

$$\begin{aligned}
\mathbb{E}[|\Delta_t|^2] &= \mathbb{E}\left[\left|\mathbf{a}_t(\phi^t{}_1)^H \mathbf{a}_t(\phi^t{}_2)\right|\right] = \mathbb{E}\left[\left|\mathbf{a}_t(\phi^t{}_1)^H \mathbf{a}_t(\phi^t{}_1 - \Theta)\right|\right] \\
&= \frac{1}{N_T{}^2} \sum_{n=0}^{N_T-1} \sum_{m=0}^{N_T-1} \mathbb{E}\left[e^{2\pi d_t(m-n)(\sin(\phi^t{}_1)+\sin(\phi^t{}_1-\Theta))}\right] \\
&= \frac{1}{N_T{}^2} \sum_{n=0}^{N_T-1} \sum_{m=0}^{N_T-1} \mathbb{E}\left[e^{2\pi d_t(m-n)(2\cos(\phi^t{}_1+\frac{\Theta}{2})\sin(\frac{\Theta}{2}))}\right]
\end{aligned} \tag{5.20}$$

Given that in practical deployments $D >> d_r$ therefore Θ has small values and the approximation $\cos(\phi^t{}_1 + \frac{\Theta}{2}) \approx \cos(\phi^t{}_1)$ holds. Therefore,

$$\begin{aligned}
\mathbb{E}[|\Delta_t|^2] &\approx \frac{1}{N_T{}^2} \sum_{n=0}^{N_T-1} \sum_{m=0}^{N_T-1} \mathbb{E}[e^{2\pi d_t(m-n)(2\cos(\phi^t{}_1)\sin(\frac{\Theta}{2}))}] \\
&\approx \frac{1}{N_T}\left(1 + 2\sum_{i=1}^{N_T-1}\left(1 - \frac{i}{N_T}\right)\mathbb{E}[e^{2\pi d_t(2\cos(\phi^t{}_1)\sin(\frac{\Theta}{2}))i}]\right)
\end{aligned} \tag{5.21}$$

where $\mathbb{E}[e^{2\pi d_t(2\cos(\phi^t{}_1)\sin(\frac{\Theta}{2}))i}] = \mathcal{J}_0(4\pi d_t \sin(\frac{\Theta}{2})i)$ given that $\phi^t{}_1 \sim U[0, 2\pi]$ and using the mathematical tools provided in [173, p. 364]. Henceforth, $\mathbb{E}[|\Delta_t|^2]$ can be expressed as follows:

$$|\Delta_t|^2 \approx \frac{1}{N_T}\left(1 + 2\sum_{i=1}^{N_T-1}\left(1 - \frac{i}{N_T}\right)\mathcal{J}_0(4\pi d_t \sin(\frac{\Theta}{2})i)\right) \tag{5.22}$$

where $\mathcal{J}_0$ is the zero order Bessel function. From Equations (5.22) and (5.6), $\mathbb{E}[\Lambda]$ is expressed as:

$$\mathbb{E}[\Lambda] \approx N_T - \left(1 + 2\sum_{i=1}^{N_T-1}\left(1 - \frac{i}{N_T}\right)\mathcal{J}_0(4\pi d_t \sin(\frac{\Theta}{2})i)\right) \tag{5.23}$$

∎

$$\begin{aligned}
|\Delta_t| &= \left|\mathbf{a}_t(\phi^t{}_1)^H \mathbf{a}_t(\phi^t{}_2)\right| = \left|\mathbf{a}_t(\phi^t{}_1)^H \mathbf{a}_t(\phi^t{}_1 - \Theta)\right| = \left|\sum_{i=0}^{N_T-1} \frac{1}{N_T} e^{-j2\pi d_t i(\cos(\phi^t{}_1 - \Theta) - \cos\phi^t{}_1)}\right| \\
&= \left|\sum_{i=0}^{N_T-1} \cos(\pi i \cos(\phi^t{}_1 - \Theta) - \pi i \cos(\phi^t{}_1)) - j\sum_{i=0}^{N_T-1} \sin(\pi i \cos(\phi^t{}_1 - \Theta) - \pi i \cos(\phi^t{}_1))\right| \\
&= \left|\sum_{i=0}^{N_T-1} \cos(\pi i(\cos(\phi^t{}_1 - \Theta))) \cos(\pi i(\cos(\phi^t{}_1))) + \sin(\pi i(\cos(\phi^t{}_1 - \Theta))) \sin(\pi i(\cos(\phi^t{}_1)))\right. \\
&\quad \left. - j\sum_{i=0}^{N_T-1} \sin(\pi i(\cos(\phi^t{}_1 - \Theta))) \cos(\pi i(\cos(\phi^t{}_1))) - \cos(\pi i(\cos(\phi^t{}_1 - \Theta))) \sin(\pi i(\cos(\phi^t{}_1)))\right| \\
&= \left|\frac{\sin(\pi N_T d_t(\cos(\phi^t{}_1 - \Theta) - \cos(\phi^t{}_1))) \cos(\pi(N_T - 1)d_t(\cos(\phi^t{}_1 - \Theta) - \cos(\phi^t{}_1)))}{\sin(\pi d_t(\cos(\phi^t{}_1 - \Theta) - cos(\phi^t{}_1)))}\right. \\
&\quad \left. - j\frac{\sin(\pi N_T d_t(\cos(\phi^t{}_1 - \Theta) - \cos(\phi^t{}_1))) \sin(\pi(N_T - 1)d_t(\cos(\phi^t{}_1 - \Theta) - \cos(\phi^t{}_1)))}{\sin(\pi d_t(\cos(\phi^t{}_1 - \Theta) - cos(\phi^t{}_1)))}\right| \\
&= \left|\frac{\sin(\pi N_T d_t(\cos(\phi^t{}_1 - \Theta) - \cos\phi^t{}_1))}{N_T \sin(\pi d_t(\cos(\phi^t{}_1 - \Theta) - \cos\phi^t{}_1))}\right|
\end{aligned} \tag{5.24}$$

After relating $|\Delta_t|^2$ and Λ in proposition 1 and deriving the average Λ for the case that $\phi^t{}_1 \sim U[0, 2\pi]$ in proposition 2, now we aim at finding the optimal transmitter deployment (optimal $\phi^t{}_1$) in order to maximize Λ and thus maximize the SE. Maximizing the scaling factor Λ is equivalent to minimizing the absolute value of the transmit spatial correlation $|\Delta_t|$. Henceforth, our objective will be to find the minimum achievable correlation Δ_{tmin}.

Given $N_R = 2$, the channel correlation matrix can be expressed as follows:

$$\mathbf{HH}^H = \begin{bmatrix} N_T & \mathbf{a}_t(\phi^t{}_1)^H N_T(\phi^t{}_2) \\ (\mathbf{a}_t(\phi^t{}_1)^H \mathbf{a}_t(\phi^t{}_2))^H & N_T \end{bmatrix} \tag{5.25}$$

Thus, $|\Delta_t|$ can be expanded as in Equation (5.24). It is clear that, in this scenario the transmit spatial correlation depends on two parameters, which are the angle of the first path $\phi^t{}_1$ and the angular difference between the two paths Θ. $\phi^t{}_1$ is a uniformly distributed random variable such that $\phi^t{}_1 \in [0, 2\pi]$ as aforementioned. Θ is a deterministic value that represents the angular difference between the path arriving at the first receive antenna and the path arriving at the second one, and is calculated based on trigonometric properties according to Figure 5.2-1 as follows:

$$\Theta = 2\arctan\left(\frac{d_r}{2D}\right) \tag{5.26}$$

such that d_r is the receive antennas inter-element spacing, and D is the distance between the transmitter and the receiver. Therefore, the angle towards the first antenna in this case is uniformly distributed $\phi^t{}_1 \sim \mathcal{U}[0, 2\pi]$ and the angle towards the second antenna depends on $\phi^t{}_1$ where $\phi^t{}_2 = \phi^t{}_1 - \Theta$, given that Θ is a deterministic value as aforementioned and depends on the deployment scenario (D and d_r).

This correlation minimization problem was similarly tackled in [116], for minimizing the correlation between the LoS and the reflected path at the receiver side and it was shown that the transmit spatial correlation between two paths can be minimized to its lower bound represented as:

$$|\Delta_t|_{min} = \begin{cases} 0, & \Theta \geq 2\arcsin(\frac{1}{2N_T d_t}), \\ \left|\frac{\sin(2\pi N_T d_t \sin\frac{\Theta}{2})}{N_T \sin(2\pi d_t \sin\frac{\Theta}{2})}\right|, & \Theta < 2\arcsin(\frac{1}{2N_T d_t}), \end{cases} \quad (5.27)$$

This can be obtained by solving the following minimization problem:

$$|\Delta_t|_{min} = \underset{\phi^t_1}{\operatorname{argmin}} \left|\frac{\sin(\pi N_T d_t(\cos(\phi^t_1 - \Theta) - \cos\phi^t_1))}{N_T \sin(\pi d_t(\cos(\phi^t_1 - \Theta) - \cos\phi^t_1))}\right|$$

$$s.t. \ \phi^t_1 \in \left[\frac{\Theta}{2}, \frac{\Theta}{2} + \pi\right] \quad (5.28)$$

This can be achieved by optimizing the deployment of the transmitter ϕ^t_1 in order to minimize the transmit spatial correlation as in proposition 1 in [116]. Therefore, the optimum transmit ULA array orientation angle ϕ^t_1 for minimizing the transmit spatial correlation in this case after deployment optimization is defined as:

$$\phi^t_{1,opt} = \begin{cases} \arcsin(\Delta\zeta) + \frac{\Theta}{2}, & \Theta \geq 2\arcsin(\frac{1}{2N_T d_t}), \\ \frac{\pi}{2} + \frac{\Theta}{2}, & \Theta < 2\arcsin(\frac{1}{2N_T d_t}), \end{cases} \quad (5.29)$$

where $\Delta\zeta = \frac{s}{2N_T d_t \sin\frac{\Theta}{2}}$ such that s is given as:

$$s = 1, 2, .., \left\lfloor 2N_T d_t \sin\frac{\Theta}{2}\right\rfloor, \mod(s, N_T) \neq 0. \quad (5.30)$$

where $\lfloor .. \rfloor$ denotes the floor operator. Thus, as shown in Equations (5.27) and (5.29), three specific cases exist to be tackled by our framework, which define our contribution over the existing work in the literature that deals with the RSM issues in pure LoS mmWave systems [149]. The three specific cases are:

- $\Theta = 2\arcsin(\frac{1}{2N_T d_t})$: This is the optimum scenario, in which the transmit spatial correlation $\Delta_t = 0$ as shown in [149]. In this case analog beamforming is enough for RSM and no ZF is needed, as the interference/leakage between the antennas does not exist. However, this is a very specific case and it is not a realistic assumption for RSM mmWave systems. Henceforth, we provide a solution for the other two cases to introduce a practical RSM framework in mmWave frequencies.

- $\Theta > 2\arcsin(\frac{1}{2N_T d_t})$: In this case using Equation (5.29), the transmit spatial correlation can be nulled by optimizing the deployment of the transmit array, such that

1) Multi-receive antennas scenario

2) Receiver rotation scenario
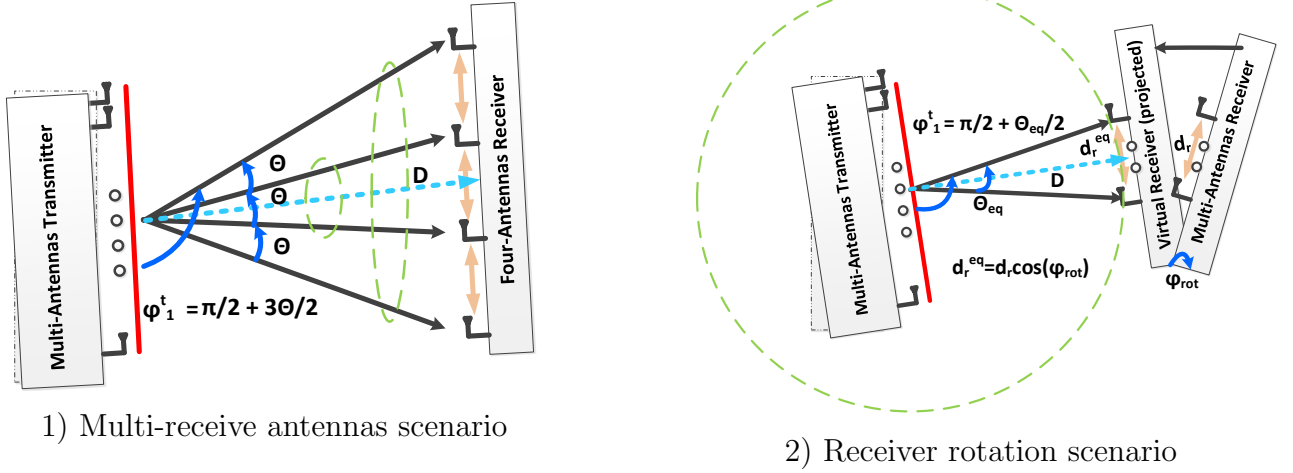
Figure 5.3: Illustration of the correlation minimization approach adopted for the RSM mmWave framework for multiple paths and multiple orientations of the receiver

$\phi^t{}_1 = \arcsin(\Delta\zeta) + \frac{\Theta}{2}$. In this case again ZF is not required, since the transmit array deployment optimization is enough to null the interference/leakage between the antennas. However, this case is not realistic in mmWave systems, due to the fact that Θ practically has very small values $\Theta \approx 0$ and thus, this condition can only be satisfied by utilizing a massive number of transmit antennas. Henceforth, we move to discussing the third case, which is the most practical one into more details.

- $\Theta < 2\arcsin(\frac{1}{2N_T d_t})$: This is the most practical and realistic scenario for mmWave RSM systems. In such case, the transmit array deployment optimization provided in Equation (5.29) is no more able to null the transmit spatial correlation, but it can minimize it to its lower bound. Thus, HBF is required in this case in order to apply ZF in the digital part to null the interference between the receive antennas. The transmit array deployment optimization step maximize the SE achieved by the HBF, since it minimizes the correlation and hence ZF precoding can be applied efficiently. In the rest of this section we will focus on this scenario, given the fact that it is the most practical and realistic one. Moreover, it is the only scenario that needs HBF, while in the other two scenarios analog beamforming is enough. Therefore, the SE for RSM in mmWave channel utilizing the HBF strategy with LoS beamsteering in the analog domain with ZF in the digital domain when $\Theta < 2\arcsin(\frac{1}{2N_T d_t})$, $N_R = 2$ and optimal deployment $\phi^t{}_1 = \phi^t{}_{1,opt}$ can be obtained from Equations (5.5), (5.6) and (5.29) can be expressed as:

$$\epsilon = \log_2\left(1 + \rho N_T\left(1 - \left|\frac{\sin(2\pi N_T d_t \sin\frac{\Theta}{2})}{N_T \sin(2\pi d_t \sin\frac{\Theta}{2})}\right|^2\right)\right) \qquad (5.31)$$

Moreover, we extend this step to include more than two receive antennas as shown in Figure 5.3-1. From Equation (5.29), it is shown that when $\Theta > 2 \arcsin(\frac{1}{2N_T d_t})$, the optimal transmit ULA array orientation $\phi^t{}_1$ in this case is to be oriented towards the center point of the receive array which is achieved by $\phi^t{}_1 = \frac{\pi}{2} + \frac{\Theta}{2}$. We show that this can be extended to multiple receive antennas in the following proposition.

Proposition 6. *For $N_R > 2$, the maximum SE ϵ_{opt} can be achieved in case $\Theta > 2 \arcsin(\frac{1}{2N_T d_t})$ by assigning the transmit array orientation such that $\phi^t{}_1 = \frac{\pi}{2} + \frac{N_R-1}{2}\Theta$*

Proof. We aim at maximizing the SE ϵ, which is equivalent to maximizing the scaling factor Λ. Therefore, the optimization problem can be reformulated as:

$$\Lambda_{max} = \underset{\phi^t{}_1}{\operatorname{argmax}} \frac{1}{\mathbb{E}\left\{\operatorname{Tr}\left(\left(\mathbf{F}^{RF}\mathbf{F}^{BB}\right)^H \mathbf{F}^{RF}\mathbf{F}^{BB}\right)\right\}}$$
$$s.t. \ \phi^t{}_1 \in \left[\frac{(N_R-1)\Theta}{2}, \frac{(N_R-1)\Theta}{2} + \pi\right] \tag{5.32}$$

Therefore, we aim at choosing the optimal transmitter deployment $\phi^t{}_1$. This optimal $\phi^t{}_1$ is the one that minimizes $\operatorname{Tr}\left(\left(\mathbf{F}^{RF}\mathbf{F}^{BB}\right)^H \mathbf{F}^{RF}\mathbf{F}^{BB}\right)$, which can be simplified, similar to Equations (5.7) and (5.8) as follows:

$$\underset{\phi^t{}_1}{\operatorname{argmin}} \sum_{i=1}^{N_R} \frac{1}{\lambda_i^{\mathbf{H}}}$$
$$s.t. \ \phi^t{}_1 \in \left[\frac{(N_R-1)\Theta}{2}, \frac{(N_R-1)\Theta}{2} + \pi\right] \tag{5.33}$$

Given that $\sum_{i=1}^{N_R} \lambda_i^{\mathbf{H}} = N_T N_R$, therefore the best achievable solution for Equation (5.33) will be the case $\lambda_1 = \lambda_2 = ... = \lambda_{N_R} = N_T$ which is achieved when the correlation matrix $\mathbf{HH}^H$ is a diagonal one as follows:

$$(\mathbf{HH}^H)_{opt} = \begin{bmatrix} N_T & \cdots & 0 \\ \vdots & \ddots & \vdots \\ 0 & \cdots & N_T \end{bmatrix} \tag{5.34}$$

while the achievable correlation matrix with residual off diagonal terms is shown in Equation (5.40), where the off diagonal terms can not be nulled in the case $\Theta > 2 \arcsin(\frac{1}{2N_T d_t})$ as aforementioned. Hence, the problem can be formulated as minimizing the mean absolute error between the correlation matrix $\mathbf{HH}^H$ in Equation (5.40) and the optimal one in Equation (5.34) as follows:

$$\underset{\phi^t{}_1}{\operatorname{argmin}} \frac{1}{N_R(N_R-1)} \sum_{i=1}^{N_R} \sum_{j=1, j\neq i}^{N_R} |\Delta_t|_{i,j}$$
$$s.t. \ \phi^t{}_1 \in \left[\frac{(N_R-1)\Theta}{2}, \frac{(N_R-1)\Theta}{2} + \pi\right] \tag{5.35}$$

where $|\Delta_t|_{i,j} = |\mathbf{a}_t(\phi^t{}_i)^H \mathbf{a}_t(\phi^t{}_j)|$ represents the absolute value of the correlation between the receive antennas i and j and is expressed according to Equation (5.24) as follows:

$$\underset{\phi^t{}_1}{\operatorname{argmin}} \sum_{i=1}^{N_R} \sum_{j=1, j \neq i}^{N_R} \left| \frac{\sin(\pi N_T d_t(\cos \phi^t{}_i - \cos \phi^t{}_j))}{N_T \sin(\pi d_t(\cos \phi^t{}_i - \cos \phi^t{}_j))} \right|$$
$$s.t. \ \phi^t{}_1 \in \left[\frac{(N_R - 1)\Theta}{2}, \frac{(N_R - 1)\Theta}{2} + \pi \right] \tag{5.36}$$

where Equation (5.36) can be simplified to

$$\underset{\phi^t{}_1}{\operatorname{argmin}} \sum_{i=1}^{N_R} \sum_{j=i+1}^{N_R} 2 \left| \frac{\sin(\pi N_T d_t(\cos \phi^t{}_i - \cos \phi^t{}_j))}{N_T \sin(\pi d_t(\cos \phi^t{}_i - \cos \phi^t{}_j))} \right|$$
$$s.t. \ \phi^t{}_1 \in \left[\frac{(N_R - 1)\Theta}{2}, \frac{(N_R - 1)\Theta}{2} + \pi \right] \tag{5.37}$$

According to [116], $\left| \frac{\sin(\pi N_T d_t(\cos \phi^t{}_i - \cos \phi^t{}_j))}{N_T \sin(\pi d_t(\cos \phi^t{}_i - \cos \phi^t{}_j))} \right|$ is a monotonously decreasing function of $\cos \phi^t{}_i - \cos \phi^t{}_j$ and achieves its minimum when $\cos \phi^t{}_i - \cos \phi^t{}_j$ is maximized. Therefore, the objective function in Equation (5.37) can be reformulated as

$$\underset{\phi^t{}_1}{\operatorname{argmax}} \sum_{i=1}^{N_R} \sum_{j=i+1}^{N_R} 2(\cos \phi^t{}_i - \cos \phi^t{}_j)$$
$$s.t. \ \phi^t{}_1 \in \left[\frac{(N_R - 1)\Theta}{2}, \frac{(N_R - 1)\Theta}{2} + \pi \right] \tag{5.38}$$

such that Equation (5.38) can be simplified as follows:

$$\underset{\phi^t{}_1}{\operatorname{argmax}} \sum_{k=1}^{\lfloor \frac{N_R}{2} \rfloor} 2(N_R - 2k + 1)(\cos \phi^t{}_k - \cos \phi^t{}_{N_R - k + 1})$$
$$s.t. \ \theta_1 \in \left[\frac{(N_R - 1)\Theta}{2}, \frac{(N_R - 1)\Theta}{2} + \pi \right] \tag{5.39}$$

where $2(N_R - 2k + 1)(\cos \phi^t{}_k - \cos \theta_{N_R - k - 1}) = 2(N_R - 1)(\cos \phi^t{}_1 - \cos \phi^t{}_{N_R}) + 2(N_R - 3)(\cos \phi^t{}_2 - \cos \phi^t{}_{N_R - 1}) + \dots + 2(N_R - 2\lfloor \frac{N_R}{2} \rfloor + 1)\left(\cos \phi^t{}_{\lfloor \frac{N_R}{2} \rfloor} - \cos \phi^t{}_{N_R - \lfloor \frac{N_R}{2} \rfloor + 1} \right)$ and the maximization of each pair separately $(\cos \phi^t{}_k - \cos \phi^t{}_{N_R - k - 1})$ is done by setting $\phi^t{}_1 = \frac{\pi}{2} + \frac{N_R - 1}{2}\Theta$ according to [116], since in this case each two opposite receive antennas are treated as illustrated in Figure 5.3-1, with $\Theta > 2 \arcsin(\frac{1}{2N_T d_t})$. Henceforth, applying the previous analysis for the case when $N_R = 2$ can be generalized for our symmetric system with $N_R > 2$ leading to the optimal transmit deployment $\phi^t{}_{1,opt} = \frac{\pi}{2} + \frac{N_R - 1}{2}\Theta$. ∎

In order to make our analysis more generic and complete, we consider the case when the receiver is misaligned with respect to the transmit direction. In this case, the receiver is virtually

$$\mathbf{HH}^H = \begin{bmatrix} \begin{bmatrix} N_T & \mathbf{a}_t(\phi^t{}_1)^H \mathbf{a}_t(\phi^t{}_1 - \Theta) & \dots \\ (\mathbf{a}_t(\phi^t{}_1)^H \mathbf{a}_t(\phi^t{}_1 - \Theta))^H & N_T & \dots \\ \vdots & \vdots & \ddots \end{bmatrix} \begin{bmatrix} \mathbf{a}_t(\phi^t{}_1)^H \mathbf{a}_t(\phi^t{}_1 - (N_R - 1)\Theta) \\ \mathbf{a}_t(\phi^t{}_1 - \Theta)^H \mathbf{a}_t(\phi^t{}_1 - (N_R - 1)\Theta) \\ \vdots \end{bmatrix} \\ \begin{bmatrix} (\mathbf{a}_t(\phi^t{}_1)^H \mathbf{a}_t(\phi^t{}_1 - (N_R - 1)\Theta))^H & \dots & \dots \end{bmatrix} \qquad\qquad N_T \end{bmatrix}$$

$$(5.40)$$

projected on the transmission plane as shown in Figure 5.3-2, resulting in virtually decreasing the inter-element antenna spacing at the receiver side as follows:

$$d_r{}^{eq} = d_r \cos(\phi_{rot}) \tag{5.41}$$

Then, later the equivalent Θ can be calculated as follows:

$$\Theta_{eq} = 2 \arctan \left(\frac{d_r{}^{eq}}{2D} \right) \tag{5.42}$$

Finally the optimal transmit array orientation $\phi^t{}_1$ can be calculated similarly as in the case when the receiver was not rotated but with considering Θ_{eq} instead of Θ.

Analytical BER Performance

Here we consider only the BER for the spatial symbols, since the BER for the IQ symbols depends on the $M-$ ary modulation applied. However, considering the BER for the spatial symbols, our analysis is generic apart from any $M-$ ary modulation used. A given detector has to analyze the following set of signals:

$$\forall j, \quad r_j = \begin{cases} \sqrt{\Lambda} + n_j & \text{if } R_j \text{ is the targeted antenna} \\ n_j & \text{otherwise} \end{cases} \tag{5.43}$$

Here we can observe the impact of the ZF digital precoding significantly on enhancing the BER compared to the analog only beamforming for the spatial symbols. It is clear now that the spatial symbol can be wrongly detected only due to the noise, thanks to the ZF that totally mitigated the inter-antenna correlation (interference). Using the maximum likelihood detection, and referring to [156], the BER performance of the RASK scheme conditioned by $\mathbf{H}$ is approximated by:

$$\text{BER}|\mathbf{H} \approx \frac{N_R}{2} Q \left(\sqrt{\Lambda/\sigma_n^2} \right). \tag{5.44}$$

In LoS scenario, while optimizing the deployment of the transmitter to the optimal position as aforementioned for transmit correlation minimization, given a fixed $\Delta\theta$ the channel could be

considered as deterministic, and so the conditioned BER is equal to the average BER. Henceforth, the average BER can be expressed as:

$$\text{BER}\text{—}\mathbf{H}_{LoS} = \frac{N_R}{2} Q \left(\frac{\sqrt{N_T (1 - |\Delta_t|^2)}}{2\sqrt{\sigma_n^2}} \right).$$
(5.45)

5.1.6   HBF with RSM for Multipath Channels

Analytical SE Performance

Here we will similarly consider the SE of the IQ symbols only since the SE of the spatial symbols can be considered as a constant factor that does not vary with the channel statistics. In case a multipath channel environment exists between the transmitter and the receiver with $N_p{}^k >> 1$, all the previous deployment optimization scenarios do not hold. In this case the EGT is used as analog beamforming, where the k-th antenna analog beamformer $\mathbf{f}^{RF}{}_k$ (will be denoted here as $\mathbf{f}_k$ for better readability) is calculated to extract the phases of the channel $\mathbf{h}_k$. In order to calculate the scaling factor Λ which is essential to derive a closed form expression for the SE in Equation (5.5), we will utilize the analytic SE derivations in [112] for iid Rayleigh channel as a tight upper bound that can be achieved asymptotically for multipath channel environments [174]. Therefore, the equivalent channel's diagonal elements $\hat{\mathbf{H}}_{k,k} = \mathbf{h}_k \mathbf{f}_k$ can be represented as follows:

$$\mathbf{h}_k \mathbf{f}_k = \frac{1}{\sqrt{N_T}} \sum_{i=1}^{N_T} |h_{i,k}|$$
(5.46)

such that $h_{i,k}$ is the ith element of the channel vector $\mathbf{h}_k$. Given that the elements of $\mathbf{h}_k$ are iid complex Gaussian random variables with $h \sim \mathcal{CN}(0, 1)$, then $|h|$ follows Rayleigh distribution with mean $\frac{\sqrt{\pi}}{2}$ and variance $1 - \frac{\pi}{4}$. According to the central limit theorem when N_T approaches infinity, the diagonal terms of the equivalent channel $\hat{\mathbf{H}}_{k,k}$ have a normal distribution as follows:

$$\mathbf{h}_k \mathbf{f}_k \sim \mathcal{N} \left(\frac{\sqrt{\pi N_T}}{2}, 1 - \frac{\pi}{4} \right).$$
(5.47)

Considering the off-diagonal terms of the equivalent channel $\hat{\mathbf{H}}_{k,j}, k \neq j$, they can be represented as follows:

$$\mathbf{h}_k \mathbf{f}_j = \frac{1}{\sqrt{N_T}} \sum_{i=1}^{N_T} h_{i,k} e^{-\phi_{i,j}}$$
(5.48)

where $e^{-\phi_{i,j}}$ is the phase element arising from the phase mismatch between the channel vector $\mathbf{h}_k$ and the analog beamforming vector $\mathbf{f}_j$. According to Lemma 1 in [112], the off-diagonal terms of the equivalent channel $\hat{\mathbf{H}}_{k,j}, k \neq j$ are distributed as follows:

$$\mathbf{h}_k \mathbf{f}_j \sim \mathcal{CN}(0, 1)$$
(5.49)

Thus, $|\mathbf{f}_k \mathbf{f}_j|$ follow Rayleigh distribution with mean $\frac{\sqrt{\pi}}{2}$ and variance $1 - \frac{\pi}{4}$, which is considered to be negligible compared to the diagonal terms $\hat{\mathbf{H}}_{k,k}$ for high N_T according to Equation (5.47).

Table 5.1: Simulation Parameters

Parameter	Value
Channel Model	Ray based Model [86]
Simulation Type	Monte Carlo (100000 realizations)
Transmit Array Architecture	ULA
Transmit Inter-antenna spacing	$\frac{\lambda}{2}$
Number of Transmit/Receive RF Chains	2

This means that the interference between the receive antennas can be considered negligible even without digital preprocessing (without ZF) for high number of transmit antennas N_T. Therefore, Λ can be approximated as the mean of the diagonal term:

$$\Lambda \approx \frac{\pi N_T}{4} \tag{5.50}$$

Therefore, using the approximation in Theorem 1 in [112] the SE for RSM in multi-path channel with using HBF (EGT - ZF) at the transmitter can be approximated to its upper bound for large N_T as follows:

$$\epsilon \approx \log_2\left(1 + \frac{\pi}{4}\rho N_T\right) \tag{5.51}$$

Analytical BER Performance

For a multi-path channel scenario, according to Equation (5.50), $\sqrt{\Lambda}$ can be approximated as:

$$\sqrt{\Lambda} \approx \sqrt{\pi N_T/4} \tag{5.52}$$

Therefore according to [156], the average BER of this scenario can be represented as:

$$\text{BER—}\mathbf{H}_{multi} \approx \frac{N_R}{2} Q\left(\frac{\sqrt{\pi N_T}}{4\sqrt{\sigma_n^2}}\right). \tag{5.53}$$

5.1.7 Numerical Analysis

In this subsection, the performance of the introduced HBF RSM framework is evaluated in details given the simulation parameters summarized in Table (5.1). Perfect CSI is assumed at the transmitter and the receiver sides.

In Figure 5.4-1 that represents the SE variation with respect to the transmit ULA orientation for different number of transmit antennas, the simulation results show that, the optimum orientation of the transmit array is achieved when $\phi^t{}_1 = \frac{\pi}{2} + \frac{\Theta}{2}$ in case $\Theta < 2\arcsin(\frac{1}{2N_T d_t})$ as shown in Equation (5.29) and mathematically proved in [116] for different number of transmit antennas N_T. Similarly in Figure 5.4-2, that represents the SE variation with respect to the
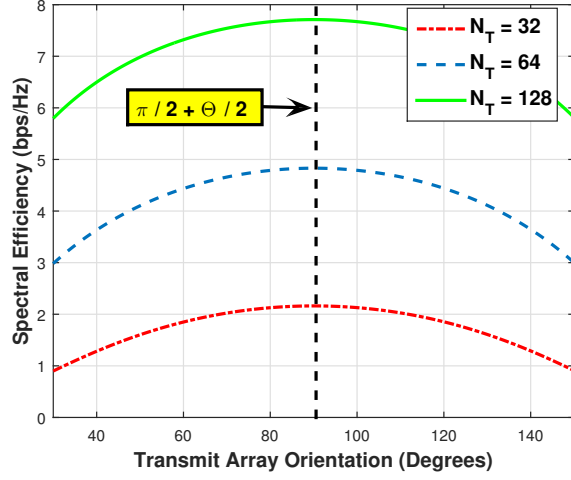
1) SE versus the ULA transmit array
orientation for a given scenario
$(N_R = 2, \rho = 10\text{dB}, d_r = 18\lambda, D = 5000\lambda)$
in pure LoS environment.
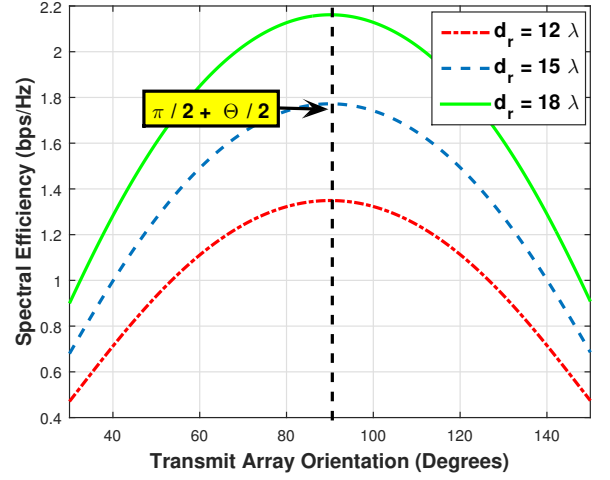
2) SE versus the ULA transmit array
orientation for a given scenario
$(N_R = 2, \rho = 10\text{dB}, N_T = 32, D = 5000\lambda)$
in pure LoS environment.

Figure 5.4: SE versus the ULA transmit array orientation for a given scenario ($N_R = 2, \rho = 10\text{dB}, D = 5000\lambda$) in pure LoS environment.
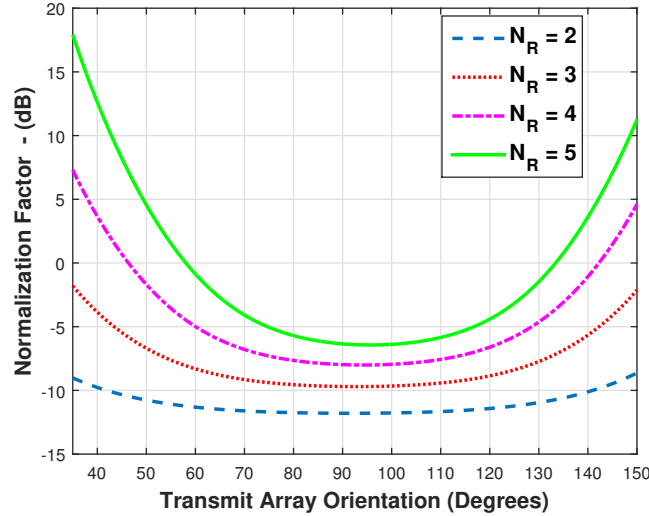
Figure 5.5: Normalization factor β versus the ULA transmit array orientation for a given scenario ($\rho = 10\text{dB}, N_T = 32, D = 500\lambda, d_r = 25\lambda$) in pure LoS environment.

transmit ULA orientation for different inter-receive antenna spacing, Equation (5.29) is validated by simulations for different values of receiver inter antenna element spacing d_r. Moreover, in Figures 5.5 and 5.6-1, the extension to more than 2 receive antennas, for the transmit ULA array deployment optimization is validated. In this scenario the Θ is calculated according to
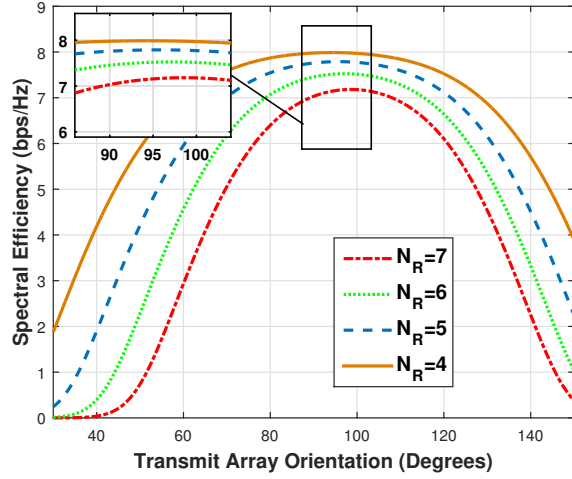
1) SE versus the ULA transmit array orientation for a given scenario ($\rho = 10$dB, $N_T = 32, D = 500\lambda, d_r = 25\lambda$) in pure LoS environment.
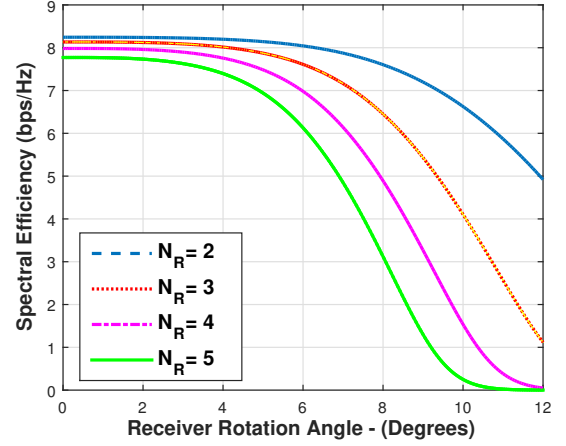
2) SE versus the ULA receive array orientation rotation for a given scenario ($\rho = 10$dB, $N_T = 32, D = 500\lambda$, $d_r = 25\lambda, \phi^t_{\ 1} = \frac{\pi}{2} + \frac{\Theta_{eq}}{2}$) in pure LoS environment.

Figure 5.6: SE versus the ULA receive array orientation rotation for a given scenario ($\rho = 10$dB, $N_T = 32, D = 500\lambda, d_r = 25\lambda$) in pure LoS environment.
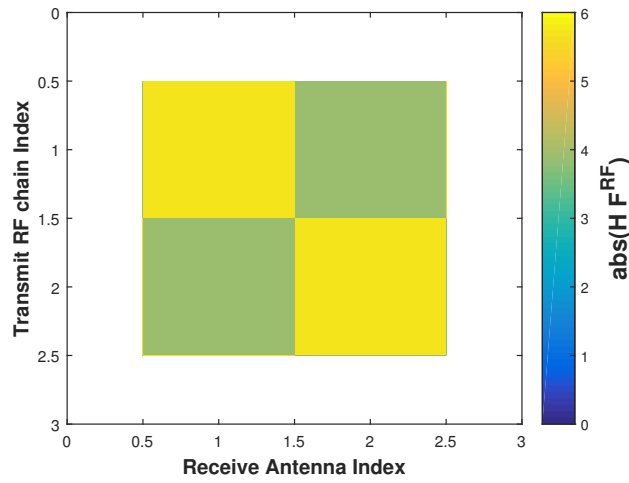
1) The equivalent channel $\hat{\mathbf{H}} \in \mathbb{C}^{N_R \times N_{TRF}}$
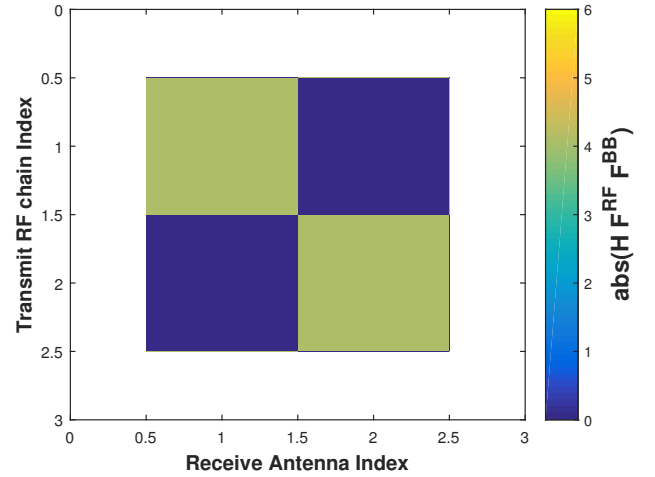
2) Applying ZF $\mathbf{F}_{ZF}$ on the equivalent channel $\hat{\mathbf{H}}$

Figure 5.7: Illustration of the effect of applying analog and hybrid beamforming for the RSM mmWave framework in pure LoS environment with transmit ULA for a given scenario ($N_T = 32, N_R = 2, d_r = 25\lambda, D = 500\lambda$)

Equation (5.26) as follows:

1) The equivalent channel $\hat{\mathbf{H}} \in \mathbb{C}^{N_R \times N_{TRF}}$

2) Applying ZF $\mathbf{F}_{ZF}$ on the equivalent channel $\hat{\mathbf{H}}$
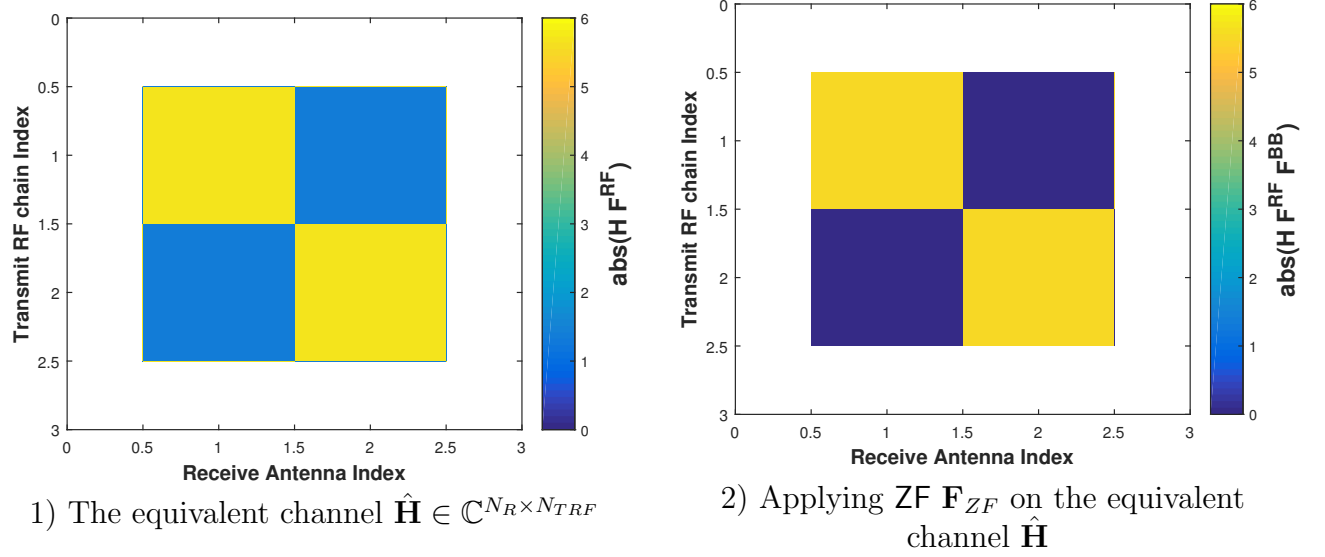
Figure 5.8: Illustration of the effect of applying analog and hybrid beamforming for the RSM mmWave framework in pure LoS environment with transmit ULA for a given scenario ($N_T = 32, N_R = 2, d_r = 25\lambda, D = 500\lambda$) after applying the transmitter deployment optimization for correlation minimization as illustrated in Figure 5.2.

1) The equivalent channel $\hat{\mathbf{H}} \in \mathbb{C}^{N_R \times N_{TRF}}$

2) Applying ZF $\mathbf{F}_{ZF}$ on the equivalent channel $\hat{\mathbf{H}}$
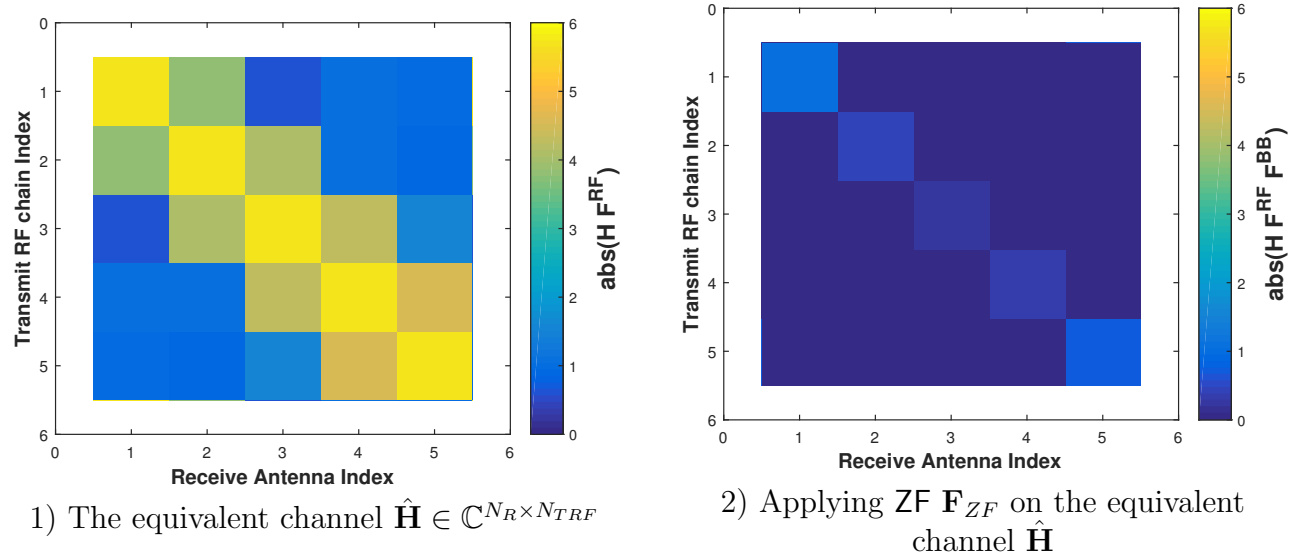
Figure 5.9: Illustration of the effect of applying analog and hybrid beamforming for the RSM mmWave framework in pure LoS environment with transmit ULA for a given scenario ($N_T = 32, N_R = 5, d_r = 25\lambda, D = 500\lambda$)

$$\Theta = 2\arctan\left(\frac{d_r}{2D}\right) = 2\arctan\left(\frac{25\lambda}{1000\lambda}\right)$$
$$= 0.05\,\text{radian} = 2.8642°$$

(5.54)

1) The equivalent channel $\hat{\mathbf{H}} \in \mathbb{C}^{N_R \times N_{TRF}}$

2) Applying ZF $\mathbf{F}_{ZF}$ on the equivalent channel $\hat{\mathbf{H}}$
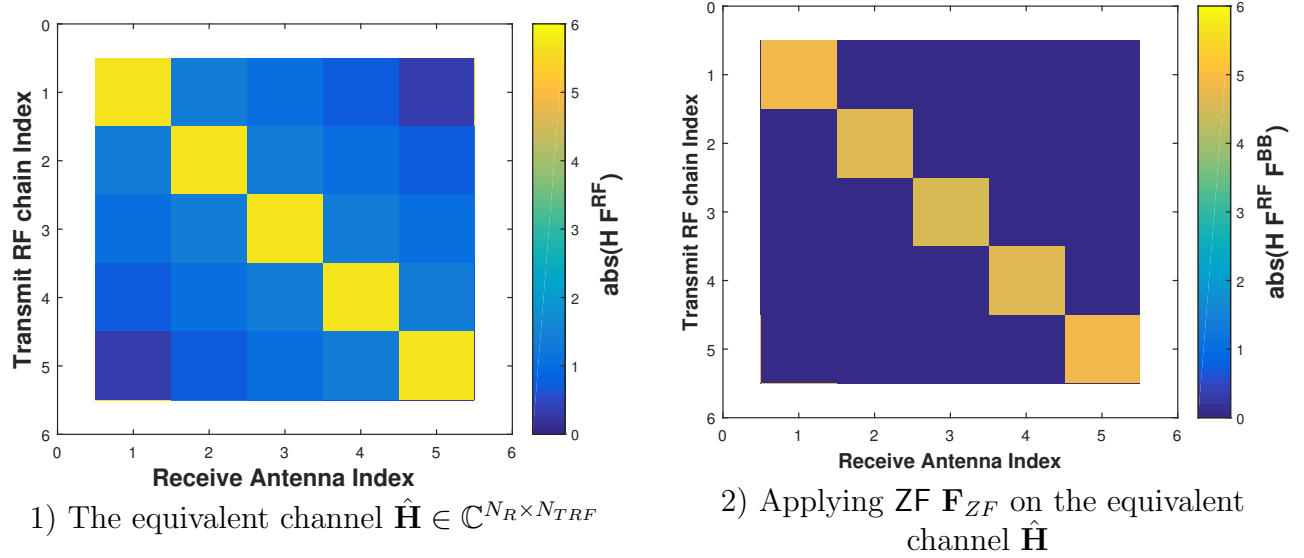
Figure 5.10: Illustration of the effect of applying analog and hybrid beamforming for the RSM mmWave framework in pure LoS environment with transmit ULA for a given scenario ($N_T = 32, N_R = 5, d_r = 25\lambda, D = 500\lambda$) after applying the transmitter deployment optimization for correlation minimization as illustrated in Figure 5.3-1.
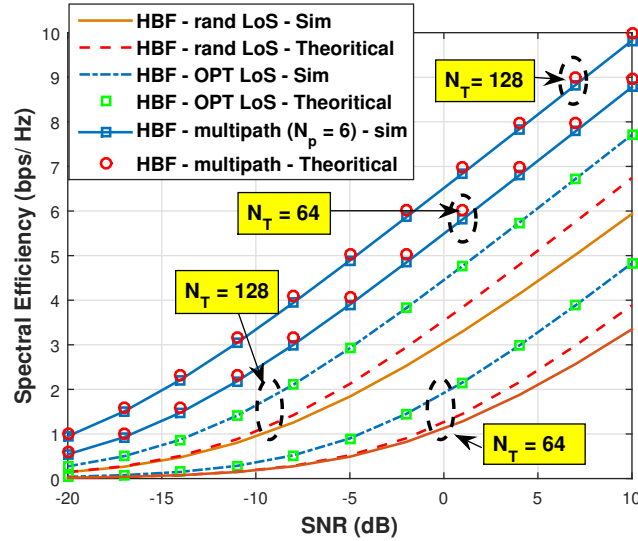
Figure 5.11: Theoretical and numerical SE versus SNR for a given scenario ($N_R = 2, d_r = 18\lambda, D = 5000\lambda$) in a pure LoS environment and in a multipath environment ($N_p = 6$).

Therefore, the optimal ULA transmit array is found to be pointing towards the center of the receive array for correlation minimization/SE maximization. This will be satisfied given that ϕ^t_1 is calculated as follows:
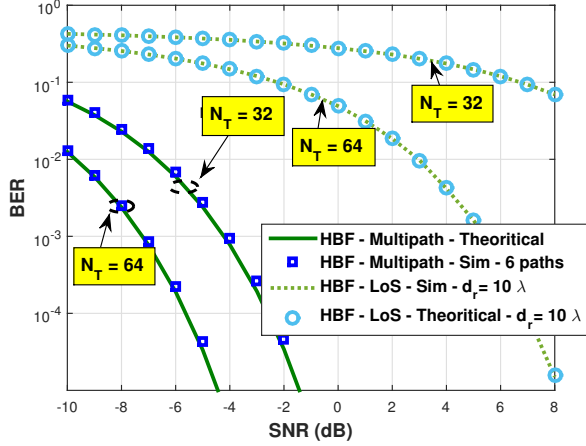
1) Theoretical and numerical average BER versus SNR for a given scenario ($N_R = 2, d_r = 10\lambda, D = 5000\lambda$) in a pure LoS environment and in a multipath environment ($N_p = 6$).
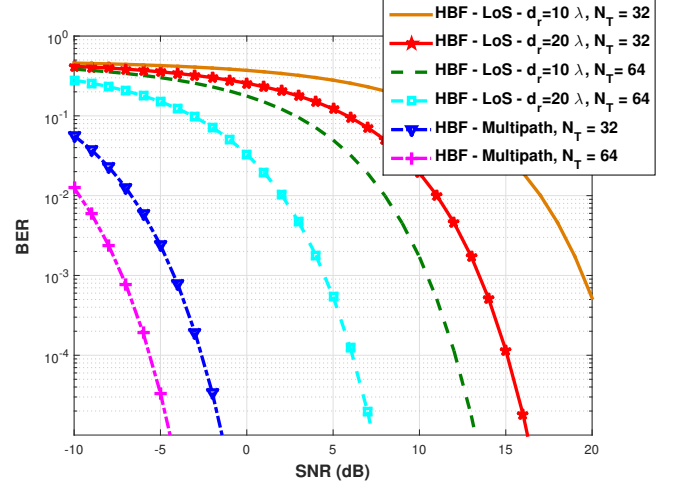
2) Theoretical average BER versus SNR for different scenarios (given $D = 5000\lambda$) in a pure LoS environment and in a multipath environment.

Figure 5.12: Average BER versus SNR.

- For $N_R = 4$: $\phi^t_1 = \frac{\pi}{2} + \frac{3\Theta}{2}$

- For $N_R = 5$: $\phi^t_1 = \frac{\pi}{2} + 2\Theta$

- For $N_R = 6$: $\phi^t_1 = \frac{\pi}{2} + \frac{5\Theta}{2}$

- For $N_R = 7$: $\phi^t_1 = \frac{\pi}{2} + 3\Theta$

As we can observe from Figure 5.6-1, that the numerical results validate the aforementioned optimal transmit orientation. Thus, in this section we provide a generic and scalable framework that can be used for practical scenarios and adapt to it for any number of receive antennas N_R. Moreover, in Figure 5.6-2 that represents the SE variation with respect to the ULA receive array orientation rotation, it is shown how the rotation of the receiver from the transmit broadside direction ϕ_{rot} affects the SE as the scenario shown in Figure 5.3-2.

In Figure 5.7- 1 that represents the equivalent channel before deployment optimization for a given channel realization, it is shown that for a highly correlated scenario ($\Theta \approx 0$), after adding the analog beamsteering, the received paths at the two receive antennas are highly correlated. However, when the transmit array is deployed as in Equation (5.29), the correlation effect decreases as expected and as shown in Figure 5.8- 1. Moreover, the effect of the deployment optimization on the correlation is more significant after applying the ZF in the digital layer and is significant in the difference between Figure 5.7- 2 and Figure 5.8- 2. Similar analysis is done in Figures 5.9 and 5.10 for higher number of receive antennas ($N_R = 5$).

In Figure 5.11, we plot the upper bound for the achieved SE in case no deployment optimization is applied for the LoS scenario (the case defined in proposition 2) using Jensen inequality

as follows:

$$\mathbb{E}[\epsilon] \leq \log_2(1 + \rho(\mathbb{E}[\Lambda])) \tag{5.55}$$

where $\mathbb{E}[\Lambda]$ is defined in Equation (5.18). We validate in Figure 5.11 the SE models by numerical SE results for different deployment scenarios for the LoS channel environment and the multi-path one. It is also shown that, in mmWave systems the SE is enhanced when optimal deployment is utilized at the transmitter at the LoS case. Moreover, the SE is further enhanced when multiple paths exists, as these multipath components offered by the channel can be captured by the EGT analog beamforming and decorrelate the received spatial streams.

In Figure 5.12-1, similarly, we validate the BER models as it is shown that both the theoretical and numerical BER results match for different deployment scenarios for the LoS channel environment and the multi-path one. Moreover, it is obvious that in the multipath case, the spatial correlation between the spatial streams decreases leading to improved BER performance compared to the pure LoS case.

Finally in Figure 5.12-2, the theoretical BER is compared for different deployment scenarios. We highlight three factors that can affect the BER performance of the system, which are the number of paths of the channel, the receive antennas' inter element spacing, and the number of the transmit antennas. The number of paths is defined by the propagation environment and can not be tuned, but we can only adapt to it using the suitable analog beamforming algorithm (EGT in case of multipath and LoS beamsteering in case of LoS channel). However, the number of the transmit antennas and the receive antennas' spacing can be adjusted given certain deployment constraints.

5.1.8   Conclusion

In this section, a detailed study for Spatial Modulation in mmWave system was given, covering all possible scenarios analytically and numerically compared to the existing work in the literature. We derived closed form solutions for the SE in case of pure LoS channel environment for any possible deployment scenario, given that two receive antennas exist, and optimal transmit array deployment optimization is applied for correlation minimization. Similarly, we derived closed form solutions for the BER in case of pure LoS channel environment for any possible deployment scenario, given that two receive antennas exist, and optimal transmit array deployment is applied for correlation minimization. Moreover, a closed form solution for the BER was derived for multipath channel environments as well to have a complete analysis for the achievable performance of the Receive Spatial Modulation with Hybrid Beamforming. All the introduced models were validated with numerical analysis.

From the analytical and numerical analysis, it is shown that RSM is practically feasible at mmWave frequencies and can achieve considerable SE and BER with carefully applying suitable beamforming and correlation minimization techniques at the transmitter, and increasing the inter antenna element spacing at the receiver. Henceforth, the low complexity receiver design gain can be completely leveraged at mmWave frequencies.

5.2 HBF with Beam Index Modulation

In this section, a novel Beam Index Modulation (BIM) architecture is introduced for mmWave communications. Indeed, Spatial Scattering Modulation (SSM) and BIM have recently been proposed as an extension for Spatial Modulation (SM) to deal with sparse non LoS channel environments. However, these approaches lack complete analyses for practical scenarios. SSM is limited to orthogonal channel paths and does not consider the cross-talk between the paths, while BIM was hitherto studied for analog beamforming scenarios in which the cross-talk between the beams is not tackled. Aiming at mitigating such inter-beam cross-talk, we propose to add a digital precoding layer to the conventional analog-BIM framework, thus leading to a hybrid-BIM scheme. We analyze the performance of such new scheme by deriving the analytic closed form approximation of the achievable SE and BEP. Simulation results validate our theoretical results and highlight the performance gain in BEP brought by the HBF strategy applied to BIM in mmWave communications.

5.2.1 Background

IM has recently been proposed as a low complexity-energy efficient technique for next generation wireless communication systems [175]. Specifically, SM has become a classical IM technique applied along the spatial axis, where the index of the transmit or receive antennas codes useful information [154]. With the emerging mmWave systems, SM has recently been adapted to sparse scattering propagation conditions. As an example SM dealing with pure LoS channels has been studied in [159], where analog beamforming is implemented.

However, in order to utilize both the transmit and receive antenna array gains, another IM technique applied to the spatial domain and referred to as SSM has been proposed in [170] in which the transmitter is equipped with a single RF chain and an array of transmit antennas and it steers the transmit beam each time on a different channel path to convey spatial information in the uplink transmission. On the other hand the receiver is equipped with an array of receive antennas and multiple RF chains, such that each RF chain is responsible for sensing the received power from a given path (beam). Afterwards, maximum likelihood detection is applied to detect the correct receive beam and extract the spatial and the IQ information. BIM has been proposed very recently [167] as a more hardware efficient extension to SSM. The idea behind BIM is similar to SSM which is exploiting the multiple path scattering in a given channel by mapping the information bits onto the indexes of the beams associated to the propagation paths that can be established between the transmitter and the receiver. The main advantage of BIM over SSM is that it only requires a single RF chain at both the transmitter and the receiver unlike the SSM that needs multiple RF chains at the receiver. This is because BIM uses power detectors at the receiver to decide which beam has been used for transmission instead of the maximum likelihood detection in SSM. In [176] the authors proposed Spatial Path Index Modulation (SPIM) which is exactly similar approach to BIM. However, they provided theoretical analysis and necessary condition for SPIM with analog beamforming to be superior in SE to analog beamforming without SPIM in mmWave MIMO channels. In [170, 167, 176], the authors restrained the study to the simple case of analog beamforming suffering from potential inter-
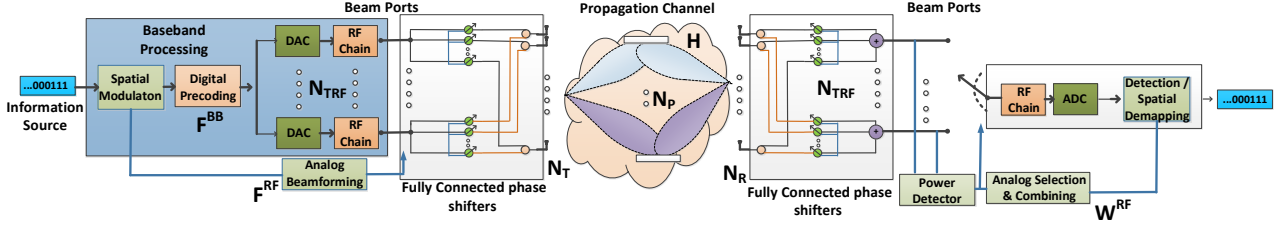
Figure 5.13: Block diagram of BIM with HBF architecture

beam cross-talk that can possibly cause wrong beam detection at the receiver.

Therefore, in this section, we extend the analog BIM and SSM approaches by making use of a HBF architecture at the transmitter instead of the pure analog one, where the additional digital precoder aims at mitigating the inter-beam cross-talk. We provide analytical approximations for the SE and BEP expressions of the proposed hybrid-BIM system when applying the ZF criterion to the digital precoder. We then highlight the enhancement provided by the hybrid-BIM approach compared to the BIM and SSM thanks to mitigating the inter-beam cross-talk.

5.2.2   Hybrid Beam Index Modulation Model

The proposed system is a MIMO one equipped with N_T transmit antennas, N_R receive antennas, N_{TRF} transmit RF chains and 1 receive RF chain, where N_{TRF} is smaller than or equal the number of physical channel paths N_p as shown in Figure 5.13. The proposed system considers ZF digital precoding in the BB part at the transmitter leading to mitigating the inter-beam cross-talk. Therefore, the received signal at the detector is given as follows:

$$\forall j, \quad r_j = \begin{cases} \sqrt{\Lambda_j} + u_j & \text{, if } j^{th} \text{ beam is targeted} \\ u_j & \text{, otherwise} \end{cases} \tag{5.56}$$

where $u_j = \mathbf{w}^{RF}_j n_j$ is the received noise at beam j after applying the analog combiner $\mathbf{w}^{RF}_j \in \mathbb{C}^{N_R \times 1}$ on the noise $n_j \sim \mathcal{CN}(0, \sigma_n^2)$ with variance σ_n^2 at the receiver. While, $\sqrt{\Lambda_j}, j \in [1, N_{TRF}]$ is the scaling factor for beam j that ensures the normalization of the transmitted power after HBF and it is calculated as:

$$\sqrt{\Lambda_j} = \sqrt{\frac{\rho}{\mathrm{Tr}\left(\left(\mathbf{F}^{RF}\mathbf{F}^{BB}\mathbf{s}_j \right)^H \mathbf{F}^{RF}\mathbf{F}^{BB}\mathbf{s}_j \right)}}. \tag{5.57}$$

where ρ is the transmit SNR, $\mathbf{H} \in \mathbb{C}^{N_R \times N_T}$ is the MIMO flat fading channel matrix. $\mathbf{F}^{RF} \in \mathbb{C}^{N_T \times N_{TRF}}$ is the analog beamformer at the transmitter. $\mathbf{F}^{BB} \in \mathbb{C}^{N_{TRF} \times N_{TRF}}$ is the digital ZF precoder used to annihilate the inter-beam cross-talk.

The transmit symbol $\mathbf{s}_j$ is the vector of IQ bits mapped to one of the $N_b = N_{TRF}$ beams denoted j to convey extra $m = \log_2(N_b)$ spatial information bits. Therefore, j denotes the index of the activated beam that should be targeted according to the spatial mapping such that for a

given transmission, the spatial mapping over the beams is as follows $\begin{bmatrix} 0 & ... & \underbrace{\mathbf{s}_j}_{j-thposition} & ... & 0 \end{bmatrix}^T$.

Then, the extra spatial $m = \log_2(N_b)$ bits can be extracted at the receiver from the knowledge of the beam index j and concatenated with the IQ bits. At the receiver side, the generalized BIM receiver has to detect the N_b targeted beams using analog beam combining and power detectors. The block diagram of the hybrid beamforming BIM system is depicted in Figure 5.13.

5.2.3 Channel Model

Then, the active path selection is done at both the transmitter and the receiver through beam training and beam alignment steps [177]. The channel matrix for each path (transmit-receive beam pair) j is represented as follows:

$$\mathbf{H}_j = \sqrt{N_T N_R}\alpha_j \mathbf{a}_r(\phi^r{}_j)\mathbf{a}_t(\phi^t{}_j)^H, \tag{5.58}$$

where α_j is the complex amplitude of propagation path j which is one of the N_b chosen and follows a complex Gaussian distribution $\alpha_j \sim \mathcal{CN}(0,1)$. $\phi^t{}_j$ represents the AoD for path j, such that $\phi^t{}_j \sim \mathcal{U}[0,2\pi]$. $\phi^r{}_j$ represents the AoA for path j, such that $\phi^r{}_j \sim \mathcal{U}[0,2\pi]$. Finally, $\mathbf{a}_t(\phi^t{}_j)$ and $\mathbf{a}_r(\phi^r{}_j)$ are the transmit array and receive array steering vectors respectively. Here, we ULA for transmit and receive arrays with half wavelength antenna spacing. Henceforth, the steering vectors $\mathbf{a}_t(\phi^t{}_j)$ and $\mathbf{a}_r(\phi^r{}_j)$ can be calculated using Equation (2.6).

5.2.4 Beamforming and Combining Technique

In the proposed scheme, the analog beamformer and combiner are designed in order to align the transmit and receive beams to discriminate between different paths of the channel, where the selection of the active paths is related to the transmitted spatial symbol using BIM. As aforementioned, only the most dominant N_b channel paths are chosen for transmission, such that N_b is chosen to satisfy $N_b \leq N_p$. The dominant paths are estimated using conventional beam training techniques [177].

Therefore, the analog beamformer at the transmitter side is calculated as follows $\mathbf{F}^{RF} = [\mathbf{a}_t(\phi^t{}_i)]_{i=[1:N_b]}$. Also, the analog beam combiner is calculated at the receiver side as follows $\mathbf{W}^{RF} = [\mathbf{a}_r(\phi^r{}_i)^H]_{i=[1:N_b]}$. Furthermore, the equivalent channel $\hat{\mathbf{H}}$ is calculated as: $\hat{\mathbf{H}} = \mathbf{W}^{RF}\mathbf{H}\mathbf{F}^{RF}$. Finally, the ZF precoder is calculated as $\mathbf{F}^{BB} = \hat{\mathbf{H}}^H(\hat{\mathbf{H}}\hat{\mathbf{H}}^H)^{-1}$ for the inter-beam cross-talk mitigation.

5.2.5 Analytical Analysis for HBF with BIM

Closed form BEP conditioned by the channel

Here, we only consider the BEP analysis for the spatial symbols, since the IQ symbols' BEP depends on the $M-ary$ IQ modulation used. Hence, we only consider the BEP of the spatial

symbols to make our analysis generic for any $M-ary$ modulation. The formula that derives the analytic average BEP conditioned by the channel $\mathcal{P}_e$ for the BIM scheme is:

$$\mathcal{P}_e = \frac{1}{N_b} \cdot \mathbb{E}\left\{ \sum_{k}^{N_{TRF}} \sum_{j \neq k}^{N_{TRF}} \mathbb{P}(\mathbf{s}_k \rightarrow \mathbf{s}_j) d_{Ham}(\mathbf{s}_k, \mathbf{s}_j) \right\}. \tag{5.59}$$

where $d_{Ham}(\mathbf{s}_k, \mathbf{s}_j)$ is the Hamming distance between two spatial symbols $\mathbf{s}_k$ and $\mathbf{s}_j$, and $\mathbb{P}(\mathbf{s}_k \rightarrow \mathbf{s}_j)$ is the Pairwise Error Probability (PEP) between $\mathbf{s}_k$ and $\mathbf{s}_j$.

Proposition 7. *Considering the maximum likelihood detection, the closed form PEP of the hybrid BIM scheme conditioned by the knowledge of the channel matrix $\mathbf{H}$ is:*

$$\mathbb{P}(\mathbf{s}_k \rightarrow \mathbf{s}_j | \mathbf{H}) = Q\left(\frac{\sqrt{\Lambda_j}}{\sqrt{2}\|\mathbf{w}^{RF}{}_k - \mathbf{w}^{RF}{}_j\|\sigma_n^2} \right) \tag{5.60}$$

Proof. The PEP is represented as,

$$\mathbb{P}(\mathbf{x}_k \rightarrow \mathbf{x}_j | \mathbf{H}) = \mathbb{P}(d_k > d_j | \mathbf{H}) = \mathbb{P}((n_j \sqrt{\Lambda_j} - n_k \sqrt{\Lambda_j}) > \frac{1}{2}(2\sqrt{\Lambda_j}^2) | \mathbf{H}) = Q(\sqrt{\xi}) \tag{5.61}$$

where $d_j = \|\mathbf{r} - \sqrt{\Lambda_j}\mathbf{s}_j\|^2$ and $Q(x)$ is the Gaussian distribution function: $Q(x) = \int_x^\infty \frac{1}{2\pi} e^{-\frac{x^2}{2}} dx$ and ξ is calculated as follows $\xi = \frac{\Lambda_j}{2\|\mathbf{w}^{RF}{}_k - \mathbf{w}^{RF}{}_j\|^2 \sigma_n^2}$. ∎

SE Analysis for hybrid BIM

Here we analyze the achievable SE of the HBF BIM system. As shown in [167], the SE can be split into two parts, one part that considers the SE from the spatial symbols ϵ_{BIM} and the other part considers the SE of the information transmitted through the IQ bits using HBF ϵ_{HBF}. The first part ϵ_{BIM} is given as follows [167, Eq. 5]:

$$\epsilon_{BIM} = \frac{1}{N_{TRF}} \sum_{i=1}^{N_{TRF}} \sum_{j=1}^{N_{TRF}} P_{i,j} \log_2\left(\frac{P_{i,j}}{\frac{1}{N_{TRF}} \sum_{s=1}^{N_{TRF}} P_{s,j}} \right) \tag{5.62}$$

where $P_{i,j}$ represents the probability that beam j is selected at the receiver when beam i is used for transmission (i.e. error in beam detection in case $i \neq j$). In [167, 170], this error in detection for the spatial beams can happen due to both the inter-beam cross talk and the AWGN noise. However, in our proposed hybrid BIM system, the inter-beam cross-talk is mitigated using ZF and only AWGN can cause a detection error. Henceforth, using our hybrid BIM scheme the probability of the detection error is decreased compared to [167, 170]. Moreover, we provide a closed form expression for the error in detection for hybrid BIM in Equation (5.60).

Moving to ϵ_{HBF}, it can be expressed as follows:

$$\epsilon_{HBF} = \frac{1}{N_{TRF}} \sum_{i=1}^{N_{TRF}} P_{i,i} \log_2(1 + \rho \Lambda_i) \tag{5.63}$$

This expression for ϵ_{HBF} differs from the one in [167, Eq. 6] in two aspects: First, the receive SNR in our case is defined by the normalization factor of ZF instead of $\rho|\hat{\mathbf{H}}(i,i)|^2$ in [167]. This is because in our scheme, using ZF in the digital layer forces the equivalent channel to an identity matrix down-scaled by Λ_i for power normalization purposes. Moreover, the cross-talk useful information term in [167, Eq. 6] $\frac{1}{N_{TRF}}\sum_{i=1}^{N_{TRF}}\sum_{j=1,j\neq i}^{N_{TRF}} P_{i,j}\log_2(1+\rho|\hat{\mathbf{H}}(i,j))|^2$ does not exist in hybrid BIM because ZF mitigates the inter-beam cross-talk and any beam detection error is only caused by the noise which does not carry any information.

SE approximation at high SNR Massive MIMO

As shown in Equation (5.60), it is clear that as the transmit SNR ρ increases, the probability of beam detection error tends to zero (i.e. $P_{i,j\neq i} = \mathbb{P}(\mathbf{s}_i \to \mathbf{s}_j|\mathbf{H}) \to 0$ when $\rho \to \infty$). Therefore, at high SNR regime, ϵ_{BIM} in Equation (5.62) can be approximated as $\epsilon_{BIM} \approx \log_2(N_{TRF})$ after substituting $P_{i,j} = 0, \forall i \neq j$ and $p_{i,j} = 1$ for $i = j$. Moreover, at high SNR regime, ϵ_{HBF} in Equation (5.63) can be approximated as $\epsilon_{HBF} \approx \frac{1}{N_{TRF}}\sum_{i=1}^{N_{TRF}} \log_2(1+\rho\Lambda_i)$. Therefore, the total SE of the hybrid BIM system at high SNR can be approximated as $\epsilon \approx \log_2(N_{TRF}) + \frac{1}{N_{TRF}}\sum_{i=1}^{N_{TRF}} \log_2(1+\rho\Lambda_i)$. Our aim in this subsection is to find the closed form approximation of the SE of hybrid BIM over the channel statistics which is more feasible when we assume high SNR regime. Since the ϵ_{BIM} is approximated as $\log_2(N_{TRF})$ at high SNR, so it does not depend on the channel statistics anymore. Therefore we will focus on finding the closed form approximation of ϵ_{HBF}. After applying the analog beamforming and combining, the equivalent channel $\hat{\mathbf{H}}$ for a given beam j is given as follows:

$$|\hat{\mathbf{H}}(j,j)| = |\mathbf{w}^{RF}{}_j\mathbf{H}_j\mathbf{f}^{RF}{}_j| = \frac{1}{\sqrt{N_T N_R}}\sum_{i=1}^{N_T}\sum_{i=1}^{N_R}|\alpha_j| = \sqrt{N_T N_R}|\alpha_j|. \quad (5.64)$$

In Equation (5.64), the cancellation of the phase effects arising from the channel spatial dimensions (AoD and AoA) through beam alignment can be observed, ending up with the amplitude of the channel gain $|\alpha_j|$ scaled by the transmit and receive antenna array gains $\sqrt{N_T N_R}$. On that basis, the equivalent channel $\hat{\mathbf{H}}$ can statistically be analyzed by splitting the diagonal and off-diagonal parts and tackling each one separately. Considering the diagonal term in Equation (5.64), and assuming that the channel complex values α are iid complex Gaussian $\alpha \sim \mathcal{CN}(0,1)$, we can conclude that $|\alpha|$ follows a Rayleigh distribution with mean $\frac{\sqrt{\pi}}{2}$ and variance $1 - \frac{\pi}{4}$. Therefore, we have:

$$|\mathbf{w}^{RF}{}_j\mathbf{H}_j\mathbf{f}^{RF}{}_j| \sim \mathbf{Rayleigh}\left(\frac{\sqrt{\pi N_T N_R}}{2}, N_T N_R(1-\frac{\pi}{4})\right). \quad (5.65)$$

Given that ϕ^t is uniformly distributed in $[0, 2\pi]$, $d_t = \frac{\lambda}{2}$ and that ϕ^t and α are statistically independent, the expected value of the off-diagonal term $\mathbb{E}\left\{|\mathbf{w}^{RF}{}_j\mathbf{H}_j\mathbf{f}^{RF}{}_{y\neq j}|\right\}$ can be expressed according to [178] as follows:

$$\mathbb{E}\left\{|\mathbf{w}^{RF}{}_j\mathbf{H}_j\mathbf{f}^{RF}{}_{y\neq j}|\right\} = \sqrt{N_R}\mathbb{E}\left\{|\alpha_j|\right\}\mathbb{E}\left\{\sum_{i=1}^{N_T}|\mathbf{a}_t(\phi^t{}_j)^H\mathbf{a}_t(\phi^t{}_y)|\right\} = \frac{\sqrt{N_R}\pi}{2N_T}\sum_{i=1}^{N_T}\mathcal{J}_0^2(\pi(i-1))$$

$$(5.66)$$

where $\mathcal{J}_0(x)$ is the zero order Bessel function of x and it decays in magnitude proportional to $\frac{1}{\sqrt{x}}$, which means that $\mathcal{J}_0^2(x)$ decays in magnitude proportional to $\frac{1}{x}$. Therefore, from Equations (5.65) and (5.66) the off diagonal term can be assumed to be negligible compared to the diagonal ones when N_T is large enough. Moreover, the off diagonal term is proved in [178] to approach 0, when $N_T \to \infty$ leading to the favourable propagation. Henceforth, considering the diagonal elements only, for tractability, the calculated SE can be considered as an upper bound for our framework.

Proposition 8. *The average ϵ_{HBF} SE tight upper bound approximation at high SNR with large number of transmit antennas is given as:*

$$\epsilon_{HBF} \approx \frac{2}{\ln 2} \left(\ln(\sqrt{\rho N_T N_R} \sigma) + \frac{\ln(2)}{2} - \frac{\kappa}{2} \right) \tag{5.67}$$

where $\kappa \approx 0.5772$ is the Euler constant and σ is the variance of α.

Proof. This upper bound for ϵ_{HBF} SE can be asymptotically achieved with increasing N_T and is represented as follows:

$$\epsilon_{HBF} \approx \mathbb{E} \left\{ \frac{1}{N_{TRF}} \sum_{j=1}^{N_{TRF}} \log_2 \left(1 + \rho |\mathbf{w}^{RF}_j \mathbf{H}_j \mathbf{f}^{RF}_j|^2 \right) \right\} \approx \mathbb{E} \left\{ \log_2 \left(1 + \rho N_T N_R |\alpha_j|^2 \right) \right\}. \tag{5.68}$$

now assuming that $\rho N_T N_R >> 1$, then $1 + \rho N_T N_R |\alpha_j|^2 \approx \rho N_T N_R |\alpha_j|^2$. Therefore, ϵ_{HBF} upper bound approximation can be expressed as:

$$\epsilon_{HBF} \approx \frac{2}{\ln 2} \mathbb{E} \left\{ \ln \left(\sqrt{\rho N_T N_R} |\alpha_j| \right) \right\} \tag{5.69}$$

where $\ln \left(\sqrt{\rho N_T N_R} |\alpha_j| \right)$ has a Log-Rayleigh distribution defined in [179] ($\ln \left(\sqrt{\rho N_T N_R} |\alpha_j| \right) \sim$ **LogRay**$(\rho N_T N_R \sigma^2)$) , where σ^2 is the variance of the complex Gaussian channel coefficients α. Then, the mean (μ) and variance (η^2) of $\ln \left(\sqrt{\rho N_T N_R} |\alpha_j| \right)$ are expressed as [179]: $\mu = \ln(\sqrt{\rho N_T N_R} \sigma) + \frac{\ln(2)}{2} - \frac{\kappa}{2}$ and $\eta^2 = \frac{\pi^2}{24}$. Therefore, the average η_{HBF} upper bound approximation can be expressed as in Equation (5.67). ∎

5.2.6 Numerical Analysis

Here, the performance of the proposed hybrid-BIM scheme is evaluated in terms of SE and BER. The number of transmit RF chains and the number of channel paths is set to $N_{TRF} = N_p = 2$ and hence $N_b = 2$, while only 1 receive RF chain exist at the receiver. Finally, we consider that perfect CSI is available at both the transmitter and the receiver.

In Figure 5.14, the performance of the proposed hybrid-BIM is evaluated through the measurement of the total SE $\epsilon = \epsilon_{BIM} + \epsilon_{HBF}$ versus the SNR. Two system configurations, namely $(N_T = 128, N_R = 8, N_b = 2)$ and $(N_T = 256, N_R = 16, N_b = 2)$, are considered. It is observed that the numerical results are tightly upper bounded by the theoretical ones for all setups and
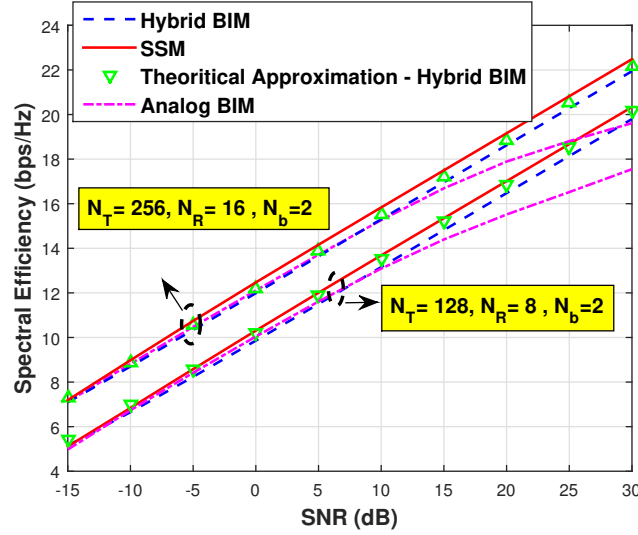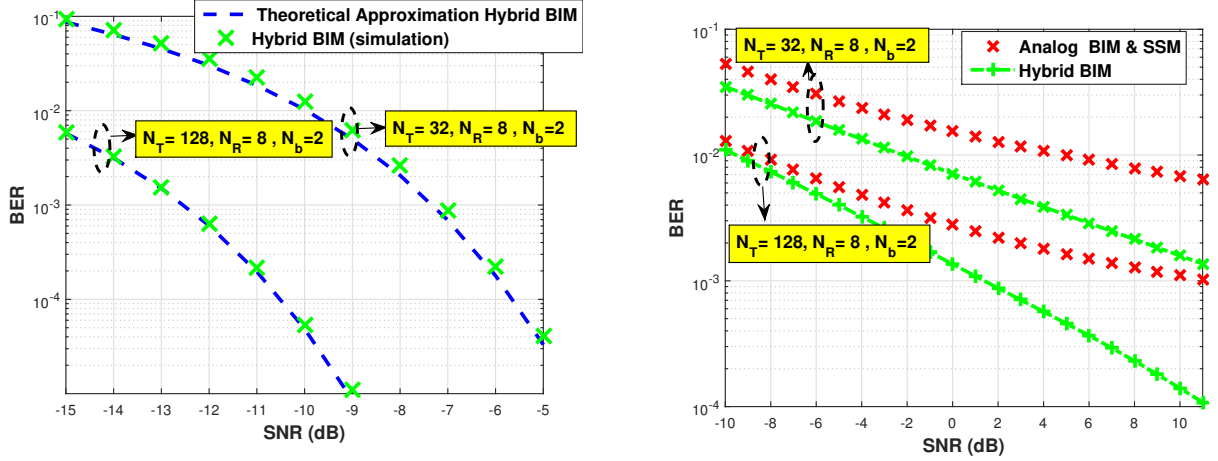
Figure 5.14: Comparing the SE for the proposed hybrid BIM with both SSM and analog BIM.

almost match asymptotically (N_T is large), hence validating the derived SE model in Proposition 2. Moreover, in order to benchmark the hybrid BIM we compare it with the SE of SSM [167, Eq. 4] and analog BIM [167, Eqs. 5-6] in the literature. As we expect, the hybrid BIM can achieve higher SE compared to the analog BIM at high SNR regime, since the system in this case is limited by the inter-beam cross talk and not the noise. However, the SSM can achieve slightly higher SE, which is again expected since the SSM has N_{TRF} RF chains at the receiver side, hence is capable of harvesting the information from the main beam and also from the cross-talk simultaneously.

In Figure 5.15a we validate the closed form BER expression for the hybrid BIM conditioned by the channel in Proposition 1 by simulations. Two system configurations, namely ($N_T = 128, N_R = 8, N_b = 2$) and ($N_T = 32, N_R = 8, N_b = 2$), are considered. As we can observe, both the theoretical curve and the simulation one perfectly match hence validating Proposition 1.

In Figure 5.15b, the performance of the proposed system is evaluated in terms of BER versus SNR over 100000 channel realizations in a Monte-Carlo fashion and using two system configurations, namely ($N_T = 128, N_R = 8, N_b = 2$) and ($N_T = 32, N_R = 8, N_b = 2$). Thanks to the inter-beam cross-talk cancellation capability, it is clearly seen that the hybrid-BIM scheme outperforms the analog-BIM and the SSM, and the performance gap increases with the SNR level due to the fact that the system becomes interference limited and no longer noise limited. Here, we assume that both analog BIM and SSM have the same BER, since we only consider the BER for the spatial bits which are not depending on the IQ modulation. Therefore, regarding the spatial bits only both SSM and analog BIM are similar in their detection mechanism [167].

(a) Comparing the analytical BER and the simulated one for hybrid BIM conditioned by the channel.

(b) Comparing the BER for the proposed hybrid BIM with both SSM and analog BIM.

Figure 5.15: Comparing the the BER for the proposed algorithms in a sparse non LoS channel.

5.2.7 Conclusion

In this section, Beam Index Modulation with Hybrid Beamforming at the transmitter and analog combining at the receiver is introduced and studied in a mmWave context. Analytical derivations of the SE and BEP of the proposed hybrid-BIM scheme are provided. Thereby, it is shown that the hybrid-BIM approach increases the system SE and decreases the BER significantly compared to the analog BIM specially at high SNR regime on the cost of increased hardware complexity (N_{TRF} RF chains at the transmitter instead of 1). On the other hand, hybrid BIM was shown to decrease the BER of the transmission significantly compared to the Spatial Scattering Modulation(SSM), on the cost of a slight degradation in the SE with the same hardware complexity (both have N_{TRF} RF chains at one end and a single RF chain at the other).

Chapter 6

Conclusion and Future Work

Contents

6.1   Conclusion

In this thesis, we studied hybrid MU mmWave massive MIMO schemes. The thesis was based on four axes for such a system which are:

- Analytical Analysis: In chapter 3, we started by considering a pure LoS channel, and defined the condition for which both HBF and full digital beamforming achieve similar SE. Then, we analytically provided a closed form expression for the SE of the analog LoS beamsteering and the corresponding HBF in pure LoS channel. Later, we analyzed the SE performance of multiple analog beamformers in sparse multipath channel and their corresponding HBF extension, and we provided a novel low complexity analog beamforming and HBF that can achieve sub-optimal SE performance. Finally, we validated all the analytical models using simulation results.

- Low Complexity Algorithms Development: In chapter 4, we provided low complexity signal processing techniques in order to enable practical MU massive MIMO mmWave systems. We started by considering a low complexity angular based beamforming and power allocation framework for LoS dominated mmWave channels. This angular framework relies on DBS for beamforming and LBPA for power allocation. Henceforth ensuring low-complexity and low overhead requirements needed for MU massive MIMO mmWave systems. Later, we proposed a novel low complexity UEs selection approach named leakage based UEs selection and studied its performance in pure LoS channels. Finally, we presented analog EGT as an effective solution for the blockage problem in mmWave channels.

- HBF with Index Modulation Analysis: In chapter 5, a detailed study for SM in mmWave system was given, covering all possible scenarios analytically and numerically compared to the existing work in the literature. We derived closed form solutions for the SE in case of pure LoS channel environment for any possible deployment scenario, given that two receive antennas exist per UE, and optimal transmit array deployment optimization is applied for correlation minimization. Similarly, we derived closed form solutions for the BER in case of pure LoS channel environment for any possible deployment scenario, given that two receive antennas exist, and optimal transmit array deployment is applied for correlation minimization. Moreover, a closed form solution for the BER was derived for multipath channel environments as well, in order to have a complete analysis for the achievable performance of the RSM with HBF. All the introduced models were validated with numerical analysis. Later, BIM with HBF at the transmitter and analog combining at the receiver was introduced and studied in a mmWave context. Analytical derivations of the SE and BEP of the proposed hybrid-BIM scheme are provided. Thereby, it was shown that the hybrid-BIM approach increases the system SE and decreases the BER significantly compared to the analog BIM in the literature.

- Channel Sounding and Simulations Verification: In chapter 6, we provided channel sounding results for two channels, one at 2.4 GHz with sparse channel environment and the other at 60 GHz. It was shown that sounded channel 2.4 GHz with sparse environment can be perfectly described by the statistical sparse channel model used throughout the thesis. On the other hand the sounded channel at 60 GHz can be better described by the pure LoS version of the sparse statistical model due to the fact that the LoS is highly dominant compared to the sparse channel components.

6.2 Future Work

In this thesis we considered a narrowband channel model for the mmWave MIMO channel. Also we assumed perfect CSI is available and assumed single cell scenarios with stationary communication terminals. Moreover, we only considered one analog hardware architecture which is the fully connected phase shifters one. Therefore, as a future work, the presented algorithms need to be extended to account for the following scenarios:

- Frequency Selective Channels: In mmWave MIMO systems with HBF, the extension from narrowband to wideband analysis is not straightforward as in microwave channels. This is due to the fact that in such systems analog beamforming exist, which has flat frequency response over wide BW and can not be changed from one sub carrier to another as the case with digital beamforming in microwave systems. Therefore, it is important to evaluate the extension of the proposed HBF techniques in this thesis to deal with the frequency selective channel scenario.

- Imperfect CSI: In realistic scenarios, the assumption of perfect CSI is no longer valid. Therefore, different channel estimation techniques need to be used in conjunction with

the proposed HBF algorithms in the thesis to evaluate the sensitivity of such algorithms with realistic channel estimation error.

- Multi Cell Scenario: In order to evaluate the scalabilty of our proposed algorithms and whether they can be applied in a distributed fashion or a centralized one, the extension from single cell to the multi cell scenario is neeeded. In such case the inter cell interference needs to be considered and tackled by the system.

- Mobility and Spatial Coherence: In order to make our propsed algorithms more efficient for realistic scenarios, considering the UEs mobility is crucial. In such case the spatial coherence needs to be evaluated to know the effect of the mobility on the degradation of the signal. Moreover, beamtracking techniques can be developed in conjunction with our proposed algorithms to ensure that no severe degradation of the received signal will happen in case of mobility.

- Different Analog Hardware Architectures: In order to have more realistic scenario for hardware prototyping, the proposed algorithms need to be extended to consider multiple possible low complexity analog hardware networks such as sub connected phase shifters networks, switching networks and fixed beamforming networks.

Appendix A

Sparse Channel Sounding at 2.4 GHz

In this part, an implementation of a sparse wireless transmission system at 2.4 GHz will be elaborated starting with the platform used and modified to reach our goal using the National Instruments (NI) massive MIMO framework. Then, we will provide a comparison between the simulation results using the statistical physical ray based channel model in Subsection 2.2.4 and the realistic one sounded using the NI massive MIMO platform for the sake of realistic validation.

A.1 Channel Sounder Brief Description

As a tool used for sounding the channel, the NI massive MIMO framework was used to emulate the BS. It implements important features of an OFDM physical layer, with 3GPP LTE TDD-like specifications. The physical layer processes 20 MHz of signal BW in real time using Field Programmable Gate Arrays (FPGAs). It includes, variable modulation schemes, MIMO equalization, channel reciprocity based linear precoding, reciprocity calibration, synchronization functionality, and other features. It can support up to 128 antennas at the BS (however, in our system we are limited to 8 antennas) with up to 12 single-antenna UEs or a multi-antenna UEs with up to 12 antennas. This is due to the downlink transmission model of the system that transmits on the same time-frequency components for the twelve spatial layers available based on one of three precoding algorithms (ZF, MMSE, MRT) using the CSI obtained from pilot symbols transmitted in the uplink (channel reciprocity).

A.2 Channel Sounding Scenario and Numerical Results

In this section, we will present the channel sounding scenario adopted using the NI massive MIMO platform. In order to have a sparse channel at 2.4 GHz we place the platform in an Anechoic chamber as shown in Figure A.1. Thus, we guarantee to have a sparse channel with only a few paths surviving from the transmitter to the receiver, unlike the nature of the propagation channel at 2.4 GHz thanks to the Anechoic chamber effect. The BS (Transmitter) is represented by the NI massive MIMO platform and two UEs (Receivers) are represented by a
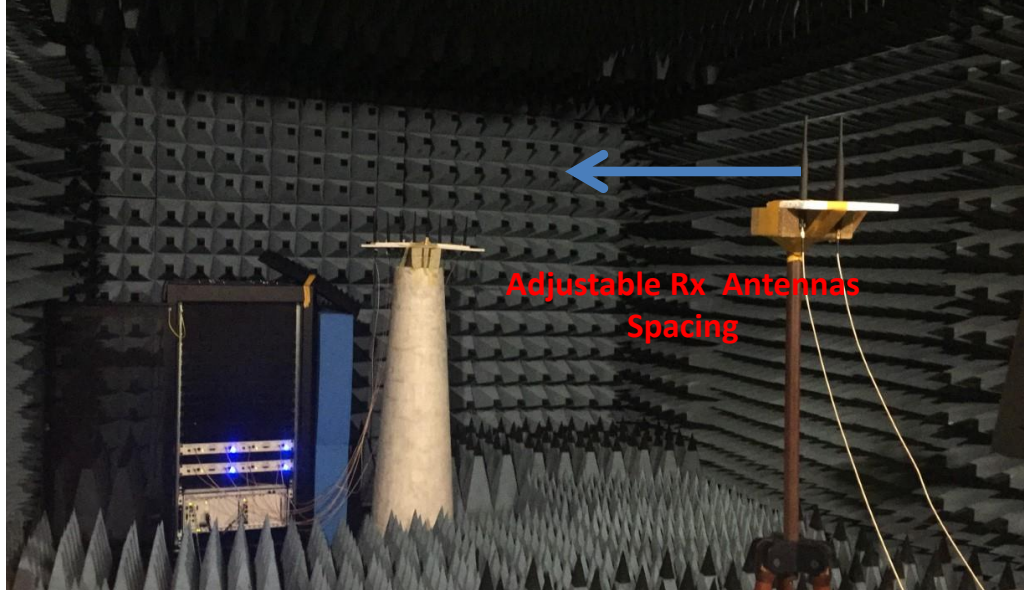
Figure A.1: The setup of our proposed channel sounder.

single Universal Software Radio Peripheral (USRP) with two antenna ports, such that each port acts as a separate UE. The parameters of the channel sounding setup are adjusted as shown in Table A.1.

Table A.1: Parameters of the proposed channel sounder.

Parameter	Value
Center Frequency	2.4 GHz
Tx Inter-antenna Spacing	$\frac{\lambda}{2} = \frac{3}{48}$ m
Transmit Power	22 dBm
BW	20 MHz
Tx-Rx Distance	3 m
Rx Antenna Spacing	2 m (MU MISO)
Number of Tx Antennas	8
Number of Rx Antennas per UE	1
Number of UEs	2
Transmit Array Architecture	ULA

As shown in Figure A.1, the distance between the two receive antennas can be adjusted and each of them act as a single mobile station, thus emulating a MU MISO scenario. In our proposed scenario we adjust the distance between the two antennas at the receiver to be 2 m in order to have enough spatial separation between the two UEs, given that the BS is equipped

with only 8 antennas. Now, in order to compare the Spectral Efficiency achieved with taking into account the proposed realistic channel sounder, and with the statistical physical ray based channel model in Subsection 2.2.4, we set up a simulation environment similar to the channel sounding scenario. In order to do this, estimating the number of significant (dominant) paths in the sounded channel is crucial. Using high resolution spatial DFT estimation, we observed that the sounded channel has approximately 4 dominant paths as shown in Figure A.2. Therefore, we set up the simulation environment using the parameters summarized in Table A.2. These simulation parameters resulted in an accurate approximation to the sounded channel as shown in Figures A.2 and A.3. In both Figures A.2 and A.3, we can observe that the channel has ≈ 4 dominant paths (LoS shown by the red arrow and the multipath components shown by the blue arrows). Thus, the channel can be approximated using only these 4 angular directions (paths/beams).

Table A.2: Parameters of the proposed simulation environment.

Parameter	Value
Channel Model	Sparse Statistical Model [86]
Number of paths	4
AoD Distribution	Uniform $[0, 2\pi]$
Tx Inter-antenna Spacing	$\frac{\lambda}{2}$
Transmit Power	30 dBm
Number of Tx Antennas	8
Number of Rx Antennas per UE	1
Number of UEs	2
Transmit Array Architecture	ULA

As shown in Figures A.4 and A.5, the SE has the same behaviour for both channels (sounded and simulated) with approximately the same slope for different beamforming algorithms. However a constant gap arises between the SE of the sounded channel and the simulated one. This gap is due to the fact that the simulated channel considers only the small scale fading and does not consider the difference in transmit power, noise power or the path loss. Therefore, in our simulations we quantified this gap in this scenario to be *approx*18 dB. Henceforth, by normalizing this gap that arises from the transmit power difference, path loss and noise both channel will approximately achieve the same SE performance. This result is a valuable one since it validates that the statistical physical ray based channel model [86] is accurate enough to model practical channels, when the channel is sparse and the channel path's powers are approximately the same (which is the case at 2.4 GHz in an Anechoic chamber).

A.2.1   Conclusion

In this section, we presented a channel sounding setup at 2.4 GHz. In order to force the channel at such frequency to be sparse we deployed our proposed channel sounder in an Anechoic
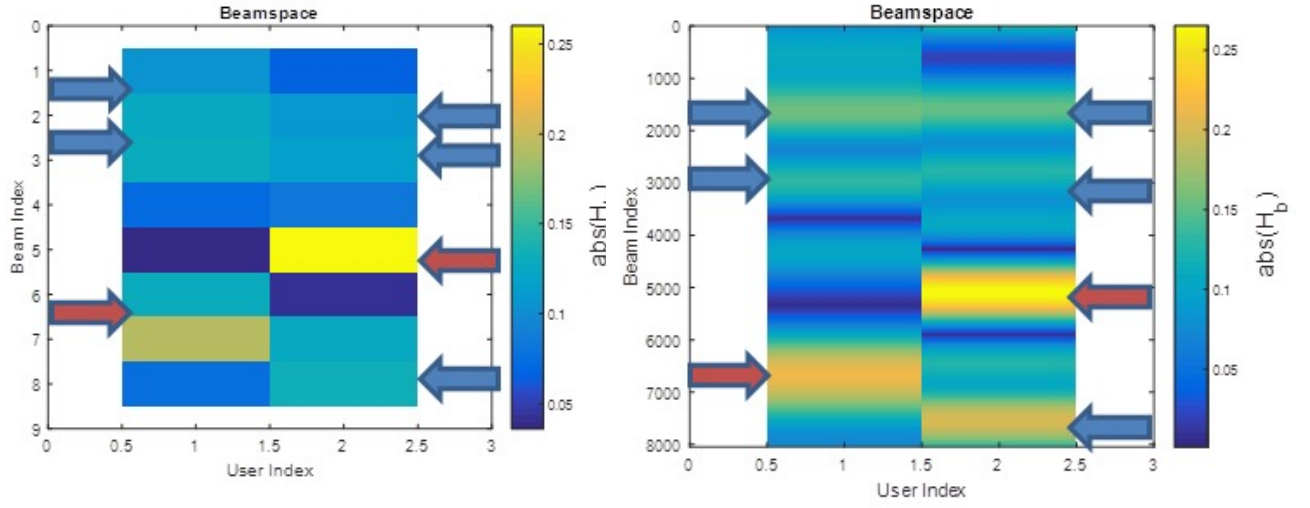
(a) The dominant channel paths received by each UE estimated using 8 point DFT for the proposed channel sounder.

(b) The dominant channel paths received by each UE estimated using 8000 point DFT for the proposed channel sounder.

Figure A.2: The beamspace channel $\mathbf{H}_b$ estimated using DFT for the proposed channel sounder.
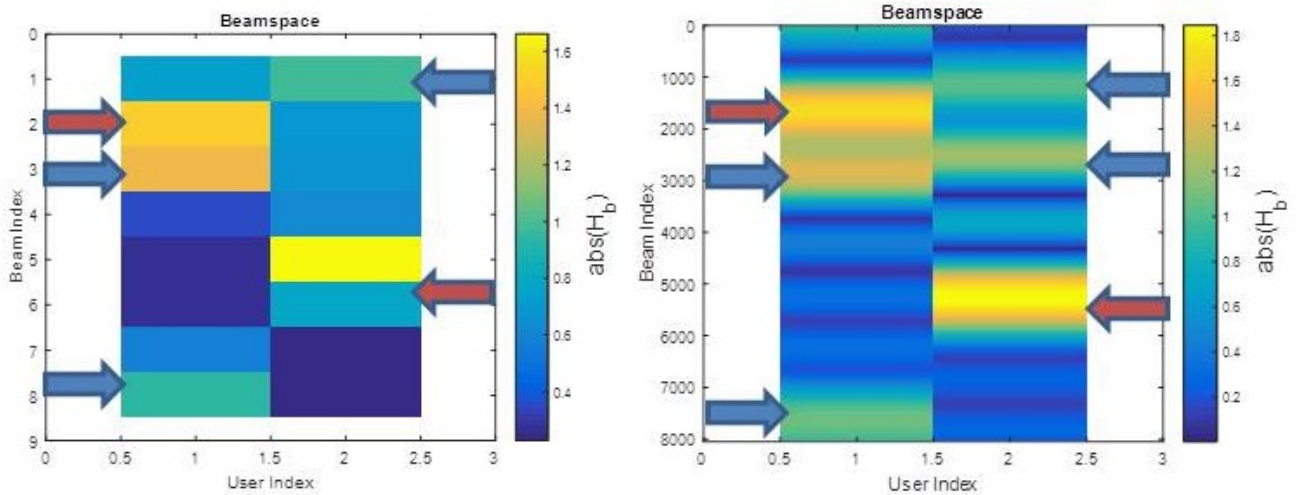
(a) The dominant channel paths received by each UE estimated using 8 point DFT for one channel realization using the proposed simulation environment.

(b) The dominant channel paths received by each UE estimated using 8000 point DFT for one channel realization using the proposed simulation environment.

Figure A.3: The beamspace channel $\mathbf{H}_b$ estimated using DFT for the proposed simulation environment.
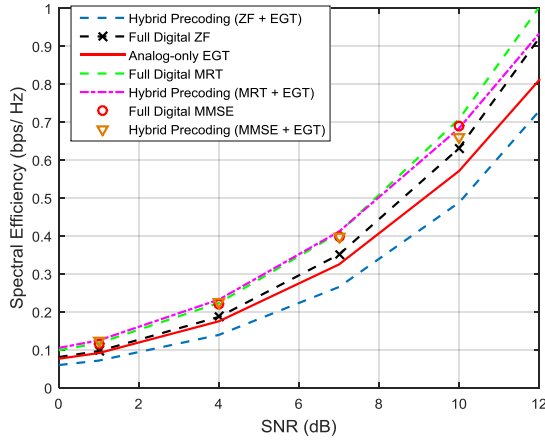
(a) The achievable SE considering the sounded channel at low SNR regime.
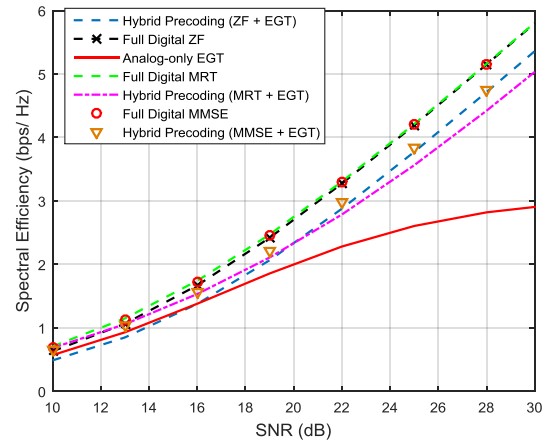
(b) The achievable SE considering the sounded channel at high SNR regime.

Figure A.4: The achievable SE considering the sounded channel.
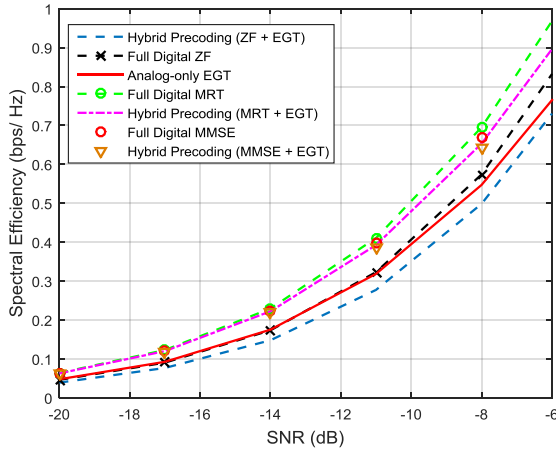
(a) The achievable SE considering the simulated channel at low SNR regime.
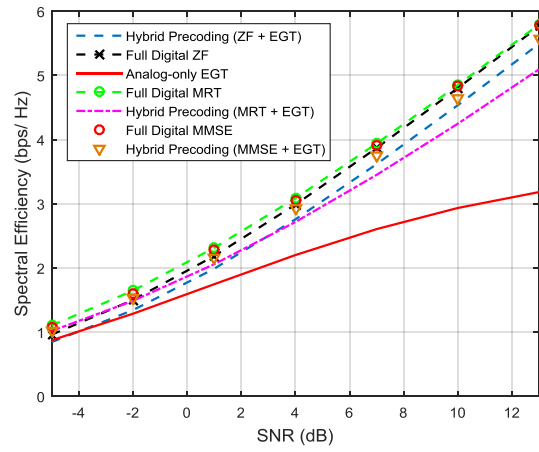
(b) The achievable SE considering the simulated channel at high SNR regime.

Figure A.5: The achievable SE considering the simulated channel.

chamber. Given that, at such frequency the path loss is not high, the powers of the sparse channel paths are approximately similar. Therefore, we compared the SE achieved by multiple beamforming techniques in such channel with the SE achieved with the statistical physical ray based channel model in [86] which is widely used in the mmWave literature for modelling the channel. We showed by numerical analysis that after normalization of the path loss and transmit power differences, both channels yield approximately the same SE behaviour for different beamforming techniques with similar slope for similar number of paths.

Bibliography

[1] H. Q. Ngo, E. G. Larsson, and T. L. Marzetta, "Aspects of favorable propagation in massive mimo," in *2014 22nd European Signal Processing Conference (EUSIPCO)*, Sep. 2014, pp. 76–80.

[2] S. Malkowsky, J. Vieira, L. Liu, P. Harris, K. Nieman, N. Kundargi, I. C. Wong, F. Tufvesson, V. Öwall, and O. Edfors, "The world's first real-time testbed for massive mimo: Design, implementation, and validation," *IEEE Access*, vol. 5, pp. 9073–9088, 2017.

[3] L. N. Ribeiro, S. Schwarz, M. Rupp, and A. L. F. de Almeida, "Energy efficiency of mmwave massive mimo precoding with low-resolution dacs," *IEEE Journal of Selected Topics in Signal Processing*, vol. 12, no. 2, pp. 298–312, May 2018.

[4] O. E. Ayach, S. Rajagopal, S. Abu-Surra, Z. Pi, and R. W. Heath, "Spatially sparse precoding in millimeter wave mimo systems," *IEEE Transactions on Wireless Communications*, vol. 13, no. 3, pp. 1499–1513, March 2014.

[5] A. Alkhateeb, O. E. Ayach, G. Leus, and R. W. Heath, "Channel estimation and hybrid precoding for millimeter wave cellular systems," *IEEE Journal of Selected Topics in Signal Processing*, vol. 8, no. 5, pp. 831–846, Oct 2014.

[6] M. Shehata, A. Mokh, M. Crussière, and M. Helard, "On the equivalence between hybrid and full digital beamforming in mmwave communications," *The 26th International Conference on Telecommunications (ICT 2019)*, 2019.

[7] F. Sohrabi and W. Yu, "Hybrid digital and analog beamforming design for large-scale antenna arrays," *IEEE Journal of Selected Topics in Signal Processing*, vol. 10, no. 3, pp. 501–513, April 2016.

[8] A. F. Molisch, V. V. Ratnam, S. Han, Z. Li, S. L. H. Nguyen, L. Li, and K. Haneda, "Hybrid beamforming for massive mimo: A survey," *IEEE Communications Magazine*, vol. 55, no. 9, pp. 134–141, Sep. 2017.

[9] Y. J. Cho, G. Suk, B. Kim, D. K. Kim, and C. Chae, "Rf lens-embedded antenna array for mmwave mimo: Design and performance," *IEEE Communications Magazine*, vol. 56, no. 7, pp. 42–48, July 2018.

[10] I.-R. M.2083-0, "Imt vision-framework and overall objectives of the future development of imt for 2020 and beyond," Tech. Rep., 2015.

[11] Y. Wu, C. Xiao, Z. Ding, X. Gao, and S. Jin, "A survey on mimo transmission with finite input signals: Technical challenges, advances, and future trends," *Proceedings of the IEEE*, vol. 106, no. 10, pp. 1779–1833, Oct 2018.

[12] T. L. Marzetta, "Noncooperative cellular wireless with unlimited numbers of base station antennas," *IEEE Transactions on Wireless Communications*, vol. 9, no. 11, pp. 3590–3600, November 2010.

[13] J. Hoydis, S. ten Brink, and M. Debbah, "Massive mimo: How many antennas do we need?" in *2011 49th Annual Allerton Conference on Communication, Control, and Computing (Allerton)*, Sep. 2011, pp. 545–550.

[14] F. Rusek, D. Persson, B. K. Lau, E. G. Larsson, T. L. Marzetta, O. Edfors, and F. Tufvesson, "Scaling up mimo: Opportunities and challenges with very large arrays," *IEEE Signal Processing Magazine*, vol. 30, no. 1, pp. 40–60, Jan 2013.

[15] A. O. Martínez, E. De Carvalho, and J. Nielsen, "Massive mimo properties based on measured channels: Channel hardening, user decorrelation and channel sparsity," in *2016 50th Asilomar Conference on Signals, Systems and Computers*, Nov 2016, pp. 1804–1808.

[16] X. Wu, N. C. Beaulieu, and D. Liu, "On favorable propagation in massive mimo systems and different antenna configurations," *IEEE Access*, vol. 5, pp. 5578–5593, 2017.

[17] J. Li, D. Yue, and Y. Sun, "Performance analysis of millimeter wave massive mimo systems in centralized and distributed schemes," *IEEE Access*, vol. 6, pp. 75 482–75 494, 2018.

[18] T. S. Rappaport, S. Sun, R. Mayzus, H. Zhao, Y. Azar, K. Wang, G. N. Wong, J. K. Schulz, M. Samimi, and F. Gutierrez, "Millimeter wave mobile communications for 5g cellular: It will work!" *IEEE Access*, vol. 1, pp. 335–349, 2013.

[19] M. Shehata, M. Helard, M. Crussiere, A. Roze, and C. Langlais, "Angular based beamforming and power allocation framework in a multi-user millimeter-wave massive mimo system," in *2018 IEEE 87th Vehicular Technology Conference (VTC Spring)*, June 2018, pp. 1–6.

[20] M. Shehata, M. Crussiere, M. Relard, and P. Pajusco, "Hybrid beamforming for multi-user miso channels with equal gain transmission: A robust and spectral efficient approach," in *2018 25th International Conference on Telecommunications (ICT)*, June 2018, pp. 57–62.

[21] M. Shehata, M. Crussière, M. Hélard, and P. Pajusco, "Leakage based users selection for hybrid beamforming in millimeterwave mimo," in *2018 IEEE 29th Annual International*

Symposium on Personal, Indoor and Mobile Radio Communications (PIMRC), Sep. 2018, pp. 1144–1150.

[22] M. Shehata, M. Crussière, and M. Helard, "On the theoretical limits of beam steering in mmwave massive mimo channels," *IEEE International Symposium on Personal, Indoor and Mobile Radio Communications (PIMRC)*, 2019.

[23] F. Rusek, D. Persson, B. K. Lau, E. G. Larsson, T. L. Marzetta, O. Edfors, and F. Tufvesson, "Scaling up mimo: Opportunities and challenges with very large arrays," *IEEE Signal Processing Magazine*, vol. 30, no. 1, pp. 40–60, Jan 2013.

[24] G. Del Galdo and M. Haardt, "Comparison of zero-forcing methods for downlink spatial multiplexing in realistic multi-user mimo channels," in *2004 IEEE 59th Vehicular Technology Conference. VTC 2004-Spring (IEEE Cat. No.04CH37514)*, vol. 1, May 2004, pp. 299–303 Vol.1.

[25] T. Yoo and A. Goldsmith, "On the optimality of multiantenna broadcast scheduling using zero-forcing beamforming," *Selected Areas in Communications, IEEE Journal on*, vol. 24, no. 3, pp. 528–541, March 2006.

[26] F. Kaltenberger, M. Kountouris, L. Cardoso, R. Knopp, and D. Gesbert, "Capacity of linear multi-user mimo precoding schemes with measured channel data," in *2008 IEEE 9th Workshop on Signal Processing Advances in Wireless Communications*, July 2008, pp. 580–584.

[27] H. Yang and T. L. Marzetta, "Performance of conjugate and zero-forcing beamforming in large-scale antenna systems," *IEEE Journal on Selected Areas in Communications*, vol. 31, no. 2, pp. 172–179, February 2013.

[28] Y. Lim, C. Chae, and G. Caire, "Performance analysis of massive mimo for cell-boundary users," *IEEE Transactions on Wireless Communications*, vol. 14, no. 12, pp. 6827–6842, Dec 2015.

[29] J. Hoydis, S. ten Brink, and M. Debbah, "Massive mimo in the ul/dl of cellular networks: How many antennas do we need?" *IEEE Journal on Selected Areas in Communications*, vol. 31, no. 2, pp. 160–171, February 2013.

[30] M. Sawahashi, Y. Kishiyama, A. Morimoto, D. Nishikawa, and M. Tanno, "Coordinated multipoint transmission/reception techniques for lte-advanced [coordinated and distributed mimo]," *IEEE Wireless Communications*, vol. 17, no. 3, pp. 26–34, June 2010.

[31] H. Huh, G. Caire, H. C. Papadopoulos, and S. A. Ramprashad, "Achieving "massive mimo" spectral efficiency with a not-so-large number of antennas," *IEEE Transactions on Wireless Communications*, vol. 11, no. 9, pp. 3226–3239, Sep. 2012.

[32] K. T. Truong and R. W. Heath, "Effects of channel aging in massive mimo systems," *Journal of Communications and Networks*, vol. 15, no. 4, pp. 338–351, Aug 2013.

[33] U. Madhow, D. R. Brown, S. Dasgupta, and R. Mudumbai, "Distributed massive mimo: Algorithms, architectures and concept systems," in *2014 Information Theory and Applications Workshop (ITA)*, Feb 2014, pp. 1–7.

[34] A. Ashikhmin and T. Marzetta, "Pilot contamination precoding in multi-cell large scale antenna systems," in *2012 IEEE International Symposium on Information Theory Proceedings*, July 2012, pp. 1137–1141.

[35] L. Li, A. Ashikhmin, and T. Marzetta, "Pilot contamination precoding for interference reduction in large scale antenna systems," in *2013 51st Annual Allerton Conference on Communication, Control, and Computing (Allerton)*, Oct 2013, pp. 226–232.

[36] S. Lakshminarayana, M. Assaad, and M. Debbah, "Coordinated multicell beamforming for massive mimo: A random matrix approach," *IEEE Transactions on Information Theory*, vol. 61, no. 6, pp. 3387–3412, June 2015.

[37] G. Caire, S. A. Ramprashad, and H. C. Papadopoulos, "Rethinking network mimo: Cost of csit, performance analysis, and architecture comparisons," in *2010 Information Theory and Applications Workshop (ITA)*, Jan 2010, pp. 1–10.

[38] E. Björnson, J. Hoydis, M. Kountouris, and M. Debbah, "Massive mimo systems with non-ideal hardware: Energy efficiency, estimation, and capacity limits," *IEEE Transactions on Information Theory*, vol. 60, no. 11, pp. 7112–7139, Nov 2014.

[39] E. Björnson, M. Matthaiou, and M. Debbah, "Massive mimo with non-ideal arbitrary arrays: Hardware scaling laws and circuit-aware design," *IEEE Transactions on Wireless Communications*, vol. 14, no. 8, pp. 4353–4368, Aug 2015.

[40] S. K. Mohammed and E. G. Larsson, "Per-antenna constant envelope precoding for large multi-user mimo systems," *IEEE Transactions on Communications*, vol. 61, no. 3, pp. 1059–1071, March 2013.

[41] C. Studer and E. G. Larsson, "Par-aware large-scale multi-user mimo-ofdm downlink," *IEEE Journal on Selected Areas in Communications*, vol. 31, no. 2, pp. 303–313, February 2013.

[42] W. Zhang, H. Ren, C. Pan, M. Chen, R. C. de Lamare, B. Du, and J. Dai, "Large-scale antenna systems with ul/dl hardware mismatch: Achievable rates analysis and calibration," *IEEE Transactions on Communications*, vol. 63, no. 4, pp. 1216–1229, April 2015.

[43] R. Rogalin, O. Y. Bursalioglu, H. Papadopoulos, G. Caire, A. F. Molisch, A. Michaloliakos, V. Balan, and K. Psounis, "Scalable synchronization and reciprocity calibration for

distributed multiuser mimo," *IEEE Transactions on Wireless Communications*, vol. 13, no. 4, pp. 1815–1831, April 2014.

[44] J. Vieira, F. Rusek, and F. Tufvesson, "Reciprocity calibration methods for massive mimo based on antenna coupling," in *2014 IEEE Global Communications Conference*, Dec 2014, pp. 3708–3712.

[45] E. Larsson, O. Edfors, F. Tufvesson, and T. Marzetta, "Massive MIMO for next generation wireless systems," *Communications Magazine, IEEE*, vol. 52, no. 2, pp. 186–195, February 2014.

[46] I. Atzeni, J. Arnau, and M. Debbah, "Fractional pilot reuse in massive mimo systems," in *2015 IEEE International Conference on Communication Workshop (ICCW)*, June 2015, pp. 1030–1035.

[47] K. Appaiah, A. Ashikhmin, and T. L. Marzetta, "Pilot contamination reduction in multiuser tdd systems," in *2010 IEEE International Conference on Communications*, May 2010, pp. 1–5.

[48] H. Yin, D. Gesbert, M. C. Filippou, and Y. Liu, "Decontaminating pilots in massive mimo systems," in *2013 IEEE International Conference on Communications (ICC)*, June 2013, pp. 3170–3175.

[49] R. R. Müller, L. Cottatellucci, and M. Vehkaperä, "Blind pilot decontamination," *IEEE Journal of Selected Topics in Signal Processing*, vol. 8, no. 5, pp. 773–786, Oct 2014.

[50] H. Q. Ngo and E. G. Larsson, "Evd-based channel estimation in multicell multiuser mimo systems with very large antenna arrays," in *2012 IEEE International Conference on Acoustics, Speech and Signal Processing (ICASSP)*, March 2012, pp. 3249–3252.

[51] X. Gao, O. Edfors, F. Rusek, and F. Tufvesson, "Linear pre-coding performance in measured very-large mimo channels," in *2011 IEEE Vehicular Technology Conference (VTC Fall)*, Sep. 2011, pp. 1–5.

[52] ——, "Massive mimo performance evaluation based on measured propagation data," *IEEE Transactions on Wireless Communications*, vol. 14, no. 7, pp. 3899–3911, July 2015.

[53] J. Hoydis, C. Hoek, T. Wild, and S. ten Brink, "Channel measurements for large antenna arrays," in *2012 International Symposium on Wireless Communication Systems (ISWCS)*, Aug 2012, pp. 811–815.

[54] S. Payami and F. Tufvesson, "Channel measurements and analysis for very large array systems at 2.6 ghz," in *2012 6th European Conference on Antennas and Propagation (EUCAP)*, March 2012, pp. 433–437.

[55] C. Shepard, H. Yu, N. Anand, E. Li, T. Marzetta, R. Yang, and L. Zhong, "Argos: Practical many-antenna base stations," in *Proceedings of the 18th Annual International Conference on Mobile Computing and Networking*, ser. Mobicom '12. New York, NY, USA: ACM, 2012, pp. 53–64. [Online]. Available: http://doi.acm.org/10.1145/2348543.2348553

[56] A. Alkhateeb, G. Leus, and R. W. Heath, Jr, "Limited Feedback Hybrid Precoding for Multi-User Millimeter Wave Systems," *ArXiv e-prints*, Sep. 2014.

[57] "Deliverable d5.3 v1.0. winner+ final channel models," Tech. Rep., March 2010.

[58] L. Liu, C. Oestges, J. Poutanen, K. Haneda, P. Vainikainen, F. Quitin, F. Tufvesson, and P. D. Doncker, "The cost 2100 mimo channel model," *IEEE Wireless Communications*, vol. 19, no. 6, pp. 92–99, December 2012.

[59] G. T. . T. S. G. R. A. Network, "Study on 3d channel model for lte (release 12)," Tech. Rep., September 2014.

[60] T. Marzetta, "Noncooperative Cellular Wireless with Unlimited Numbers of Base Station Antennas," *Wireless Communications, IEEE Transactions on*, vol. 9, no. 11, pp. 3590 – 3600, Nov 2010.

[61] S. L. Loyka, "Channel capacity of mimo architecture using the exponential correlation matrix," *IEEE Communications Letters*, vol. 5, no. 9, pp. 369–371, Sep. 2001.

[62] A. Adhikary, J. Nam, J. Ahn, and G. Caire, "Joint spatial division and multiplexing—the large-scale array regime," *IEEE Transactions on Information Theory*, vol. 59, no. 10, pp. 6441–6463, Oct 2013.

[63] T. Bai and R. W. Heath, "Uplink massive mimo sir analysis: How do antennas scale with users?" in *2015 IEEE Global Communications Conference (GLOBECOM)*, Dec 2015, pp. 1–6.

[64] C. Masouros and M. Matthaiou, "Space-constrained massive mimo: Hitting the wall of favorable propagation," *IEEE Communications Letters*, vol. 19, no. 5, pp. 771–774, May 2015.

[65] S. Wu, C. Wang, e. M. Aggoune, M. M. Alwakeel, and Y. He, "A non-stationary 3-d wideband twin-cluster model for 5g massive mimo channels," *IEEE Journal on Selected Areas in Communications*, vol. 32, no. 6, pp. 1207–1218, June 2014.

[66] S. Wu, C. Wang, H. Haas, e. M. Aggoune, M. M. Alwakeel, and B. Ai, "A non-stationary wideband channel model for massive mimo communication systems," *IEEE Transactions on Wireless Communications*, vol. 14, no. 3, pp. 1434–1446, March 2015.

[67] X. Li, S. Zhou, E. Björnson, and J. Wang, "Capacity analysis for spatially non-wide sense stationary uplink massive mimo systems," *IEEE Transactions on Wireless Communications*, vol. 14, no. 12, pp. 7044–7056, Dec 2015.

[68] Z. Pi and F. Khan, "An introduction to millimeter-wave mobile broadband systems," *IEEE Communications Magazine*, vol. 49, no. 6, pp. 101–107, June 2011.

[69] T. S. Rappaport, S. Sun, R. Mayzus, H. Zhao, Y. Azar, K. Wang, G. N. Wong, J. K. Schulz, M. Samimi, and F. Gutierrez, "Millimeter wave mobile communications for 5g cellular: It will work!" *IEEE Access*, vol. 1, pp. 335–349, 2013.

[70] J. G. Andrews, S. Buzzi, W. Choi, S. V. Hanly, A. Lozano, A. C. K. Soong, and J. C. Zhang, "What will 5g be?" *IEEE Journal on Selected Areas in Communications*, vol. 32, no. 6, pp. 1065–1082, June 2014.

[71] F. Boccardi, R. W. Heath, A. Lozano, T. L. Marzetta, and P. Popovski, "Five disruptive technology directions for 5g," *IEEE Communications Magazine*, vol. 52, no. 2, pp. 74–80, February 2014.

[72] S. Rajagopal, S. Abu-Surra, and M. Malmirchegini, "Channel feasibility for outdoor non-line-of-sight mmwave mobile communication," in *2012 IEEE Vehicular Technology Conference (VTC Fall)*, Sep. 2012, pp. 1–6.

[73] T. S. Rappaport, F. Gutierrez, E. Ben-Dor, J. N. Murdock, Y. Qiao, and J. I. Tamir, "Broadband millimeter-wave propagation measurements and models using adaptive-beam antennas for outdoor urban cellular communications," *IEEE Transactions on Antennas and Propagation*, vol. 61, no. 4, pp. 1850–1859, April 2013.

[74] T. S. Rappaport, G. R. MacCartney, M. K. Samimi, and S. Sun, "Wideband millimeter-wave propagation measurements and channel models for future wireless communication system design," *IEEE Transactions on Communications*, vol. 63, no. 9, pp. 3029–3056, Sep. 2015.

[75] C. R. Anderson and T. S. Rappaport, "In-building wideband partition loss measurements at 2.5 and 60 ghz," *IEEE Transactions on Wireless Communications*, vol. 3, no. 3, pp. 922–928, May 2004.

[76] B. Langen, G. Lober, and W. Herzig, "Reflection and transmission behaviour of building materials at 60 ghz," in *5th IEEE International Symposium on Personal, Indoor and Mobile Radio Communications, Wireless Networks - Catching the Mobile Future.*, vol. 2, Sep. 1994, pp. 505–509 vol.2.

[77] A. V. Alejos, M. G. Sanchez, and I. Cuinas, "Measurement and analysis of propagation mechanisms at 40 ghz: Viability of site shielding forced by obstacles," *IEEE Transactions on Vehicular Technology*, vol. 57, no. 6, pp. 3369–3380, Nov 2008.

[78] T. Bai and R. W. Heath, "Analysis of self-body blocking effects in millimeter wave cellular networks," in *2014 48th Asilomar Conference on Signals, Systems and Computers*, Nov 2014, pp. 1921–1925.

[79] T. S. Rappaport and S. Deng, "73 ghz wideband millimeter-wave foliage and ground reflection measurements and models," in *2015 IEEE International Conference on Communication Workshop (ICCW)*, June 2015, pp. 1238–1243.

[80] A. Y. Nashashibi, K. Sarabandi, S. Oveisgharan, M. C. Dobson, W. S. Walker, and E. Burke, "Millimeter-wave measurements of foliage attenuation and ground reflectivity of tree stands at nadir incidence," *IEEE Transactions on Antennas and Propagation*, vol. 52, no. 5, pp. 1211–1222, May 2004.

[81] T. S. Rappaport, E. Ben-Dor, J. N. Murdock, and Y. Qiao, "38 ghz and 60 ghz angle-dependent propagation for cellular peer-to-peer wireless communications," in *2012 IEEE International Conference on Communications (ICC)*, June 2012, pp. 4568–4573.

[82] D. E. Berraki, S. M. D. Armour, and A. R. Nix, "Application of compressive sensing in sparse spatial channel recovery for beamforming in mmwave outdoor systems," in *2014 IEEE Wireless Communications and Networking Conference (WCNC)*, April 2014, pp. 887–892.

[83] A. Alkhateeb, G. Leus, and R. W. Heath, "Compressed sensing based multi-user millimeter wave systems: How many measurements are needed?" in *2015 IEEE International Conference on Acoustics, Speech and Signal Processing (ICASSP)*, April 2015, pp. 2909–2913.

[84] M. Jacob, S. Priebe, R. Dickhoff, T. Kleine-Ostmann, T. Schrader, and T. Kurner, "Diffraction in mm and sub-mm wave indoor propagation channels," *IEEE Transactions on Microwave Theory and Techniques*, vol. 60, no. 3, pp. 833–844, March 2012.

[85] P. Karadimas, B. Allen, and P. Smith, "Human body shadowing characterization for 60-ghz indoor short-range wireless links," *IEEE Antennas and Wireless Propagation Letters*, vol. 12, pp. 1650–1653, 2013.

[86] A. M. Sayeed, "Deconstructing multiantenna fading channels," *IEEE Transactions on Signal Processing*, vol. 50, no. 10, pp. 2563–2579, Oct 2002.

[87] S. Singh, F. Ziliotto, U. Madhow, E. Belding, and M. Rodwell, "Blockage and directivity in 60 ghz wireless personal area networks: from cross-layer model to multihop mac design," *IEEE Journal on Selected Areas in Communications*, vol. 27, no. 8, pp. 1400–1413, October 2009.

[88] J. Mo and R. W. Heath, "Capacity analysis of one-bit quantized mimo systems with transmitter channel state information," *IEEE Transactions on Signal Processing*, vol. 63, no. 20, pp. 5498–5512, Oct 2015.

[89] A. Alkhateeb, J. Mo, N. Gonzalez-Prelcic, and R. W. Heath, "Mimo precoding and combining solutions for millimeter-wave systems," *IEEE Communications Magazine*, vol. 52, no. 12, pp. 122–131, December 2014.

[90] R. Méndez-Rial, C. Rusu, N. González-Prelcic, A. Alkhateeb, and R. W. Heath, "Hybrid mimo architectures for millimeter wave communications: Phase shifters or switches?" *IEEE Access*, vol. 4, pp. 247–267, 2016.

[91] Á. Gonzalo, I. Santamaría, J. Vía, F. Gholam, and R. Eickhoff, *Equal Gain MIMO Beamforming in the RF Domain for OFDM-WLAN Systems*. Berlin, Heidelberg: Springer Berlin Heidelberg, 2010, pp. 136–147. [Online]. Available: https://doi.org/10.1007/978-3-642-16644-0_13

[92] D. J. Love and R. W. Heath, "Equal gain transmission in multiple-input multiple-output wireless systems," *IEEE Transactions on Communications*, vol. 51, no. 7, pp. 1102–1110, July 2003.

[93] R. Méndez-Rial, C. Rusu, A. Alkhateeb, N. González-Prelcic, and R. W. Heath, "Channel estimation and hybrid combining for mmwave: Phase shifters or switches?" in *2015 Information Theory and Applications Workshop (ITA)*, Feb 2015, pp. 90–97.

[94] F. Sohrabi and W. Yu, "Hybrid beamforming with finite-resolution phase shifters for large-scale mimo systems," in *2015 IEEE 16th International Workshop on Signal Processing Advances in Wireless Communications (SPAWC)*, June 2015, pp. 136–140.

[95] K. Roth, H. Pirzadeh, A. L. Swindlehurst, and J. A. Nossek, "A comparison of hybrid beamforming and digital beamforming with low-resolution adcs for multiple users and imperfect csi," *IEEE Journal of Selected Topics in Signal Processing*, vol. 12, no. 3, pp. 484–498, June 2018.

[96] F. Sohrabi and W. Yu, "Hybrid digital and analog beamforming design for large-scale mimo systems," in *2015 IEEE International Conference on Acoustics, Speech and Signal Processing (ICASSP)*, April 2015, pp. 2929–2933.

[97] R. Méndez-Rial, C. Rusu, N. González-Prelcic, and R. W. Heath, "Dictionary-free hybrid precoders and combiners for mmwave mimo systems," in *2015 IEEE 16th International Workshop on Signal Processing Advances in Wireless Communications (SPAWC)*, June 2015, pp. 151–155.

[98] A. M. Sayeed, "Multi-aperture phased arrays versus multi-beam lens arrays for mmw multiuser mimo," in *2017 51st Asilomar Conference on Signals, Systems, and Computers*, Oct 2017, pp. 943–950.

[99] J. Li, L. Xiao, X. Xu, X. Su, and S. Zhou, "Energy-efficient butler-matrix-based hybrid beamforming for multiuser mmwave mimo system," *Science China Information Sciences*, vol. 60, no. 8, p. 080304, May 2017. [Online]. Available: https://doi.org/10.1007/s11432-016-0640-5

[100] J. Brady, N. Behdad, and A. M. Sayeed, "Beamspace mimo for millimeter-wave communications: System architecture, modeling, analysis, and measurements," *IEEE Transactions on Antennas and Propagation*, vol. 61, no. 7, pp. 3814–3827, July 2013.

[101] D. Tse and P. Viswanath, *Fundamentals of Wireless Communication*. Cambridge University Press, 2005.

[102] X. Zhang, A. F. Molisch, and S.-Y. Kung, "Variable-phase-shift-based rf-baseband codesign for mimo antenna selection," *IEEE Transactions on Signal Processing*, vol. 53, no. 11, pp. 4091–4103, Nov 2005.

[103] T. E. Bogale, L. B. Le, A. Haghighat, and L. Vandendorpe, "On the number of rf chains and phase shifters, and scheduling design with hybrid analog–digital beamforming," *IEEE Transactions on Wireless Communications*, vol. 15, no. 5, pp. 3311–3326, May 2016.

[104] H. Tataria, P. J. Smith, L. J. Greenstein, P. A. Dmochowski, and M. Matthaiou, "Impact of line-of-sight and unequal spatial correlation on uplink mu-mimo systems," *IEEE Wireless Communications Letters*, vol. 6, no. 5, pp. 634–637, Oct 2017.

[105] M. El Hajj, G. Zaharia, G. El Zein, H. Farhat, and S. Sadek, "Millimeter-wave propagation measurements at 60 ghz in indoor environments," in *2019 International Symposium on Signals, Circuits and Systems (ISSCS)*, July 2019, pp. 1–4.

[106] S. Li, P. J. Smith, P. A. Dmochowski, H. Tataria, M. Matthaiou, and J. W. Yin, "Massive MIMO for ray-based channels," in *2019 Internantional Conference on Communications (ICC) - (submitted)*, 2019.

[107] M. Roy, S. Paquelet, L. L. Magoarou, and M. Crussière, "MIMO channel hardening: A physical model based analysis," *The 14th International Conference on Wireless and Mobile Computing, Networking and Communications (WiMob 2018) - (Accepted)*, vol. abs/1804.07491, 2018. [Online]. Available: http://arxiv.org/abs/1804.07491

[108] X. Wu, N. C. Beaulieu, and D. Liu, "On favorable propagation in massive MIMO systems and different antenna configurations," *IEEE Access*, vol. 5, pp. 5578–5593, 2017.

[109] Q. Zhang, S. Jin, K. Wong, H. Zhu, and M. Matthaiou, "Power scaling of uplink massive MIMO systems with arbitrary-rank channel means," *IEEE Journal of Selected Topics in Signal Processing*, vol. 8, no. 5, pp. 966–981, Oct 2014.

[110] S. Li, P. Smith, P. Dmochowski, and Y. Jingwei, "Analysis of analog and digital mrc for distributed and centralized mu-MIMO systems," *IEEE Transactions on Vehicular Technology*, pp. 1–1, 2018.

[111] J. M. Aldaz, S. Barza, M. Fujii, and M. S. Moslehian, "Advances in operator cauchy–schwarz inequalities and their reverses," *Ann. Funct. Anal.*, vol. 6, no. 3, pp. 275–295, 2015. [Online]. Available: https://doi.org/10.15352/afa/06-3-20

[112] L. Liang, W. Xu, and X. Dong, "Low-complexity hybrid precoding in massive multiuser mimo systems," *IEEE Wireless Communications Letters*, vol. 3, no. 6, pp. 653–656, Dec 2014.

[113] S. Tsai, "Equal gain transmission with antenna selection in mimo communications," *IEEE Transactions on Wireless Communications*, vol. 10, no. 5, pp. 1470–1479, May 2011.

[114] D. Zhang, P. Pan, R. You, and H. Wang, "Svd-based low-complexity hybrid precoding for millimeter-wave mimo systems," *IEEE Communications Letters*, vol. 22, no. 10, pp. 2176–2179, Oct 2018.

[115] Y. Zou, W. Rave, and G. Fettweis, "Analog beamsteering for flexible hybrid beamforming design in mmwave communications," in *2016 European Conference on Networks and Communications (EuCNC)*, June 2016, pp. 94–99.

[116] W. Cai, P. Wang, Y. Li, Y. Zhang, and B. Vucetic, "Deployment optimization of uniform linear antenna arrays for a two-path millimeter wave communication system," *IEEE Communications Letters*, vol. 19, no. 4, pp. 669–672, April 2015.

[117] C.-A. Deledalle, L. Denis, S. Tabti, and F. Tupin, "Closed-form expressions of the eigen decomposition of 2 x 2 and 3 x 3 Hermitian matrices," Université de Lyon, Research Report, 2017. [Online]. Available: https://hal.archives-ouvertes.fr/hal-01501221

[118] X. Zheng, Y. Xie, J. Li, and P. Stoica, "Mimo transmit beamforming under uniform elemental power constraint," *IEEE Transactions on Signal Processing*, vol. 55, no. 11, pp. 5395–5406, Nov 2007.

[119] W. Fang, H. Sun, and L. Yang, "Power allocation for maximizing sum capacity of multiuser mimo downlink with transmit precoding based on slnr," in *2011 IEEE 73rd Vehicular Technology Conference (VTC Spring)*, May 2011, pp. 1–5.

[120] J. Jang, K. B. Lee, and Y.-H. Lee, "Transmit power and bit allocations for ofdm systems in a fading channel," in *Global Telecommunications Conference, 2003. GLOBECOM '03. IEEE*, vol. 2, Dec 2003, pp. 858–862 Vol.2.

[121] J. Zhang, Y. Jiang, P. Li, F. Zheng, and X. You, "Energy efficient power allocation in massive mimo systems based on standard interference function," in *2016 IEEE 83rd Vehicular Technology Conference (VTC Spring)*, May 2016, pp. 1–6.

[122] L. Zhao, H. Zhao, F. Hu, K. Zheng, and J. Zhang, "Energy Efficient Power Allocation Algorithm for Downlink Massive MIMO with MRT Precoding," in *Vehicular Technology Conference (VTC Fall), 2013 IEEE 78th*, Sep. 2013, pp. 1–5.

[123] I. K. Choi and S. K. Lee, *Method and apparatus for allocating transmission power in multi input multi output system.* Google Patents, Nov. 2014, uS Patent 8,891,643.

[124] L. Dong, G. Wu, H. Feng, and S. Li, "Leakage-based power allocation for relaxed SLNR beamforming in multi-cell MU-MIMO systems," in *2014 IEEE International Conference on Communication Systems (ICCS)*, Nov. 2014, pp. 512–516.

[125] A. Roze, M. Helard, M. Crussiere, and C. Langlais, "Linear Precoder Performance for Massive MIMO Systems in near LOS Environments: Application to mmWave Transmission," in *European Wireless 2015; 21th European Wireless Conference; Proceedings of.* VDE, 2015.

[126] A. Rozé, M. Helard, M. Crussiere, and C. Langlais, "Millimeter-Wave Digital Beamsteering in Highly Line-of-Sight Environments for Massive MIMO Systems," in *Wireless World Research Forum Meeting 35*, 2015.

[127] C. S. Park, Y. S. Byun, A. M. Bokiye, and Y. H. Lee, "Complexity reduced zero-forcing beamforming in massive mimo systems," in *2014 Information Theory and Applications Workshop (ITA)*, Feb 2014, pp. 1–5.

[128] "IMT vision – framework and overall objectives of the future development of IMT for 2020 and beyond," M.2083-0, International Telecommunication Union – ITU, Sep. 2015.

[129] T. Bai and R. W. Heath, "Coverage analysis for millimeter wave cellular networks with blockage effects," in *2013 IEEE Global Conference on Signal and Information Processing*, Dec 2013, pp. 727–730.

[130] Y. Oguma, T. Nishio, K. Yamamoto, and M. Morikura, "Performance modeling of camera-assisted proactive base station selection for human blockage problem in mmwave communications," in *2016 IEEE Wireless Communications and Networking Conference*, April 2016, pp. 1–7.

[131] J. Arnold, L. Simic, M. Petrova, and P. Mahonen, "Radar-enhanced mm-wave agile beamsteering: Demo," in *Proceedings of the Tenth ACM International Workshop on Wireless Network Testbeds, Experimental Evaluation, and Characterization*, 2016, pp. 83–84.

[132] S. Biswas, S. Vuppala, J. Xue, and T. Ratnarajah, "On the performance of relay aided millimeter wave networks," *IEEE Journal of Selected Topics in Signal Processing*, vol. 10, no. 3, pp. 576–588, April 2016.

[133] N. Wei, X. Lin, and Z. Zhang, "Optimal relay probing in millimeter-wave cellular systems with device-to-device relaying," *IEEE Transactions on Vehicular Technology*, vol. 65, no. 12, pp. 10 218–10 222, Dec 2016.

[134] S. Sur, X. Zhang, P. Ramanathan, and R. Chandra, "Beamspy: Enabling robust 60 ghz links under blockage," in *Proceedings of the 13th Usenix Conference on Networked Systems Design and Implementation*, ser. NSDI'16. Berkeley, CA, USA: USENIX Association, 2016, pp. 193–206. [Online]. Available: http://dl.acm.org/citation.cfm?id=2930611.2930625

[135] Y. R. Ramadan, A. S. Ibrahim, and M. M. Khairy, "Robust rf beamforming for millimeter wave mimo–ofdm systems," *International Journal of Wireless Information Networks*, vol. 22, no. 4, pp. 327–335, Dec 2015. [Online]. Available: https://doi.org/10.1007/s10776-015-0287-7

[136] M. Park and H. K. Pan, "A spatial diversity technique for ieee 802.11ad wlan in 60 ghz band," *IEEE Communications Letters*, vol. 16, no. 8, pp. 1260–1262, August 2012.

[137] Z. Xiao, X.-G. Xia, D. Jin, and N. Ge, "Multipath grouping for millimeter-wave communications," in *2013 IEEE Global Communications Conference (GLOBECOM)*, Dec 2013, pp. 3378–3383.

[138] Z. Li, S. Han, and A. F. Molisch, "Hybrid beamforming design for millimeter-wave multi-user massive mimo downlink," in *2016 IEEE International Conference on Communications (ICC)*, May 2016, pp. 1–6.

[139] J. Noh, T. Kim, J. Y. Seol, and C. Lee, "Zero-forcing based hybrid beamforming for multi-user millimeter wave systems," *IET Communications*, vol. 10, no. 18, pp. 2670–2677, 2016.

[140] T. Yoo and A. Goldsmith, "On the optimality of multiantenna broadcast scheduling using zero-forcing beamforming," *IEEE Journal on Selected Areas in Communications*, vol. 24, no. 3, pp. 528–541, March 2006.

[141] J. Mao, J. Gao, Y. Liu, and G. Xie, "Simplified semi-orthogonal user selection for mu-mimo systems with zfbf," *IEEE Wireless Communications Letters*, vol. 1, no. 1, pp. 42–45, February 2012.

[142] D. L. Ruyet, H. Khanfir, and B. Ozbek, "Performance of semi-orthogonal user selection for multiuser miso systems," in *2008 IEEE 9th Workshop on Signal Processing Advances in Wireless Communications*, July 2008, pp. 321–325.

[143] S. Nam, J. Kim, and Y. Han, "A user selection algorithm using angle between subspaces for downlink mu-mimo systems," *IEEE Transactions on Communications*, vol. 62, no. 2, pp. 616–624, February 2014.

[144] X. Yi and E. K. S. Au, "User scheduling for heterogeneous multiuser mimo systems: A subspace viewpoint," *IEEE Transactions on Vehicular Technology*, vol. 60, no. 8, pp. 4004–4013, Oct 2011.

[145] K. Ko and J. Lee, "Multiuser mimo user selection based on chordal distance," *IEEE Transactions on Communications*, vol. 60, no. 3, pp. 649–654, March 2012.

[146] ——, "Determinant based multiuser mimo scheduling with reduced pilot overhead," in *2011 IEEE 73rd Vehicular Technology Conference (VTC Spring)*, May 2011, pp. 1–5.

[147] X. Lu, J. Wu, X. Huang, W. Li, J. Lu, and Z. Gong, "An improved semi-orthogonal user selection algorithm based on condition number for multiuser mimo systems," *China Communications*, vol. 11, no. 13, pp. 23–30, Supplement 2014.

[148] M. Sadek and S. Aissa, "Leakage based precoding for multi-user mimo-ofdm systems," *IEEE Transactions on Wireless Communications*, vol. 10, no. 8, pp. 2428–2433, August 2011.

[149] N. S. Perović, P. Liu, M. D. Renzo, and A. Springer, "Receive spatial modulation for los mmwave communications based on tx beamforming," *IEEE Communications Letters*, vol. 21, no. 4, pp. 921–924, April 2017.

[150] J. Xu, L. Qiu, and C. Yu, "Improving energy efficiency through multimode transmission in the downlink mimo systems," *EURASIP Journal on Wireless Communications and Networking*, vol. 2011, no. 1, pp. 1–12, 2011.

[151] M. D. Renzo, H. Haas, and P. M. Grant, "Spatial modulation for multiple-antenna wireless systems: a survey," *IEEE Communications Magazine*, vol. 49, no. 12, pp. 182–191, December 2011.

[152] Y. A. Chau and S.-H. Yu, "Space modulation on wireless fading channels," in *Vehicular Technology Conference, 2001. VTC 2001 Fall. IEEE VTS 54th*, vol. 3. IEEE, 2001, pp. 1668–1671.

[153] J. Jeganathan, A. Ghrayeb, L. Szczecinski, and A. Ceron, "Space shift keying modulation for mimo channels," *IEEE Transactions on Wireless Communications*, vol. 8, no. 7, pp. 3692–3703, 2009.

[154] M. Di Renzo, H. Haas, A. Ghrayeb, S. Sugiura, and L. Hanzo, "Spatial modulation for generalized mimo: Challenges, opportunities, and implementation," *Proceedings of the IEEE*, vol. 102, no. 1, pp. 56–103, 2014.

[155] D.-T. Phan-Huy and M. Hélard, "Receive antenna shift keying for time reversal wireless communications," in *2012 IEEE International Conference on Communications (ICC)*. IEEE, 2012, pp. 4852–4856.

[156] A. Mokh, M. Crussiere, M. Helard, and M. D. Renzo, "Theoretical performance of coherent and incoherent detection for zero-forcing receive antenna shift keying," *IEEE Access*, 2018.

[157] J. Wang, L. He, and J. Song, "An overview of spatial modulation techniques for millimeter wave mimo systems," in *2017 IVth International Conference on Engineering and Telecommunication (EnT)*, Nov 2017, pp. 51–56.

[158] P. Liu and A. Springer, "Space shift keying for los communication at mmwave frequencies," *IEEE Wireless Communications Letters*, vol. 4, no. 2, pp. 121–124, April 2015.

[159] P. Liu, M. D. Renzo, and A. Springer, "Line-of-sight spatial modulation for indoor mmwave communication at 60 ghz," *IEEE Transactions on Wireless Communications*, vol. 15, no. 11, pp. 7373–7389, Nov 2016.

[160] R. Mesleh and A. Younis, "Capacity analysis for los millimeter–wave quadrature spatial modulation," *Wireless Networks*, Jan 2017. [Online]. Available: https://doi.org/10.1007/s11276-017-1444-y

[161] P. Liu, M. D. Renzo, and A. Springer, "Variable- n_u generalized spatial modulation for indoor los mmwave communication: Performance optimization and novel switching structure," *IEEE Transactions on Communications*, vol. 65, no. 6, pp. 2625–2640, June 2017.

[162] P. Liu, J. Blumenstein, N. S. Perović, M. D. Renzo, and A. Springer, "Performance of generalized spatial modulation mimo over measured 60ghz indoor channels," *IEEE Transactions on Communications*, vol. 66, no. 1, pp. 133–148, Jan 2018.

[163] I. A. Hemadeh, M. El-Hajjar, S. Won, and L. Hanzo, "Multi-set space-time shift keying and space- frequency space-time shift keying for millimeter-wave communications," *IEEE Access*, vol. 5, pp. 8324–8342, 2017.

[164] I. A. Hemadeh, P. Botsinis, M. El-Hajjar, S. Won, and L. Hanzo, "Reduced-rf-chain aided soft-decision multi-set steered space-time shift-keying for millimeter-wave communications," *IEEE Access*, vol. 5, pp. 7223–7243, 2017.

[165] N. Ishikawa, R. Rajashekar, S. Sugiura, and L. Hanzo, "Generalized-spatial-modulation-based reduced-rf-chain millimeter-wave communications," *IEEE Transactions on Vehicular Technology*, vol. 66, no. 1, pp. 879–883, Jan 2017.

[166] S. Luo, X. T. Tran, K. C. Teh, and K. H. Li, "Adaptive spatial modulation for uplink mmwave communication systems," *IEEE Communications Letters*, vol. 21, no. 10, pp. 2178–2181, Oct 2017.

[167] Y. Ding, V. Fusco, A. Shitvov, Y. Xiao, and H. Li, "Beam index modulation wireless communication with analog beamforming," *IEEE Transactions on Vehicular Technology*, pp. 1–1, 2018.

[168] M. Lee and W. Chung, "Adaptive multimode hybrid precoding for single-rf virtual space modulation with analog phase shift network in mimo systems," *IEEE Transactions on Wireless Communications*, vol. 16, no. 4, pp. 2139–2152, April 2017.

[169] L. He, J. Wang, and J. Song, "On generalized spatial modulation aided millimeter wave mimo: Spectral efficiency analysis and hybrid precoder design," *IEEE Transactions on Wireless Communications*, vol. 16, no. 11, pp. 7658–7671, Nov 2017.

[170] Y. Ding, K. J. Kim, T. Koike-Akino, M. Pajovic, P. Wang, and P. Orlik, "Spatial scattering modulation for uplink millimeter-wave systems," *IEEE Communications Letters*, vol. 21, no. 7, pp. 1493–1496, July 2017.

[171] L. He, J. Wang, and J. Song, "Spatial modulation for more spatial multiplexing: Rf-chain-limited generalized spatial modulation aided mm-wave mimo with hybrid precoding," *IEEE Transactions on Communications*, vol. 66, no. 3, pp. 986–998, March 2018.

[172] A. Mokh, M. Shehata, M. Crussiere, and M. Helard, "Analytical performance of hybrid beam index modulation," in *IEEE Wireless Communication Letters - (submitted)*, 2019.

[173] M. Abramowitz, *Handbook of Mathematical Functions, With Formulas, Graphs, and Mathematical Tables,*. New York, NY, USA: Dover Publications, Inc., 1974.

[174] Z. Gao, L. Dai, C. Yuen, and Z. Wang, "Asymptotic orthogonality analysis of time-domain sparse massive mimo channels," *IEEE Communications Letters*, vol. 19, no. 10, pp. 1826–1829, Oct 2015.

[175] E. Basar, M. Wen, R. Mesleh, M. Di Renzo, Y. Xiao, and H. Haas, "Index modulation techniques for next-generation wireless networks," *IEEE Access*, vol. 5, pp. 16 693–16 746, 2017.

[176] J. Wang, L. He, and J. Song, "Towards higher spectral efficiency: Spatial path index modulation improves millimeter-wave hybrid beamforming," *CoRR*, vol. abs/1902.09709, 2019. [Online]. Available: http://arxiv.org/abs/1902.09709

[177] Y. M. Tsang, A. S. Y. Poon, and S. Addepalli, "Coding the beams: Improving beamforming training in mmwave communication system," in *2011 IEEE Global Telecommunications Conference - GLOBECOM 2011*, Dec 2011, pp. 1–6.

[178] X. Wu, N. C. Beaulieu, and D. Liu, "On favorable propagation in massive mimo systems and different antenna configurations," *IEEE Access*, vol. 5, pp. 5578–5593, 2017.

[179] B. Rivet, L. Girin, and C. Jutten, "Log-rayleigh distribution: A simple and efficient statistical representation of log-spectral coefficients," *IEEE Transactions on Audio, Speech, and Language Processing*, vol. 15, no. 3, pp. 796–802, March 2007.

AVIS DU JURY SUR LA REPRODUCTION DE LA THESE SOUTENUE

Titre de la thèse:
Hybrid Analog and Digital Techniques Applied to Massive MIMO systems for 5G Transmissions at millimeter waves

Nom Prénom de l'auteur : SHEHATA MOHAMED

Membres du jury :
- Monsieur PAJUSCO Patrice
- Monsieur ROY Sébastien
- Monsieur DOLL André
- Monsieur DEBBAH Mérouane
- Madame HELARD Maryline
- Monsieur CRUSSIERE Matthieu
- Madame BOUCHERET Marie-Laure
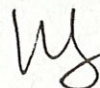
Président du jury : *Prof. Merouane DEBBAH*

Date de la soutenance : 07 Novembre 2019

Reproduction de la these soutenue

☑ Thèse pouvant être reproduite en l'état
☐ Thèse pouvant être reproduite après corrections suggérées

Fait à Rennes, le 07 Novembre 2019

Signature du président de jury

Le Directeur,

M'hamed DRISSI

Titre : Techniques Hybrides Analogiques et Numériques Appliquées aux Systèmes MIMO Massif pour la Transmission 5G aux Ondes Millimétriques.

Mots clés : MIMO Massif, Ondes Millimétriques, Techniques Hybrides, Efficacité Spectrale

Résumé : L'objectif principal de ce travail est d'analyser analytiquement les performances de la formation de faisceaux hybrides (HBF) dans des systèmes MIMO massifs à ondes millimétriques (mmWave), de développer des algorithmes HBF de faible complexité et optimiser les systèmes hybrides comprenant des analogiques et numériques pour s'adapter à ces systèmes et enfin de vérifier la validité pratique de ces algorithmes. Le système MIMO massif fournit un gain de transmission élevé, permettent de compenser les pertes importantes en espace libre inhérentes aux transmissions mmWave. D'autre part, l'utilisation de système HBF dans des canaux clairs offre une performance proche de l'efficacité spectrale (SE) par rapport à la formation de faisceau entièrement numérique, avec un coût matériel et une consommation d'énergie inférieurs.

Dans cette thèse, nous commençons par définir les conditions pour lesquelles le HBF et la formation de faisceau entièrement numérique peuvent atteindre des performances SE similaires. Ensuite, nous analysons l'écart de performance SE qui se produit entre eux dans des canaux MIMO mmWave. De plus, nous fournissons des modèles analytique SE pour les techniques de base analogiques et HBF dans des canaux MIMO mmWave typiques. Nous considérons ensuite une structure MIMO HBF massive multi-utilisateurs (MU) qui prend en compte plusieurs techniques de traitement de signaux spatiaux de faible complexité afin de fournir un système HBF de faible complexité de mise en œuvre pour les futurs réseaux de communication sans fil.

Title : Hybrid Analog and Digital Techniques Applied to Massive MIMO Systems for 5G Transmission at Millimeter Waves.

Keywords : Massive MIMO, Millemeter Wave, Hybrid Beamforming, Spectral Efficiency

Abstract : The main aim of this work is to analytically analyze the performance of Hybrid Beamforming (HBF) in Millimeter Wave (mmWave) massive MIMO systems, to develop low complexity HBF algorithms to adapt with such systems and finally to verify the practical validity of these algorithms. The massive MIMO array provides high transmit gain overcoming the severe path-loss limitation of the mmWave systems. On the other hand applying HBF in sparse channels achieves close Spectral Efficiency (SE) performance compared to the full digital beamforming, however with lower hardware cost and power consumption. In this thesis we start by defining the conditions for which both the HBF and full digital beamforming can achieve similar SE performance.

Then, we analyze the SE performance gap that arise between them in sparse mmWave MIMO channels. Moreover, we provide closed form SE models for basic analog and HBF techniques in typical mmWave MIMO channels. Later we consider a Multi User (MU) massive MIMO HBF framework that considers multiple spatial signal processing techniques for the analog domain processing, digital domain processing, power allocation and users scheduling. We develop low complexity algorithms for such framework in order to provide a low complexity practical HBF for future wireless communication networks that can cope with the challenges of mmWave transmission.